EXPERIMENTAL CONSTRAINTS ON CRUSTAL CONTAMINATION IN PROTEROZOIC ANORTHOSITE PETROGENESIS

Catherine Mary Hill

A Dissertation submitted to the Faculty of Science, University of the Witwatersrand, Johannesburg, in fulfilment of the requirements for the degree of Master of Science.

Johannesburg, 2017

I declare that this dissertation is my own, unaided work. It is being submitted for the Degree of Master of Science at the University of the Witwatersrand, Johannesburg. It has not been submitted before for any degree or examination at any other University.

____

Catherine Mary Hill

______________ day of May 2017 in _______________________________

Abstract

Massif-type anorthosites formed in the Proterozoic Eon are the most voluminous anorthosite occurrences on Earth, reaching tens of thousands of square kilometers in aerial extent. While they formed throughout the Proterozoic, most formed during a 700 Ma period between 1800 and 1100 Ma. The rocks are dominated by plagioclase (typically 70 – 95 volume %) of intermediate composition (An_{40-65}). Olivine, orthopyroxene, clinopyroxene and Fe-Ti oxides make up the minor mafic proportion. While most researchers agree that the anorthosites formed from a high-alumina basaltic parental magma, there are disparate views on how that parental magma was generated. Whether the parental magma formed by partial melting of the lower crust, or by mantle melting, is a topic of much debate. The anorthosites commonly have crust-like isotopic signatures, but this could be produced by melting of the lower crust, or by crustal contamination of mantle-derived magmas. Many Proterozoic anorthosite complexes consist of both olivine-bearing and orthopyroxene-bearing anorthosites. This has been attributed to variable amounts of crustal contamination of mantle-derived magmas, based on evidence from isotopes and field relations. While geochemical and petrologic evidence for crustal contamination is plentiful, existing experimental work shows that a thermal divide exists for high-alumina basalts fractionating at lower crustal depths, casting doubts on whether fractionation of a mantle melt could produce anorthosite. Here I use high-pressure experiments to test whether the fractionation of high-alumina basalt can form anorthosites, and to what extent crustal contamination affects the fractionation sequence. The results are compared to new geochemical and petrologic data from the Kunene Anorthosite Complex (KAC), in Angola and Namibia.

The KAC is one of the largest anorthosite complexes in the world, with an area of ~18 000 km^2. The KAC (1438 – 1319 Ma) has an elongate shape and intruded into Palaeoproterozoic to Mesoproterozoic country rocks (~2200 to 1635 Ma) at the southern margin of the Congo craton. It is associated with a suite of granitoid rocks of variable composition, which are akin to the granitoids associated with nearly all Proterozoic anorthosites. The granitoids have been shown to be coeval with the anorthosites, but were from a chemically independent magma series. The most distinctive granitoids in the KAC are the Red Granites, which outcrop around the southern margins of the complex, and also cross-cut the complex in a NE-SW linear belt, dividing the complex roughly into northern and southern domains. The rocks of the KAC are highly variable in terms of mode, mineral chemistry, and texture, but there is a general trend of more olivine-bearing anorthosites north of the granite belt, and orthopyroxene-bearing anorthosites to the south. The olivine-bearing rocks (or

leucotroctolites) typically contain plagioclase and cumulus and/or intercumulus olivine, with lesser interstitial orthopyroxene and/or clinopyroxene, Fe-Ti oxides, and biotite. The orthopyroxene-bearing anorthosites (or leuconorites) contain cumulus plagioclase ± cumulus orthopyroxene, and interstitial orthopyroxene, clinopyroxene, oxides and biotite. The leucotroctolites are characterized by more calcic plagioclase (An_{56-75}), while the leuconorites contain more intermediate plagioclase (An_{48-56}). The variability of the rocks across the complex suggests that the KAC consists of several coalesced plutons with different histories. The petrologic data and field observations in this study are consistent with the leuconorites of the complex being derived from a mantle-derived magma that experienced contamination by silica-rich rocks, crystallizing orthopyroxene rather than olivine, and less calcic plagioclase. The leucotroctolites experienced less or no contamination.

To test whether the mineral dichotomy and the variations in plagioclase chemistry observed in Proterozoic anorthosites are due to variably contaminated mantle-derived magma, piston cylinder experiments were conducted on a synthetic high-alumina basalt (HAB) composition, as well as a mixture of this HAB with 30% of a Red Granite composition. Experiments were conducted at 10 kbar, to simulate the depth at which anorthosite differentiation most likely begins (based on Al-in-orthopyroxene geobarometry of highly aluminous orthopyroxene megacrysts that occur in many massifs). The uncontaminated experiments produced olivine as the first liquidus phase, followed by plagioclase (An_{65-68}), and then by clinopyroxene, pigeonite and ilmenite at progressively lower temperatures. Residual liquids evolve towards more silica-rich compositions with decreasing temperature. The contamination experiments produced liquidus orthopyroxene, followed by plagioclase (An_{51-56}), and then by pigeonite at lower temperatures. The experiments show that contamination of a primitive HAB magma by granitic material, most likely produced by partial melting of the lower crust during anorthosite formation, can shift the mineral assemblages of the crystallizing anorthosite from olivine-bearing to orthopyroxene-bearing, and produce less calcic plagioclase than the uncontaminated HAB magma. This could explain the observation of olivine-bearing and orthopyroxene-bearing anorthosites in the KAC and many other Proterozoic anorthosites.

Previous high-pressure experimental studies, using a slightly more evolved HAB composition, indicated the presence of a thermal divide, which causes liquids to evolve to more Si-poor compositions. The experimental results presented in this study however, do not show a thermal divide, indicating that small variations in experimental starting composition can cause large differences in the liquid line of descent. The results of this study indicate that partial melting of the mantle can produce anorthosite parental magmas, and that the range in mineral assemblages of the anorthosites can be accounted for by crustal contamination of a mantle-derived magma.

Fractionation of the experimental starting compositions was also modeled using the MELTS algorithm. These calculations produce a close match to the experimental liquid trends. This allows for modeling of a variety of compositional and environmental variables. The MELTS modeling shows that as little as 10% contamination of HAB magma with a granitic composition may position the magma in the orthopyroxene stability field, forming orthopyroxene-bearing anorthosites. The modeling also shows that a variety of silica-rich contaminants, including granites, granodiorites and tonalities, produce similar results and liquid evolution trends, so a range of granitoid compositions may successfully produce the shift in mineral assemblages of the anorthosites. This suggests that crustal contamination of mantle-derived HAB could be a widespread process and the primary mechanism that produces the distinctive crust-like signatures in Proterozoic anorthosites.

In summary, the mineralogical and chemical diversity observed in Proterozoic anorthosites can be produced by variable amounts of crustal contamination of mantle-derived, high-alumina basaltic magma. The experimental results in this study combined with field observations, and geochemical and isotopic data, provide evidence for a model of massif-type anorthosite petrogenesis. Orthopyroxene-bearing rocks formed from an originally high-alumina basaltic magma that experienced contamination by granitic partial melts of the lower crust, during ponding of the magma at the Moho. This process preconditioned the surrounding crust and possibly prevented further anatexis. Following emplacement of orthopyroxene-bearing anorthosites, subsequent magma pulses ponded at the Moho did not assimilate any/as much granitic material, as they were interacting with preconditioned crust, and formed olivine-bearing anorthosites. With better constraints on the parental magma composition, magma source, and crustal contamination processes, addressing aspects such as the tectonic setting and emplacement mechanisms of these massive intrusions should be prioritized. Understanding these enigmatic aspects of anorthosite petrogenesis is leading the anorthosite community towards answering the ultimate questions of why massif-type anorthosites are restricted to the Proterozoic.

Acknowledgements

The research in this dissertation involved work in several countries, and as a result, many people and organizations played crucial roles in the acquisition and interpretation of data and compilation of the results. The National Research Foundation (NRF) funded a major portion of the project, including two field expeditions to Angola, to collect samples from the Kunene Anorthosite Complex. The NRF also funded living expenses for a total of seven months spent in Providence, R.I., for use of the experimental petrology laboratories at Brown University. The Geological Society of South Africa funded travel expenses for both trips to Providence, through the Research, Education and Investment fund. At Brown University, Stephen Parman taught me everything I needed to know to conduct piston cylinder experiments, and how to process and interpret experimental data. Thank you to John Krantz, for help with my experiments whenever I needed it. Joseph Boesenberg, the electron microprobe manager at Brown, spent many hours training me to use the microprobe, and was always on hand to help. Martin le Roux guided our excited team through much of Angola and Namibia. Thanks also to the rest of the Angola team: Grant Bybee, Lew Ashwal, Jeremie Lehmann, Trishya Owen-Smith, Alan Brower, and Ben Hayes, for your scientific and logistical help in the field. Trishya Owen-Smith assisted a great deal with analysis of our KAC samples using the electron microprobe at the University of Johannesburg.

Throughout the work done over the past 2 years, I have had the supervision and guidance of 3 very talented and dedicated scientists. Stephen Parman introduced me to the world of experimental petrology, and made himself available for many lengthy discussions via skype. Thank you Steve, and thank you as well for helping me settle into life in Providence. At Wits University, Lew Ashwal has been a constant scientific inspiration, having written an entire book on anorthosites. Lew, thank you for your guidance and advice throughout the project. I feel privileged to have been able to work with such a distinguished geologist. Finally, thanks must go to Grant Bybee, who has supervised my undergraduate and postgraduate work. Grant, thank you for always having an open door and for fuelling my interest in petrology and geochemistry. Thank you also for the countless travel opportunities, including several trips to the U.S. and Angola, and four conference trips in the last 2 years. Your dedication and enthusiasm for geoscience have been a constant source of motivation and inspiration. Thank you lastly to the School of Geoscience at Wits University, for promoting and supporting research.

List of Abbreviations

Anorthosite complexes

KAC:	Kunene Anorthosite Complex
LAC:	Laramie Anorthosite Complex
MMIS:	Mealy Mountains Intrusive Suite
NPS:	Nain Plutonic Suite
RAP:	Rogaland Anorthosite Province

AMCG:	Anorthosite-Mangerite-Charnockite-Granodiorite suites
CMH_HAB:	Synthetic High-Alumina Basalt starting composition used in baseline experiments
CMH+KAC:	Starting composition used for contamination experiments. A mixture of CMH_HAB and a granitic composition from the KAC
HLCA:	Experimental starting composition used by Longhi *et al.* (1999)
HAOM:	High-Alumina Orthopyroxene Megacryst
LGN:	Leucogabbronorite
LN:	Leuconorite
LT:	Leucotroctolite

Contents

List of Figures

List of Tables

1 Introduction

1.1 PROTEROZOIC MASSIF-TYPE ANORTHOSITES

A rock type that is dominated by one mineral, forms as huge intrusions covering tens of thousands of square kilometers, and is only formed during a limited period of Earth's history, is bound to attract the attention of any scientist interested in the evolution of our planet. Despite extensive study on these fascinating intrusions, their formation is poorly understood. The term "anorthosite" strictly refers to a rock consisting of at least 90% plagioclase (Streckeisen, 1976). Anorthosites are common in layered intrusions, as inclusions in island and continental arcs, as megacrystic intrusions formed in the Archaean Eon, and form a significant portion of the Moon's crust (Ashwal, 1993). However, no terrestrial anorthosites are as voluminous as those formed in the Proterozoic Eon. Proterozoic anorthosites occur as massive intrusions known as "massifs", and typically contain 70% – 95% plagioclase of intermediate composition (~An$_{40\text{-}65}$; Ashwal, 2010, Duchesne, 1984). The intrusions occur on all continents except for Australasia (Fig. 1.1; Ashwal, 1993). The largest examples are the Lac Saint-Jean Complex in Quebec (~17 000 km^2) and the Kunene Complex in Angola and Namibia (~18 000 km^2). Massif-type anorthosites are restricted to the Proterozoic, and most formed during a ~700 m.y. period of Earth's history (1800 – 1100 Ma; (Ashwal, 2010; Morse, 1982).

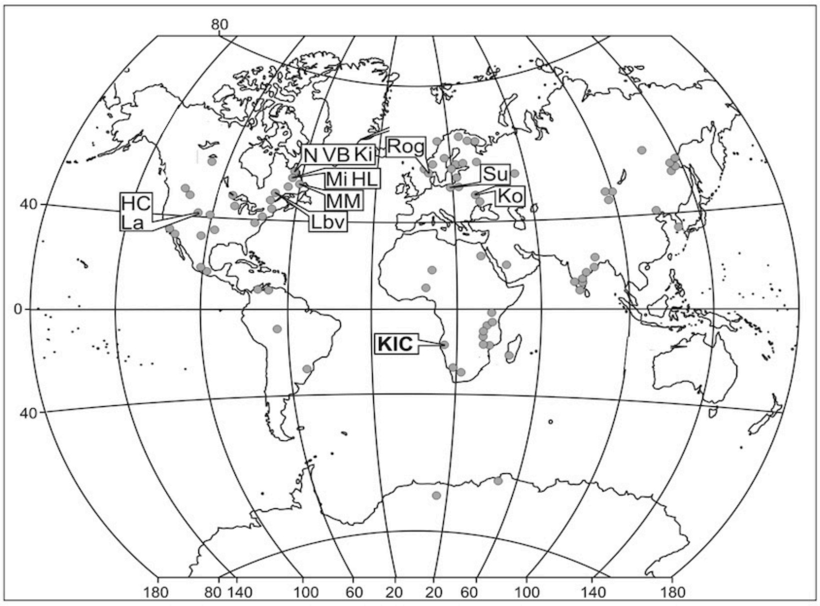

Figure 1.1 Distribution of major Proterozoic anorthosites around the world (after Gleiβner, 2011). HC, Horse Creek; HL: Harp Lake; KIC: Kunene; Ko: Korosten; La: Laramie; Lbv: Labrieville; Mi: Michikamau; MM: Mealy Mountains; N: Nain; Rog: Rogaland; Su: Suwalki. Associated mafic intrusions are also shown. Ki: Kiglapait; VB: Voisey's Bay.

The anorthosites that formed in the Archaean are very different to the Proterozoic occurrences, containing megacrysts of highly calcic plagioclase in a fine-grained mafic groundmass (Ashwal, 2010). Anorthosites that formed in the Phanerozoic occur on much smaller scales, as inclusions in arcs and in layered mafic intrusions (Ashwal, 1993). The restriction of massif-type anorthosites to a relatively short period of Earth's history, as well as the change in composition of plagioclase in anorthosites from the Archaean to the Proterozoic (Fig. 1.2), suggests that a unique set of tectonic and crust-forming conditions may have characterized the Proterozoic Eon.

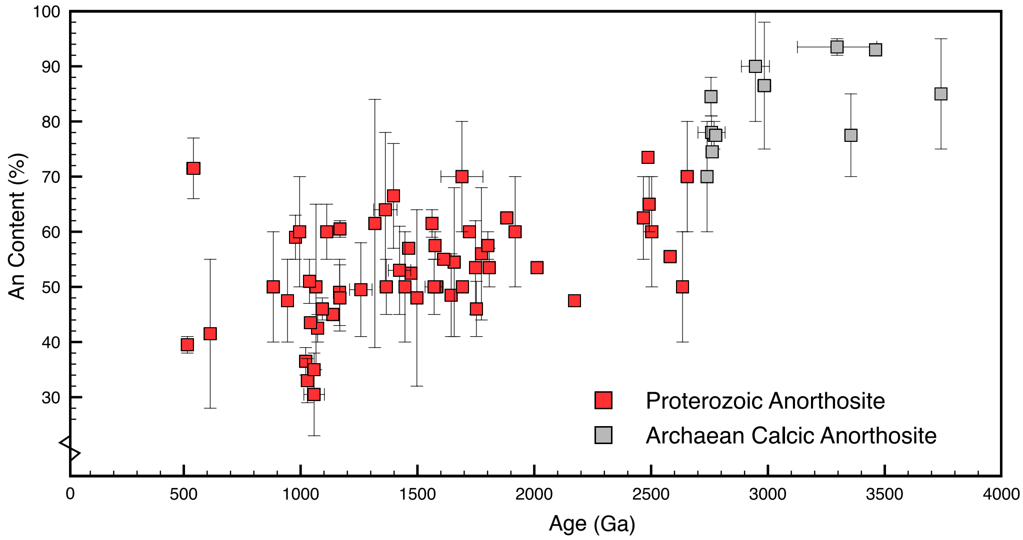

Figure 1.2 Graph of An content (%) vs. age (Ga) for anorthosite occurrences, showing the decrease in An content at the Archaean-Proterozoic boundary. After Ashwal and Bybee (2017).

The combination of the almost monomineralic composition, massive volumes, and temporal restriction of Proterozoic anorthosites has been puzzling petrologists for decades, but many critical aspects of their petrogenesis remain unresolved. The tectonic setting, emplacement mechanisms, and the composition and source of the parental magmas are among the many topics of debate regarding anorthosite petrogenesis. Primary basaltic magma is known to crystallize at most 50-60% plagioclase (Müntener and Ulmer, 2006), so the composition of the anorthosites leaves a significant mafic component unaccounted for, assuming they formed from basaltic magmas. Major volumes of mafic and ultramafic bodies are generally absent from the anorthosite complexes.

Nearly all Proterozoic anorthosite complexes are associated with a suite of silicic rocks, with compositions ranging from diorite to granite. These rocks, together with the anorthosites, are collectively referred to as anorthosite-mangerite-charnockite-granodiorite (AMCG) complexes (Emslie and Hunt, 1990; Ashwal, 1993). The silicic rocks of the suite were previously thought to be comagmatic with the anorthosites (Duchesne and Demaiffe, 1978; Philpotts, 1981), but field relations as well as isotopic and rare earth element (REE) signatures demonstrate that the granitoids and anorthosites formed from chemically independent magmas (Ashwal and Seifert, 1980; Duchesne, 1990). Although typically coeval, the granitoids are commonly intrusive into the anorthosites, and are believed to have formed by partial melting of lower crustal material due to the heat of ponding anorthosite parental magmas at depth (Emslie *et al.,* 1994; Duchesne and Demaiffe, 1978). Many anorthosite complexes are also intruded by dykes of a broad range of compositions, from norite and ferrodiorite, to a more silicic group including monzonorite, high-Al gabbro and even anorthosite. In many cases, the dykes are argued to represent either the parental magma of the anorthosites (Mitchell *et al*., 1995; Vander Auwera and Longhi, 1994), or liquids residual to anorthosite crystallization (Emslie *et al*., 1994; Morse, 1982).

1.2 FORM AND ROCK TYPES

1.2.1 General petrographic and geochemical properties

Proterozoic anorthosite complexes commonly consist of several coalesced plutons, commonly with distinct compositions. The suite of rock types generally includes anorthosite *senso stricto* (> 90% plagioclase), leuconorite/leucogabbro and leucotroctolite, as well as lesser norite/gabbro and troctolite (Emslie *et al.*, 1994). The anorthosites have variable grain size, but are most commonly coarse-grained. The rocks are plagioclase cumulates, but adcumulus growth may obscure the original lath-shaped plagioclase in some cases. Plagioclase occurs as tabular crystals, typically $An_{40-65.}$ Some anorthosites show distinctly homogeneous compositions, with An-content differing by less than 3 mole % across an entire complex (Duchesne and Demaiffe, 1978). However, reverse zoning of plagioclase occurs in many complexes, while normal zoning is very rare. Minute inclusions of Fe-Ti oxides commonly occur in plagioclase of the anorthosites, giving the rocks their range of colors, commonly dark grey to bluish-black (Ashwal, 1993). Iridescent (or labradorescent) plagioclase is very common. Plagioclase megacrysts up to a meter in length have been documented in many complexes, and are believed to represent a high-pressure stage of crystallization (Charlier *et al.*, 2010; Xue and Morse, 1994)

The dominant mafic phases in the anorthosites include olivine, orthopyroxene, and clinopyroxene in variable proportions and textures. The mafic silicates generally have Mg# between 55 and 70. Olivine is commonly interstitial, but cumulus olivine also occurs (Ashwal, 1993). Olivine is commonly surrounded by rims of orthopyroxene, formed as a peritectic reaction between olivine and liquid. Orthopyroxene is generally interstitial, and is rarely seen as a cumulus phase. Clinopyroxene and inverted pigeonite are less common, but occur as interstitial phases where present. Biotite and amphibole are common as secondary phases in metamorphosed anorthosites, but also occur in small amounts as late-stage magmatic phases in some unmetamorphosed complexes. These minerals are generally observed as rims on pyroxenes or Fe-Ti oxides (Ashwal, 1993).

1.2.2 High-alumina orthopyroxene megacrysts

A characteristic feature of Proterozoic anorthosites is the occurrence of high-alumina orthopyroxene megacrysts (HAOMs). These crystals occur either as individual, subhedral megacrysts up to 1 m in length, or in aggregates with other phases, commonly interstitial to plagioclase, implying that they are comagmatic with the anorthosites. (Bybee *et al.*, 2014a; Charlier *et al.*, 2010; Emslie, 1975; Wiebe, 1986). The HAOMs have variable alumina contents (3 - 9 wt. % Al_2O_3), and are more magnesium-rich than the typical intercumulus orthopyroxene of the host anorthosites (Ashwal, 1993; Bohlen and Essene, 1978), implying that they are the most primitive component of the anorthosite system.

The highest-alumina megacrysts have been invaluable in efforts to understand anorthosite petrogenesis. It has been suggested based on field relations, REE patterns, and other chemical characteristics, that the high-Al content of the megacrysts may be explained by rapid in-situ crystallization at the anorthosite emplacement level (Dymek and Gromet, 1984; Morse, 1975). However, Al-in-orthopyroxene geobarometry (Emslie, 1975; Fram and Longhi, 1992) has indicated that the HAOMs crystallized at depths of 35 - 45 km, at/near the Moho, far deeper than the emplacement level of the anorthosites in the middle crust (10 – 20 km; (Emslie *et al.*, 1994; Charlier *et al.*, 2010; Longhi *et al.*, 1993). Geobarometry calculations have shown that Al_2O_3 content gives a reliable indication of the crystallization pressure of the HAOMs (Fig. 1.3A; Bybee *et al.,* 2014b). In addition, the high Mg# of the megacrysts suggests that they are an early, primitive phase, and thus are unlikely to have formed during the late stages of intrusion at shallow crustal levels. Rapid crystallization would also produce low Cr_2O_3 in the megacrysts, which is not observed (Dymek and Gromet, 1984; Emslie, 1975). The HAOMs contain exsolution lamellae of plagioclase, most likely formed as a result of decompression during ascent of the megacrysts from Moho depths to their ultimate level of emplacement in the shallower crust (Bybee *et al.* 2014a; Charlier *et al.,* 2010; Emslie, 1975). The highest pressure HAOMs are the most primitive, with Mg# decreasing in HAOMs formed at progressively shallower depths (Fig. 1.3B; Bybee *et al.,* 2014b). It is therefore implied that the anorthosites began their formation at Moho depths, and that crystallization continued during ascent towards the shallower crust over time, entraining some of the HAOMs (Charlier *et al.*, 2010; Wiebe, 1986). Variable Eu anomalies (Eu/Eu* = 0.6 to 1) in the highest pressure HAOMs (> 8 wt. % Al_2O_3) suggest that plagioclase started forming during crystallization of the HAOMs at high pressure (Bybee *et al.,* 2014b). This observation, together with clear trends in geochemistry between higher and lower pressure HAOMs (Charlier *et al.,* 2010) provide further support for HAOMs being comagmatic with the anorthosites, and for the anorthosites having crystallized polybarically (Bybee *et al.,* 2014b). What is less clear is where the majority of anorthosite crystallization took place. Did most crystals form at the crust-mantle boundary where HAOMs originate, followed by emplacement of crystal-rich mamas or mushes into the mid-crust? Or did much of the crystallization of the anorthosites happen at shallower depths within the crust, or during intrusion from the Moho to the shallow crust? These are some of the crucial questions currently under investigation.

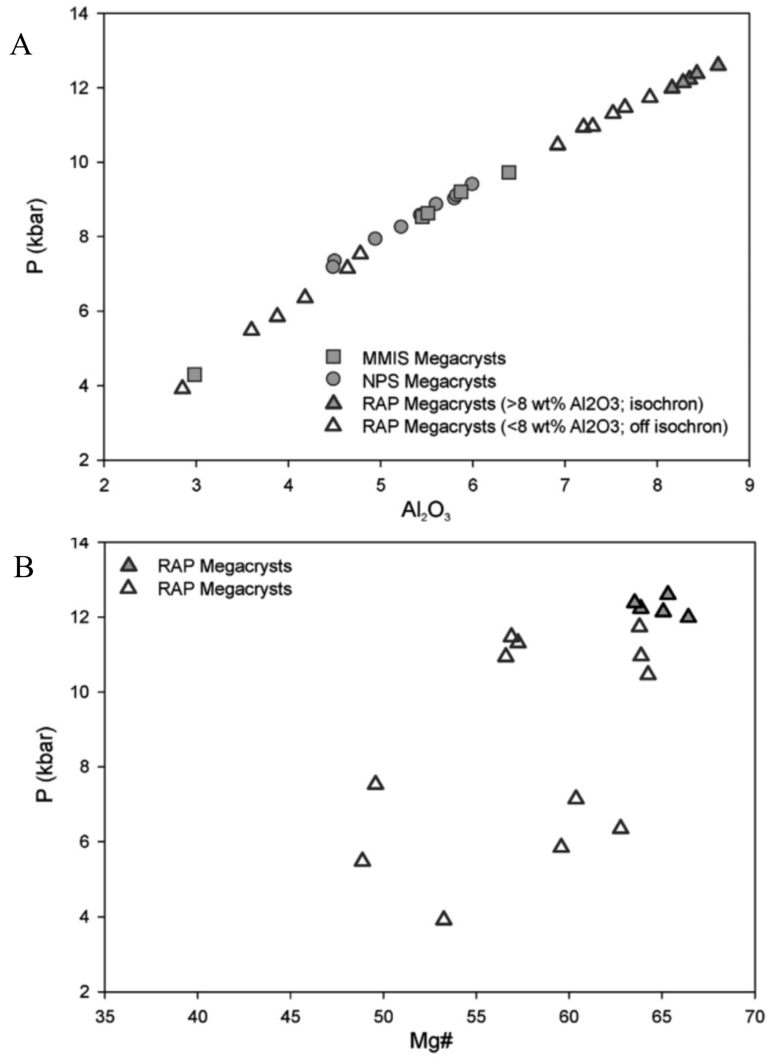

Figure 1.3 A) Al_2O_3 contents in high-alumina orthopyroxene megacrysts (HAOMs) vs. depth of crystallization, calculated using the Al-in-orthopyroxene geobarometer. HAOM samples from the Rogaland Anorthosite Province, Mealy Mountains Intrusive Suite, and the Nain Plutonic Suite are plotted. B) Calculated crystallization pressure vs. Mg# for HAOM samples from the Rogaland Anorthosite Complex. Both plots after Bybee *et al.* (2014b).

Another crucial piece of information comes from the isotopic signatures of the HAOMs. Sm-Nd isotope geochronology on megacrysts in the MMIS, RAP and NPS shows that the megacrysts formed ~100 m.y. before the anorthosites were emplaced (Bybee *et al.*, 2014a). These age data, combined with the information from geobarometry, imply that the anorthosites formed in long-lived magmatic systems, with crystallization commencing at lower crust or upper mantle depths. Sm-Nd ages for plagioclase exsolution lamellae on the HAOMs correspond (within error) with the ages of emplacement of the anorthosites, 70 – 100 Ma after HAOM formation (Charlier *et al.*, 2010). The information from the HAOMs has been interpreted to suggest that the anorthosites began crystallizing mafic components at Moho depths, and that they spent as much as 100 Ma making their way towards the shallow crust (Bybee *et al.,* 2014a). These are crucial pieces of information in our attempts to understand anorthosite petrogenesis.

1.2.3 The olivine-orthopyroxene dichotomy

In many Proterozoic anorthosites, individual plutons within a single complex show differences in mineral assemblages, with the dominant mafic mineral being either olivine or orthopyroxene (opx). While there are anorthosites containing only olivine or only orthopyroxene as the mafic phase, many intermediate compositions exist, with olivine accompanied by interstitial and peritectic opx. The opx-bearing anorthosites, or leuconorites, are generally more evolved than the olivine-bearing rocks, or leucotroctolites, displaying more enriched isotopic signatures (Drüppel *et al.*, 2007; Emslie, 1985; Gleiβner *et al.*, 2010; Gray, 1987). The composition of the plagioclase is generally more calcic in leucotroctolites, and more sodic in leuconorites (Emslie, 1980; 1985, Lindsley *et al.,* 2010; Philpotts, 1966). These features have been interpreted to suggest that opx-bearing anorthosites were subjected to contamination by surrounding crustal rocks, while olivine-bearing anorthosites experienced less contamination, or none at all (Drüppel *et al.*, 2007; Gleiβner *et al.*, 2010; Gray, 1987; Slejko *et al*., 2002). Further evidence for contamination and the mineral dichotomy is discussed in Chapter 2.

1.3 TECTONIC SETTING

The tectonic setting for Proterozoic anorthosites has been extensively debated. Theories range from convergent settings including collision zones and arcs, to divergent and intra-plate settings including rifts and plumes, and are discussed below. Rift systems are appealing because they can account for several features of the anorthosite complexes, such as the linear topology observed in many anorthosite terranes and the large volumes of basaltic magma required (Anderson, 1983; Berg, 1977; Emslie, 1980; McLelland, 1986; Morse, 1982). However, it is unlikely that rifts could have been in operation for timescales long enough to produce the anorthosites without resulting in continental break-up (Ashwal, 1993). The voluminous magmatic activity and bimodal chemistry in rocks generated by mantle plumes have lead some workers to suggest a direct link between anorthosites and plumes (Emslie, 1978; McLelland, 1986). The main problem with this theory is that there is no age progression in the rocks of large anorthosite complexes, as would be expected in plume-generated rocks. In addition, while Phanerozoic plumes can produce anorthosites, they are much smaller than the anorthosite complexes of the Proterozoic (Ashwal, 1993). Another anorogenic theory involves a Proterozoic supercontinent acting as a thermal insulator, reducing heat loss from the mantle and resulting in a mantle "superswell". This would initiate uplift of the lithosphere and the emplacement of mantle-derived magmas into the continental crust (Hoffman, 1989). As with the rift idea, this scenario would most likely result in continental break-up. In addition, if thermal insulation by a supercontinent explains the formation of the Proterozoic anorthosites, then younger supercontinents would be expected to preserve the huge intrusions as well, and so this theory does not account for the temporal restriction of the massif-type anorthosites.

Continental collision zones have been proposed due to their ability to account for many of the deformational and metamorphic characteristics of anorthosites (Dewey and Burke, 1973; Rivers *et al*., 1989). However, this setting is only applicable if anorthosites are formed from crustal magmas or residues (Ashwal, 1993). Several subduction-related settings have been proposed for various reasons. Back-arc settings (Brown *et al*., 1975; McLelland *et al.,* 1988) and ridge subduction (Vlaar, 1985; Taylor *et al*., 1984) have been suggested as possibilities for anorthosite production, due to the presence of associated calc-alkaline rocks and the chemical bimodality of Proterozoic anorthosites (anorthosite and granitoid rocks). Where collisional events of appropriate age are associated with anorthosite complexes, McLelland et al. (2010) propose that delamination of over-thickened orogenic lithosphere, followed by ponding and ascent of gabbroic melts, could produce the anorthosites in the late- to post-orogenic stages. This, however, does not account for anorthosite complexes where no appropriately timed collisional events have been recorded (Bybee *et al.*, 2014a).

Processes operating at convergent, Andean-type margins seem to be the most successful at accounting for the main characteristics of Proterozoic anorthosites. These convergent settings have the ability to produce large quantities of basaltic magma over a significant period of time (Bybee *et al.,* 2010), an important prerequisite for anorthosite production. Several arc settings have been demonstrated to have been in operation for more than 150 m.y. (Ducea, 2001; Hervé *et al*., 2007). An arc setting can also account for the long, linear topologies of many anorthosite complexes. One problem with this setting is that Andean margins typically produce rocks of the series basalt-andesite-dacite-rhyolite, and the intermediate compositions in the series are not typical of anorthosite suites (Ashwal, 1993). Another major obstacle is the absence of massif-type anorthosites in modern day arc settings. It may be that there are anorthosites in these settings that have not yet been exposed due to insufficient erosion. Small anorthosite xenoliths do occur in modern arc environments, but are far more calcic than Proterozoic anorthosites (Ashwal, 2010; Bybee *et al.*, 2014a). This compositional difference may be due to differences in the composition of the parental magma (e.g. water content) or to different conditions of formation (perhaps related to tectonics) in the Proterozoic (e.g. pressure, angle of subduction, heat flow, etc.)

1.4 PARENTAL MAGMAS

The nature and compositions of anorthosites, far exceeding basaltic cotectic proportions of plagioclase, make determination of a plausible parental magma challenging. The cumulate nature of the rocks means that the bulk compositions of the intrusions do not represent liquid compositions, making inferring the parental magma difficult. An anorthositic parental magma has been suggested based on the occurrence of anorthosite dykes in several complexes (Wiebe, 1979; Simmons and Hanson, 1978). While the dykes may represent liquid compositions (fine-grained, lacking in phenocrysts, strong normal zoning in plagioclase), they are not likely to be parental to the anorthosites. Huge quantities of anorthositic magma would be required to form the anorthosite complexes, and it is not clear how such a vast amount of an unusual magma composition could be generated (Green, 1969; Emslie, 1970; Longhi and Ashwal, 1974). In addition, high-pressure experiments on an anorthositic liquid composition at temperatures within the stability range of plagioclase, produced more calcic plagioclase and more magnesian mafic silicates than are observed in anorthosites (Fram and Longhi, 1992). The experiments also indicate a very high anorthite solidus temperature, so high-An plagioclase would not be able to exist as a liquid at lower crustal depths where anorthosites are believed to start crystallizing.

Monzonoritic rocks associated with anorthosite complexes have been proposed as being representative of parental magma compositions (Duchesne *et al.*, 1974; Vander Auwera *et al.*, 1998). This is based on field relations and monzonorite REE patterns that lack Eu anomalies, as well as 5 kbar experiments on monzonoritic chill margin and dyke compositions (Vander Auwera *et al.,* 1998). A calc-alkaline parental magma was proposed by Philpotts (1966). It is suggested that the Fe-enrichment trend in the rocks is the result of differentiation of a calc-alkaline magma in a very dry environment (Philpotts, 1966). Green (1969) suggests that fractional crystallization or partial melting of a quartz diorite parental magma could produce anorthosite as a crystalline residuum in the lower crust. Olivine basalt with low normative clinopyroxene was suggested by Wiebe (1986), and a low wollastonite component in the parental magma has also been suggested by several other authors (Wilson *et al.*, 1996; Longhi *et al*., 1999; Morse, 1982).

Despite the range of parental magma compositions that have been proposed, the mineral assemblages of anorthosites indicate that a basaltic parent is likely. High-alumina basaltic/gabbroic dykes and "chill margins" have been documented in many anorthosite complexes and associated intrusions, such as Nain (Berg, 1980; Wiebe and Snyder, 1993), Harp Lake (Emslie *et al.,* 1994), Kiglapait (Nolan and Morse, 1986), Laramie (Mitchell *et al*., 1995), Michikamau (Emslie, 1970) and Rogaland (Demaiffe *et al*., 1990; Duchesne *et al.,* 1989). These rocks are fine-grained, have positive Eu anomalies, intermediate plagioclase, and generally have isotopic compositions that cover the range of anorthositic rocks (Mitchell *et al.*, 1995). These features have lead many workers to suggest that they represent the parental magmas of the anorthosites. There is significant evidence favoring high-alumina basalt (HAB) as a parental magma composition. A high-alumina basaltic composition would be in equilibrium with plagioclase cumulates (Emslie *et al.*, 1994). Vander Auwera *et al*. (2000) demonstrated that the calculated concentrations of Sr and Cr in liquids in equilibrium with plagioclase and orthopyroxene are in the range of concentrations found in natural HAB. Analysis of An relations in the Nain complex suggested that a basaltic magma would be capable of producing the full range of plagioclase compositions in the anorthosites (Morse, 1968). Several experimental investigations have been conducted on a composition called HLCA, a synthetic composition designed to match high-alumina basaltic dykes proposed to be the parental composition of the Harp Lake anorthosites (Emslie, 1980; Fram and Longhi, 1992; Longhi *et al.,* 1999). The dykes are similar in texture and composition to dykes in other anorthosite complexes. The experiments at 10 kbar produce intermediate plagioclase and aluminous orthopyroxene, and the mineral compositions overlap with natural compositions in anorthosites (Fram and Longhi, 1992).

It is important to address the water content of magmas parental to anorthosites, since water has notable effects on the phase equilibria controlling the amount and composition of plagioclase that forms (Sisson and Grove, 1993). Water also needs to be addressed if the anorthosites are thought to have formed in an arc environment. Experiments on hydrous basaltic compositions show that increased water in magmas produces a smaller amount of plagioclase, but with higher An content (Sisson and Grove, 1993; Yoder, 1968). Anorthosites do not have any features that suggest that they formed from hydrous magmas. Amphibole and biotite are only present in small amounts, and are generally secondary (Ashwal, 1993; Emslie, 1980). The mineral assemblages in the anorthosite suite, even those that crystallized from late-stage residual liquids, as well as the assemblages in contact aureoles, suggest very low activity of H_2O (Morse, 1982; Ashwal, 1993). Anorthosite suites also show a strong Fe-enrichment trend, which is unlikely to occur in liquids with oxygen content buffered by the presence of water (Emslie, 1965; Philpotts, 1966). Based on these characteristics, Proterozoic anorthosites are generally considered to have formed from anhydrous parental magmas.

1.5 MAGMA SOURCES

While many workers agree that high-alumina basalt is the most likely parental magma composition, the question of whether the magmas were derived from partial melting of the depleted upper mantle or of the lower crust is one of the most debated topics in Proterozoic anorthosite petrogenesis. What is clear is that the rocks have a definite crustal component in their isotopic signatures (addressed in the following sections), but what is less obvious is whether this is a result of the anorthosites being derived from partial melts of the crust, or from crustal contamination of mantle-derived magmas. A review of the evidence and the obstacles for both scenarios follows.

1.5.1 Lower crustal anatexis

A wide variety of lithologies has been proposed as being representative of the lower crust, based on granulite xenoliths, exposed high pressure granulite terranes, and crustal cross sections (Rudnick and Gao, 2003). Due to the poorly constrained and most likely heterogeneous composition of the lower crust, there are several variations of theories on how anorthosite parental magmas could have been derived from the lower crust It was suggested by Taylor *et al*. (1984) that the high Al content and low Mg# of anorthosites, as well as the low An content of the plagioclase, are features incompatible with a mantle source. Instead, they suggested that the lower continental crust became enriched in Al, Sr and Eu during the extraction of the K-rich granites that make up most of the continental crust, and that partial melting of this aluminous lower crust could produce anorthosites (Taylor *et al.*, 1984). In another study, Schiellerup *et al.* (2000) noted that anorthosites worldwide have ε_{Nd} from +5 to -7, and that the positive and nearly chondritic values have commonly been interpreted as evidence for mantle derivation (while more negative values may be the result of crustal contamination). However, Schiellerup *et al.* (2000) argue that the decrease in ε_{Nd} in the lower crust is slow, so that lower crust derived from depleted mantle may retain its positive ε_{Nd} for significant time periods. Due to variability in mantle reservoirs, ε_{Nd} alone does not distinguish between mantle and lower crustal reservoirs. However, Re is very efficiently fractionated from Os during mantle melting and crust formation, so the in $^{187}Re/^{188}Os$ in lower crust is far larger than in the mantle and thus, the Re-Os isotopic system may be a more robust evaluation of the source of the parental magma (Schiellerup *et al.,* 2000). In the study, ten anorthosite samples from the Rogaland Anorthosite Province were found to have $^{187}Os/^{188}Os$ of 0.63 ± 0.25, which corresponds to a γ_{Os} value (the percent deviation in $^{187}Os/^{188}Os$ from chondritic mantle at the time of formation) of +419. The upper mantle has γ_{Os} around 0 (±15). The extreme γ_{Os} value of the RAP anorthosites was interpreted as evidence for a crustal origin for the anorthosites. Crustal contamination of mantle-derived magma was shown through mixing models to be improbable, because the isotopes would require too much contamination by crust with unrealistically high concentrations of Os than is plausible (Schiellerup *et al.*, 2000). In an experimental study on three proposed parental magma compositions, Green (1969) concluded that anorthosites could be produced as a crystalline residuum from partial melting or fractional crystallization of lower crustal material of andesitic composition. Seismic profiles and structural observations in the Sveconorwegian Province lead to the development of a model involving under-thrusting and subsequent partial melting of tongues of mafic lower crust to generate anorthosite parental magmas (Duchesne *et al.*, 1999). Bédard (2001) calculated equilibrium melt trace element contents for the Nain anorthosites. The calculated model melts have trace element profiles enriched in incompatible elements relative to normal mid-ocean ridge basalt, commonly with negative Nb and Th anomalies, and these anorthosite model melt profiles very closely match the profiles of crustal melts such as tonalites (Bédard, 2001). Inversion and melting models in the same study suggest that the anorthosites are derived from depleted garnet-granulite lower crust (Bédard, 2001).

Longhi (2005) showed through phase equilibria calculations involving several primitive mantle-derived compositions (including a Barberton komatiite, Baffin Island olivine-tholeiite, Kilauea olivine-tholeiite, and a Karoo picrite) that processes of fractional crystallization and assimilation-fractional crystallization (AFC; using a mafic assimilant) could not produce the compositions of a suite of proposed HAB parental magmas. On plots of Mg# vs. incompatible trace elements, the arrays of proposed parental magmas form steep slopes, while the calculated liquid lines of descent for selected primitive basalts form much shallower slopes, and reach plagioclase saturation at lower Mg# than the anorthosite parental magmas. In addition, the calculations show that high wollastonite (Wo) residual liquids are produced during fractionation of the primitive mantle-derived compositions, while the proposed parental magmas of anorthosites have low Wo contents (Nolan and Morse, 1986; Robins *et al.,* 1997). Longhi (2005) concludes that partial melting of mafic lower crust produces a closer (but not perfect) match to the possible parental compositions than fractional crystallization of a primitive basalt does, with or without assimilation (Longhi, 2005).

Since the plots of Longhi (2005) may have important implications for anorthosite petrogenesis, it is necessary to address the array of proposed parental magmas used. The points plotted to form the array are compositions of dykes and chill margins from anorthosite complexes worldwide, proposed by various authors to be likely parental magmas. While many of the dykes have characteristics that suggest they might represent liquid compositions (fine grain size, no Eu anomalies), it is possible that some of them might have undergone some amount of fractionation and/or contamination, and so not all the compositions may represent parental magmas. Many of the dykes and chill margins in anorthosites are depleted in incompatible trace elements and have positive anomalies of Eu and Sr, and so may be partly cumulate (Bédard, 2001). In addition, some of the compositions have been shown to be chemically unrelated to the anorthosites they are associated with (Demaiffe *et al.*, 1990; Duchesne *et al.*, 1985). If some of the plotted compositions do not represent plausible parental magmas, testing the origin of anorthosites against this array may be inconclusive, or lead to over-interpretation. The difference in slopes between the calculated crystallization paths of primitive basalts and the array of proposed parental magmas may not necessarily preclude the production of parental magmas by fractionation of a more primitive composition.

Many workers who favor a crustal source for the anorthosite parental magma make reference to experimental phase equilibria produced by Longhi *et al.* (1999). Experiments were conducted on HLCA, the average composition of the primitive high-Al gabbros in the Harp Lake Complex, a composition commonly proposed to be parental to anorthosites. At 11.5 kbar, the phase boundaries constructed from the experiments indicate that mantle-derived liquids fractionate away from SiO_2 and towards nepheline-normative compositions with decreasing temperature. The positions of the phase boundaries on the diagram result in the proposed parental magma (HLCA) plotting on a thermal maximum on the plagioclase-pyroxene plane of the diagram, and as a result, the authors conclude that HLCA (and anorthosite parental magmas in general) may not be produced by fractionation of a more primitive mantle-derived melt (Longhi *et al*., 1999). It is suggested that anorthosite parental magmas must form instead by partial melting of a composition that already lies in the thermal divide, such as a lower crustal gabbronoritic composition. The experiments on HLCA are discussed in more detail in Chapter 3.

Despite the evidence favoring a lower crustal source for anorthosites, a major obstacle for this hypothesis is that a large volume of crust would need to be melted in order to generate enough magma with a composition suitable to crystallize Proterozoic anorthosites (Gleiβner, 2011; Longhi, 2005; Morse, 2006). Longhi (2005) suggests that as much as 90% melting at a temperature exceeding 1200°C would be required. Since the geothermal gradient of the crust is typically parabolic, Bybee *et al.* (2014b) suggest that the temperature of the lower crust rarely exceeds ~1050°C, insufficient to produce any high volume, basaltic magmas. Taylor *et al.* (1984) suggest that the anorthosites may have formed by partial melting of Al-enriched lower crust, but this idea suffers the same ultimate problem of accounting for a heat source to generate sufficient volumes of melt. It is suggested by Taylor *et al.* (1984) that an underlying mantle plume would provide enough heat to partially melt enough lower crust, but this would require that portion of crust to remain above the plume for a timescale long enough to produce the huge volumes of anorthositic rocks in the complexes. In addition, the variability in Eu anomalies (Eu/Eu* = ~0.6 to 1) of the primitive HAOMs cannot be explained if the HAOMs represent crystallization products from lower crustal melts, and are not comagmatic with the anorthosites (Bybee *et al.,* 2014b). Morse (1991) provides strong arguments against derivation of basaltic magma by melting of the crust. Crustal melts are generally accepted to be formed by heating from below, particularly underplating of basalt. This process is capable of supplying a significant amount of heat, but the melts produced are of granitic composition. To generate basalt from crustal melting, it is suggested by Morse (1991), that underplating of material at about 1650°C is required. However, hot mantle material would melt through decompression before coming into contact with the lower crust, and thus, the amount of basaltic magma produced through decompression melting of mantle material far exceeds the amount that could be produced by melting of the lower crust (Morse, 1991). In addition, many workers believe that the lower crust is basaltic. To generate basaltic magma from basaltic lower crust, all of it needs to be melted, which is an unrealistic prerequisite (Morse, 1991). An alternative hypothesis for generating large amounts of crustal melt is the model of down-thrusting of tongues of crustal material along lithospheric-scale weakness zones (Duchesne *et al.*, 1999), but this type of tectonic event is believed to be short-lived, and would not be able to continually produce magma on the timescales required to produce Proterozoic anorthosites (Bybee *et al.*, 2014a). Further argument against a crustal origin comes from variation in the degree and polarity of isotopic disequilibrium in plagioclase between olivine- and orthopyroxene-bearing anorthosites. Bybee and Ashwal (2015) define ΔNd as the deviation in $^{143}Nd/^{144}Nd$ of an internal phase from a whole-rock isochron. In the MMIS, plagioclase in leucotroctolites has ΔNd = 0.1032 while plagioclase in leuconorites has ΔNd = -0.072. In general, melting of a single source will not produce isotopic variation in a mineral phase crystallizing from that melt. Therefore, the variations in isotopic disequilibrium observed between leuconorites and leucotroctolites must be the result of some process that occurred after separation of the melt from the source (Bybee and Ashwal, 2015). This suggests that the isotopic variations cannot be caused by melting of a lower crustal source.

1.5.2 Partial melting of the mantle

1.5.2.1 Evidence for a mantle origin

The generally basaltic mineralogy and low water contents are good indications that Proterozoic anorthosites have a mantle origin (Ashwal, 1993; Morse, 1982; Wiebe, 1986). Studies of stable and radiogenic isotopes in anorthosites show that they are similar to upper, depleted mantle-derived mafic rocks. While oxygen isotope values in anorthosites are variable (δ^{18}O between 4‰ and 11‰), the most primitive values are within the range of fresh basalts, implying a mantle origin (Drüppel *et al.*, 2007; Peck *et al.,* 2010). Isotopic studies of the Kunene Anorthosite Complex show δ^{18}O values for plagioclase (5.88 ±0.19‰) and a lower range of initial Os compositions (0.2 ± 0.1) that are in agreement with a mantle source (Drüppel *et al.*, 2007; Gleiβner *et al.*, 2012). However, the isotopic compositions of the rocks also show that a mantle source needs to be addressed in conjunction with the influence of crustal contamination on producing Proterozoic anorthosites.

1.5.2.2 Evidence for crustal contamination of a mantle-derived magma

In the Nain Plutonic Suite (NPS), Labrador, studies of O, Sr and Nd isotopes show that the compositions of the anorthosites (δ^{18}O = 4.1‰ to 8.2‰, ε_{Nd} = -0.3 to -4.4 and I_{Sr} = 0.7032 to 0.7066) reflect those of the country rocks into which the anorthosites intruded (δ^{18}O = 5.72‰ to 11.23‰), and are consistent with being derived from a mantle-derived magma mixed with continental crust composition (Ashwal *et al.,* 1986; Peck *et al.*, 2010). High values of δ^{18}O (8.7 ± 0.6‰ to 9.6‰ ± 0.7) are also documented in anorthosites of the Morin Complex, Quebec, and interpreted as the result of melting and assimilation of buried supracrustal material by the parental magma (Peck and Valley, 2000). Anorthosites in the Atikonak River Complex of the Grenville Province have ε_{Nd} values of +2.0 to -1.3, interpreted by Hegner *et al,* (2010) to suggest that they crystallized from a mantle-derived melt contaminated by plagioclase-pyroxene cumulates, which formed as residues in collapsing sills during extraction of granite and monzonite. Initial Pb isotopes are consistent with contamination by old, lower crust in the Atikonak River Complex (Hegner *et al.*, 2010). A similar process has been ascribed to anorthosites of the NPS, where the Nd and Sr isotopic data (given above) have been interpreted to suggest contamination of basaltic magma by depleted plagioclase-pyroxene granulites. The granulites are proposed to represent residues formed during extraction of the spatially associated granitoid rocks in Nain by partial melting of lower crust (Emslie *et al.*, 1994). In Rogaland, Nd and Sr isotopes (values given below) indicate significant crustal contamination and fractional crystallization of mantle-derived magma (Menuge, 1988).

Anorthosite complexes that have intruded at boundaries between terranes of different ages illustrate the influence of crustal contamination on the isotopic compositions of the anorthosites (Ashwal *et al.,* 1986). An example is listed in Table 1.1, comparing the isotopic signatures of three anorthosite complexes (Bybee *et al.*, 2014a). The Mealy Mountains Intrusive Suite (MMIS; 1650 - 1630 Ma; Gower *et al.*, 2008) intruded into immature, Palaeoproterozoic to Mesoproterozoic gneisses of the Grenville Province. The gneisses are juvenile with ε_{Nd} = -2.27 to +0.59 (Bybee and Ashwal, 2015). The Rogaland Anorthosite Province (RAP; 949 - 920 Ma; Bybee *et al.*, 2014a) also intruded into juvenile, Mesoproterozoic to Neoproterozoic country rocks, with ε_{Nd} = -3.28 to -0.35 (Menuge, 1988). The anorthosites in both the MMIS ($\varepsilon_{Nd;T}$ = +2.3 to +3.6) and RAP ($\varepsilon_{Nd;T}$ = +2.2 to +4.4) show isotopic compositions that deviate only slightly from the depleted mantle signature, supporting a mantle origin with contamination by only marginally evolved crust (Bybee *et al.*, 2014a). In comparison, the anorthosites of the Nain Plutonic Suite (NPS; 1330 - 1290 Ma; Emslie *et al.*, 1994) intruded into significantly older and more evolved crust (Archaean as opposed to Proterozoic), with approximate ε_{Nd} = -7 to -20 (Bybee *et al.*, 2014a). The NPS anorthosites display more enriched isotopic signatures ($\varepsilon_{Nd;T}$ = -1.6 to -8.5) with a larger shift from the depleted mantle (Fig. 1.4). The older crust around the NPS has an evolved composition further displaced from depleted mantle than the younger crust intruded by the MMIS and RAP, and thus has a higher potential to change the isotopic signature of the anorthosites that intrude into and are contaminated by it. The early-forming HAOMs plot at the most primitive section of the range of anorthosite compositions in each complex. The Harp Lake anorthosites, like the NPS, intruded Archaean crust, and have ε_{Nd} = -3 to -6, significantly lower than the MMIS and RAP (Demaiffe *et al.*, 1986; Ashwal *et al.*, 1986).

Table 1.1 Comparison of the isotopic compositions (Bybee *et al.,* 2014a) of three Proterozoic anorthosite complexes intruded into terranes of different ages.

	MMIS	RAP	NPS
Age of emplacement	1650 – 1630 Ma	949 – 920 Ma	1330 – 1290 Ma
ε_{Nd} country rocks	-2.27 to +0.59	-3.28 to -0.35	-7 to -20
ε_{Nd} anorthosites	+2.33 to +3.62	+2.2 to +4.4	+1.57 to -8.49

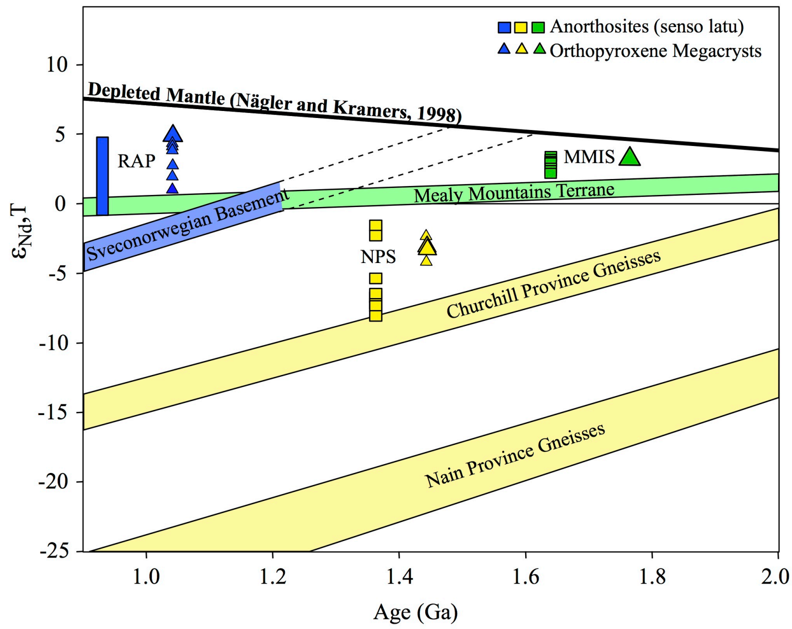

Figure 1.4 $\varepsilon_{Nd;T}$ vs. age plot showing the influence of the age of the terrane into which anorthosites intrude, modified from Bybee *et al.,* (2014a). Anorthosites that intrude into young terranes of juvenile composition are only slightly displaced from the depleted mantle (DM) evolution curve. This is seen in the MMIS and RAP, intruding the Mealy Mountains Terrane and the Sveconorwegian Basement, respectively. The NPS, which intrudes the older, more evolved Nain and Churchill Province Gneisses, has an isotopic signature further displaced from the DM curve. HAOMs in all three complexes plot closest to the DM curve.

Contamination by crust of different ages has also been documented within individual complexes, such as the NPS and the Laramie Anorthosite Complex (LAC). In the LAC, the Snow Creek massif, which intruded into Archaean country rocks, has a more radiogenic signature of I_{Sr} (0.7051 to 0.7056) and ε_{Nd} (-1.3 to -4.7) than the Chugwater massif (I_{Sr} = 0.7039 to 0.7045; ε_{Nd} = +2.4 to -1.5), which intruded into Proterozoic crust (Frost *et al.*, 2010). The trend of decreasing ε_{Nd} with increasing I_{Sr} in the LAC is indicative of a mantle-derived magma mixed with Archaean crust (Scoates and Frost, 1996), and this trend is observed in many anorthosite complexes. In the NPS, anorthositic rocks in the western part of the complex that intruded into early Archaean basement (>3.5 Ga) have ε_{Nd} as low as -15 and I_{Sr} up to 0.708. Further to the east of the complex, the isotopic signatures of the anorthosites are less radiogenic, indicating contamination by mid- to late-Archaean country rocks (Ashwal, 1993). The variations in isotopic composition for anorthosites emplaced into crust of different ages highlight the significance of crustal assimilation by mantle-derived melts in producing the observed compositions in Proterozoic anorthosites.

1.6 Purpose of this study

Contamination of a mantle-derived melt by crustal material provides a valid hypothesis for addressing the variation in isotopic signatures of Proterozoic anorthosites, and demonstrates the viability of anorthosites having been derived from a mantle source. In addition to accounting for the isotopic variation in anorthosites, the contamination hypothesis may also explain the variable proportions of olivine and orthopyroxene in the rocks. While there is abundant evidence for crustal contamination of mantle-derived magma and its effects on the anorthosite complexes, the hypothesis has not been tested directly, and the evidence in favor of a crustal source cannot be disregarded. The first component of this study presents field observations and geochemical data from the Kunene Anorthosite Complex (KAC) in Angola, to assess the distribution of olivine-bearing and orthopyroxene-bearing anorthosites. A review of the research on the KAC is presented, and compared to the data obtained from two recent field excursions to the complex. The second section of the study aims to experimentally test whether contamination of a high-alumina basaltic composition can shift the mineral assemblage of anorthosites, produced as crystal cumulates from this magma, from olivine-bearing to orthopyroxene-bearing. High pressure experiments were performed on a primitive HAB composition, as well as a mixture of this composition with a likely crustal contaminant from the KAC. Phase equilibria of high-alumina basalts are investigated, to test whether anorthosite parental magmas could be derived by partial melting of the mantle. The experiments in this study test similar experimental work of Longhi *et al.* (1999), widely cited in support of a lower crustal origin for anorthosites. The experimental results are compared to anorthositic rocks of the KAC and other anorthosite complexes around the world. In addition, the experimental conditions are modeled in MELTS to assess whether modeling could be used to test several other enigmatic aspects of anorthosite petrogenesis.

2 A Case Study: The Kunene Anorthosite Complex

2.1 INTRODUCTION

Possibly the largest Proterozoic anorthosite complex on Earth, rivaled only by the Lac St. Jean complex of the Grenville Province in Quebec, is the 18 000 km^2 Kunene Anorthosite Complex (KAC). The complex is a composite, elongate body, mostly in southern Angola, with a small portion in northern Namibia (the Zebra Mountain lobe). It is 30 – 50 km wide and about 300 km long in a N-S direction (Mayer *et al.*, 2004). The KAC intruded the southern margin of the Congo craton in the Mesoproterozoic Eon, into high-grade Palaeoproterozoic to Mesoproterozoic metamorphic basement (Carvalho and Alves, 1990). The eastern margin is covered by Kalahari sediments, so the full extent of the complex is unknown. Suggestions of regional cryptic variation across the complex have lead some workers to liken the KAC to a layered mafic intrusion (Stone and Brown, 1958; Silva, 1992), although satellite imagery and field observations indicate that the complex is more typical of massif-type anorthosite, consisting of several individual plutons that may have distinct histories (Ashwal and Twist, 1994; Brower *et al*., 2016; Morais *et al*., 1998; Simpson and Otto, 1960). The rocks of the KAC have not been subjected to any metamorphism, and have very well preserved igneous textures in most cases. The complex thus provides a window into magma chamber dynamics involved in Proterozoic anorthosite petrogenesis, and the tectonic and thermal conditions at this stage of the Proterozoic Eon.

Due to the remote location of the complex and political unrest between 1975 and 2002, the Angolan portion of the complex has not been extensively studied. The complex was mapped as part of a large-scale geological map of Angola by the Serviços de Geologica e Minas de Angola and the Geological Survey of Namibia before 1975 and in 1998. Several researchers have since performed fieldwork in Angola, but most studies focused on limited regions within the complex. In this chapter, I report field observations as well as petrographic and geochemical data for samples collected from across the Angolan sector of the complex during field excursions in 2015 and 2016. The lithologies, mineral assemblages, and textures of the rocks are variable throughout the complex, so samples from as many regions as possible are included in the study in an effort to be representative of the entire KAC.

2.2 GEOLOGIAL FRAMEWORK AND PREVIOUS STUDIES

The Kunene Complex was emplaced at the southern margin of the Congo Craton. It intrudes into biotite granites, granodiorites and tonalites of the Regional Granite (1847 ± 62 Ma to 2236 ± 48 Ma; Carvalho *et al*., 2000; Torquato *et al*., 1979) and a variety of igneous and metamorphic rocks including granites, gneisses and migmatites of the Basement Complex (Fig. 2.1; Carvalho *et al.*, 2000). The Basement Complex is also commonly referred to as the Gneiss-Migmatite-Granite Complex, and corresponds with the high-grade metamorphic rocks of the Epupa Complex in Namibia (Carvalho, 1982; Seth *et al.*, 2003). The Epupa Complex is made up of upper amphibolite facies and granulite facies rocks with protolith ages of 2200 Ma to 1635 Ma (Carvalho and Alves, 1990; Carvalho *et al.*, 2000*;* Seth *et al.*, 2003; Tegtmeyer and Kröner, 1985). The rocks show evidence of metamorphism during the Kibaran orogeny, and give a peak Pb-Pb garnet metamorphic age of 1450 ± 50 Ma (Drüppel *et al*., 2007). The rocks on the Basement Complex in Angola have protolith ages of 2220 Ma to 1830 Ma, corresponding with the Eburnean orogenic event (Carvalho *et al.,* 2000). Rocks of the KAC are dominated by anorthosite and leucotroctolite, with lesser leuconorite and leucogabbronorite (Beetz, 1933; De Carvalho and Alves, 1990; Ashwal and Twist, 1994; Silva, 1992). Most of the Angolan section of the KAC consists of olivine-bearing anorthosites and leucotroctolites. The rocks are generally medium to coarse-grained and massive, with cumulus plagioclase as the dominant mineral. The plagioclase contains abundant Fe-Ti oxide needles, giving the anorthosites their dark color (Ashwal and Twist, 1994; Mayer *et al.*, 2004). The main mafic phases include olivine, orthopyroxene, clinopyroxene, and oxide minerals (generally magnetite and ilmenite), with small proportions of biotite and amphibole, and accessory apatite, zircon and sulphides in some rocks (Drüppel *et al.*, 2007; Silva, 1990). In some areas, the anorthosites consist of plagioclase crystals that are aligned, while the mafic minerals are generally interstitial and non-aligned, implying that the foliation is synmagmatic. The laminated anorthosites occur in belts less than a meter to hundreds of meters wide (Mayer *et al.*, 2004; Morais *et al*., 1998). The complex is intruded by an acidic series of rocks including granites, monzonites, syenites, charnockites and rhyolitic porphyries (Carvalho and Alves, 1990; Mayer *et al.,* 2004; McCourt *et al.,* 2013; Morais *et al.,* 1998), collectively referred to as the Red Granites due to their red weathered color (Mayer *et al.*, 2004). These rocks are akin to the granitoids that, together with the anorthosites, make up AMCG suites around the world.

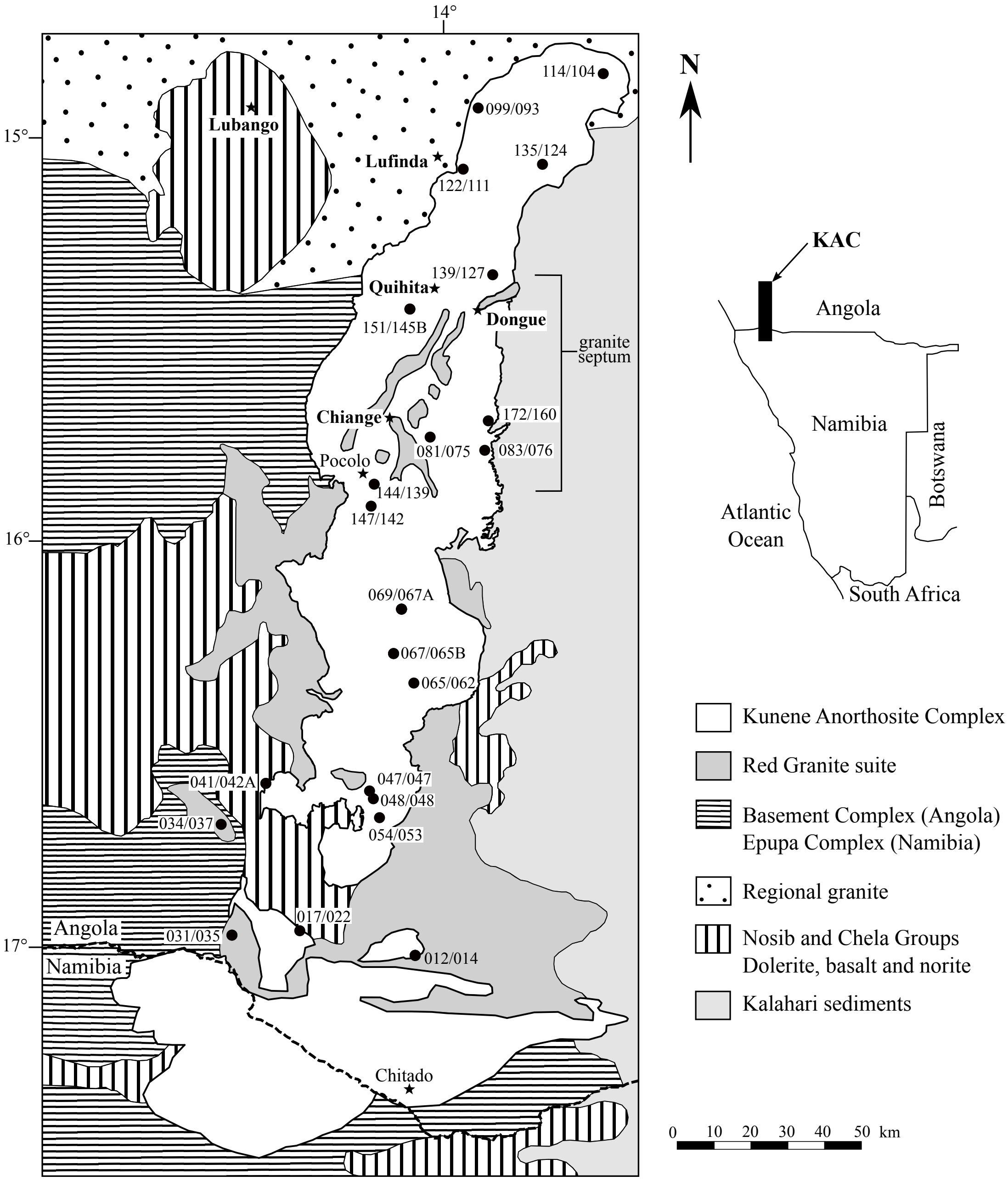

Figure 2.1 Simplified geological map of the Kunene Anorthosite Complex, associated rock types, and country rocks. Map is modified from Drüppel *et al.* (2007), Slejko *et al.* (2002), and Brower *et al.* (2016). Black circles show sample localities, and corresponding sample numbers are given.

It is apparent that the rocks of the KAC are not homogeneous. Mineral assemblages, textures, and chemistry are highly variable across the complex, probably correlating with distinct plutonic entities. Based mainly on variable proportions of olivine and orthopyroxene, many workers have divided the complex into at least two domains, generally a more olivine-rich domain in the north of the complex, and more orthopyroxene (opx)-bearing rocks in the south. However, the distribution of these domains is not well defined, and many different interpretations are given in the literature, discussed here. Common terms given to the domains of the KAC are the “white anorthosites”, generally described as being opx-bearing and mainly lacking olivine, and the “dark anorthosites”, which are dominated by olivine rather than pyroxene. The definitions of these subdivisions, however, are inconsistent in many previous studies. One of the earliest reports of “white” and “dark” anorthosite was given by Köstlin (1967). A large area of massive, white anorthosite was documented in the Namibian section of the KAC, with dark anorthosites further north. The dark anorthosite was described as “troctolitic anorthosite” similar to the anorthosites of the Bushveld Complex, while the white anorthosite was interpreted as a product of calcium metasomatism of the regional gneiss (Köstlin, 1967). Some of the altered, white anorthosite has also been documented in the southern Angolan section of the complex. A more common interpretation of the white anorthosite is that it is an altered version of the normal dark anorthosite, due to its chalky white color and replacement of primary phases (Carvalho and Alves, 1990; Menge, 1998; Silva, 1990; 1992). Plagioclase of the white anorthosite is mainly altered to sericite and epidote, and most pyroxenes have been altered to amphiboles (Ashwal and Twist, 1994). However, due to the fact that not all rocks of the white anorthosite exhibit alteration, and that some fresh examples have been found, the white anorthosite may not exclusively represent an alteration product of the dark. The higher proportion of orthopyroxene in the white anorthosites may be due to their formation from contaminated parental magmas. The altered white anorthosites may have formed as opx-bearing anorthosites from contaminated parental magmas and experienced subsequent alteration. In the Namibian KAC, the altered white anorthosite is dominant, but is intruded by sheets of dark anorthosite (Drüppel *et al.*, 2007; Gleiβner *et al.*, 2011). The white anorthosite has cumulus plagioclase and both cumulus and interstitial orthopyroxene, and the dark anorthosite has cumulus plagioclase and both cumulus and interstitial olivine. There is abundant isotopic evidence to support the formation of the opx-bearing anorthosites by crustal contamination of the anorthosite parental magma (Drüppel *et al.*, 2007; Gleiβner *et al.*, 2010; 2011; 2012; Maier *et al.*, 2013; Slejko *et al.*, 2002).

While the white anorthosites are commonly documented in the Namibian KAC and only the southernmost region of the Angolan KAC, more recent studies (Mayer *et al.,* 2004; Morais *et al.,* 1998; Slejko *et al.,* 2002) interpret the distribution differently. A NE-SW striking belt of Red Granites runs through the Northern section of the complex in Angola, here referred to as the granite septum (Fig. 2.1). It has been suggested that rocks north of the septum are dominated by leucotroctolite and olivine-bearing anorthosite with more calcic plagioclase (close to An_{70}), while rocks to the south of the granite septum contain more orthopyroxene and intermediate plagioclase (An_{40-60}; Mayer *et al.*, 2004; Morais *et al.*, 1998; Slejko *et al.*, 2002). Regardless of where the boundary between the two domains occurs, it seems apparent from the literature that the northern KAC contains more olivine, while the southern portion contains more orthopyroxene. The mineral dichotomy has been attributed to crustal contamination by some workers (Drüppel *et al.*, 2007; Gleiβner *et al,* 2011; Slejko *et al.* 2002).

Fine-grained rocks mapped as marginal dolerite and norite occur along most of the contact of the KAC with the country rocks, and have variable compositions. On the north-west margin of the complex, the dolerites are continuous and commonly foliated parallel to the contact (Mayer *et al*., 2004; Morais *et al*., 1998). In Namibia, the dolerites intrude as dykes into shear zones and brittle faults between the anorthosites and country rocks (Drüppel *et al.*, 2007). Younger dykes intrude the rocks of the KAC, and are likely unrelated to the marginal dolerite (Carvalho and Alves, 1990; Silva, 1990). Dykes of similar composition intruding other anorthosite complexes have been interpreted as possible residual liquids to the anorthositic magma (Ashwal, 1982; Emslie *et al.*, 1994; Mitchell *et al.,* 1996), as anorthosite parental magmas (Duchesne *et al.*, 1974; Longhi *et al.,* 1999; Mitchell *et al.,* 1995) or to be an independent magma series (Vander Auwera *et al.*, 1998). A series of mafic and ultramafic satellite intrusions of variable size and composition occurs on the western margin of the complex, and their relationship with the KAC has not been properly investigated (Drüppel *et al.*, 2007; Maier *et al.,* 2013; Menge, 1998). Bodies of Fe-Ti oxide are common throughout the complex, often in close proximity to the intrusive granites. The ore bodies are generally characterized by massive magnetite and ilmenite, and the observation of poikilitic Fe-Ti oxides in the anorthosites approaching the ore bodies has been interpreted to imply a cogenetic relationship (Mayer *et al.*, 2004; Morais *et al*., 1998).

2.3 GEOCHRONOLOGY

The most recent geochronological studies of the KAC have produced results that show variable ages for different sections of the complex. An internal biotite-plagioclase whole-rock Rb-Sr isochron from an anorthosite sample in the northern part of the complex yielded an age of 1347 ± 13 Ma (Mayer *et al*., 2000). A subsequent study by Mayer *et al*. (2004) used zircons from a mangerite vein, believed to be comagmatic with the anorthosites, to produce an age of 1371 ± 2.5, while a Sm-Nd bulk rock age of 1319 ± 13 Ma for an anorthosite sample and was interpreted to mark the end of anorthosite activity. A subcordant U-Pb single zircon age of 1385 ± 25 Ma was produced from a leucogabbronorite in the Namibian portion of the complex (Drüppel *et al*., 2000). This is corroborated by a SHRIMP U-Pb age of 1385 ± 7 on a mangerite dyke near Lubango in Angola (McCourt *et al.*, 2013). A U-Pb study on leucotroctolites from the Zebra Mountain Lobe in Namibia yielded an age of 1363 ± 17 Ma (Maier *et al.*, 2013). The geochronology results from several authors are summarized in Figure 2.2. Combined with previous geochronological work, Maier *et al*. (2013) inferred that the Kunene magmatism spanned a period of at least 140 m.y. Episodes of magmatism spanning such lengths of time are also implied by Sm-Nd isochrons of HAOMs and host anorthosites in complexes such as the Mealy Mountains Intrusive Suite and the Nain Province in Canada, and the Rogaland Anorthosite Province in Norway. In these complexes, HAOMs are 80 to 120 m.y. older than the emplacement ages of their host anorthosites (Bybee *et al.*, 2014a). Other cases include the Laramie Anorthosite Complex, which intruded over ~330 m.y. (Scoates and Chamberlain, 1997) and the Lac St. Jean massif, forming over ~85 m.y. (Higgins and van Breemen, 1989).

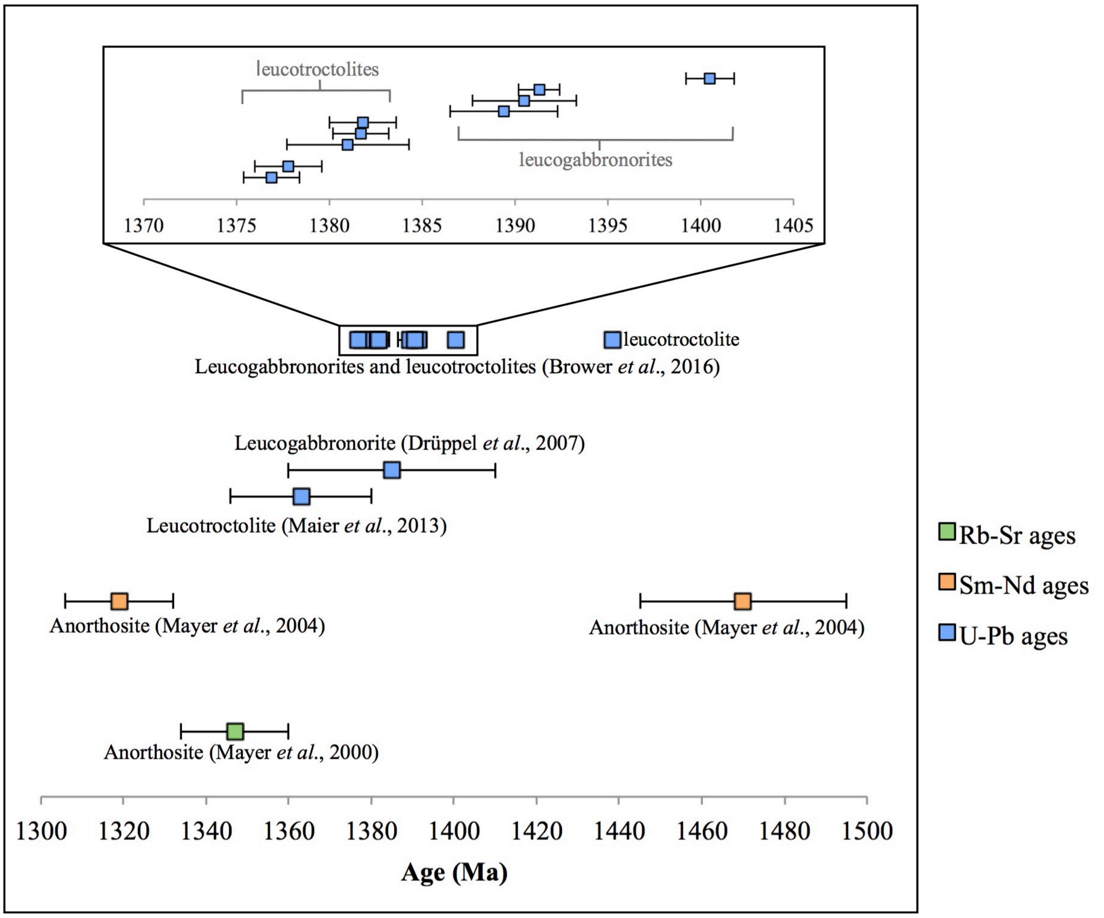

Figure 2.2 Summary of age data for anorthositic rocks of the KAC.

Following a recent expedition to the KAC, samples from across the complex were dated to assess the variability in ages of different plutonic entities, and better quantify the duration of magmatism. Brower *et al.* (2016) produced ten ages for samples spanning most of the length of the Angolan portion of the complex, using ID-TIMS U-Pb in zircon and baddeleyite. For the southern portion (south of the red granite septum), dating of five samples produced ages ranging from 1438.4 ± 1.1 Ma to 1389.4 ± 2.9 Ma. The rocks to the north of the granite septum are slightly younger, with ages between 1381.8 ± 1.8 Ma and 1376.9 ± 1.5 Ma produced by another five samples. This age difference between the northern, olivine-dominated anorthosites and the more pyroxene-rich rocks to the south is comparable with the Nain Complex, where leucotroctolitic rocks on the eastern side of the complex are younger than the leuconoritic rocks to the west (Morse, 2006). A similar relationship occurs in Laramie, where the opx-dominated Chugwater massif is older than the more olivine-rich Poe Mountain massif (Frost *et al*., 2010). The age variations in the KAC also attest to the complex representing a composite intrusion of several coalesced plutons of different ages and compositions, rather than a layered mafic intrusion.

The suite of felsic rocks known as the Red Granites includes granites, syenites, monzonites, charnockites, mangerites and porphyries (Carvalho and Alves, 1990; Mayer *et al.,* 2004; McCourt *et al.,* 2013; Morais *et al.,* 1998). The NE-SW striking granite septum intrudes the rocks of the KAC, but the Red Granites are also prominent in many localities along the margin of the KAC, south of the granite septum. The granites have been dated in several studies, and it is clear that they are coeval (but not comagmatic) with the anorthosites of the KAC. Whole-rock Rb-Sr ages of 1400 – 1300 Ma and 1411 – 1302 Ma were obtained by Carvalho *et al.,* (1987) and Torquato *et al*., (1979). More recently, U-Pb dating of a syenodiorite dyke in the Namibian KAC yielded an age of 1376 ± 2 Ma, which coincides with a U-Pb age of 1371 ± 2.5 Ma for a mangerite vein in the Angolan KAC (Mayer *et al.*, 2004). The Red Granite suite is suggested by many workers to be the product of lower crustal anatexis, formed by partial melting during anorthosite formation. This will be discussed in more detail later in this chapter.

2.4 SAMPLING AND ANALYTICAL METHODS

Samples were collected during a field excursion to the Angolan KAC in September 2015. Samples were taken from as many localities as were accessible, from across the entire Angolan section of the complex. A subset of samples was chosen from across the complex, for detailed petrographic study and analysis of mineral chemistry, ultimately to assess the variability in rock types and mineral chemistry across the complex. This could provide insight into the petrogenetic history of the plutons that make up the complex, and contribute towards understanding Proterozoic anorthosites in general. A variety of rock types was sampled, including all variations of anorthosite, as well as plagioclase and pyroxene megacrysts, marginal dolerites/norites, intrusive dykes of variable composition, Red Granites, and country rocks. Thin sections were prepared from all samples at the University of the Witwatersrand for petrographic study.

Major element mineral compositions were obtained for selected samples by electron microprobe analysis (EPMA), using a Cameca SX100 instrument at the University of Johannesburg. For plagioclase, SiO_2, TiO_2, Al_2O_3, FeO*, MnO, MgO, CaO, K_2O, Cr_2O_3 and BaO were measured, with a beam current of 20 nA, 15 kV accelerating voltage, and a 20 µm beam diameter. For pyroxene and olivine, SiO_2, TiO_2, Al_2O_3, FeO*, MnO, MgO, CaO, K_2O, Cr_2O_3, NiO and ZnO were measured, using a beam current of 20 nA, accelerating voltage of 20 kV, and a focused beam. Average analytical uncertainties are given in Table B5 in Appendix B. Whole-rock compositions of selected Red Granite samples were obtained using X-Ray Fluorescence (XRF) by SGS analytical laboratories in Johannesburg. The samples were prepared into fused beads by the borate fusion method, using a lithium tetraborate flux and an automatic fusion unit (fluxer). Loss on Ignition (LOI) was determined separately by roasting ~1 g of sample at 1000°C for one hour in a furnace. The prepared samples were analyzed by XRF using a PANalytical Axios WDXRF spectrometer. The standard used was SARM-5, a pyroxenite from the Bushveld Complex.

2.5 RESULTS

2.5.1 Field observations and petrographic results

Outcrops of anorthosite commonly occur on ridges and rounded hills, or "koppies" between valleys and plains. All rocks in the KAC are medium to coarse-grained cumulates (Fig 2.3A). Weathered surfaces are typically brownish-grey to dark brown, and fresh surfaces are dark grey, due to Fe-Ti oxide inclusions in plagioclase. Grain size is variable throughout the complex. Plagioclase most commonly occurs as tabular laths between 1 and 3 cm long, but slightly smaller grains do occur, as do grains as large as 5-7 cm in very coarse-grained rocks. On fresh surfaces, labradorescence of plagioclase may be seen. Megacrysts of plagioclase are also common in certain areas (Fig. 2.3C). The plagioclase megacrysts are as large as 15 – 20 cm in some outcrops. Pyroxene megacrysts may be euhedral to subhedral (Fig. 2.3D) or interstitial (Fig. 2.3E). In certain regions of the complex, it is common to see plagioclase-rich blocks surrounded by more mafic material, often coarser-grained or pegmatitc (Fig. 2.3F). This feature occurs on a range of scales, from autoliths of feldspathic material a few cm wide (Fig. 2.3B), to huge feldspathic blocks several meters wide (Fig. 2.3G).

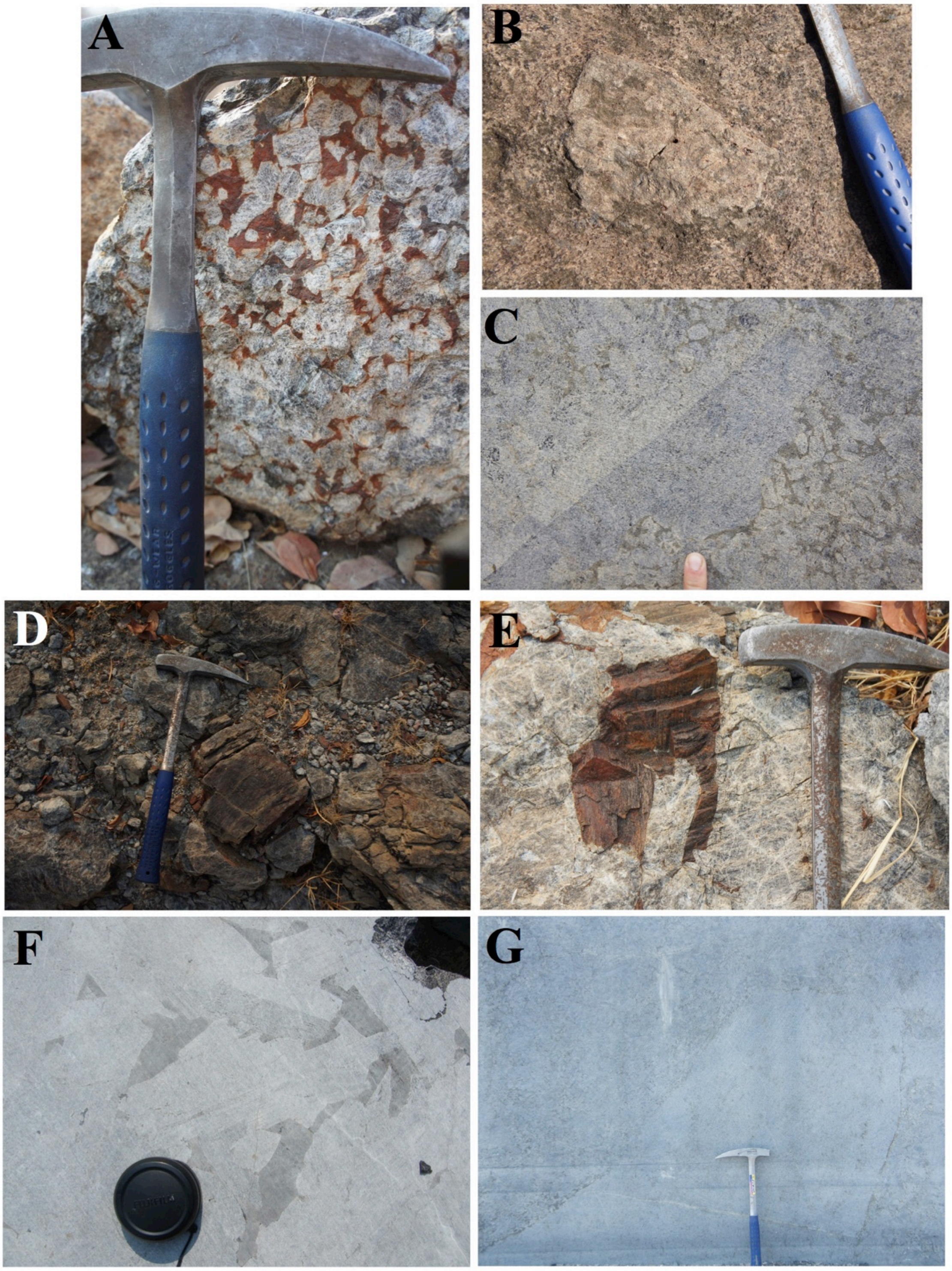

Figure 2.3 Some general field observations in the KAC. A) Coarse-grained leucotroctolite, showing typical cumulate texture. B) Autolith of feldspathic material in leucotroctolite. C) Plagioclase megacryst in leuconorite. D) Subhedral megacryst of orthopyroxene. E) Interstitial orthopyroxene megacryst. F) Pegmatitic anorthosite, showing large euhedral tabular plagioclase and intercumulus orthopyroxene. G) Feldspathic "block" in more mafic-rich leucotroctolite.

In thin section, mafic minerals occur as both cumulus and interstitial phases. Most rocks contain olivine, orthopyroxene, and clinopyroxene in variable proportions, but many rocks south of the granite septum do not contain any olivine. The rocks are mainly characterized as leucotroctolites, leuconorites, leucogabbronorites, olivine-bearing leucogabbronorites, and anorthosites. Anorthosites *senso stricto* mainly occur in the middle and eastern portion of the complex, and contain very small proportions of olivine and/or pyroxene. Fe-Ti oxide minerals occur as small irregular grains adjacent to or between mafic phases, or as larger (~5 mm) rounded oikocrysts or clots, with inclusions of mafic minerals. The oxides are predominantly magnetite, ilmenite and hercynite. Biotite is almost always associated with the oxides, and minor amphibole is also present with oxides in some samples. In some opx-bearing samples, oxides are intergrown with orthopyroxene to form symplectites.

Most rocks in the KAC are fresh, and clearly display magmatic textures, although some magmatic deformation and alteration is evident in certain regions. Banding is evident in some regions on satellite images, generally trending roughly N-S. In these regions, the plagioclase in the rocks commonly displays bent twin planes and undulatory extinction. Recrystallization of plagioclase along grain boundaries is also observed. In addition, white metasomatic veins and metasomatized rocks occur in few isolated regions, as well as narrow shear zones. In some outcrops near the north-central part of the complex, the anorthosites are characterized by prominent white recrystallized rims around plagioclase grains. The grains have typically become rounded at their corners, and are often aligned and bent or kinked. This recrystallization texture has become known as "mortar" texture (Ashwal and Twist, 1994). Its origin is unclear, but it has been suggested to be the result of mechanical comminution of plagioclase in a flowing crystal-rich magma (Buddington, 1939; Ashwal and Twist, 1994). Some rocks contain isolated pockets with a unique mineral assemblage, believed to be late-stage differentiates of the anorthosite system. The pockets typically contain quartz and K-feldspar in graphic intergrowths, plagioclase, magnetite, apatite, epidote, and Cu-sulphide minerals.

Samples were grouped into three rock types, based on their ratio of olivine to orthopyroxene. These are leucotroctolite (LT), olivine-bearing leucogabbronorite (Ol-LGN), and leucogabbronorite (LGN). Anorthosites *senso stricto* (< 10% mafic minerals) are also divided among these categories for simplicity, based on the mafic minerals they contain. A hand sample and petrographic description of each rock type follows.

2.5.1.1 Leucotroctolites

Leucotroctolite and pyroxene-bearing leucotroctolite make up most of the northern sector of the KAC, as well as smaller sections in the south, near the border with Namibia. All rocks in this category have olivine as the dominant mafic mineral, but most also have a smaller proportion of ortho- and/or clinopyroxene. Few *senso stricto* anorthosites with olivine and no pyroxene have been observed. Grain size is variable, with plagioclase ranging from about 1 to 4 cm long. Megacrysts of plagioclase were observed in several outcrops. Mafic minerals are generally smaller and appear interstitial in hand specimen. Olivine is usually a rusty red-brown color on weathered surfaces, and may be dark green-yellow to dark grey on fresh surfaces. Weathered surfaces are sometimes pockmarked from the weathering out of small mafic or oxide minerals. Black oxides are observed in many rocks, generally as large (~1 cm) rounded clots associated with mafic minerals. A patchy texture is seen in many rocks in the north, with feldspathic patches in more mafic-rich rocks (Fig. 2.4A).

In thin section, plagioclase is generally fresh and subhedral to euhedral (Fig. 2.4C,D). Olivine is commonly euhedral and cumulus (Fig. 2.4B), but may also be intercumulus, enveloping plagioclase and developing poikilitic relationships (Fig. 2.4C). In altered samples, olivine may be partially or completely replaced by iddingsite. The euhedral shape of plagioclase in many cases appears to have been interrupted by adjacent olivine crystals, suggesting that olivine and plagioclase may have grown simultaneously. Further evidence for simultaneous growth is the occurrence of small olivine grains included in plagioclase, as well as small plagioclase grains included in olivine in the same sample. Orthopyroxene occurs predominantly as rims on olivine, and more rarely as independent intercumulus grains. Interstitial clinopyroxene oikocrysts surrounding olivine and plagioclase grains are large (~1 cm) in many samples, forming ophitic networks (Fig. 2.4D). The interconnected mafic networks are apparent on the outcrop scale in many localities. Oxide minerals are magnetite, ilmenite and hercynite, and sometimes occur as independent grains, but are commonly intergrown with each other. Many oxides occur in symplectic intergrowths with orthopyroxene (Fig. 2.4E).

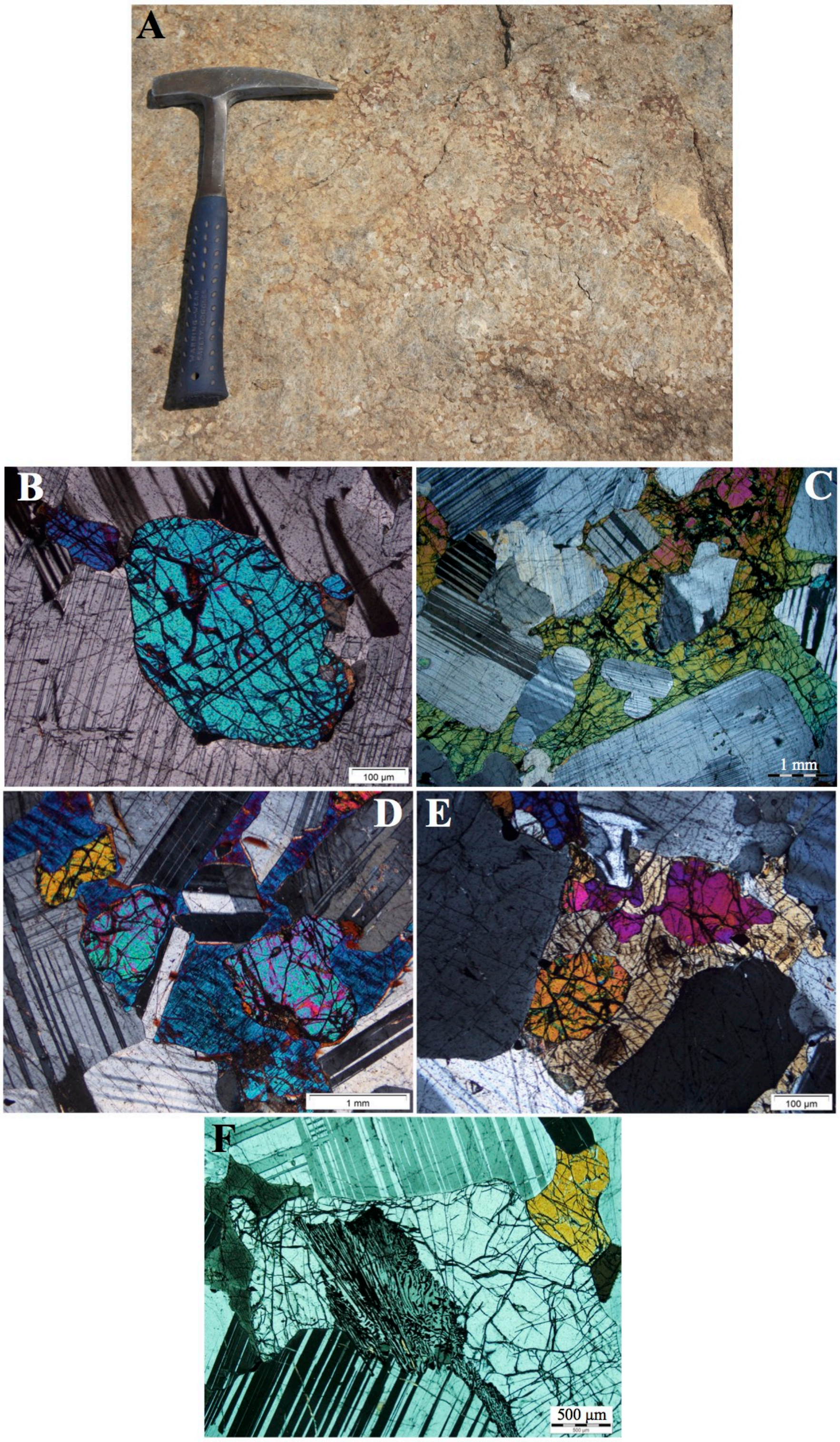

Figure 2.4 A) Patchy texture, with plagioclase-rich patches surrounded by more mafic material (KAC114/104). B) Cumulus olivine and plagioclase in leucotroctolite (KAC122/111). C) Olivine oikocryst surrounding sub-euhedral plagioclase grains (KAC115/105). D) Cumulus olivine and plagioclase with an interstitial ophitic network of clinopyroxene (KAC012/014). E) Interstitial olivine with extensive rims of peritectic orthopyroxene (KAC122/111). F) Symplectic intergrowth of magnetite and orthopyroxene, surrounded by olivine and plagioclase (KAC099/093).

2.5.1.2 Olivine leucogabbronorites

Rocks in this category contain similar proportions of olivine and orthopyroxene, with neither mineral being obviously more abundant than the other. Most rocks contain olivine with prominent rims of orthopyroxene (Fig. 2.5A), as well as intercumulus ortho- and clinopyroxene (Fig. 2.5C). Some cumulus orthopyroxene is also observed. Rusty brown olivine and dark brown pyroxene surround cumulus plagioclase (1-3 cm). Unlike the leucotroctolites, olivine in this category of rocks rarely forms large interstitial networks or oikocrysts. Rather, orthopyroxene occurs as large interstitial oikocrysts surrounding smaller plagioclase and olivine grains (Fig. 2.5B). Recrystallization of plagioclase along grain boundaries is observed in some rocks, and shear zones cross-cut the subtle magmatic foliation observed in rocks in banded sections. Oxides are magnetite, ilmenite and hercynite, and commonly occur as small individual grains rather than larger oikocrysts as in the leucotroctolites. Oxides are associated with mafic minerals and biotite.

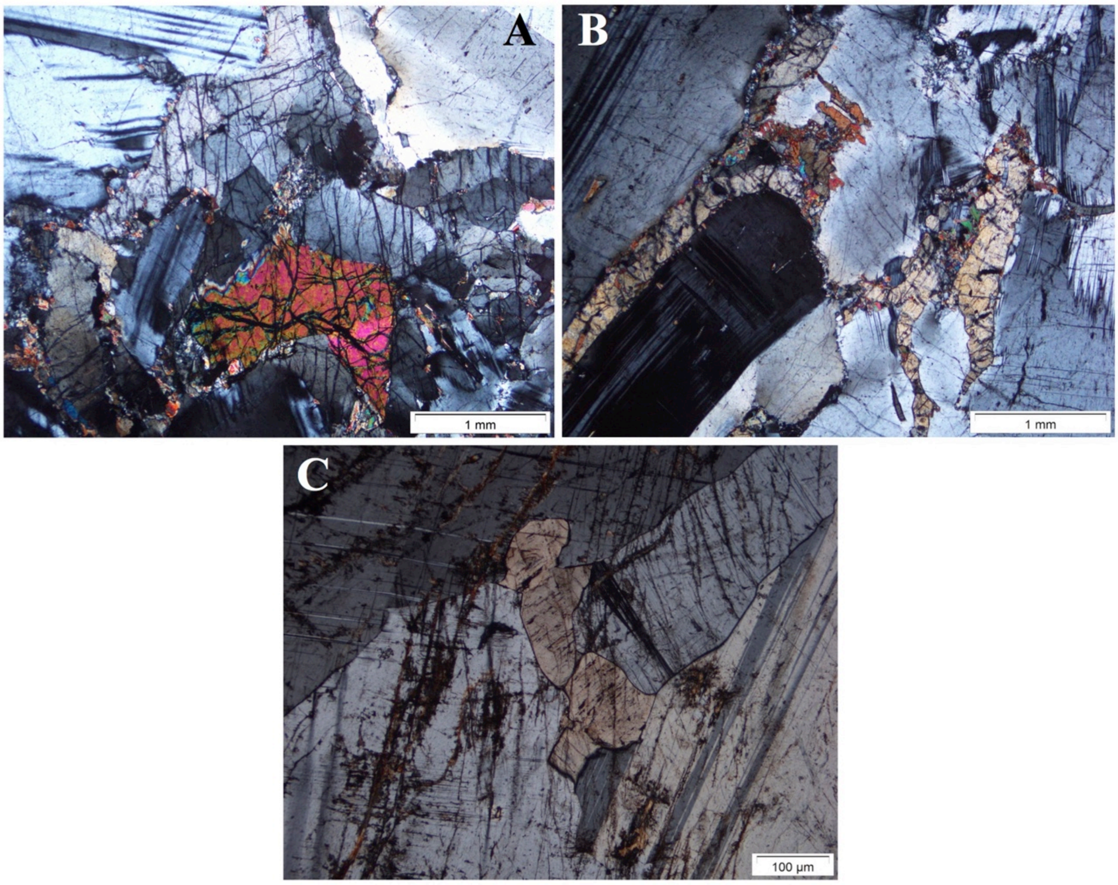

Figure 2.5 A) Interstitial olivine and orthopyroxene in olivine leuconorite (KAC047/047). B) Interstitial ophitic network of orthopyroxene, surrounding plagioclase. Note deformation of plagioclase (KAC047/047). C) Cumulus plagioclase and interstitial orthopyroxene in olivine leucogabbronorite (KAC147/142).

Megacrysts of orthopyroxene occur in many outcrops. These range in size from 10 to 30 cm, and many contain exsolution lamellae of plagioclase and/or clinopyroxene. Most megacrysts are clearly interstitial, but more cumulus and euhedral examples were also observed (Fig. 2.3D and 2.3E).

2.5.1.3 Leucogabbronorites

Rocks of this category have similar textures to leucotroctolites and olivine leucogabbronorites, but contain no olivine, and generally have a lower mafic proportion overall. Not all rocks contain both ortho- and clinopyroxene, but the rocks are grouped together as leucogabbronorites for simplicity. These rocks are mainly restricted to the central and southern portions of the complex. Cumulus plagioclase is commonly surrounded by interstitial networks of dark brown pyroxene (Fig. 2.6B). Orthopyroxene may be cumulus (Fig. 2.6A) or interstitial, while clinopyroxene only occurs as interstitial grains or small grains adjacent to orthopyroxene. Intercumulus megacrysts of orthopyroxene occur in rocks of this type, and one particularly large (several meters wide) clinopyroxene megacryst (KAC069/067A), or aggregation of megacrysts, was observed. Oxide minerals occur as small individual grains and as larger oikocrysts or clots (up to a few cm wide in some outcrops). White veins of alteration as well as very white, altered rocks were observed in certain areas (Fig. 2.6C).

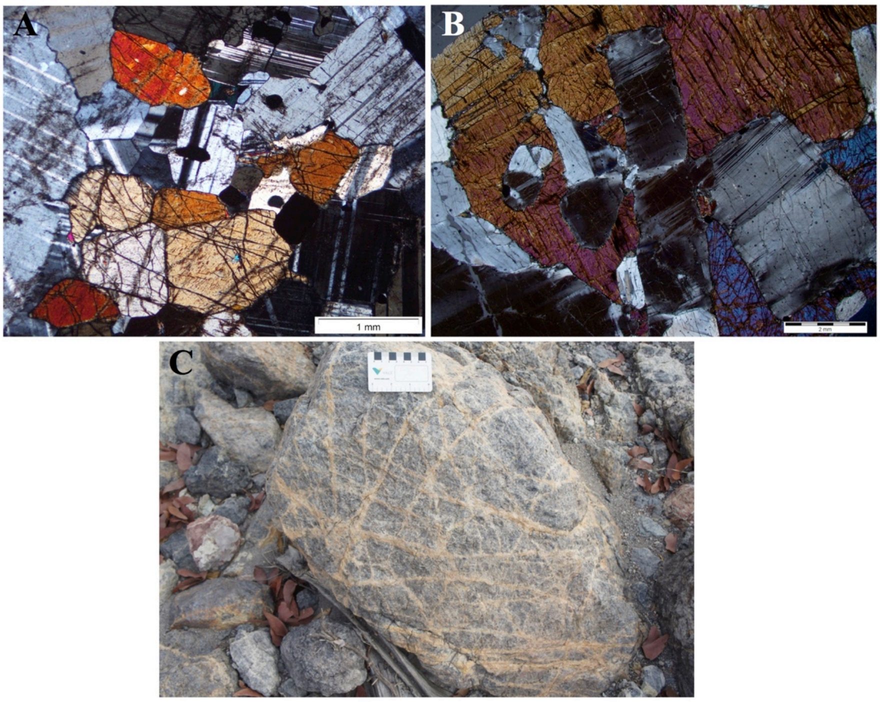

Figure 2.6 A) Cumulus plagioclase and orthopyroxene in leucogabbronorite (KAC041/042A). B) Interstitial ophitic orthopyroxene in leuconorite (KAC067/065B). C) Alteration veins cutting through leuconorite (KAC070/068).

2.5.1.4 Red Granites

Two Red Granite samples were collected for study during the 2015 field excursion, both from the southwest margin of the complex. One sample (KAC031/035) is a fine–medium grained (1-5 mm) pink-colored granite that is dominated by K-feldspar and has a very low mafic proportion. In thin section, the rock consists of roughly equal proportions of quartz, K-feldspar and plagioclase, with a small component (<10%) of altered biotite. Quartz and K-feldspar are commonly intergrown to form a granophyric texture. The other (KAC034/037) is a porphyritic granite, with rounded and euhedral pink K-feldspar phenocrysts (~3 cm) in a finer (~5 mm) equigranular groundmass of hornblende, quartz, and plagioclase. K-feldspar phenocrysts commonly contain small rounded quartz inclusions, and some granophyric texture and perthite are observed. Hornblende grains appear in the groundmass, along with quartz, opaque minerals, and a high proportion of biotite grains aligned around larger mineral grains.

2.5.2 Geochemical results

Electron microprobe analyses were obtained for plagioclase and mafic silicates on the selected KAC samples. Mean analyses are given in Tables 2.1 – 2.5 below. Just as rock types and mineral proportions vary in different regions of the complex, so does the mineral chemistry. Plagioclase is commonly zoned, but the zoning pattern varies by rock type. Core compositions range from An_{56} to An_{75}. An-rich rims are common in many samples, up to An_{83}. The data given in Table 2.2 are for core analyses. Mafic silicates are generally homogeneous in each sample, but also show variability by rock type or region. Not all samples contain olivine, but most contain orthopyroxene. Clinopyroxene has the highest Mg# (66-80) in all rocks, followed by orthopyroxene (Mg# 63-77), and olivine (Mg# 55-74) has the lowest value.

Table 2.1 Mean major element compositions of olivine in sampled KAC rocks. Major oxides in wt. %.

	Leucotroctolites									Olivine Leucogabbronorites			
	KAC 012/014	KAC 017/022	KAC 081/075	KAC 099/093	KAC 114/104	KAC 122/111	KAC 135/124	KAC 139/127	KAC 151/145 B	KAC 047/047	KAC 054/053	KAC 144/139	KAC 147/142
SiO_2	36.55	38.36	35.53	38.24	37.69	38.21	37.90	36.23	37.41	37.95	37.49	36.84	36.81
TiO_2	0.02	0.01	0.00	0.01	0.01	0.01	0.01	0.01	0.00	0.00	0.01	0.01	0.01
Al_2O_3	0.01	0.01	0.02	0.00	0.01	0.01	0.00	0.02	0.00	0.01	0.00	0.00	0.01
FeO*	33.74	24.21	38.26	24.82	26.19	25.48	26.95	35.31	30.03	26.51	26.38	29.45	31.30
MnO	0.47	0.33	0.45	0.37	0.38	0.35	0.38	0.46	0.44	0.34	0.35	0.36	0.39
MgO	29.74	37.75	26.14	36.65	35.89	36.68	35.80	28.70	32.99	35.30	35.43	33.30	31.72
CaO	0.05	0.02	0.03	0.03	0.03	0.02	0.02	0.03	0.02	0.02	0.02	0.02	0.02
Na_2O	0.01	0.00	0.01	0.01	0.00	0.01	0.01	0.00	0.01	0.01	0.01	0.00	0.00
K_2O	0.00	0.00	0.00	0.01	0.01	0.00	0.00	0.00	0.00	0.00	0.00	0.00	0.00
Cr_2O_3	0.01	0.00	0.00	0.00	0.00	0.00	0.01	0.02	0.01	0.00	0.01	0.00	0.00
NiO	0.08	0.17	0.01	0.16	0.10	0.14	0.14	0.06	0.09	0.16	0.15	0.11	0.11
ZnO	0.03	0.02	0.02	0.02	0.03	0.03	0.03	0.02	0.03	0.02	0.02	0.03	0.02
Total	100.70	100.89	100.46	100.32	100.31	100.93	101.24	100.84	101.04	100.33	99.87	100.10	100.41
Fo	60.77	73.27	54.61	72.16	70.65	71.67	70.01	81.03	65.87	70.09	70.26	66.56	64.08
Fa	38.69	26.37	44.86	27.42	28.93	27.93	29.57	17.05	33.64	29.54	29.35	33.02	35.47
Te	0.55	0.37	0.53	0.41	0.42	0.39	0.42	1.92	0.49	0.38	0.39	0.41	0.45
Mole % Fo[a]	61	74	55	72	71	72	70	59	66	70	71	67	64
Fo range	59-70	73-74	55	72-73	71	72	70-71	59	66	69-71	70-71	67	64-65
n	24	11	2	15	2	10	5	2	5	11	6	4	16

* Total Fe as FeO
- Below detection limits
[a] Mole % Fo = molar Mg/(Mg+Fe) *100
n = number of anaylses

Table 2.2 Mean major element compositions of plagioclase in sampled KAC rocks. Major oxides in wt. %.

	Leucotroctolites								
	KAC 012/014	KAC 017/022	KAC 081/075	KAC 099/093	KAC 114/104	KAC 122/111	KAC 135/124	KAC 139/127	KAC 151/145B
SiO_2	53.81	50.58	55.09	50.28	50.13	49.46	49.16	50.41	50.25
TiO_2	0.09	0.03	0.22	0.08	0.03	0.03	0.05	0.04	0.04
Al_2O_3	28.24	30.45	24.38	30.36	30.85	31.45	31.30	31.10	31.46
FeO*	0.33	0.31	1.29	0.45	0.33	0.31	0.34	0.41	0.32
MnO	0.01	0.01	0.01	0.01	0.00	0.01	0.00	0.00	0.00
MgO	0.03	0.17	1.48	0.11	0.05	0.04	0.03	0.05	0.03
CaO	11.59	14.41	11.47	14.27	14.88	15.59	15.70	15.04	15.07
Na_2O	4.84	3.38	5.04	3.27	3.17	2.81	2.82	3.03	3.09
K_2O	0.37	0.16	0.48	0.24	0.15	0.13	0.12	0.18	0.15
Cr_2O_3	0.00	-	0.00	0.01	0.00	0.00	0.00	0.01	0.01
BaO	0.04	-	0.00	0.01	0.03	0.01	0.01	0.00	0.03
Total	99.34	99.51	99.46	99.07	99.64	99.85	99.55	100.27	100.43
An	55.76	69.52	54.20	69.72	71.53	74.81	74.94	72.54	72.31
Ab	42.14	29.54	43.10	28.89	27.61	24.44	24.38	26.43	26.82
Or	2.10	0.93	2.70	1.40	0.87	0.75	0.68	1.02	0.88
Mole % An[a]	57	70	56	71	72	75	75	73	73
An range	53-62	65-83	56	69-72	70-79	73-77	71-78	72-75	71-74
n	10	8	1	8	6	11	12	5	6

* Total Fe as FeO
- Below detection limits
[a] Mole % An = molar Ca/(Ca+Na) * 100
n = number of anaylses

Table 2.2 continued

	Olivine Leucogabbronorites				Leucogabbronorites				
	KAC 047/047	KAC 054/053	KAC 144/139	KAC 147/142	KAC 041/042A	KAC 065/062	KAC 067/065B	KAC 083/076	KAC 172/160
SiO_2	52.59	53.02	53.65	55.15	56.66	55.31	54.39	54.62	54.61
TiO_2	0.04	0.23	0.05	0.05	0.04	0.06	0.04	0.04	0.04
Al_2O_3	29.11	28.26	28.20	27.50	26.71	28.17	27.91	27.48	28.01
FeO*	0.21	0.38	0.22	0.16	0.27	0.13	0.18	0.20	0.21
MnO	0.01	0.02	0.01	0.01	0.01	0.00	0.01	0.00	0.01
MgO	0.02	0.22	0.03	0.02	0.02	0.02	0.02	0.02	0.02
CaO	12.58	12.05	11.80	10.76	9.74	10.69	11.07	10.81	11.35
Na_2O	4.38	4.60	4.87	5.36	5.86	5.27	5.04	5.32	5.02
K_2O	0.29	0.36	0.35	0.48	0.43	0.51	0.40	0.45	0.45
Cr_2O_3	0.00	0.00	0.01	0.00	0.01	0.00	0.00	0.00	0.00
BaO	0.03	0.02	0.03	0.03	0.10	0.04	0.03	0.03	0.03
Total	99.25	99.14	99.22	99.51	99.85	100.21	99.07	98.97	99.75
An	60.30	57.91	56.09	51.19	46.69	51.32	53.56	51.53	54.09
Ab	38.03	40.02	41.93	46.11	50.86	45.76	44.12	45.92	43.34
Or	1.67	2.07	1.98	2.70	2.45	2.93	2.32	2.54	2.57
Mole % An[a]	61	59	57	53	48	53	55	53	56
An range	60-63	57-70	57-58	51-55	44-52	50-56	53-56	51-54	53-58
n	20	6	7	12	18	5	17	12	15

* Total Fe as FeO
- Below detection limits
[a] Mole % An = molar Ca/(Ca+Na) *100
n = number of anaylses

Table 2.3 Mean major element compositions of orthopyroxene in sampled KAC rocks. Major oxides in wt. %.

	Leucotroctolites								**Olivine Leucogabbronorites**			**Leucogabbro-norites**	
	KAC 012/014	KAC 017/022	KAC 099/093	KAC 114/104	KAC 122/111	KAC 135/124	KAC 139/127	KAC 151/145 B	KAC 047/047	KAC 054/053	KAC 147/142	KAC 041/042 A	KAC 067/065 B
SiO_2	53.45	54.19	54.23	53.89	54.31	53.93	53.11	54.30	54.11	53.10	52.49	52.61	53.23
TiO_2	0.28	0.21	0.30	0.20	0.25	0.22	0.20	0.17	0.12	0.10	0.22	0.44	0.14
Al_2O_3	0.97	1.97	1.75	1.18	1.56	1.37	0.95	1.24	2.05	2.50	2.11	0.83	1.81
FeO*	20.10	15.13	15.60	17.74	15.89	16.86	21.93	17.93	16.48	16.97	18.63	22.74	18.93
MnO	0.45	0.34	0.37	0.38	0.35	0.38	0.47	0.42	0.33	0.32	0.37	0.71	0.38
MgO	23.65	27.68	26.95	25.84	27.10	26.35	22.73	25.55	26.58	25.99	24.54	22.10	24.60
CaO	1.20	0.65	0.83	0.79	0.84	0.75	0.79	0.73	0.52	0.51	0.82	0.90	0.68
Na_2O	0.02	0.01	0.01	0.02	0.01	0.01	0.02	0.01	0.01	0.01	0.02	0.01	0.01
K_2O	0.00	0.00	0.01	0.00	0.00	0.00	0.00	0.00	0.00	0.00	0.00	0.00	0.00
Cr_2O_3	0.00	0.01	0.02	0.01	0.02	0.01	0.00	0.01	0.01	0.01	0.05	0.01	0.05
NiO	0.02	0.03	0.03	0.02	0.03	0.03	0.02	0.03	0.04	0.03	0.03	0.02	0.04
ZnO	0.03	0.02	0.02	0.02	0.02	0.02	0.03	0.03	0.02	0.02	0.01	0.04	0.02
Total	100.18	100.23	100.11	100.09	100.41	99.93	100.27	100.38	100.26	99.55	99.27	100.41	99.89
Wo	2.42	1.27	1.65	1.56	1.65	1.49	1.59	1.45	1.03	1.02	1.66	1.82	1.37
En	66.08	75.56	74.24	71.07	74.00	72.49	63.85	70.71	73.43	72.45	68.97	62.25	68.89
Fs	31.50	23.17	24.11	27.37	24.35	26.02	34.56	27.84	25.54	26.53	29.36	35.93	29.74
Aeg	0.41	1.12	0.18	1.10	0.95	0.94	0.72	0.04	0.24	1.23	1.59	0.98	0.64
Jd	0.59	1.27	1.46	0.53	0.92	0.76	0.57	1.28	1.96	1.98	1.31	0.04	1.52
Di	99.00	97.62	98.37	98.37	98.12	98.30	98.72	98.68	97.80	96.79	97.10	98.98	97.84
Molar Mg#[a]	68	77	75	72	75	74	65	72	74	73	70	63	70
Mg# range	67-75	76-77	73-82	69-75	74-76	72-75	63-68	72	73-75	71-75	69-70	62-64	69-71
n	14	13	9	8	11	11	7	2	11	12	4	12	15

* Total Fe as FeO
- Below detection limits
[a]Mg# calculated as molar Mg/(Mg+Fe) * 100
n = number of anaylses

Table 2.4 Mean major element compositions of clinopyroxene in sampled KAC rocks. Major oxides in wt. %.

	Lecotroctolites						Olivine Leucogabbronorites			Leucogabbronorites			
	KAC 012/014	KAC 017/022	KAC 099/093	KAC 114/104	KAC 122/111	KAC 151/145 B	KAC 047/047	KAC 144/139	KAC 147/142	KAC 041/042 A	KAC 067/065 B	KAC 083/076	KAC 172/160
SiO_2	51.30	51.18	50.73	50.67	51.23	52.72	51.21	50.05	50.28	51.85	50.66	49.49	50.34
TiO_2	0.78	0.79	0.76	0.82	0.82	0.36	0.55	0.82	0.89	0.34	0.84	0.77	0.70
Al_2O_3	2.38	3.36	4.22	2.73	3.19	1.95	3.17	3.58	3.74	1.62	3.52	3.58	3.48
FeO*	8.66	7.56	6.54	8.93	7.32	6.60	6.95	7.58	8.20	9.32	7.14	10.52	8.35
MnO	0.24	0.19	0.19	0.22	0.20	0.22	0.15	0.18	0.19	0.35	0.16	0.24	0.22
MgO	14.32	14.82	14.45	14.63	15.20	15.09	14.03	14.30	13.55	13.85	13.84	11.53	13.16
CaO	21.62	21.63	22.46	20.98	21.49	22.59	23.37	21.99	22.16	22.13	22.90	22.67	23.03
Na_2O	0.35	0.41	0.30	0.34	0.37	0.23	0.39	0.45	0.51	0.36	0.44	0.56	0.42
K_2O	0.00	0.01	0.01	0.01	0.01	0.00	0.00	0.01	0.00	0.01	0.00	0.00	0.00
Cr_2O_3	0.04	0.07	0.03	0.01	0.15	0.05	0.01	0.02	0.10	0.02	0.09	0.00	0.01
NiO	0.02	0.03	0.02	0.02	0.02	0.01	0.02	0.02	0.02	0.01	0.02	0.02	0.02
ZnO	0.01	0.01	0.01	0.01	0.01	0.01	0.01	0.01	0.01	0.02	0.03	0.01	0.01
Total	99.70	100.07	99.72	99.38	99.99	99.83	99.84	98.99	99.63	99.88	99.65	99.38	99.72
Wo	44.76	44.92	47.11	43.43	44.45	46.35	48.38	46.00	46.75	45.46	47.98	48.31	48.12
En	41.24	42.83	42.18	42.13	43.74	43.08	40.40	41.62	39.76	39.59	40.35	34.20	38.26
Fs	13.99	12.25	10.71	14.43	11.81	10.57	11.23	12.38	13.49	14.94	11.68	17.49	13.61
Aeg	3.84	4.38	3.17	4.85	4.14	1.41	4.57	6.02	5.36	4.53	4.65	6.57	5.48
Jd	2.00	3.13	4.02	1.75	2.69	2.51	3.02	2.78	3.54	1.54	3.28	3.33	2.89
Di	94.16	92.49	92.81	93.40	93.17	96.07	92.41	91.20	91.10	93.93	92.07	90.10	91.62
Molar Mg#[a]	75	78	80	74	79	80	78	77	75	73	78	66	74
Mg# range	67-80	75-79	78-82	73-76	78-79	80	75-78	76-78	74-76	71-74	78	65-68	73-74
n	13	11	13	3	2	1	4	5	8	5	1	6	4

* Total Fe as FeO
- Below detection limits
[a]Mg# calculated as molar Mg/(Mg+Fe) *100
n = number of anaylses

Table 2.5 Mean major element compositions of orthopyroxene, clinopyroxene, and plagioclase in sampled KAC pyroxene megacrysts, exsolution lamellae, and inclusions. Major oxides in wt. %.

	KAC48/48A			KAC069/067A		
	Opx megacryst	Cpx inclusions	Plag lamellae	Cpx megacryst	Opx inclusions	Plag lamellae
SiO_2	52.77	51.83	47.35	49.17	51.49	55.05
TiO_2	0.11	0.36	0.10	0.88	0.14	0.03
Al_2O_3	1.51	2.15	27.34	4.67	2.39	27.38
FeO*	21.32	8.04	3.35	9.61	22.78	0.33
MnO	0.43	0.18	0.05	0.23	0.50	0.01
MgO	22.13	13.90	3.69	12.22	21.60	0.01
CaO	1.39	23.03	14.84	21.68	0.61	10.75
Na_2O	0.02	0.30	1.84	0.73	0.01	5.39
K_2O	0.00	0.00	0.09	0.00	0.00	0.38
Cr_2O_3	0.04	0.10	0.02	0.13	0.06	0.00
NiO	0.02	0.01	-	0.02	0.03	-
ZnO	0.03	0.01	-	0.01	0.03	-
BaO	-	-	0.03	-	-	0.02
Total	99.77	99.89	98.70	99.34	99.65	99.34
Wo	2.85	47.35		46.95	1.27	
En	63.07	39.75		36.81	62.03	
Fs	34.08	12.90		16.25	36.71	
Aeg	0.07	3.48		7.32	1.62	
Jd	1.64	2.09		4.99	1.67	
Di	98.29	94.43		87.68	96.71	
An			81.24			51.30
Ab			18.19			46.53
Or			0.57			2.17
Molar Mg#[a]	65	76		69	63	
Mole % An[b]			82			52
Mg#/An range	64-67	74-76	79-86	68-71	62-64	48-55
n	16	4	8	12	10	6

* Total Fe as FeO

\- Below detection limits

[a]Mg# calculated as molar Mg/(Mg+Fe) *100

[b] Mole % An = molar Ca/(Ca+Na) *100

n = number of anaylses

2.5.2.1 *Leucotroctolites*

The olivine-dominated anorthosites, or leucotroctolites (LT), have the most calcic plagioclase, ranging from An_{56-75}, but mostly exceeding An_{70}. The two samples with lower mean An contents are KAC012/014 (An_{57}) and KAC081/075 (An_{56}). Plagioclases in these samples also have higher TiO_2 and K_2O than the feldspars in leucotroctolite samples. KAC081/075, located just south of the granite septum, is a *senso stricto* anorthosite, with a mafic proportion less that 5%. Other *senso stricto* anorthosites in the complex (KAC065/062, KAC083/076, and KAC172/160) have similarly low An plagioclase (An_{53} and An_{56} respectively). However, these are pyroxene-bearing anorthosites with no olivine present. Most plagioclase in the leucotroctolite samples has minimal zoning, apart from the only two samples in the far south of the complex (KAC012/014 and KAC017/022), which display normal zoning of up to 6 mole %, and sample KAC099/093 which has patchy zoning. Some samples display An-rich rims up to 10 mole % higher than cores, generally adjacent to mafic silicates.

Olivine in the LT samples is within the range Fo_{55-74}. The only two samples with olivine less magnesian than Fo_{60} are KAC081/075 and KAC139/127 (Fo_{55} and Fo_{59}, respectively). These samples are both *senso stricto* anorthosites. KAC012/014 also falls in the lower end of the range, at Fo_{61}. The other samples all have $Fo_{>66}$. KAC017/022 has the most magnesian olivine (Fo_{74}). Orthopyroxene ranges from En_{65} to En_{77}. Orthopyroxene in LT has higher Mg# than in LGN and Ol-LGN. The lowest value (En_{65}) comes from the *senso stricto* anorthosite KAC139/127. The other *senso stricto* anorthosite (KAC081/075) contains no orthopyroxene. KAC012/014 also has fairly low En orthopyroxene, at En_{68}, and it also has higher CaO than all other orthopyroxene. As with olivine, KAC017/022 has the most magnesian orthopyroxene (En_{77}). Clinopyroxene in leucotroctolites has Mg# in the range 74 – 80. Pyroxenes in all samples are displayed in Figure 2.7.

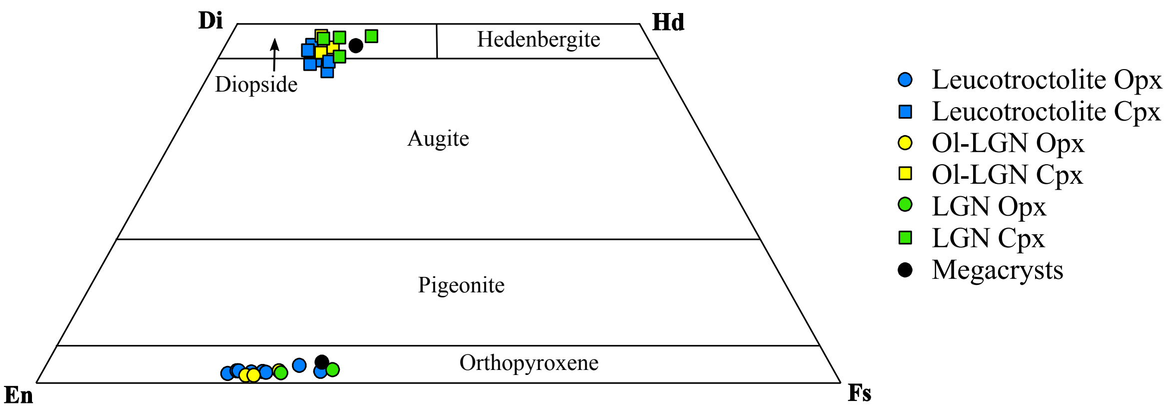

Figure 2.7 Pyroxene quadrilateral showing all pyroxenes in sampled KAC rocks, including megacrysts.

2.5.2.2 Olivine leucogabbronorites

The olivine-bearing leucogabbronorites contain generally less calcic plagioclase than the LT, ranging from An_{53} to An_{61}. All samples display slight reverse zoning in plagioclase (± 3 mole %) and An-rich rims up to 10 mole % higher than cores are present in some rocks. Plagioclase also contains less FeO* than the LT. Olivine is within the range Fo_{64-71}. Orthopyroxene ranges from En_{70} to En_{74}, and is slightly more aluminous than the LT or LGN. KAC147/142 contains the least calcic plagioclase, and lowest Mg# olivine and orthopyroxene. Clinopyroxene in the Ol-LGN has a mean Mg# of 75 - 78.

2.5.2.3 Leucogabbronorites

Leucogabbronorites contain the least calcic plagioclase of all lithologies (An_{48-56}). Some samples have plagioclase with slight reverse zoning (2 – 3 mole %) but An-rich rims are uncommon. Less mafic mineral data is available for this rock category, since three of the samples are *senso stricto* anorthosites with a very low mafic proportion. No samples contain olivine. Orthopyroxene ranges from En_{63} to En_{70}, which, despite fewer representative samples, is lower than for the LT and Ol-LGN. Sample KAC041/042A has the lowest En orthopyroxene, with slightly higher MnO than the other orthopyroxene. It also has the least calcic plagioclase (An_{48}). This sample is from the southwest margin of the complex, near to the Red Granites. Clinopyroxene in the LGN ranges from Mg# 66 – 78.

2.5.2.4 Megacrysts

Mean microprobe data for two pyroxene megacrysts is given in Table 2.5. Sample KAC048/048 is a polycrystalline orthopyroxene megacryst with thin lamellae and inclusions of plagioclase, and small irregular clinopyroxene inclusions. The megacryst has En_{65}, falling in the lower end of the range of orthopyroxene in the other samples. It has an average Al_2O_3 of 1.51 wt. %, with exsolution lamellae of very calcic plagioclase (An_{82}). The lamellae are more calcic than any other plagioclase sampled, and are also richer in FeO* and MgO. The clinopyroxene inclusions have average Mg# of 76, within the range of other samples.

KAC069/067A is from a very large (several meters wide) aggregate of clinopyroxene megacrysts, with lamellae and small blocky inclusions of orthopyroxene, as well as lamellae and inclusions of plagioclase, commonly containing oxide minerals. The megacryst has average Mg# of 69, falling at the lower end of the range for other clinopyroxene. It has the highest Al_2O_3 of all the sampled clinopyroxene (4.67 wt. %) as well as slightly higher Na_2O and Cr_2O_3. The plagioclase lamellae are on the least calcic end of the range (An_{52}). The orthopyroxene inclusions and lamellae have an average Mg# of 63, corresponding with the lowest Mg# of orthopyroxene in the other samples. The orthopyroxene also has higher Cr_2O_3

and MnO than in other samples. A summary of the An content of plagioclase and Mg# of mafic silicates is given in Table 2.6.

Table 2.6 Summary of the chemistry of plagioclase and mafic silicates in leucotroctolites, olivine leucogabbronorites, and leucogabbronorites of the KAC, excluding pyroxene megacrysts.

	Pl An	**Opx Mg#**	**Cpx Mg#**	**Ol Mg#**
Leucotroctolite	56 - 75	65 - 77	74 - 80	61 - 74
Olivine leucogabbronorite	53 - 61	70 - 74	75 - 80	64 - 71
Leucogabbronorite	48 - 56	63 - 70	66 - 78	

2.5.2.5 Red Granites

Whole-rock major element compositions for the two sampled Red Granites are given in Table 2.7 below. Since the Red Granite suite includes such a wide range of felsic rock types, the chemical compositions of the rocks are variable. Samples KAC031/035 and KAC034/037 are clearly very different based on appearance and petrography, and so it is expected that they differ chemically as well. Both have the normative composition of granite on a QAPF diagram (Streckeisen, 1976), but on a Total Alkali vs. Silica (TAS) diagram, 031/035 plots as a granite while 034/037 is a syenite. Both are K-rich granites, have higher Na_2O than CaO, and high Fe/Fe+Mg ratios. Sample 031/035 is ~10% more silicic than 034/037. The deficit in SiO_2 in 034/037 is balanced by higher Al_2O_3, CaO, FeO*, MgO, TiO_2 and MgO, due to the higher mafic proportion in the sample, particularly hornblende.

Table 2.7 Whole-rock major element data for Red Granite samples. Major oxides in wt. %.

	KAC 031/035	KAC 034/037A
SiO_2	76.7	66.8
TiO_2	0.2	0.59
Al_2O_3	11.8	14.7
FeO*	2.29	4.55
MnO	0.04	0.11
MgO	-	0.39
CaO	0.29	1.9
Na_2O	3.4	3.22
K_2O	5.31	6.4
P_2O_5	0.06	0.15
V_2O_5	0.01	-
Cr_2O_3	-	-
LOI	0.31	0.6
Total	100.41	99.41

* Total Fe and FeO (originally given total Fe as Fe_2O_3)

- Below detection limits

2.6 DISCUSSION OF KAC RESULTS

It is clear that the Kunene Complex exhibits significant heterogeneity in modal composition and mineral chemistry, as well as in texture and state of alteration or deformation. According to field observations and the data presented in this study, there is little evidence to suggest that the KAC is a layered mafic intrusion. This is in agreement with the study of Ashwal and Twist (1994). No trends of layering in rock type or chemistry have been observed, and the observed heterogeneity occurs between distinct regions in the complex. These regions are likely to be individual intrusions or plutons with different petrogenetic histories. The geochronology data (Brower *et al*., 2016) produced 10 different ages (between 1438.4 ± 1.1 Ma and 1376.9 ± 1.5 Ma) for samples taken from different regions of the complex. This, as well as the patterns of variability across the complex, provides support for the KAC being a composite massif-type anorthosite rather than a layered mafic intrusion (Ashwal and Twist, 1994).

2.6.1 Classification and distribution of rock types

Most sampled rocks may be classified as leucotroctolite (LT) or leucogabbronorite (LGN) based on the abundance of plagioclase and the ratio of olivine to pyroxene. Not all samples contain olivine, but most contain orthopyroxene. Those that contain roughly equal proportions of olivine and pyroxene are classified as olivine-bearing leucogabbronorite (Ol-LGN). The distribution of rock types in the complex is shown in Figure 2.8A. While a few exceptions do exist, it is clear from the data and Figure 2.8 that there is a difference in mineralogy and mineral chemistry between rocks in the northern and southern sections of the KAC. Olivine-bearing anorthosites or leucotroctolites are dominant in the north of the complex. Many of these rocks do contain orthopyroxene and clinopyroxene as well (most commonly as rims on olivine, and minor interstitial grains), but all contain a higher proportion of olivine than pyroxene as the mafic phase, leading to their classification as olivine-bearing anorthosites. Orthopyroxene-dominated anorthosites only occur to the south of the granite septum. There are two samples in the far south that do not fit the general trend. Samples KAC012/014 and KAC017/022 are olivine-dominated. The olivine leucogabbronorites with roughly equal olivine to orthopyroxene ratios also only occur south of the granite septum. It is interesting that these samples seem to be located between regions of olivine-dominated and orthopyroxene-dominated anorthosites, making them appear as a kind of transition from one rock category to the other. However, since only four samples classify as olivine-leucogabbronorite, this could be an artefact of sampling, and further detailed sampling and mapping would be needed to confirm this observation.

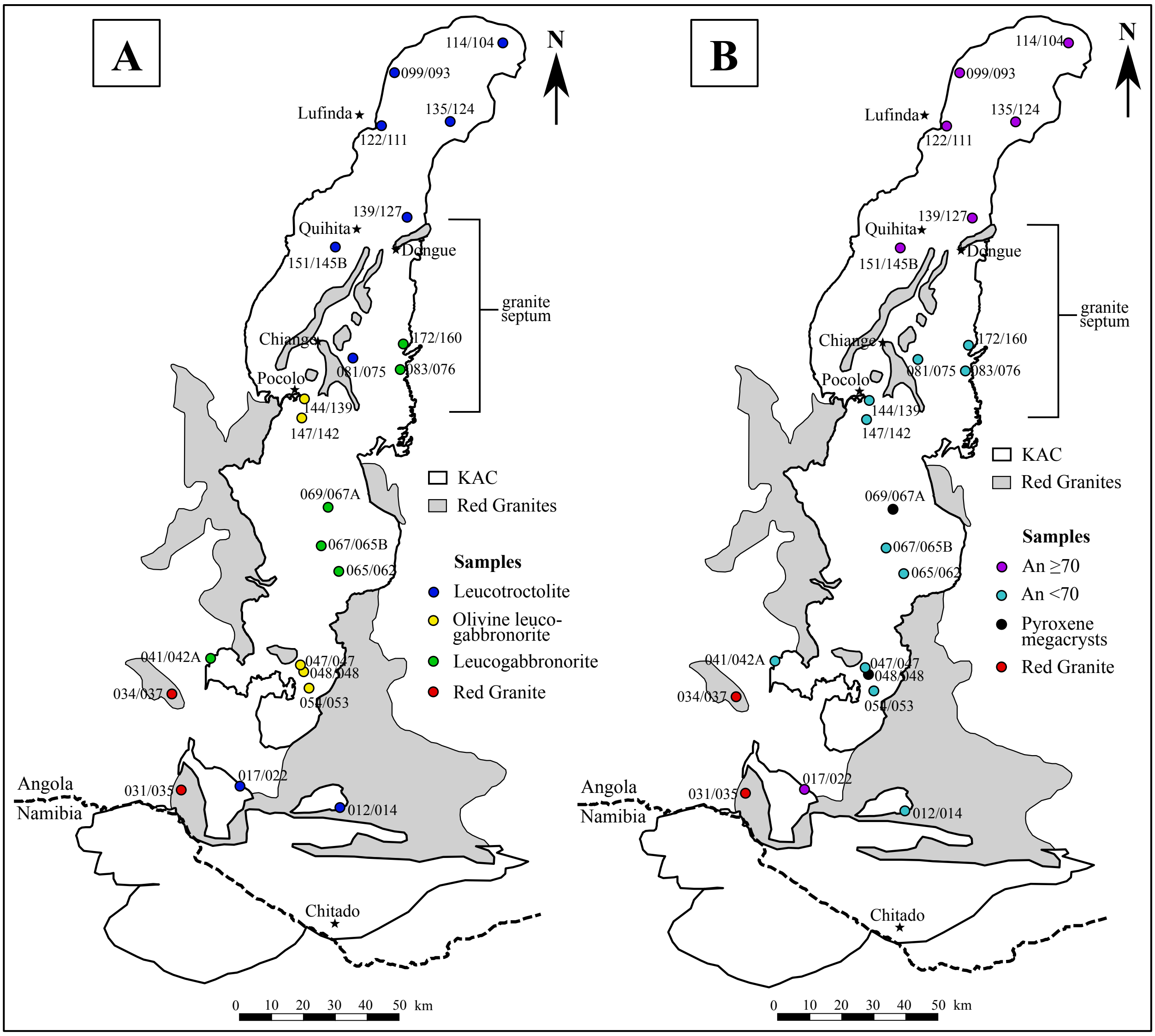

Figure 2.8 Simplified maps of the KAC and Red Granites. A) Distribution of rock types sampled. Rocks of the KAC are classified as leucotroctolite, olivine leucogabbronorite, and leucogabbronorite, based on the ratio of olivine to pyroxene. With few exceptions, leucotroctolites prevail in the north of the complex, while leucogabbronorites are more dominant in the south. B) An-content variation in the KAC rocks. Rocks with An_{70} or higher are dominant north of the granite septum. Rocks with An-content less than An_{70} are more dominant south of the granite septum.

It has been previously noted that anorthosites north of the granite septum have more calcic plagioclase than those in the south (Mayer *et al.*, 2004; Morais *et al.*, 1998; Silva, 1992). The data in this study agree with this statement in general. All sampled rocks north of the granite septum have plagioclase with An content of 70 or greater. Most samples south of the septum have plagioclase with An less than 70 (Fig. 2.8B). The outlier in the south is the LT sample

KAC017/022, which has plagioclase of An_{70}, higher than any other sample in the south. Excluding this sample, all rocks south of the granite septum have plagioclase with An content of 61 or less. This trend of more calcic plagioclase in the north, and more sodic or intermediate plagioclase in the south, generally correlates with the distribution of rock types, since olivine-bearing anorthosites dominate in the north, and more pyroxene-rich rocks are restricted to the south. There is a general correlation between An content of plagioclase and the proportion of olivine in the rocks sampled (Table 2.6 above). The more olivine-rich rocks contain more calcic plagioclase, followed by the olivine-bearing leucogabbronorites. The olivine-free rocks have the lowest An plagioclase. This trend also roughly correlates with the Mg# of mafic silicates in the rocks, particularly orthopyroxene, and to a lesser degree clinopyroxene. The olivine composition is fairly consistent among all sampled rocks. The trend of more calcic plagioclase in olivine-bearing anorthosites, and more sodic plagioclase in orthopyroxene-bearing anorthosites is a common feature in Proterozoic anorthosites around the world (Emslie, 1980; 1985; Gleiβner *et al.,* 2010; Lindsley *et al.,* 2010; Philpotts, 1966). Figure 2.9 shows the An content of plagioclase vs. Fo content of olivine in leucotroctolites and En content of orthopyroxene in leuconorites/leucogabbronorites for several other Proterozoic anorthosite complexes (blue and green fields) and for the KAC samples (blue and green points). Note that the rocks in the olivine leucogabbronorite category have been grouped into either the leucotroctolite or leucogabbronorite categories for this plot, depending on which mafic mineral appeared even marginally more abundant than the other.

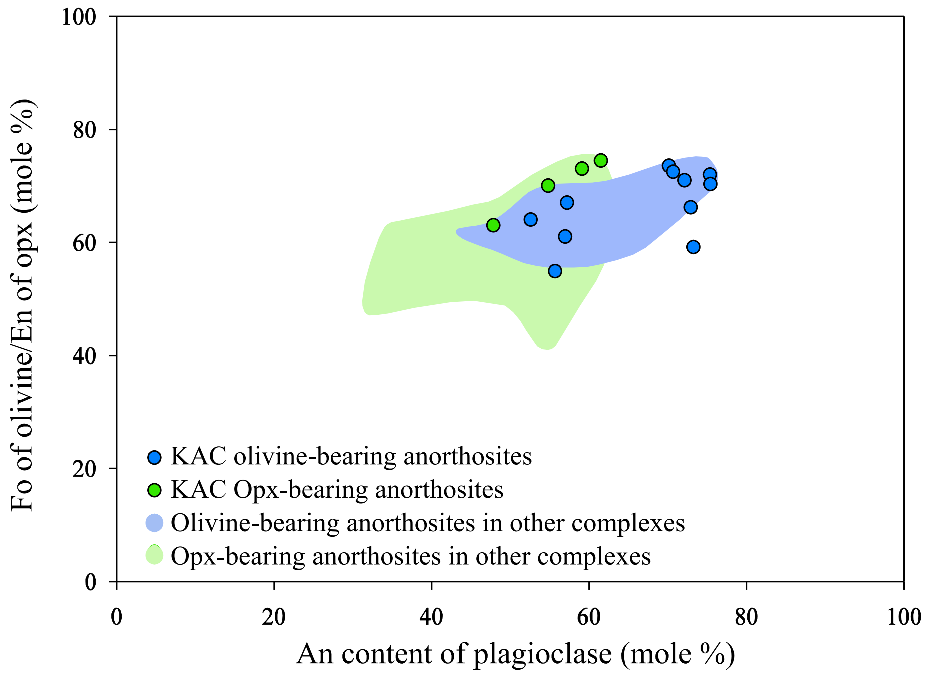

Figure 2.9 An of plagioclase vs. Fo of olivine in olivine-bearing anorthosites (with a higher proportion of olivine than orthopyroxene) and En of orthopyroxene in orthopyroxene-bearing anorthosites (with more orthopyroxene than olivine) for the Kunene Complex and other Proterozoic anorthosites, including the Adirondacks, Harp Lake, Labrieville, Laramie, Mealy Mountains, Michikamau, Morin, and Paul Island complexes. Data sources: Emslie (1980; 1985); Lindsley *et al.* (2010); Philpotts (1966).

2.6.2 Olivine- vs. Orthopyroxene-bearing anorthosites and crustal contamination

While the distribution of olivine-bearing and orthopyroxene-bearing anorthosites in the Kunene Complex has been interpreted differently by a number of researchers (Drüppel *et al.*, 2007; Köstlin, 1967; Mayer *et al.,* 2004; Menge, 1998; Silva, 1992) the existence of (at least) two different lithologies, one dominated by orthopyroxene and the other by olivine, has always been noted. Most samples in this study contain both olivine and orthopyroxene (and clinopyroxene), but in variable proportions, leading to their classification into three lithologies. There are several samples from the south of the complex that have orthopyroxene and no olivine. Many of these samples are fresh and unaltered. In several other localities, a distinct type of leucogabbronorite (LGN) was identified. Progressive fluid alteration is apparent in these areas, ranging from white veins cutting through otherwise normal, fresh LGN, to completely altered, very white-colored rock. Several authors divided the KAC rocks into "dark" olivine-bearing anorthosite and "white" orthopyroxene-bearing, described as a metasomatic alteration product of the original dark anorthosite, or of the country rocks (Carvalho and Alves, 1990; Drüppel *et al.*, 2007; Köstlin, 1967; Menge, 1988 Silva, 1990;

1992). Since both fresh and altered orthopyroxene-bearing bearing anorthosites were observed on the 2015 field excursion, it is most likely that the "white anorthosite" documented by previous authors is the product of metasomatism of pre-existing orthopyroxene-bearing anorthosite, and not of the dark, leucotroctolitic anorthosite or of the country rocks. Generally fresh olivine- and orthopyroxene-bearing anorthosites make up most of the KAC, and some of the orthopyroxene-bearing anorthosites that occur in the south have been locally metasomatized.

The mineral dichotomy of olivine- vs. orthopyroxene-bearing anorthositic rocks in the KAC (and other Proterozoic anorthosites globally) has been ascribed to crustal contamination by many researchers (Bybee *et al.* 2015; Demaiffe *et al.* 1986; Drüppel *et al.,* 2007; Duchesne *et al.,* 1985; Emslie *et al,* 1994; Gleiβner *et al.,* 2011). It has been suggested that a primitive mantle-derived magma, saturated with olivine, crystallized olivine-bearing anorthosites. Contamination of this magma by assimilation of silicic crustal material would enrich the magma in SiO_2 enough that it would crystallize orthopyroxene as the mafic phase instead of olivine, forming orthopyroxene-bearing anorthosites (Ashwal *et al*., 1986; Gray, 1987; Morse, 2006). The orthopyroxene-bearing rocks in some anorthosite complexes contain minor amounts of interstitial quartz, suggesting contamination by Si-rich material (Emslie, 1980; Wiebe, 1978). Note that while both olivine- and orthopyroxene-bearing anorthosites commonly contain interstitial clinopyroxene, these rocks are referred to here as leucotroctolites and leuconorites, respectively, for simplicity. A likely scenario is that while the primitive, mantle-derived magma ponded and intruded through the crust, it partially melted and assimilated some crust, becoming Si-enriched and crystallizing orthopyroxene and intermediate-An plagioclase, resulting in the emplacement of leuconorite. This initial leuconorite parental magma may have "presealed" the surrounding crust, so that later pulses of the original primitive magma composition could not assimilate any or as much crustal material, and thus crystallize leucotroctolites (Schmidt and Grunder, 2010; Scoates and Frost, 1996). This process of presealing the crust surrounding a magma chamber has been described for shallower magmatic systems (Schmidt and Grunder, 2010). An alternative theory is that the magma that formed the leucotroctolites did not spend a significant amount of time ponded at the base of the crust, while to produce the leuconorites, the same primitive magma composition ponded for a longer time period, allowing for more assimilation and a shift in the mineral assemblage (Emslie *et al.*, 1994; Frost *et al*., 2010).

Significant research has been done to assess the likelihood of crustal contamination accounting for the olivine-orthopyroxene mineral dichotomy in many Proterozoic anorthosite complexes worldwide, and there is a vast amount of evidence in its favor, discussed here. The general lower An content of plagioclase in leuconorites is consistent with contamination by granitic material, richer in Na than Ca. In most complexes, the leuconorites have trace element and isotopic compositions that deviate from mantle signatures and are more similar to those of the crust, while leucotroctolites have compositions closer to those of the mantle (Bybee *et al.,* 2014; Frost *et al.,* 2010; Peck *et al.,* 2010). In the KAC, Drüppel *et al*. (2007) demonstrated that the leuconorites are LREE-enriched and HREE-depleted relative to the leucotroctolites, and interpreted this to have been caused by contamination with crustal material. Leuconorites also have higher I_{Sr} and lower ε_{Nd} than leucotroctolites (Emslie, 1985; Gleiβner *et al.*, 2011; Gray, 1987; Slejko *et al.*, 2002). In the KAC, leuconorites have $I_{Sr} =$ 0.7031 to 0.7042 and ε_{Nd} = +2.1 to -3.1. Leucotroctolites have I_{Sr} = 0.7028 to 0.7036 and ε_{Nd} = +6.4 to +0.8 (Gleiβner, 2011). Figure 2.10 shows the variation in I_{Sr} compositions of leucotroctolites and leuconorites for some anorthosite complexes (for which this information is available), clearly demonstrating the greater deviation from "bulk earth" values for leuconorites, highlighting the influence of contamination by enriched crust. Gleiβner *et al.* (2010) conducted a thorough investigation into crustal contamination in the KAC, using trace elements and isotopes. The $\delta^{18}O$ values in plagioclase of the leuconorites were found to be higher ($\delta^{18}O$ = 6.2 – 7.6 ‰) than for plagioclase of the leucotroctolites ($\delta^{18}O$ = 5.6 – 6.2 ‰), supporting more contamination in the leuconorites. Plagioclase in leuconorites was also found to show a strong increase in Zr from core to rim (Gleiβner *et al.*, 2012). Late magmatic biotite and amphibole in leuconorites do not show negative Eu anomalies, implying that they did not form from magma that had undergone significant plagioclase extraction. This suggests a degree of contamination and magma replenishment after production of plagioclase. Whole-rock Re/Os isotope systematics range from values close to mantle compositions ($^{187}Os/^{188}Os$ = 0.2 ± 1) to very radiogenic values indicative of crustal contamination ($^{187}Os/^{188}Os$ = 5 ± 2; Gleiβner *et al.*, 2012). Oxide minerals in the rocks also provide evidence for contamination. In leuconorites, Nb/Ta ratios in ilmenite are lower and closer to a crustal composition than in leucotroctolites. Ilmenite in leucotroctolite has Nb/Ta ranging from 14.5 to 20.5, whereas ilmenite in leuconorites has Nb/Ta = 11.5 – 13. The mantle Nb/Ta composition is approximately 17, while that of the crust ranges from 11 to 12 (Gleiβner *et al.*, 2010).

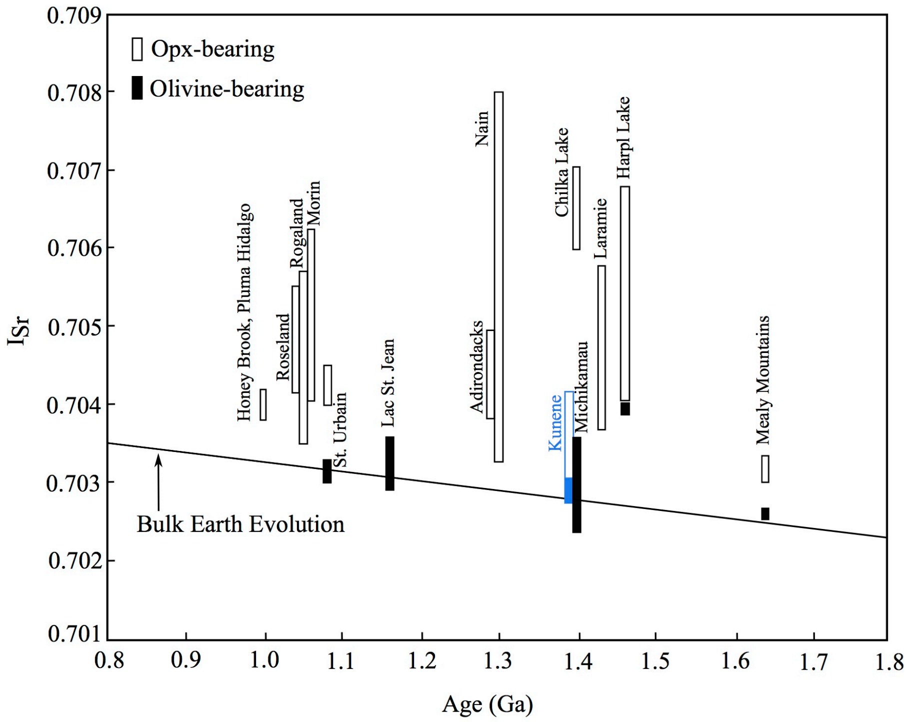

Figure 2.10 I_{Sr} values for Proterozoic anorthosites, showing the closer composition of olivine-bearing anorthosites to the "bulk earth" evolution (DePaolo and Wasserburg, 1976), while orthopyroxene-bearing anorthosites have higher I_{Sr} values. Note that not all complexes have both olivine- and opx-bearing anorthosites. Figure has been modified after Ashwal (1993) and the data for the Kunene Anorthosite Complex has been added (blue).

Field observations and the data presented in this study support the theory that leuconorites of the KAC were produced from contaminated magmas, and leucotroctolitic rocks originated from magmas that experienced less or no contamination. In addition to the chemical evidence, geochronological investigations have found that the leucotroctolitic rocks are generally slightly younger than the leuconorites (Brower *et al.,* 2016; Köstlin, 1974; Mayer *et al.*, 2004; Maier *et al.*, 2013). Many studies document field relationships that suggest that the leucotroctolite is intrusive into the leuconorite (Ashwal and Twist, 1994; Gleiβner *et al.*, 2011; Maier *et al.*, 2013). The age data for ten samples from our 2015 field excursion are in agreement with previous ages. Leucotroctolites in the north of the complex yield ages from 1381.8 ± 1.8 Ma to 1376.9 ± 1.5 Ma, whereas ages from the LGN rocks in the south of the complex range from 1400.5 ± 1.3 Ma to 1389.4 ± 2.9 Ma (Brower *et al.* 2016). There is one exception to this general trend. Sample KAC012/014 has several characteristics that do not fit in with many of the trends identified for the distribution of rocks and their chemical characteristics. This sample is one of two leucotroctolites identified south of the granite septum, the other being KAC017/022. Both samples occur in the far south, near the border with Namibia. KAC017/022 has plagioclase of $An_{70,}$ and therefore fits in with the general leucotroctolite character of having plagioclase of An_{70} or higher. KAC012/014, however, has much lower An plagioclase (An_{57}), well outside of the general leucotroctolite range. The plagioclase in this sample also displays normal zoning, which is not observed in most other samples. Several other rocks sampled nearby have the same characteristics, and are believed to make up one of the individual plutons of the KAC. Despite being a leucotroctolite, this sample yielded the oldest age for the complex, of 1438.4 ± 1.1 Ma. The inconsistency of this sample, and others from the same pluton, in terms on mineralogy, texture, chemistry and age, imply that it has a unique petrogenetic history, probably forming from an earlier pulse of magma. The fact that the sample is a leucotroctolite suggests that it has not experienced any/much contamination, but its plagioclase An-content is far lower than the other uncontaminated leucotroctolites in the north. It is possible that the parental magma of this pluton had a slightly different composition to the parental magma of the rest of the complex, explaining the intermediate plagioclase composition despite being a leucotroctolite. Since the pluton seems to be fairly small and isolated, it may have formed from a magma body too small to release enough heat to partially melt and assimilate any crust, therefore escaping contamination and forming a leucotroctolite. It is also interesting to note that samples KAC144/139 and KAC147/142 come from the pluton region with the second-oldest age (1400.5 ± 1.3 Ma), and these samples also have low An-contents (An_{57} and An_{53}, respectively), although they are classified as olivine leucogabbronorites.

2.6.3 The Red Granites as a contaminant

With many features of Proterozoic anorthosites pointing towards crustal contamination of mantle-derived magmas, it is necessary to address what type of crustal material may have been assimilated, and at what stage the contamination fits into the petrogenetic model. The high-alumina orthopyroxene megacrysts with plagioclase exsolution lamellae found in anorthosite complexes worldwide are evidence that the anorthosite system started forming at high pressure (Ashwal, 1993; Bybee *et al*., 2014a; Emslie, 1975). Al-in-opx geobarometry suggests that the HAOMs formed at 10 -15 kbar, corresponding to 30 – 40 km depth, at or near the continental Moho (Emslie, 1975; Bybee *et al.* 2014a). The magma must have remained at this depth for a long enough period of time to grow the large orthopyroxene crystals. Bodies of magma large enough to produce anorthosite plutons on the scale seen in Proterozoic anorthosite complexes, if ponded at the base of the crust, would be hot enough to start to partially melt and assimilate some of the surrounding lower crust (Ashwal, 2010; Demaiffe *et al.*, 1986; Emslie *et al.*, 1994; Maji *et al.*, 2010; Morse, 2006; Peck *et al.*, 2010). Since the composition of the lower crust is poorly constrained, it is difficult to estimate the composition of a partial melt of this crust.

Anorthosites make up one part of anorthosite-mangerite-charnockite-granodiorite (AMCG) suites, and are characteristically associated with a suite of felsic rocks with a range of compositions. In the KAC, the associated felsic rocks belong to the Red Granite Suite. The chemical data presented in this work for two KAC Red Granite samples is similar to Red Granite data obtained by other authors, showing the same ranges and variability between samples (Carvalho *et al.*, 1987; Drüppel *et al.*, 2007). The data have also been compared to felsic rocks in other AMCG suites, and all show similar general characteristics: a range in SiO_2 from ~ 66 – 76 wt. %, high K_2O (~ 4 – 6 wt. %), Na_2O greater than CaO, and high Fe/Fe+Mg ratios (Emslie *et al.*, 1994; Hegner *et al.*, 2010). The subject of whether the acidic rocks in Proterozoic anorthosite complexes come from the same magma series as the anorthosites was highly debated for many years. However, it is now generally accepted that the granitoids are cogenetic with the anorthosites, but originate as chemically independent magmas (Ashwal and Seifert, 1980; Buddington, 1939; Duchesne, 1990). The evidence comes mainly from isotopic data and field relations. Higher $\delta^{18}O$ and I_{Sr} values in the granitoids indicate a crustal origin, while the compositions of the anorthosites suggest a mantle source (Drüppel *et al.*, 2007; Emslie, 1978). There is also a compositional gap between the anorthosites and granitoids in the KAC on plots of major element compositions, particularly for Al_2O_3 and Fe/Mg ratios (Drüppel *et al.*, 2007). In the Nain Complex, variations in $\delta^{18}O$ of plagioclase in the anorthosites correlate with intrusion into country rocks of variable age, while the variation in $\delta^{18}O$ of the granitoids does not, suggesting they do not have the same origin (Peck *et al.*, 2010). There are also generally no negative Eu anomalies in the granitoids, implying that they are not residual liquids following anorthosite formation (Ashwal and Seifert, 1980).

Investigation into the origin and petrogenesis of the granitoids in anorthosite complexes has been extensive. Geochemical studies of anorthosites and granitoids from AMCG suites such as Nain, Rogaland, Marcy, Morin, Mealy Mountains, Kunene, and many others have yielded significant evidence for granitoids being the products of partial melting of the lower crust during anorthosite formation (Emslie *et al.*, 1994; Hegner *et al.*, 2010; Maji *et al.*, 2010; Mayer *et al.*, 2004; McLelland *et al.*, 2010). The high $\delta^{18}O$ and I_{Sr} values have already been addressed, but it is also suggested that the large spread of I_{Sr} values is indicative of lower crustal melting (Mayer *et al.*, 2004). The high K, high Fe/Fe+Mg, and incompatible trace element-enriched nature of the granitoids are further evidence for derivation by partial melting of undepleted lower crust (Emslie *et al.*, 1994; Maji *et al.*, 2010; McLelland *et al.*, 2010). In the Mealy Mountains Intrusive Suite, the granitoids have high concentrations of U and Th relative to La, and exhibit HREE depletion; these features have been interpreted to suggest melting of fertile, garnet-bearing lower crust (Hegner *et al.*, 2010). Heat from the ponding basaltic magmas, as well as heat flux from the latent heat of crystallization of plagioclase and olivine, would be able to induce partial melting of lower crustal material (Ashwal, 2010; Demaiffe *et al.*, 1986; Emslie *et al.*, 1994; Maji *et al.*, 2010; Morse, 2006; Peck *et al.*, 2010). The granitoids are generally slightly younger than, or the same age as the anorthosites in AMCG suites, and may contain xenoliths of anorthosite (Brower *et al.,* 2016; Maji *et al.*, 2010; Mayer *et al.*, 2004; Morse, 1982).

The evidence for the Red Granites (and acidic rocks associated with anorthosites in general) being derived from partial melting of lower crust is plentiful. However, the plausibility of this scenario is dependent on the composition of the lower crust that is subjected to partial melting. Many workers favor a mafic lower crust, based on crustal xenoliths, seismic velocities, and heat flow in the mantle and on the surface (Huang *et al*., 2013; Rudnick and Fountain, 1995; Rudnick and Gao, 2003). Experiments on partial melting of natural amphibolite compositions, believed to be representative of the lower crust, have been done at several pressures, to assess the compositions of melts and residues at various degrees of melting. Partial melting of these mafic compositions at pressures of 8 - 9 kbar produces melts of tonalitic to granodioritic compositions, rather than granites. The melts contain significantly less K_2O (~0.5 – 2 wt. %) than the Red Granites and other granitoids in AMCG suites (Beard and Lofgren, 1991; Rapp and Watson, 1995). Many of these experiments however, produced fairly high melt fractions (~20 – 66 %). In all cases, the melts produced in runs with the lowest degrees of melting (between 5 % and 10 % melt) are the closest match to the AMCG granitoids, with the highest proportion of K_2O. Very low degrees of partial melting of mafic lower crust compositions may thus be able to produce granitoid rocks similar in composition to those of AMCG suites, under the right conditions.

Even if there is some difficulty in producing true potassic granites (such as those in AMCG suites) by partial melting of mafic lower crust, there is some evidence to suggest that the lower crust may not necessarily be entirely mafic, and could vary from place to place, with a high proportion of felsic rocks in some regions. The range of seismic velocities determined for the lower crust corresponds to a density range of 2.9 – 3.2 g/cm^3 (Christensen and Mooney, 1995). These values have been used to infer that the lower crust is mafic, but the densities could be satisfied by a range of rock compositions with up to 65 wt. % SiO_2 (Hacker *et al.*, 2011). In addition, the heat producing elements and mantle heat flow used to infer a mafic lower crust are poorly constrained properties. Overestimation of either of these properties would favor a mafic composition, so the lower crust may be significantly more felsic than the calculations suggest (Hacker *et al.*, 2011). It is suggested by Hacker *et al.* (2015) that during subduction of sediments, arcs and continental crust, mafic rocks are transformed into eclogites, and their density may lead them to continue descending into the mantle. More felsic rocks would be transformed into gneisses that are less dense than the mantle, and may be relaminated to the base of the crust (Hacker *et al.*, 2015). If this is the case, the lower crust may be more felsic than previously estimated, at least in some places. Partial melting of felsic lower or middle crust could generate granitic partial melts similar to the AMCG suite granitoids. The composition of partial melts of the lower crust is addressed in detail in Chapter 4.

If, as the evidence suggests, the Red Granites were produced by lower crustal anatexis due to heat from ponding basaltic magmas, it is likely that some of the granitic partial melt would have been assimilated into the ponded magma chambers. This would change the composition of the magmas and enrich them in Si, and also increase the Na:Ca ratio. Orthopyroxene and intermediate plagioclase would crystallize from the contaminated magma and be emplaced as leuconorite/leucogabbronorite. Later pulses of magma could escape contamination due to the preconditioned crust, and would be emplaced to form the leucotroctolites. After the emplacement of most/all of the anorthosite in the KAC, the remaining lower crustal partial melts could be emplaced in and around the complex as the slightly younger Red Granite Suite. Leucotroctolites in the north of the KAC and leucogabbronorites in the south are roughly separated by a septum of the Red Granites. The septum divides the complex broadly into a generally older, southern portion that formed from contaminated basaltic magma, and a younger northern portion that experienced less or no contamination. The Red Granites also occur around most of the margin of the complex in the south, highlighting their close association with orthopyroxene-dominated, contaminated anorthosites with the granites.

2.7 SUMMARY AND CONCLUSIONS

The Kunene Anorthosite Complex is an 18 000 km^2 Proterozoic anorthosite complex, possibly emplaced over ~120 m.y, from 1438 Ma to 1319 Ma. The rocks of the complex are highly variable in mode and mineral chemistry, but do not display layering or trends akin to layered mafic intrusions. The variations in mineral assemblages, mineral chemistry, textures, and ages suggest that the KAC is a composite anorthosite complex, made up of several coalesced plutons with different evolution histories and ages. Rocks in the northern part of the complex are leucotroctolites, with plagioclase of An_{70} or higher and mafic silicates of Mg# 65 – 80. The southern part of the complex is dominated by orthopyroxene-bearing anorthosites, classified as leucogabbronorites and olivine-bearing leucogabbronorites. These rocks have more intermediate plagioclase (most An_{61} or lower) and slightly more Fe-rich mafic silicates (Mg# 63 – 78). The northern leucotroctolitic and southern leucogabbronoritic sections are roughly separated by a belt of coeval granitoids. These acidic rocks, known as the Red

Granites, also occur on the margins of the complex in the southern part of the KAC. There is evidence to suggest that the granitoids formed by partial melting of lower crustal material during ponding of the anorthosite HAB parental magmas at the Moho. The partial melts are believed to have been assimilated by ponding, olivine- and plagioclase-saturated parental magma, enriching it in silica and shifting the composition to orthopyroxene- and plagioclase-saturation. Cumulates of plagioclase and orthopyroxene (± clinopyroxene) were emplaced at mid-crustal depths as leucogabbronorites. The assimilation process would condition or seal the surrounding lower crust, so that later pulses of magma would not become contaminated by it. These later magma pulses would remain olivine- and plagioclase-saturated, and be emplaced as leucotroctolites in and around the older leucogabbronorites, mostly to the north of the Red Granite septum. Crustal contamination at depth is a probable scenario for the KAC, and for explaining the olivine-orthopyroxene dichotomy in anorthosites all over the world, but there have, until this study, been no experimental investigations that have tested this hypothesis. Such work formed part of this study, and is described in the following chapters.

3 Investigating Anorthosite Petrogenesis using Experimental Petrology

3.1 INTRODUCTION

A highly debated aspect of Proterozoic anorthosite petrogenesis at present, is the composition of the parental magma that generates these massive, plagioclase-dominated intrusions, and whether the magmas were derived from partial melting of the mantle or the lower crust. This question cannot be fully answered without recognizing the effects of contamination by surrounding crustal material on the mineralogical and isotopic composition of the anorthosites. Despite the proportion of plagioclase in anorthosites being far higher than predicted cotectic proportions, the mineralogy of the anorthosites is basaltic, with olivine, orthopyroxene and clinopyroxene making up the small mafic component. This, along with isotopic evidence ($\delta^{18}O$, ε_{Nd}, I_{Sr}, I_{Os} generally close to mantle values) suggests that the parental magmas were mantle-derived (Bybee *et al.,* 2014a; Drüppel *et al.,* 2007; Gleiβner *et al.*, 2012; Morisset *et al.,* 2009). However, the rocks have a definite crustal component in their compositions, with some isotopic systems showing a shift towards compositions more typical of the crust. Many authors use this to suggest that the parental magmas are derived from partial melting of the lower crust (Bédard, 2001; Taylor *et al.,* 1984; Schiellerup *et al.,* 2000). The main argument against crustal derivation for anorthosites is the huge volume of lower crustal material that would be required to generate enough magma to crystallize the massive intrusions, as well as a heat source for melting this much crust (Gleiβner *et al.*, 2011; Morse, 1991). Crustal contamination of mantle-derived magma provides a way to account for both the mantle and crustal components in the compositions of Proterozoic anorthosites.

A common feature in many anorthosite complexes around the world is the occurrence of some anorthosites that contain olivine as the mafic phase, while others in the same complex are characterized by orthopyroxene instead of olivine. This mineral dichotomy is particularly apparent in the Kunene Anorthosite Complex, as discussed in Chapter 2. Combined with differences in the isotopic signatures of olivine- and orthopyroxene-bearing anorthosites, the dichotomy has been attributed to variable amounts of crustal contamination, whereby the parental magma of the orthopyroxene-bearing rocks may have assimilated some surrounding silicic material in the crust, while the olivine-bearing anorthosites assimilated less or no material (Ashwal *et al*, 1986; Frost *et al*., 2010; Gleiβner *et al*., 2011; Morse, 2006). The composition of assimilated crustal material is not clear, but a good candidate may be the associated granitoids that occur in nearly all Proterozoic anorthosite complexes, since these are suggested to have formed from partial melts of lower crust during anorthosite formation.

Many experimental investigations have focused on constraining the composition of the anorthosite parental magma (Green, 1969; Longhi *et al,* 1999; Vander Auwera *et al.,* 1998; Vander Auwera and Longhi, 1994). The studies have shown that a high-alumina basaltic (HAB) composition is the most plausible parental magma for crystallizing feldspar-rich rocks with mafic silicates typical of basalts (Fram and Longhi, 1992; Longhi *et al.*, 1999). Several experimental studies (cited below) have shown that HAB can produce the assemblages and mineral compositions observed in the anorthosites. However, experimental investigations testing the mineral dichotomy and the effects of crustal contamination on anorthosite composition have not been carried out. Since the contamination hypothesis is proposed by a great number of workers to explain olivine- and orthopyroxene-bearing anorthosites, as well as the mechanism by which mantle-derived magmas can produce the compositions of the anorthosites, testing the plausibility of this theory is essential. In this chapter, I use experimental petrology to test the hypothesis that crustal contamination of mantle-derived magma shifts the mineral assemblages in anorthosites from olivine- to orthopyroxene-bearing. I use the phase equilibria of HAB to assess whether the parental magma could be derived from partial melting of a mantle source. The experiments test how the addition of a granitic component changes the mineral assemblage and evolution of a HAB magmatic system. The results may be applied to natural systems to help us understand the complex processes operating on Earth, today and in the Proterozoic Eon.

3.2 PREVIOUS EXPERIMENTAL STUDIES

Most experimental studies related to anorthosites thus far have focused on testing the compositions of proposed parental magmas, as well as whether these magmas were more likely derived from the mantle or the lower crust. Years of debate regarding the composition of the magma parental to Proterozoic anorthosites has resulted in a plethora of proposed compositions, including anorthositic liquids, high-alumina basalts (HAB), jotunites and quartz diorites (see review in Chapter 2). In addition to partial melting of upper, depleted mantle or of lower crust, other suggestions as to the source of the parental magmas include direct partial melting of mantle peridotite, as well as by melting of a sunken layered mafic intrusion (Longhi, 2005). Experiments on various starting compositions and under a range of pressures and conditions have been carried out in an attempt to constrain the parental magma composition, and to test other controversial aspects of Proterozoic anorthosites and their petrogenesis.

It was observed by Green (1969) that the bulk composition of most anorthosite complexes, including the associated felsic rocks, approximates a quartz-diorite composition. If the felsic rocks are excluded, the bulk composition approximates gabbroic anorthosite. He conducted high-pressure anhydrous experiments to compare the fractionation patterns of quartz diorite, gabbroic anorthosite, and high-alumina basalt. In the experiments on gabbroic anorthosite and HAB magmas, plagioclase was the dominant phase to crystallize, so these magmas could, in theory, produce anorthositic rocks. However, Green (1969) argues that it is unlikely that these types of high-Al liquids may be produced at depth by fractionation of a parent basaltic composition, and thus, these compositions are unlikely to be parental to Proterozoic anorthosites. Subsequent studies have shown that HAB magmas may be generated at depth by mechanisms such as direct partial melting of suitable mantle peridotite, early fractionation of mafic silicates from a more primitive mantle-derived melt, and assimilation of high-Al material in the crust by a mantle-derived melt (Draper and Johnston, 1992; Emslie *et al.*, 1994). The results of the experiments on the quartz diorite composition indicate a large field of crystallization of plagioclase, along with subordinate pyroxenes and opaque minerals, up to 13.5 kbar (Green, 1969). The residual liquid has an acidic composition. These features were interpreted to suggest that the quartz diorite magma may be able to produce rocks with the compositions of Proterozoic anorthosites, either by fractional crystallization or by partial melting of quartz diorite crustal rocks (Green, 1969). However, this does not account for olivine-bearing anorthosites, and it has since been shown that the coeval granitoids are not residual liquids to anorthosite production, but are from a chemically independent, crustally-derived magma series (Ashwal, 2010; Duchesne, 1978; Emslie, 1978; Morse, 1982; Wiebe, 1978).

The mineral assemblages of anorthosites and the chemistry of the phases, as well as increasing evidence against other parental magma candidates, have made high-alumina basalt the favored composition of anorthosite parental magma. A review of the evidence is given in Chapter 2. Chill margins and fine-grained dykes of high-alumina basalt in several anorthosites and associated intrusions (Nain, Harp Lake, Laramie, Hettasch, Michikamau, and Baffin Island; Morse, 1982) have been shown to have very similar compositions, leading many researchers to believe that they represent the anorthosite parental magma composition (Duchesne *et al.*, 1974; Emslie *et al.,* 1994; Longhi *et al.,* 1999; Mitchell *et al.,* 1995). Multiple experimental studies have been undertaken on a particular composition, known as HLCA, a synthetic HAB material designed from a combination of dykes and marginal rocks from the Harp Lake anorthosite in Labrador. The averaged composition is believed to be an estimate of the parental magma of the Harp Lake anorthosites, and possibly of Proterozoic anorthosites in general. In anhydrous experiments on HLCA, Fram and Longhi (1992) showed that at 11.5 kbar, plagioclase, orthopyroxene and clinopyroxene are liquidus phases, while between 1 and 10 kbar, only plagioclase is on the liquidus, followed at lower temperature by olivine at ≤ 5 kbar or orthopyroxene at > 5 kbar. The authors concluded that HLCA is capable of producing the mineral compositions in anorthosites. The plagioclase that formed in the experiments between 1 and 11.5 kbar overlaps with the majority of the compositions of natural plagioclases in the Harp Lake anorthosite, while the higher-pressure experimental plagioclase compositions correlate with a smaller group of Harp Lake plagioclase. This lends support to the idea that the anorthosites crystallized over a range of pressures during ascent from the Moho to the shallower crust. In addition, orthopyroxene that formed in the high-pressure experiments is similar to the HAOMs found in Harp Lake. Fram and Longhi (1992) also used the composition of an anorthositic dyke in the Nain Complex in experiments at 10 kbar. The anorthositic starting composition was found to crystallize plagioclase and clinopyroxene only. The plagioclase produced from this composition was more calcic and the pyroxene was more magnesian than that of the natural sample, leading to the conclusion that the anorthosite dyke does not represent a liquid composition, and is not a good candidate for the parental magma of anorthosites. Another important result of the study is the strong pressure dependence of the composition of plagioclase. Plagioclase An content decreases with pressure, and high pressure is needed to crystallize plagioclase of intermediate composition seen in Proterozoic anorthosites (Fram and Longhi, 1992). The decrease in An content of plagioclase with pressure, as well as increased Al_2O_3 in orthopyroxene with pressure, have been demonstrated in several other studies (Emslie, 1971; Green, 1969; Longhi *et al.*, 1993).

The HLCA composition has been used in a subsequent set of experiments, (again producing plagioclase and two pyroxenes on the liquidus at high pressure), where the results were used to assess whether the HLCA composition could be derived from the mantle (Longhi *et al.*, 1999). While the crystallization paths of many anorthosite complexes can be linked to parental magmas with a composition similar to HLCA, the phase diagrams produced in this study position HLCA on a thermal divide. This suggests that the composition cannot have been produced by fractionation of a more primitive mantle-derived magma, as it would require the melts to fractionate up temperature. It is proposed that HLCA must have originated by melting of a source with a composition already on the thermal divide, such as a sunken layered intrusion, or restite left over from partial melting of the lower crust (Longhi *et al.,* 1999). The significance of the thermal divide will be addressed in more detail in a subsequent section.

An experimental study by Baker and Eggler (1987) on low-MgO HAB from the Aleutian Islands (Mg# = 43 – 54; Al_2O_3 = 18.7 – 19.7 wt. %) show that the compositions have plagioclase on the liquidus over a range of pressures from 1 atm to 8 kbar. At 8 kbar, liquidus plagioclase is followed by pigeonite, and olivine and augite join the assemblage at lower temperatures (Baker and Eggler, 1987). Primitive high-alumina basalt from the South Sandwich Islands (Mg# = 63; Al_2O_3 = 18.5 wt. %) was shown by Johnston (1986) to have plagioclase on the liquidus at 10 kbar, followed at much lower temperatures by clinopyroxene. No olivine crystallized in these experiments (Johnston, 1986). Experiments on primitive HABs from Medicine Lake volcano show plagioclase and olivine on the liquidus at 10 kbar, followed at slightly lower temperature by clinopyroxene (Bartels *et al.*, 1991).

While some variation in experimental results exists due to differences in the specific HAB starting material, many experiments on HABs produce mineral assemblages similar to what is observed in Proterozoic anorthosites. In particular, experiments on HLCA by Fram and Longhi (1992) produced phases that overlap well with the mineral compositions in natural anorthosites. While the experimental studies related to anorthosites over the past few decades have been pivotal in constraining the parental magma composition, none have specifically addressed the olivine-orthopyroxene dichotomy or critically tested the crustal contamination hypothesis. It is evident from the experiments that HAB (particularly compositions close to HLCA, given in table 3.1) can produce the appropriate minerals, but most of the studies ignore the fact that at least two variations in mineral assemblage (olivine-bearing and orthopyroxene-bearing) exist in many Proterozoic anorthosite complexes. In this study, the effects of crustal contamination are tested by comparing the phase assemblages and liquid evolution trends of two different starting compositions: a primitive HAB and a mixture of this HAB with a proportion of a likely crustal contaminant.

3.3 METHODS

3.3.1 Starting materials

Experiments were conducted on synthetic starting compositions, given in Table 3.1. The baseline (or uncontaminated) starting composition, CMH_HAB has a composition similar to that of HLCA (also listed in Table 3.1 for comparison), but was designed to be slightly more primitive. Many of the high-alumina gabbro dykes that intrude the Laramie Anorthosite Complex, known as the Greaser dykes, have higher Mg# than HLCA (up to 65), so the compositional trend of these dyke compositions was used as a guide in designing the CMH_HAB starting composition. Note that such an extensive database for dyke compositions in the KAC is not yet available. The Greaser dykes are the most primitive component in Laramie, and are suggested to represent the parental melt of the complex (Mitchell *et al.*, 1995). The contamination experiments (CMH+KAC) were conducted on a calculated mixture of 70% of CMH_HAB and 30% of a granitoid composition from the Kunene Complex (Red Granite sample KAC031/035, also shown in Table 3.1). A ratio of 70:30 was chosen to ensure that the changes in phase equilibria caused by contamination could be effectively tested, and a discussion on how much contamination may be realistic in the anorthosite system is given in Chapter 4. The starting materials were prepared by mixing powdered oxides and carbonates. Calcium, sodium and potassium were added as carbonates, and phosphorus was added as $CaHPO_4$, due to the highly reactive nature of CaO, Na_2O, K_2O and P_2O_5 with carbon dioxide and/or water in air. Magnesium was added as MgO, but was dried in a furnace overnight and weighed out first, to prevent any moisture from air being incorporated into the mix. The mixes were ground by hand in an agate mortar and pestle under ethanol for 45 minutes and dried in a fume hood overnight. After regrinding, the mixes were placed in ceramic crucibles and conditioned in a furnace at QFM for 3 hours at 950°C to convert the carbonates into oxides. The oxygen fugacity was controlled by mixing CO and CO_2. The conditioned mixes were vialed and stored in a desiccator until use.

Table 3.1 Compositions of starting materials used in experiments. Note that the values for KAC031/035 have been normalized to exclude traces of Cr_2O_3 and V_2O_5. HLCA is shown for comparison. Major oxides in wt. %.

	CMH_HAB	KAC 031/035[a]	CMH+KAC[b]	HLCA[c]
SiO_2	49.04	76.30	57.23	50.02
TiO_2	0.85	0.59	0.77	1.85
Al_2O_3	17.62	11.74	15.85	17.51
FeO*	10.99	2.27	8.37	10.97
MnO	0.09	0.04	0.07	0.15
MgO	9.42	0.05	6.61	6.67
CaO	9.15	0.29	6.49	8.78
Na_2O	2.37	3.38	2.67	2.93
K_2O	0.31	5.28	1.80	0.44
P_2O_5	0.17	0.06	0.13	0.16
Total	100.00	100.00	100.00	99.48
Molar Mg#[d]	60		58	52

* Total Fe as FeO

[a] Granitoid from the KAC

[b] 70% CMH_HAB and 30% KAC031/035

[c] Composition of dykes in the Harp Lake anorthosite complex used in previous experimental studies (Fram and Longhi, 1992; Longhi *et al.,* 1999)

[d] Mg# calculated as molar Mg/(Mg+Fe) *100

3.3.2 Procedure

All experiments were conducted in the experimental petrology laboratory at the Department of Earth, Environmental and Planetary Science at Brown University. All runs were done at 10 kbar, to simulate the high-pressure stages of crystallization indicated by high-alumina orthopyroxene megacrysts in Proterozoic anorthosites (Charlier *et al.,* 2010; Emslie, 1975; Emslie *et al.,* 1994). Due to the general lack of hydrous mineral assemblages, the anorthosites are suggested to have crystallized from anhydrous magmas (Ashwal, 1993; Berg, 1977; Longhi *et al*., 1999; Morse, 1982), so all runs were done without the addition of water. The experiments were conducted in a standard half-inch piston cylinder apparatus (Boyd and England, 1960). Powdered starting material was packed into capsules machined from rods of graphite. The use of graphite capsules ensures that no sample-container reactions take place during the experiments. The graphite capsules were surrounded by crushable alumina rings, and stacked into graphite furnaces with crushable MgO spacers above and below (Fig. 3.1). Barium carbonate cells were used as the pressure media, and the assemblies were wrapped in a layer of Pb foil to minimize friction during compression. A steel base plug was positioned around the thermocouple tube above the assembly, and surrounded by a ring of pyrophyllite.

The experiments were pressurized to 10 kbar at room temperature. At 10 kbar and at the temperatures investigated, oxygen fugacity in graphite capsules is close to the QFM buffer (~log fO_2 = -9). All runs were heated to 650°C at a rate of 60°C/min, while maintaining the desired run-pressure (hot-piston in). This temperature was held for 12 minutes to allow for compaction of the barium carbonate. The temperature was then ramped up to the target value at 60°C/min. All experiments were run under isobaric and isothermal conditions. Temperature was controlled by a Eurotherm 818 controller (temperature uncertainty ±10°C), and measured by $W_{97}Re_3$–$W_{75}Re_{25}$ thermocouples. The thermocouple junction was separated from the graphite capsule by a 0.75 mm slice of MgO. Calibration experiments determined the location of the hot spot at 40% from the top of the graphite furnace, and the experiments were assembled to position the capsule at this location to minimize the effects of the thermal gradient. No pressure correction was applied to the measured emf, and pressure was not corrected for friction. Pressure was monitored carefully for the duration of the experiments, and restored if necessary. The experiments ran for between 18 and 34 hours, after which they were quenched by shutting off the power supply, allowing them to cool almost to room temperature within minutes. The conditions of all experiments are given in Table 3.2.

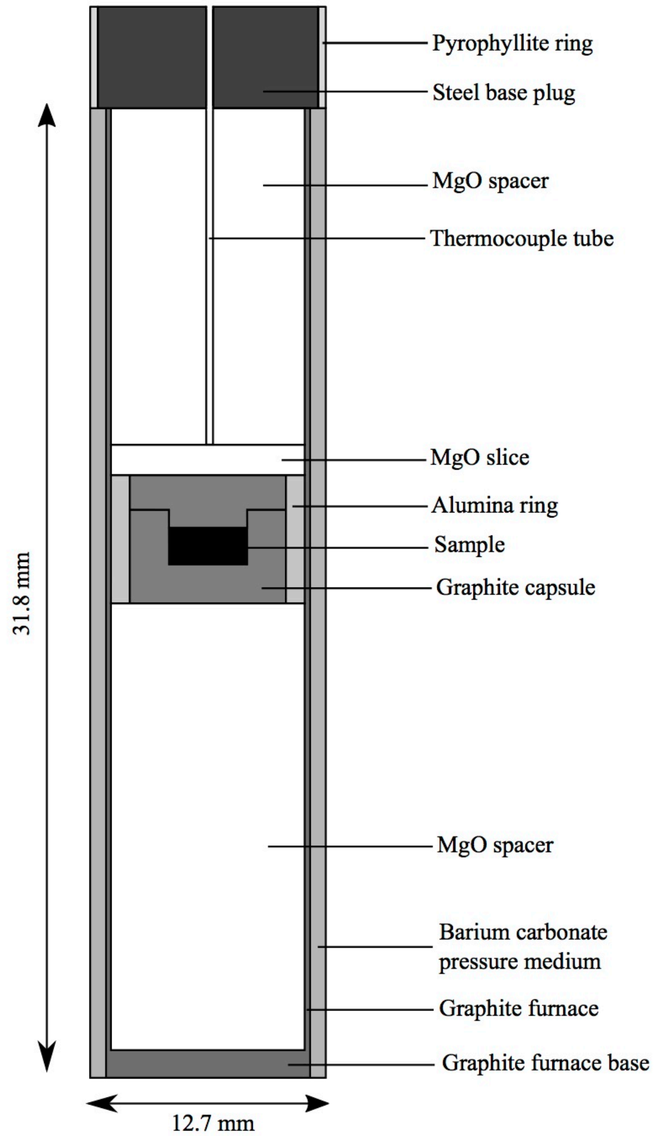

Figure 3.1 Schematic diagram of the experimental assembly (not to scale).

Table 3.2 Run conditions, products, and phase proportions of all experiments. Ca/Na K_D (for plagioclase) and Fe/Mg K_D (for mafic silicates) ±1σ are given.

Run	T (°C)	Duration (h)	Glass	Ol	Pl	Cpx	Pgt	Opx	Ilm	ΣR[2]	Mg# glass[a]
Baseline experiments on CMH_HAB											
CMH16-4	1322	22	100								62
T1290-1	1326	24	100								61
CMH16-11	1332	28	100								61
T1350-1	1327	24	100								60
T1315-1	1325	18	100								60
T1225-1	1287	24	96	4						0.19	57
CMH16-6	1273	23	67	6	17		10			0.18	51
T1250-5	1204	34	50	18	32					0.55	42
T1200-4	1203	23	47	15	30	8				0.16	41
CMH16-3	1203	22	48	12	30	4		6		0.02	41
T1325-1	1117	24	9	18	51	7	15		trace	0.79	27
T1300-2	1124	24	-5	11	60	2	31		1	0.2	22
T1275-2	1128	22	14	22	50	12	3		trace	1.08	19
Mean K_D ±1σ				0.245 ±0.08	1.084 ±0.13	0.232 ±0.03	0.262 ±0.06	0.193 ±0.06	2.217 ±0.10		
Contamination experiments on CMH+KAC											
CMH+KAC10	1256	24	99					1		1.06	59
CMH+KAC8	1210	24	92					8		0.38	51
CMH+KAC6	1193	25	89					11		0.27	49
CMH+KAC4	1156	24	86		trace		5	9		0.31	45
CMH+KAC9	1078	24	43		30		8	19		0.28	22
Mean K_D ±1σ				0.236 ±0.07	0.947 ±0.19		0.228 ±0.06				

[a]Mg# calculated as molar Mg/(Mg+Fe) *100

Ol = olivine; Pl = plagioclase; Cpx = clinopyroxene; Pgt = pigeonite; Opx = orthopyroxene; Ilm = ilmenite

Some problems occurred in maintaining the experiments at the desired temperature. In many runs, it was observed that the thermocouple was being pushed upwards and away from the sample by a few millimeters during initial compression to 10 kbar. The result is that the thermocouple did not read the temperature at the hotspot of the assembly where the sample was contained, and therefore a lower temperature was measured. As a result, the Eurotherm controller would increase power supply to heat the sample up to the desired temperature, and would thus heat the sample up to a higher temperature than what was desired. Many experiments therefore ran at a higher temperature than desired, and several ran at temperatures greater than the liquidus, and were found to consist only of glass.

Th relative temperatures of the experiments are apparent from the degrees of melt and the Mg# of the melts. To constrain the actual temperatures of the experiments, an olivine-liquid thermometer (Beattie, 1993) was used. The thermometer uses the Mg partitioning between olivine and liquid to calculate temperature. In a recent review of thermometers for volcanic systems, this thermometer was found to be the most accurate (Putrika, 2008). An advantage of the Beattie thermometer is that it may also be used as a liquid-only thermometer for samples that do not contain olivine, by calculating the temperature at which the liquid would become saturated with olivine at a given pressure. This thermometer could therefore be used to calculate the temperatures for all experiments, with or without olivine. The olivine-liquid thermometer is accurate to within 44°C and has $R^2 = 0.94$ for 1302 calibration experiments. The results are believed to be accurate, since the calculated temperatures fit the data well, and the temperatures decrease with Mg# of the residual liquids. Experiments 1200-4 and CMH16-3 have the same Mg# and very similar melt fractions, and the calculated temperatures for these runs differed by ~3°C, so the temperatures of these runs were made to be equal. Since this study is concerned mainly with the phases that form from two different starting compositions, and not with the exact temperatures of the appearance of phases, the calculated temperatures are adequate for the study. The calculated temperatures should not be used to infer the precise temperature of appearance of minerals, or the liquidus and solidus of the HAB composition. For a full account of the thermometry calculations, see Appendix C.

3.3.3 Analytical methods

After quenching, each experiment was broken open and the graphite capsule was sectioned longitudinally so that the sample could be examined in cross section. One half of the capsule was mounted in epoxy and polished for analysis by electron microprobe. Chemical analyses and BSE images were obtained at the electron microprobe facility at Brown University, using a Cameca SX100 wavelength dispersive system. An accelerating voltage of 15 kV and a beam current of 10 nA for glass and feldspars, and 20 nA for mafic phases and ilmenite were used. Where mineral grains or melt pockets were large enough, a 5 μm or 10 μm beam was used, but smaller phases were analyzed with a focused beam. Multiple analyses (between 2 and 26) were obtained for each phase in a sample. Mean analyses of the phases in each sample are listed in Table 3.3 for the baseline experiments on CMH_HAB and in Table 3.4 for the contamination experiments on CMH+KAC. Standard deviations (1σ) for each element are also given.

Table 3.3 Mean major element compositions of all phases in the baseline experiments. Major oxides in wt. %.

Run	Phase	SiO_2	TiO_2	Al_2O_3	FeO*	MnO	MgO	CaO	Na_2O	K_2O	P_2O_5	Total	Molar Mg#/*An*[a]	n
CMH16-4	Glass	47.84	0.85	17.71	10.51	0.10	9.79	9.75	2.98	0.31	0.19	100.03	62	8
	±1σ	0.12	0.06	0.15	0.10	0.02	0.03	0.09	0.12	0.01	0.03		0.00	
T1290-1	Glass	47.04	0.82	16.88	10.39	0.07	9.00	8.75	2.28	0.29	0.16	95.68	61	3
	±1σ	0.14	0.04	0.21	0.05	0.01	0.03	0.09	0.25	0.01	0.01		0.00	
CMH16-11	Glass	48.08	0.84	17.79	10.64	0.08	9.33	9.24	3.13	0.30	0.18	99.59	61	6
	±1σ	0.16	0.04	0.11	0.10	0.01	0.05	0.10	0.05	0.01	0.02		0.00	
T1350-1	Glass	48.68	0.84	17.52	10.98	0.09	9.40	9.08	2.31	0.30	0.17	99.35	60	10
	±1σ	0.45	0.03	0.32	0.08	0.03	0.14	0.13	0.14	0.03	0.04		0.00	
T1315-1	Glass	48.46	0.85	17.34	10.76	0.09	9.19	9.08	2.50	0.33	0.17	98.76	60	3
	±1σ	0.10	0.03	0.10	0.02	0.02	0.18	0.09	0.20	0.03	0.02		0.00	
T1225-1	Glass	48.61	0.87	18.47	10.68	0.09	7.95	9.59	2.45	0.33	0.17	99.21	57	10
	±1σ	0.17	0.06	0.13	0.11	0.02	0.10	0.08	0.14	0.02	0.05		0.00	
	Ol	39.06	0.02	0.09	17.85	0.13	42.33	0.01	0.24			99.72	81	3
	±1σ	0.14	0.01	0.04	0.20	0.03	0.37	0.01	0.01				0.00	
CMH16-6	Glass	48.60	1.16	17.26	12.40	0.11	7.30	9.85	2.54	0.39	0.26	99.87	51	10
	±1σ	0.34	0.21	0.76	0.34	0.03	0.13	0.08	0.11	0.02	0.06		0.01	
	Ol	38.69	0.04	0.06	22.69	0.16	39.44	0.37	0.03			101.47	76	3
	±1σ	0.38	0.01	0.02	0.63	0.02	0.39	0.03	0.01				0.01	
	Pl	51.48	0.04	30.60	0.44		0.20	13.26	3.89	0.12		100.02	*66*	9
	±1σ	0.38	0.01	0.20	0.08		0.01	0.21	0.19	0.01			*0.01*	
	Pgt	51.46	0.52	7.18	12.65	0.15	22.73	6.34	0.18			101.21	76	3
	±1σ	0.78	0.14	0.99	0.47	0.01	1.48	1.61	0.05				0.00	
T1250-5	Glass	49.77	1.65	15.60	13.03	0.13	5.21	9.24	2.65	0.54	0.27	98.08	42	10
	±1σ	0.13	0.07	0.11	0.12	0.02	0.12	0.13	0.16	0.02	0.07		0.01	
	Ol	37.98	0.03	0.04	26.01	0.19	36.51	0.00	0.27			101.04	71	7
	±1σ	0.40	0.01	0.02	1.31	0.01	1.06	0.01	0.02				0.02	
	Pl	51.16	0.04	31.06	0.44		0.18	13.68	3.78	0.10		100.46	*68*	18
	±1σ	0.28	0.02	0.23	0.13		0.04	0.13	0.21	0.01			*0.01*	
T1200-4	Glass	49.15	1.62	16.14	12.83	0.11	5.01	8.90	3.05	0.65	0.27	97.73	41	10
	±1σ	0.35	0.05	0.21	0.17	0.02	0.19	0.22	0.17	0.04	0.06		0.01	
	Ol	38.10	0.02	0.05	24.84	0.18	37.31	0.02	0.30			100.82	73	5
	±1σ	0.39	0.01	0.02	1.03	0.01	0.82	0.02	0.03				0.01	
	Pl	51.52	0.04	31.05	0.48		0.15	13.39	3.96	0.11		100.70	*66*	8
	±1σ	0.29	0.01	0.41	0.10		0.02	0.31	0.23	0.01			*0.02*	
	Cpx	51.51	0.68	5.15	12.37	0.18	18.49	0.28	11.95			100.58	73	2
	±1σ	0.54	0.08	1.09	1.26	0.04	1.21	0.02	1.89				0.01	
CMH16-3	Glass	49.16	1.83	16.16	13.42	0.11	5.27	8.97	2.46	0.65	0.39	98.42	41	7
	±1σ	0.31	0.05	0.60	0.09	0.04	0.20	0.23	0.19	0.05	0.04		0.01	
	Ol	37.38	0.03	0.05	24.91	0.17	36.94	0.34	0.01			99.82	73	7
	±1σ	0.12	0.01	0.02	0.80	0.02	0.62	0.02	0.01				0.01	
	Pl	50.79	0.08	30.70	0.63		0.23	13.40	3.64	0.13		99.58	*68*	2
	±1σ	0.03	0.02	0.17	0.12		0.11	0.08	0.54	0.00			*0.03*	
	Cpx	48.58	1.10	3.99	18.20	0.23	15.11	10.95	0.23			98.39	75	9
	±1σ	0.54	0.28	0.79	2.67	0.04	1.40	2.93	0.08				0.01	
	Opx	51.63	0.30	5.63	12.94	0.13	26.31	2.37	0.08			99.40	78	9
	±1σ	0.59	0.03	0.64	0.30	0.02	0.27	0.21	0.03				0.00	

* Total Fe as FeO

[a]Mg# calculated as molar Mg/(Mg+Fe) *100. An calculated as molar Ca/(Ca+Na) *100

n = number of analyses

Ol = olivine; Pl = plagioclase; Cpx = clinopyroxene; Pgt = pigeonite; Opx = orthopyroxene; Ilm = ilmenite

Table 3.3 continued

Run	Phase	SiO_2	TiO_2	Al_2O_3	FeO*	MnO	MgO	CaO	Na_2O	K_2O	P_2O_5	Total	Molar Mg#/*An*[a]	n
T1325-1	Glass	51.38	2.08	15.12	11.35	0.10	2.36	5.93	2.28	1.43	0.81	92.84	27	8
	±1σ	0.73	0.12	0.28	0.80	0.03	0.16	0.18	0.48	0.11	0.12		0.01	
	Ol	36.69	0.04	0.02	32.39	0.23	30.29	0.00	0.35			99.99	63	4
	±1σ	0.18	0.01	0.01	0.82	0.02	0.78	0.01	0.00				0.01	
	Pl	51.73	0.05	30.56	0.55		0.18	13.12	3.95	0.15		100.29	*66*	11
	±1σ	0.33	0.02	0.25	0.08		0.03	0.22	0.23	0.01			*0.02*	
	Cpx	48.28	2.15	4.69	14.24	0.20	12.03	0.28	17.37			99.24	60	5
	±1σ	0.58	0.17	0.52	0.62	0.02	0.73	0.02	0.76				0.02	
	Pgt	50.20	0.70	2.30	22.87	0.30	16.33	0.14	6.24			99.05	56	2
	±1σ	0.17	0.10	0.54	0.70	0.02	0.43	0.01	0.05				0.01	
	Ilm		52.37	0.37	41.74	0.24	4.22					98.94	15	9
	±1σ		0.19	0.02	0.38	0.02	0.21						0.01	
T1300-2	Glass	51.59	2.08	14.77	14.67	0.14	2.19	6.99	2.34	1.41	1.12	97.30	21	7
	±1σ	0.42	0.12	0.20	0.70	0.03	0.21	0.17	0.17	0.08	0.14		0.02	
	Ol	36.87	0.04	0.03	31.25	0.22	31.64	0.00	0.28			100.34	64	3
	±1σ	0.32	0.02	0.02	1.45	0.01	1.13	0.00	0.03				0.02	
	Pl	52.13	0.05	30.50	0.52		0.15	12.98	4.09	0.16		100.57	*65*	10
	±1σ	0.39	0.02	0.24	0.06		0.03	0.27	0.18	0.02			*0.01*	
	Cpx	50.33	0.83	2.46	21.38	0.27	14.17	0.18	10.15			99.76	54	3
	±1σ	0.59	0.13	0.87	0.37	0.02	0.53	0.04	0.77				0.01	
	Pgt	51.80	0.40	1.18	23.44	0.31	17.56	0.05	5.30			100.05	57	1
	±1σ												0.00	
	Ilm		52.16	0.34	43.53	0.25	3.03					99.30	11	8
	±1σ		0.23	0.04	0.24	0.02	0.11						0.00	
T1275-2	Glass	51.38	2.20	13.73	15.90	0.14	2.04	6.83	2.80	1.51	0.74	97.27	19	9
	±1σ	1.15	0.20	0.17	0.72	0.03	0.13	0.25	0.11	0.16	0.13		0.01	
	Ol	37.05	0.04	0.03	30.87	0.23	32.43	0.03	0.37			101.04	65	3
	±1σ	0.23	0.02	0.03	0.98	0.03	0.88	0.03	0.04				0.01	
	Pl	51.97	0.05	30.48	0.50		0.18	12.98	4.10	0.15		100.40	*65*	8
	±1σ	0.72	0.02	0.35	0.07		0.03	0.40	0.22	0.02			*0.02*	
	Cpx	48.79	1.74	4.80	16.52	0.23	12.32	0.33	15.52			100.24	57	5
	±1σ	0.50	0.37	0.80	1.52	0.03	0.83	0.06	0.85				0.03	
	Pgt	49.57	1.16	3.07	22.72	0.26	14.00	0.17	9.31			100.25	52	3
	±1σ	0.85	0.40	0.62	1.02	0.03	1.84	0.02	1.54				0.04	
	Ilm		51.82	0.33	44.57	0.25	2.53					99.50	9	7
	±1σ		0.49	0.05	0.43	0.03	0.20						0.01	

* Total Fe as FeO

[a]Mg# calculated as molar Mg/(Mg+Fe) *100. An calculated as molar Ca/(Ca+Na) *100

n = number of analyses

Ol = olivine; Pl = plagioclase; Cpx = clinopyroxene; Pgt = pigeonite; Opx = orthopyroxene; Ilm = ilmenite

Table 3.4 Mean major element compositions of all phases in the contamination experiments. Major oxides in wt. %.

Run	Phase	SiO_2	TiO_2	Al_2O_3	FeO*	MnO	MgO	CaO	Na_2O	K_2O	P_2O_5	Total	Molar Mg#/*An*[a]	n
CMH+ KAC10	Glass	56.58	0.74	15.39	8.05	0.09	6.54	7.19	2.84	1.28	0.14	98.84	59	20
	±1σ	0.33	0.04	0.08	0.12	0.02	0.09	0.10	0.12	0.03	0.02		0.00	
	Opx	54.22	0.18	3.07	11.87	0.14	28.82	1.48	0.04			99.82	81	10
	±1σ	0.17	0.01	0.33	0.17	0.01	0.10	0.11	0.02				0.00	
CMH+ KAC8	Glass	57.28	0.81	16.63	7.80	0.08	4.65	7.13	2.96	1.40	0.22	98.95	52	26
	±1σ	0.37	0.04	0.26	0.12	0.02	0.07	0.10	0.12	0.03	0.04		0.01	
	±1σ	54.00	0.19	3.64	11.92	0.14	28.87	1.45	0.04			100.25	81	24
	±1σ	0.49	0.03	0.61	0.52	0.02	0.67	0.14	0.02				0.01	
CMH+ KAC6	Glass	57.40	0.82	17.14	7.77	0.08	4.15	6.99	3.03	1.44	0.15	98.95	49	10
	±1σ	0.30	0.04	0.16	0.11	0.03	0.08	0.14	0.13	0.02	0.02		0.01	
	Opx	54.15	0.19	3.39	12.71	0.15	28.29	1.55	0.05			100.48	80	8
	±1σ	0.45	0.02	0.78	0.53	0.02	0.65	0.42	0.03				0.01	
CMH+ KAC4	Glass	57.89	0.84	17.61	7.31	0.07	3.33	7.17	3.24	1.54	0.18	99.15	45	10
	±1σ	0.41	0.04	0.26	0.25	0.02	0.13	0.16	0.12	0.06	0.04		0.01	
	Opx	53.27	0.23	3.61	13.44	0.18	26.32	2.72	0.10			99.85	78	4
	±1σ	1.03	0.03	0.65	0.24	0.01	0.75	0.15	0.02				0.01	
	Pl	57.46	0.36	23.60	2.72		1.23	8.98	5.02	0.86		100.21	*51*	4
	±1σ	0.60	0.07	0.75	0.66		0.57	0.28	0.13	0.07			*0.01*	
	Pgt	52.21	0.31	4.66	14.37	0.19	24.13	4.09	0.12			100.08	75	12
	±1σ	0.52	0.03	0.44	0.45	0.01	0.90	0.59	0.03				0.01	
CMH+ KAC9	Glass	61.87	1.56	13.96	8.34	0.08	1.33	5.06	2.74	2.73	0.29	97.96	22	18
	±1σ	0.38	0.10	0.12	0.23	0.02	0.04	0.08	0.10	0.04	0.02		0.01	
	Opx	50.47	0.38	6.07	17.85	0.19	22.60	2.05	0.07			99.68	69	3
	±1σ	0.72	0.04	1.77	1.42	0.01	0.56	0.10	0.03				0.02	
	Pl	55.60	0.06	28.02	0.51		0.14	10.89	4.88	0.49		100.60	*56*	15
	±1σ	0.66	0.01	0.49	0.08		0.02	0.44	0.20	0.04			*0.02*	
	Pgt	50.72	0.53	3.28	20.65	0.26	18.01	5.93	0.13			99.51	61	7
	±1σ	0.19	0.09	0.90	1.64	0.03	1.07	0.62	0.04				0.03	

* Total Fe as FeO

[a]Mg# calculated as molar Mg/(Mg+Fe) *100. An calculated as molar Ca/(Ca+Na) *100

n = number of analyses

Pl = plagioclase; Pgt = pigeonite; Opx = orthopyroxene

3.3.4 Phase proportions and equilibrium

A least-squares multiple linear regression using the composition of the starting material and the analyzed compositions of all phases present in each sample (including melt) was used to determine the proportion of each phase. The phase proportions are listed in Table 3.2. In most cases, the sum of squared residuals is low, although runs T1325-1 and T1275-2 have higher ΣR^2 values (0.79 and 1.08, respectively). The regression for T1300-2 also gives a negative liquid proportion (-5%). These three runs are the lowest temperature and most evolved experiments on CMH_HAB, with very small melt fractions remaining and low Mg#. Experiments at lower temperatures require longer run times to achieve equilibrium, due to slower diffusion of elements into phases, so it is likely that these low-temperature runs did not completely equilibrate, resulting in a degree of heterogeneity of the phases and higher ΣR^2

values. Run CMH+KAC10 also has a high ΣR^2 (1.06). This experiment was conducted at a temperature just below the liquidus, with only a few small orthopyroxene grains having formed. The very small fraction of crystals (~ 1% calculated by the regression) results in a melt composition that is very similar to the bulk starting composition, and this is likely to affect the accuracy of the output of the regression, producing a higher ΣR^2.

The mineral-melt exchange coefficients for the experimental phases are mostly in agreement with other experimental studies on HAB at these conditions (Bartels *et al.,* 1991; Draper and Johnston, 1992; Fram and Longhi, 1992; Johnston, 1986). The average Fe-Mg K_D values for pyroxenes and olivine, and average Ca-Na K_D for plagioclase are given in Table 3.2, and are calculated by the following formulae:

$K_D^{min/melt}\ (Fe/Mg)$ = ([$X_{Fe}^{mineral}$][X_{Mg}^{melt}])/([$X_{Mg}^{mineral}$][X_{Fe}^{melt}])

$K_D^{min/melt}\ (Ca/Na)$ = ([$X_{Ca}^{mineral}$][X_{Na}^{melt}])/([$X_{Ca}^{mineral}$][X_{Na}^{melt}])

For plagioclase, the average K_D for the contamination experiments (0.947 ± 0.19) is slightly lower than for the baseline experiments (1.084 ± 0.13). The partitioning of Ca and Na into plagioclase is pressure dependent, with $K_D^{Ca\text{-}Na}$ increasing at higher pressures (Bartels *et al.*, 1991), and the K_D values in both the CMH_HAB and CMH+KAC experiments are within the range reported in other studies (Baker and Eggler, 1987; Draper and Johnston, 1992; Fram and Longhi, 1992; Johnston, 1986; Longhi *et al.*, 1999). The other phases show less variability than plagioclase, seen in the lower standard deviations for their K_D values, and in general all fit well within the ranges reported by previous studies. Experiment T1275-2 has a slightly lower $K_D^{Fe\text{-}Mg}$ for olivine and clinopyroxene than the other experiments. The crystal shapes and textures in this experiment do not suggest a significant degree of disequilibrium, but the mafic phases in the experiment have quite high standard deviations for some elements (FeO*, MgO, Na_2O; Table 3.3). Experiment CMH+KAC9 also has a lower $K_D^{Fe\text{-}Mg}$ for orthopyroxene. Some areas in this sample show skeletal textures with small mineral grains intergrown, implying that equilibrium may not have been reached. Only one experiment on CMH_HAB was found to contain orthopyroxene (CMH16-3). The effects of the thermal gradient across the experiment are visible in the sample, with a higher melt fraction near the bottom of the capsule, and anhedral crystal shapes, suggesting that the desired conditions of this run may not have been achieved. The orthopyroxene has a slightly lower $K_D^{Fe\text{-}Mg}$ than the opx in the CMH+KAC runs. These three experiments are included in the study, despite their inconsistencies, because their liquid compositions fit the general evolutionary trend of the bulk of the experiments, which did equilibrate. They may, therefore, add value to the study, as long as they are interpreted within their limits.

3.4 RESULTS

3.4.1 Baseline, uncontaminated experiments

The liquid compositions for experiments on CMH_HAB are shown on a pseudoternary diagram in Fig. 3.2. The liquid compositions were recalculated in oxygen units using the mineral component system of Longhi *et al.* (1999), and projected from wollastonite (Wo) onto the quartz-olivine-plagioclase (qtz-ol-pl) plane. This mineral projection scheme is effective for representing compositions with low-wo contents, and has been used here so that the phase equilibria may easily be compared to those for the HLCA composition of Longhi *et al*. (1999). At 10 kbar, CMH_HAB has olivine (ol) on the liquidus, followed by plagioclase (pl) after only 4% crystallization of olivine, and then by clinopyroxene (cpx) with decreasing temperature. The low-Ca pyroxene is pigeonite (pgt), forming at lower temperatures with small amounts of ilmenite (Ilm). The low-Ca pyroxene forms as a result of a reaction between olivine and the liquid. All clinopyroxene produced in the experiments is augite, and all orthopyroxene is enstatite. Pyroxenes will be referred to as opx, cpx and pgt for simplicity. Following the convention of Longhi *et al*. (1999) the field "lpyx" on the phase diagrams designates low-Ca pyroxenes, including both px and pgt.

Phase boundaries were constructed (thick black lines) based on the compositions of the experimental liquids. Arrows on the phase boundaries indicate the direction of decreasing temperature, and the double arrow on the ol-lpyx division indicates a reaction boundary. Light grey lines represent the 1 bar phase boundaries for HAB compositions, calculated by Longhi (1991). The compositions of pyroxenes produced in the experiments are also plotted on the phase diagram, along with a field of natural HAOM compositions for comparison. Pyroxene compositions will be addressed in more detail in Section 3.5. The starting composition CMH_HAB lies in the olivine-saturated field, crystallizing only olivine initially, and causing the liquid to evolve away from the ol component of the pseudoternary diagram. When plagioclase starts to form, the liquid curve bends upwards sharply towards qtz, evolving away from ol and pl. Since the liquid is crystallizing a higher proportion of plagioclase than olivine, the liquid evolution trend bends away from the pl corner. After an interval of ol, pl and cpx crystallization, the liquids start to produce lpyx (pgt), as a result of reaction with olivine. The phase boundary begins to curve towards the qtz-pl side of the diagram as a result of fractionation of pyroxenes, but continues the general trend towards the qtz apex as pl fractionates. The liquids evolve towards more qtz-rich compositions with progressive fractionation.

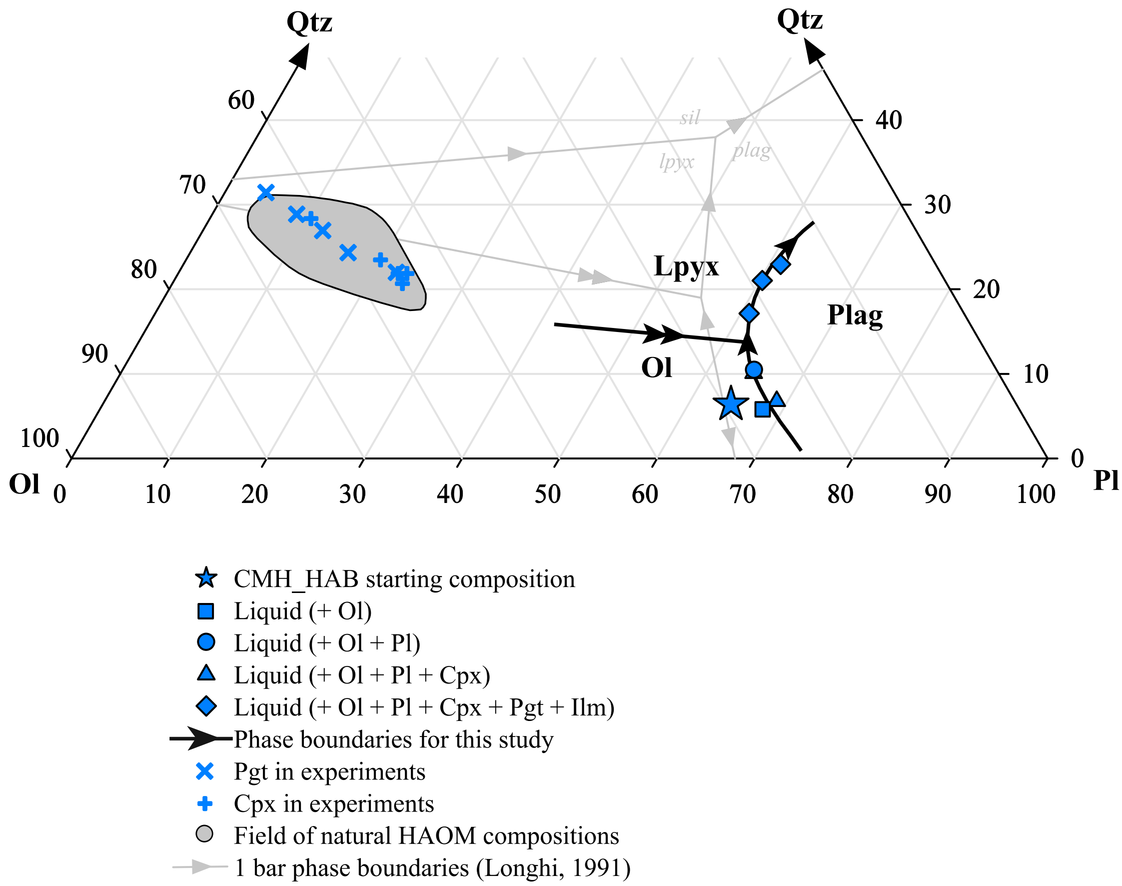

Figure 3.2 Liquidus equilibria of 10 kbar experiments on CMH_HAB. Liquid compositions are projected from the wollastonite and ilmenite components onto the quartz-olivine-plagioclase plane in terms of oxygen units, using the mineral component system of Longhi *et al*. (1999). The 1 bar phase boundaries for HAB compositions (Longhi, 1991) are shown for reference as light grey lines. The "Lpyx" region designates opx and pgt.

In all runs that crystallized plagioclase, it makes up the highest proportion of the crystalline phases, and its proportion increases with decreasing temperature. Plagioclase composition shows very little variability with temperature, with An content ranging from An_{65} to An_{68}. Plagioclase generally appears as long rectangular crystals with sharp, straight edges (Fig. 3.3). The mafic phases show more variability with temperature. Olivine ranges from Fo_{68} to Fo_{81}. With decreasing temperature, FeO in olivine increases from ~18 wt. % to ~32 wt. %, after which it decreases slightly at the onset of ilmenite crystallization. SiO_2 and MgO decrease with temperature, while MnO increases slightly. The pyroxene in the experiments is mostly Cpx with Mg# ranging from 55 to 75 and CaO decreasing with temperature from ~4 wt. % to ~2.5 wt. %. Pigeonite has Mg# from 52 to 57. All pyroxenes become less aluminous with decreasing temperature as more plagioclase is produced. The compositions of ilmenite also show little variation with temperature, and Mg# is consistently low (Mg# 9 to 15). Other than a slight decrease in FeO in olivine, ilmenite has little effect on the mineral compositions when it starts to crystallize, because only very minor proportions (<1%) form. The compositions of crystallizing phases are displayed on the SiO_2-MgO-Al_2O_3 ternary diagram below (Fig. 3.4).

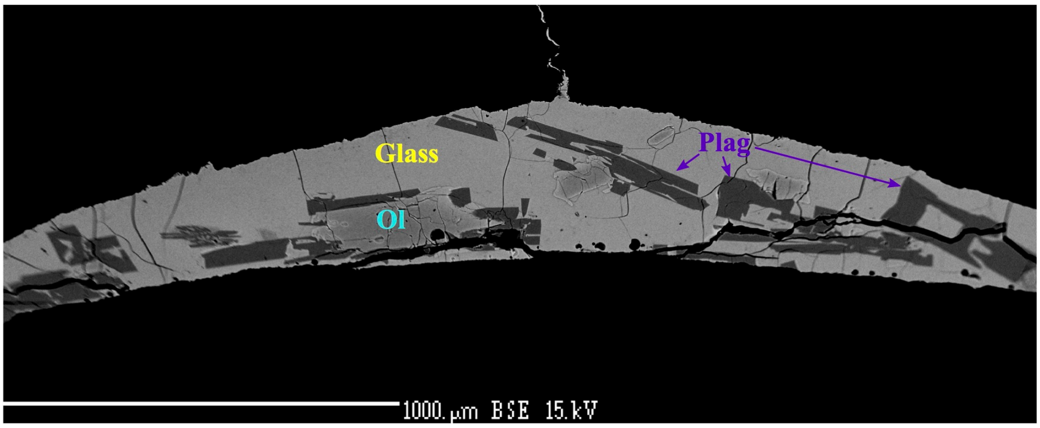

Figure 3.3 BSE image of experimental charge CMH16-6, showing olivine and plagioclase crystals surrounded by glass.

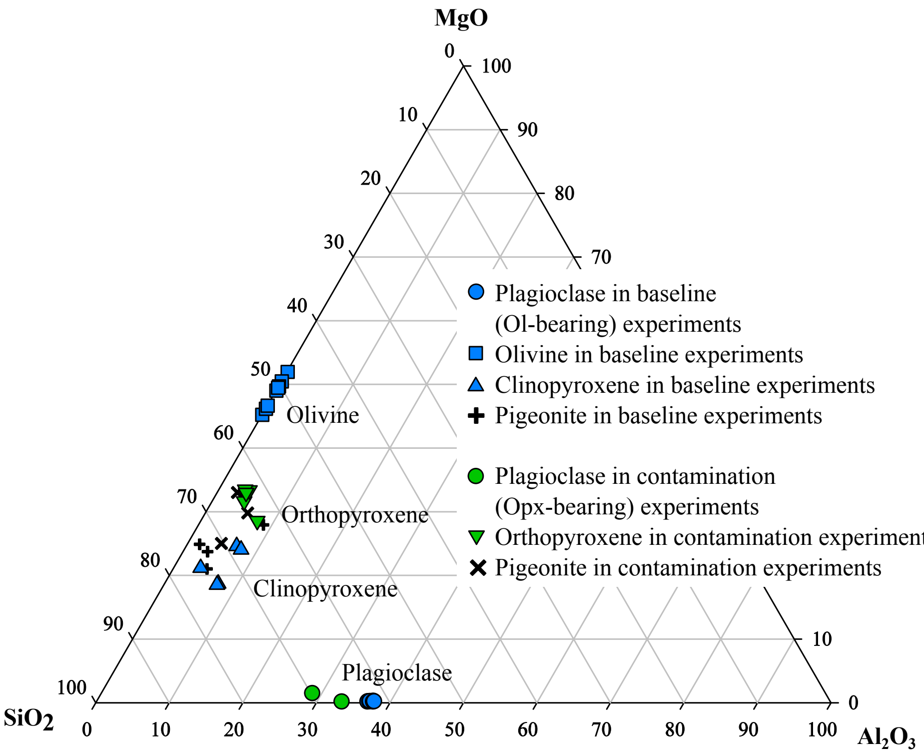

Figure 3.4 Ternary diagram showing the compositions of experimental phases in baseline experiments on CMH_HAB and contaminated experiments on CMH+KAC.

The liquid compositions follow systematic trends with decreasing temperature, mainly reflecting the extraction of large amounts of plagioclase. The average liquid compositions for each experiment are plotted in Fig. 3.5, along with the 1σ error bars. In the baseline experiments, runs T1250-5, T1200-4 and CMH16-3 plot very close together, since they ran at similar temperatures and have almost identical Mg#. In many cases, the most evolved experiments at the lowest temperatures show a greater spread in composition, seen by the larger error bars. The phases in these evolved experiments are not as homogeneous as the higher temperature runs, because lower temperature results in slower diffusion of elements and thus an increased duration required to fully equilibrate. There is a consistent trend of silica enrichment with decreasing temperature in the liquid compositions, as has also been shown on the liquid evolution trend on the phase diagram in Fig. 3.2. Experiment T1325-1 lies slightly off the general trends for some oxides, most noticeably for FeO*. Since this is the first experiment with ilmenite as a crystallizing phase, the FeO* and TiO_2 contents are expected to level off or decrease slightly in the melt, but not to the extent of the decrease seen in FeO* for this experiment. The glass in T1325-1 has a low total (~93 wt. %) for the mean microprobe composition, and so it is likely that there was a problem with the analysis. T1325-1 most likely has more FeO* than indicated in the analyses, and therefore a lower Mg#, shifting it up and to the left on the Mg# vs. FeO* plot. While the low microprobe total for this experiment is a drawback in the data series, it does not have an effect on the topology of the phase diagram and the results of the study. Al_2O_3 and CaO contents show an initial increase in the liquids, from the starting composition to the first experiment, reflecting the crystallization of only olivine at the liquidus. After the onset of plagioclase crystallization, Al_2O_3 and CaO decrease consistently.

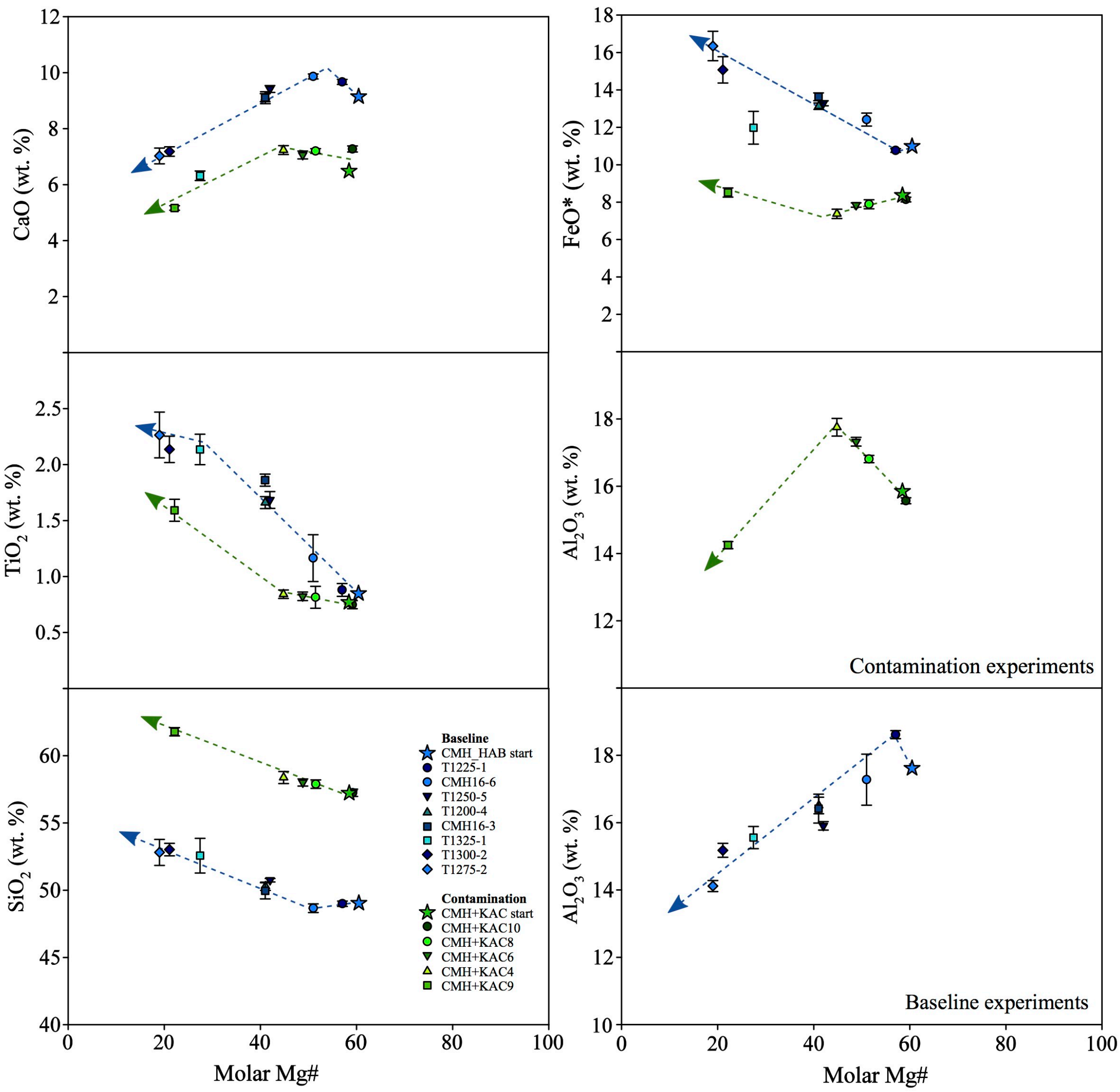

Figure 3.5 Major element compositions of glasses in baseline (CMH_HAB) and contamination (CMH+KAC) experiments, plotted against Mg#, to show the evolution of the liquids with decreasing temperature. Arrows are used to show the general trends of the liquids, and point in the direction of decreasing temperature.

3.4.2 Contamination experiments

The liquid compositions of the contamination experiments are shown on the pseudoternary in Figure 3.6. The starting composition plots higher up on the diagram, nearer to qtz than the CMH_HAB composition. These experiments have orthopyroxene as the first liquidus phase. About 11% opx crystallizes before the liquid becomes plagioclase saturated, and plagioclase and pigeonite start to form at a similar temperature. No olivine or cpx forms in the contamination experiments. The liquids initially evolve horizontally from the starting composition, away from the location of the opx compositions. Once plagioclase begins to form, the liquids evolve up towards the qtz apex, as with the baseline experiments. The angle of liquid evolution trend also bends back upon itself once plagioclase saturation has occurred, because a higher proportion of plagioclase than pyroxene is crystallizing, causing the liquids to evolve primarily away from the pl apex. Phase boundaries constructed from the liquid compositions are shown as solid black lines. Dashed black lines are used to indicate inferred phase boundaries. The exact location of these boundaries is estimated, since those regions were not explored in the experiments.

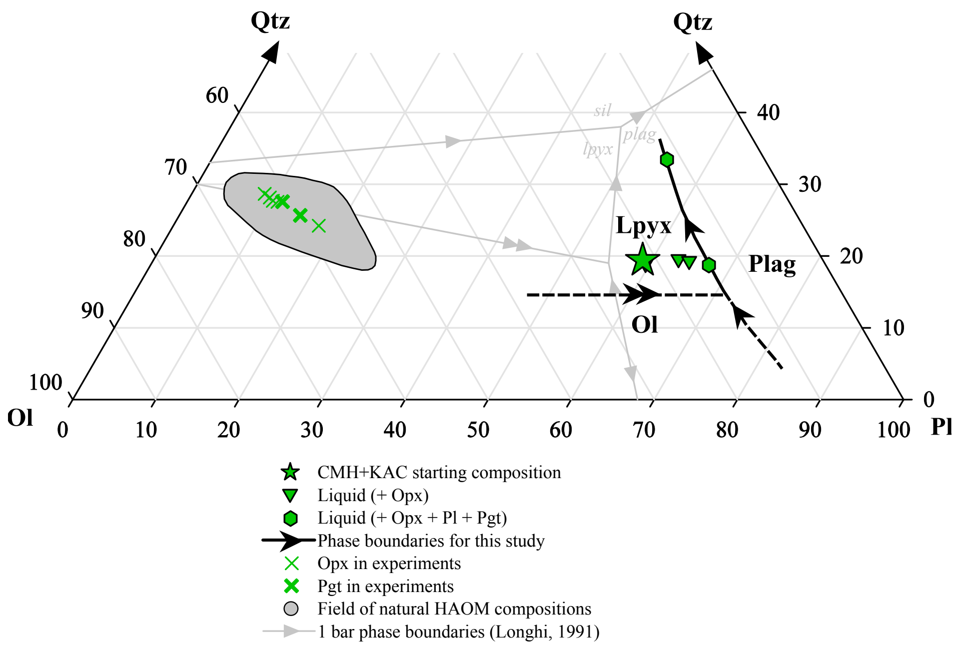

Figure 3.6 Liquidus equilibria of 10 kbar contamination experiments on CMH+KAC. Liquid compositions are projected as in the baseline phase diagram. Dashed black lines are inferred phase boundaries with estimated positions.

Plagioclase is less calcic than in the baseline experiments, with a range of An contents from An_{51} to An_{56}. It is also richer in K_2O (0.49 – 0.86 wt. %) than the baseline experiments (0.01 – 0.16 wt. %), directly reflecting the change in starting composition due to the addition of the contaminant. The orthopyroxene shows very little variability in composition, with the exception of CMH+KAC9, which is unlikely to have completely equilibrated. The Mg# of opx ranges from 78 to 81 (excluding CMH+KAC9), and contains between 3.08 wt. % and 3.62 wt. % Al_2O_3. Opx is generally square or rectangular with straight edges and sharp corners (Fig. 3.7) Pigeonite contains between 2.30 wt. % and 4.66 wt. % Al_2O_3, and is less calcic than in the baseline experiments. Mineral compositions for the contamination experiments are plotted in Figure 3.4 along with those for the baseline experiments.

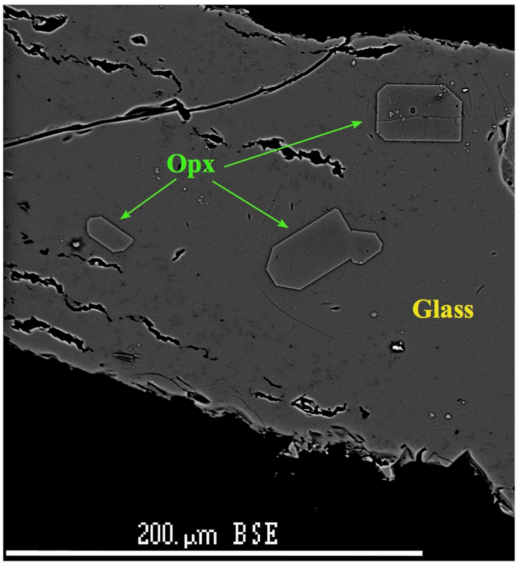

Figure 3.7 BSE image of experiment CMH+KAC8, showing the shape of straight-edged orthopyroxene grains surrounded by glass.

The liquid compositions in the contamination runs are also shown in Figure 3.5. The plots show consistent increases in SiO_2 and TiO_2 in the liquids. In experiment CMH+KAC9 the liquids plot away from the rest of the trend in all cases, due to the experiment being significantly more evolved (molar Mg# = 22) than the higher temperature experiments, and due to it being the only run that produced a significant proportion of plagioclase. For clarity, Al_2O_3 contents of the liquids in the contamination experiments have been plotted on separate axes to the baseline runs, due to the ranges being very similar (between 14 and 18 wt. %) and strongly overlapping on the graph, making them difficult to read on the same axes. Al_2O_3 in the liquids of the contaminated experiments also increases initially while orthopyroxene is forming, and then starts to decrease at the onset of plagioclase saturation. More runs on the contaminated starting composition were done above the temperature of plagioclase saturation, so the initial increase in Al_2O_3 is more apparent than for the baseline experiments. Although plagioclase is stable from run CMH+KAC4, only a very small amount of plagioclase (< 1%) has formed in this run, so the liquids do not reflect much change in composition due to plagioclase formation. The effects of plagioclase extraction are seen from the composition of CMH+KAC9. The CaO content remains fairly constant, at just above 7 wt. % in the liquid and dropping to just over 5 wt. % after about 30% plagioclase has crystallized. The FeO proportion decreases steadily with temperature as orthopyroxene crystallizes, and increases when significant plagioclase forms. The TiO_2 content increases steadily with decreasing temperature, and increases more sharply in the evolved CMH+KAC9 liquid. No Fe-Ti oxides formed in the contamination experiments over the temperature range investigated.

3.5 DISCUSSION OF EXPERIMENTAL RESULTS

The olivine-orthopyroxene dichotomy has been observed in the Kunene Anorthosite Complex and many other Proterozoic anorthosite complexes. The suggestion of the mineral dichotomy being the result of variable amounts of crustal contamination is supported by substantial evidence, both in field observations and in geochemistry. This study tests the crustal contamination theory using experiments and phase equilibria, and shows that contamination of high-alumina basalt with granitic material can shift the dominant crystallizing mafic mineral from olivine to orthopyroxene.

3.5.1 Comparison with natural rocks

The experiments on CMH_HAB and CMH+KAC clearly show different phase assemblages and liquid evolution paths. The baseline experiments on CMH_HAB produce olivine and plagioclase, with lesser clinopyroxene and pigeonite at lower temperatures, and minor ilmenite. The contaminated experiments on CMH+KAC crystallize orthopyroxene and plagioclase, with a smaller proportion of pigeonite at lower temperatures. Adding a granitic contaminant to the original HAB starting composition results in orthopyroxene crystallizing as the dominant mafic phase as opposed to olivine in the uncontaminated experiments. This is consistent with the hypothesis of crustal contamination producing the mineral dichotomy in the natural rocks in anorthosite complexes. While the experiments have shown that contamination of HAB can produce the correct mineral assemblages of anorthosites, it is necessary to address the chemical compositions of the phases that are produced, and compare these, as well as their proportions and order of appearance, to natural anorthosites.

3.5.1.1 Mineral chemistry

The chemistry of the phases produced in the experiments shows a close match with natural minerals in the rocks. Figure 3.8 shows the experimental phase compositions plotted on a SiO_2-MgO-Al_2O_3 ternary diagram, as in Figure 3.4 above, but underlain by fields of compositions for natural minerals in anorthosites from around the world, including the KAC data from this study (see Chapter 2). While there is significant overlap, the plagioclase fields show more aluminous (and hence more calcic) plagioclase in olivine-bearing anorthosites than in opx-bearing anorthosites, and this trend is reproduced in the experiments. Plagioclase compositions in both the baseline and contamination experiments plot within the fields for natural plagioclase in anorthosites, with the contaminated runs showing slightly less aluminous (and hence less calcic) plagioclase. Clinopyroxene in the baseline experiments and orthopyroxene in the contaminated experiments also generally plot well within the fields for natural pyroxenes, with a few points plotting just outside the natural fields. Pigeonite in the baseline experiments mostly plots within the natural field of clinopyroxene compositions, while pigeonite in the contaminated runs generally overlaps with the natural orthopyroxene field. The baseline pigeonite is slightly higher in CaO than in the contamination runs, resulting in the closer match to the compositions of cpx than to opx. All experimental pyroxenes are shown on the pyroxene quadrilateral in Figure 3.9, and pyroxenes from natural anorthosites are plotted for comparison. It is apparent from the diagram that, in natural anorthositic rocks, distinct fields of ortho- and clinopyroxene occur. Orthopyroxene is entirely enstatite, and most clinopyroxene is diopside, with augite being less common. Pigeonite is absent from mineral compositions given in the literature, but inverted pigeonite has been documented in several anorthosite complexes. Very few workers have recalculated the bulk pigeonite compositions from the host and lamellae, explaining the small number of natural pyroxenes plotted in the pigeonite field. Natural pigeonite compositions displayed on the diagram are recalculated compositions of inverted pigeonite from the Adirondack anorthosites (Ashwal, 1982; Bohlen and Essene, 1978). Pyroxenes produced in the experiments span a continuous range from augite to enstatite. Diopside was not produced in the experiments. A similar continuous range in pyroxene compositions was produced in experiments on HLCA (Fram and Longhi, 1992; Longhi *et al.*, 1999). Experimental olivine compositions also overlap with natural olivine in anorthosites, but plot in the more MgO-rich region of the field.

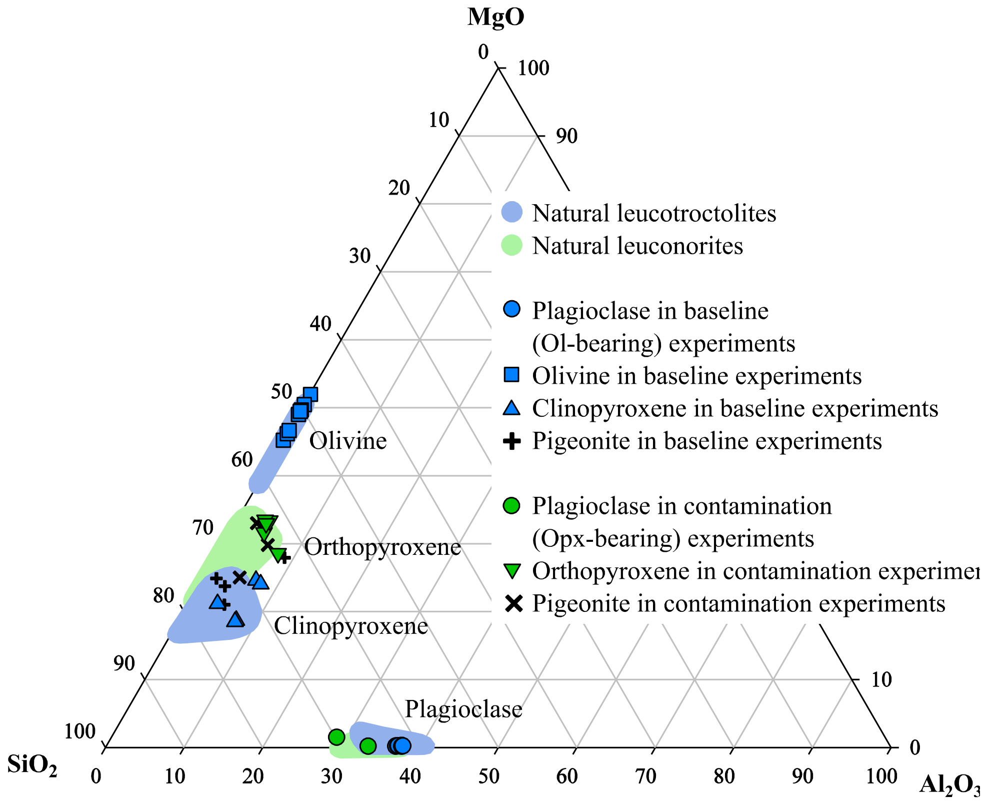

Figure 3.8 Compositions of phases produced in the experiments on CMH_HAB and CMH+KAC, plotted against fields of compositions of natural minerals in anorthosites.

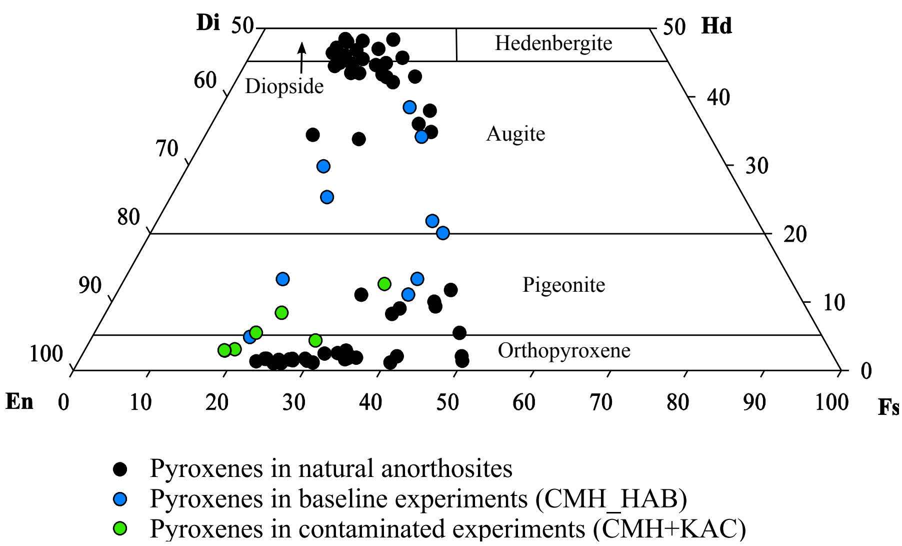

Figure 3.9 Pyroxene quadrilateral for pyroxenes produced in experiments on CMH_HAB and CMH+KAC, as well as natural pyroxenes in anorthosites.

The locations of the experimentally-produced pyroxenes on the phase diagrams for both sets of experiments plot well within the field for natural HAOM compositions (Fig. 3.2 and Fig. 3.6). While not as high as some of the highest-Al HAOMs, some of the opx and pigeonite produced in the experiments does have high alumina contents (mostly ~2 - 5 wt. % Al_2O_3). Their compositions plot closer to the compositions of HAOM than to the non-megacrystic, mostly intercumulus opx in the anorthosites (Fig. 3.10A). Experiments on HLCA at high pressure by Fram and Longhi (1992) also produced pyroxenes with compositions similar to HAOMs. At 10 kbar, the opx produced from HLCA has ~6 wt. % Al_2O_3, and at 11.5 kbar, Al_2O_3 content is ~8 wt. % (Fram and Longhi, 1992). It is likely that at slightly higher pressure, the CMH+KAC composition would produce more aluminous opx, with Al_2O_3 contents closer to that of the highest-Al megacrysts (8 - 9 wt. %). The closer match of 10 kbar experimental pyroxenes with HAOMs than with intercumulus opx suggests that, during the formation of anorthosites, the opx that forms at depth is primarily of the HAOM-type. Since pressure exerts a strong control on the alumina contents of the pyroxene, the balance of the opx in the rocks that is non-megacrystic, and most commonly interstitial, most likely forms at shallower depths. What is less clear is at exactly what depth most of the crystallization occurs, or whether crystallization occurs continuously from the stage of ponding at the Moho to emplacement in the shallower crust. The pressure control on the An content of plagioclase, and the range of An contents for plagioclase in both leuconorites and leucotroctolites, suggest that crystallization may occur polybarically, beginning at the Moho and continuing during movement of the crystallizing magma to shallower depths in the crust. Experiments on HLCA over a range of pressures from 1 bar to 11.5 kbar (Fram and Longhi, 1992) demonstrate the pressure effect on plagioclase composition. Experiments at 10 - 11.5 kbar produced plagioclase between An_{54} and An_{60}, overlapping with a cluster of Harp Lake plagioclase. Lower pressure experiments produced more calcic plagioclase, which match the rest of the range of Harp Lake compositions (Fram and Longhi, 1992). This suggests that significant plagioclase crystallization may occur at depth, where the primitive HAOMs form, followed by subsequent crystallization of more calcic plagioclase at shallower levels in the crust. The emplacement mechanisms of anorthosite plutons are not well understood, but several features (discussed below) suggest that they are emplaced as crystal-liquid mixtures, or mushes. Many of the intrusions have a domical structure, and some anorthosites exhibit a protoclastic, or "mortar" texture, formed due to mechanical abrasion of plagioclase crystals in an ascending mush (Buddington, 1939; Duchesne, 1984; Longhi and Ashwal, 1985). It is likely that significant plagioclase is required to make the mushes buoyant enough to rise through the crust from Moho depths, and sufficient crystallinity is also required to be able to entrain the megacrysts of orthopyroxene that formed at depth. It is thought that crystal-rich magmas or mushes ascend through the crust, carrying HAOMs and continuing to crystallize plagioclase and interstitial mafic minerals during ascent (Ashwal, 1993, Duchesne, 1984; Emslie, 1985; Longhi *et al.*, 1993).

Plagioclase produced in the contamination experiments is noticeably different in terms of major element composition to the baseline plagioclase. Figure 3.10B shows major element compositions of experimental plagioclase plotted against the An content (mole %), with fields of natural plagioclase from leucotroctolites and leuconorites around the world. It is clear that the experimental plagioclase compositions plot within the fields of natural leucotroctolites and leuconorites. Plagioclase in the baseline experiments has lower K_2O and very consistently low FeO*. These correlate with the higher An content of plagioclase in the baseline experiments. The trend of more calcic plagioclase in leucotroctolites than in leuconorites is a common feature documented in anorthosite complexes. Fields of plagioclase compositions for leucotroctolites and leuconorites are shown in Figure 3.11, along with the experimental plagioclase compositions. While there is significant overlap between the olivine-bearing and opx-bearing compositional fields, the plagioclase in olivine-bearing rocks extends to higher An contents, and that in opx-bearing anorthosites extends to lower An contents. The same pattern is observed for the experimental plagioclase compositions. This observation has been used as another piece of evidence for opx-bearing anorthosites having formed from contaminated magmas. (Drüppel *et al.,* 2007; Frost *et al.,* 2010; Gleiβner *et al.,* 2010; Lindsley *et al.,* 2010; Xue and Morse, 1993). Contamination of basaltic magma by a granitoid composition with higher Na_2O than CaO (such as KAC031/035) would increase the Na:Ca ratio in the magma, and result in the crystallization of less calcic plagioclase.

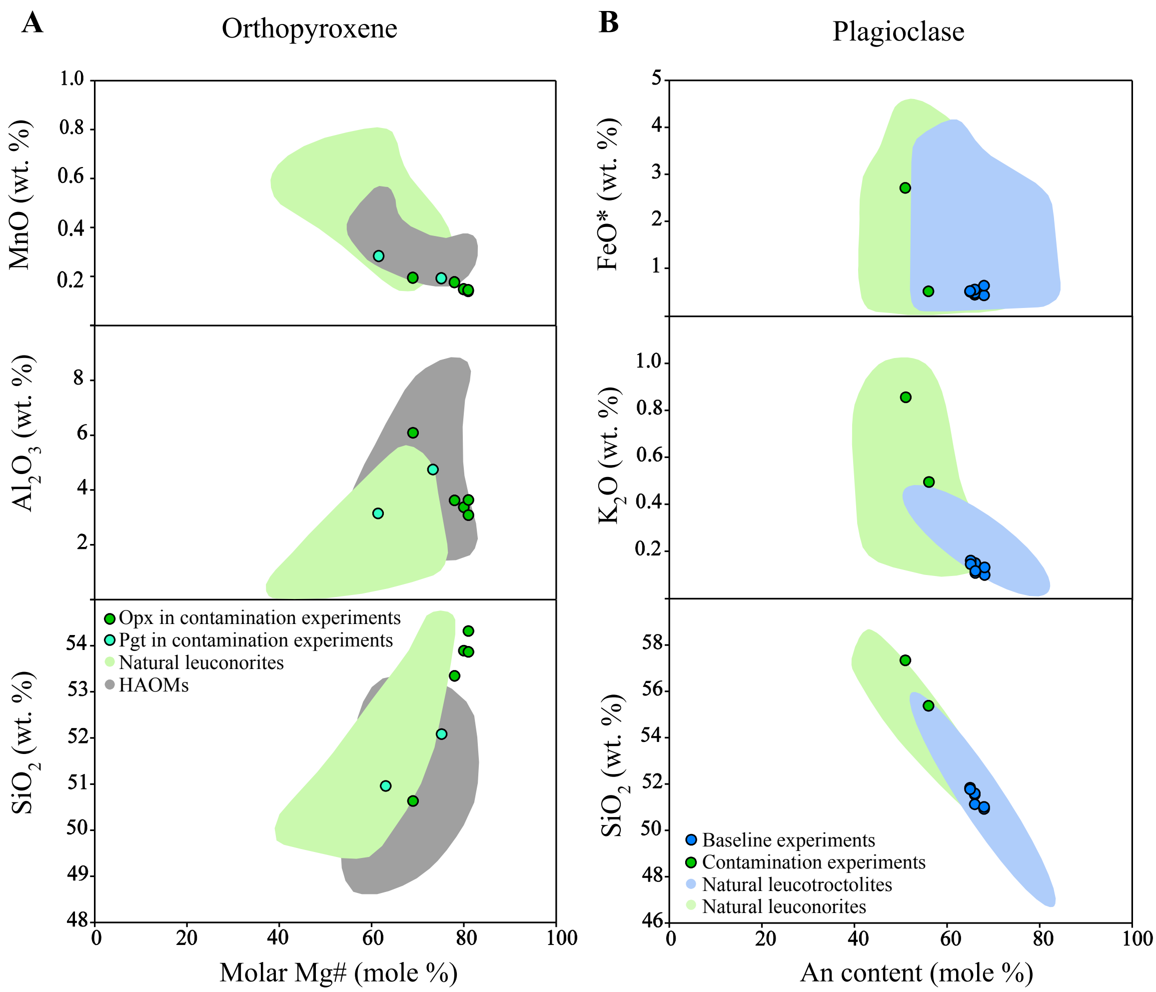

Figure 3.10 A) Selected major element compositions of experimental orthopyroxene and pigeonite in contamination experiments, plotted against natural pyroxenes and HAOMs in anorthosite complexes around the world. B) Experimental plagioclase compositions plotted against natural plagioclase in leucotroctolite and leuconorite from anorthosite complexes around the world. Natural data for both plots includes the Adirondacks, Atikonak River, Ahvenisto, Harp Lake, Kunene, Labrieville, Lac St. Jean, Laramie, Mealy Mountains, Morin, Nain, Rogaland, and St. Urbain complexes. Data sources: Ashwal and Twist (1994); Emslie (1978, 1980); Frost *et al.* (2010); Gleiβner *et al.* (2010); Hegner *et al.* (2010); Lindsley *et al.* (2010); Owens and Dymek (1995); Philpotts (1966); Silva (1992).

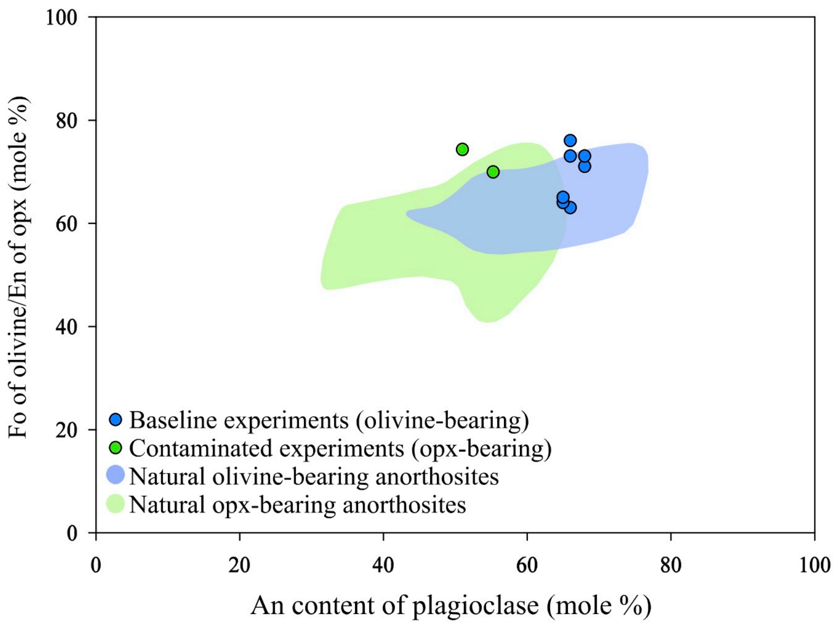

Figure 3.11 An content of plagioclase plotted against Fo content of olivine in baseline experiments and En content of opx for contaminated experiments respectively. Fields of plagioclase compositions in natural leucotroctolites and leuconorites from the Adirondacks, Harp Lake, Kunene, Labrieville, Laramie, Mealy Mountains, Michikamau, Morin, and Paul Island complexes are shown for comparison, including the KAC data obtained in this study. Data sources: Emslie (1980; 1985); Lindsley *et al*. (2010); Philpotts (1966).

3.5.1.2 Crustal contamination and the mineral dichotomy

The experiments in this study on CMH_HAB, as well as those on HLCA and other high-alumina basaltic compositions, show that HAB magmas can produce the minerals and mineral compositions seen in Proterozoic anorthosites. However, a single magma composition cannot produce the full range of rock types observed in anorthosite complexes. While pressure plays an important role in the mineral assemblage that forms from the magmas, as well as the chemistry of those minerals, it is unlikely that only variations in depth of crystallization of a single magma composition can produce the range of mineral assemblages seen in anorthosites, as well as the range of plagioclase compositions (Longhi *et al.*, 1993). The results of the experiments on CMH_HAB and CMH+KAC show that a high-alumina basaltic magma, as well as a magma that has undergone some degree of contamination by a crustal component, *can* produce the variety of mineral assemblages and compositions that characterize Proterozoic anorthosites. A high-alumina basalt composition such as CMH_HAB can produce rocks dominated by plagioclase and olivine at 10 kbar, while a granitoid-contaminated HAB may crystallize plagioclase and opx dominated rocks. For the Harp Lake anorthosites, experiments have shown that the HLCA composition can generate the olivine-bearing anorthosites, while a more quartz-rich magma can account for the opx-bearing anorthosites (Longhi *et al*., 1999). Inversion calculations on the major element compositions of plagioclase from the Nain complex produce an olivine-normative parental magma for the olivine-bearing rocks and a silica-saturated parental magma for the opx-bearing rocks (Morse, 2006).

The baseline experiments on CMH_HAB have olivine on the liquidus, followed very closely by plagioclase. Clinopyroxene forms at lower temperatures, along with pigeonite and minor ilmenite. This crystallization sequence would result in plagioclase-olivine cumulate rocks with interstitial clinopyroxene and pigeonite. This texture is what is typically observed in the natural olivine-bearing anorthosites, including the leucotroctolites of the KAC described in this study (Fig. 2.4D). The rocks contain cumulus olivine and plagioclase that in many cases appear to have grown simultaneously. Clinopyroxene is entirely an interstitial phase, and ilmenite occurs in small interstitial pockets associated with late stage biotite and/or amphibole, indicating its crystallization from evolved residual liquids (biotite and amphibole are not observed in the experiments since they were conducted under anhydrous conditions). Leucotroctolites in many anorthosite complexes, including the leucotroctolites and olivine-leucogabbronorites of the KAC, commonly display rims of orthopyroxene on olivine grains (Fig. 2.4E), indicating their formation by peritectic reactions between olivine and liquid. The pigeonite that forms in the experiments may also indicate a reaction between olivine and liquid, but rims of pigeonite composition have not been documented in the natural rocks. Inverted pigeonite has been observed in some anorthosites (Ashwal, 1982; Bohlen and Essene, 1978) so it is likely that the pigeonite produced in the experiments would invert upon slow cooling of the rock, and this would then match what is observed in the natural rocks. The overall results of experiments on CMH_HAB are a good match for the mineral assemblages and textures in natural olivine-bearing anorthosites.

The contamination experiments on CMH+KAC produced liquidus orthopyroxene, followed by plagioclase and a small proportion of pigeonite. Natural opx-bearing anorthosites typically contain cumulus plagioclase, with orthopyroxene most commonly occurring as an interstitial phase (Fig. 2.5C) along with clinopyroxene and minor oxide minerals. Plagioclase and orthopyroxene cumulates do occur in some anorthosites, but are less common (Ashwal, 1993; Longhi *et al*., 1999). The KAC anorthosites also contain predominantly interstitial opx, with few cumulus grains observed in thin section (Fig. 2.6A). Since the contaminated experiments produce orthopyroxene as the liquidus phase, it is necessary to address why cumulus opx is rarely observed in the natural rocks. It is possible that all the opx crystallizing as a liquidus phase at depth, before plagioclase saturation is reached, forms as the characteristic HAOMs found in most complexes. While the experimental pyroxenes do not have Al_2O_3 contents as high as what is documented in the megacrysts, pressures slightly higher than 10 kbar have been shown to crystallize more aluminous pyroxenes from HLCA (Fram and Longhi, 1992). Since the megacrysts would have a high density, not all of those that crystallized would be carried up to the emplacement level. Following the crystallization of HAOMs, the magma would reach the opx-pl cotectic and start to crystallize plagioclase. Continued crystallization of opx along with plagioclase would produce the more common interstitial opx that surrounds cumulus plagioclase grains in the rocks. This process could happen during the intrusion of the crystal mushes towards the shallow crust, accounting for the lower Al_2O_3 contents of the intercumulus opx, and the reverse zoning observed in many plagioclase crystals. Many opx-bearing anorthosites in the KAC also contain some interstitial clinopyroxene. No cpx is produced in the contamination experiments, but some pigeonite does form.

The experimental results demonstrate that contamination of HAB magma with siliceous material can account for one of the enigmatic features of Proterozoic anorthosites, the olivine-orthopyroxene dichotomy. The chemistry and mineralogy of olivine-bearing anorthosites can be accounted for by crystallization of a high-alumina basalt, like CMH_HAB, at 10 kbar. Contamination experiments show that a basaltic composition that has undergone contamination by surrounding lower crustal melts, such as CMH_KAC, is capable of producing the features that characterize the opx-bearing rocks. Anorthosites that contain only orthopyroxene (± clinopyroxene) as the mafic phase and lack olivine are seen in some areas in the southern KAC, and are the dominant rock type in many, if not most anorthosite complexes, including the Adirondacks, Rogaland, Morin, Lac Allard and Nain complexes (Buddington, 1939; Charlier *et al.,* 2010; Demaiffe *et al.,* 1986; Duchesne *et al.*, 1985; Hargraves, 1962; Wiebe, 1978). These rocks must have crystallized from magma that had been sufficiently contaminated to shift the starting composition from the olivine field of the phase diagram into the opx field, as a result of the addition of a silica-rich granitic component. In the KAC, there are rocks in the north of the complex classified as leucotroctolites, characterized by having olivine as the dominant mafic phase, with opx only as reaction rims on olivine grains. These rocks most likely experienced very little, or no contamination. However, the intermediate classification, the olivine-bearing leucogabbronorites, must also be accounted for. This rock type is characterized by cumulus olivine and plagioclase, with thick reaction rims of opx on many olivine grains, as well as interstitial opx ± cpx. It is possible that these rocks represent magma that was subjected to some degree of contamination, but not as much as the magmas that generated the leuconorites. If the magma was subjected to some contamination, but not enough to move the composition into the opx field, then olivine and plagioclase would still crystallize as the cumulus phases, but the magma could be enriched enough in SiO_2 to initiate peritectic reactions between olivine and the residual liquid, forming prominent rims of orthopyroxene replacing the olivine. Another possibility is that the contamination may have happened only after some olivine and plagioclase had crystallized, so that the newly Si-enriched magma could react with the pre-existing olivine to form reaction rims, and then possibly crystallize subsequent interstitial opx. This, however, seems like a less likely scenario, since the magma fractionating olivine and plagioclase would be cooling from its initial super-liquidus temperature, so it does not make sense for partial melting and assimilation to occur only at a later, cooler stage of magma ponding. In addition, if some olivine and plagioclase had crystallized before the assimilation of the granitoid composition, then it would be a case of the residual liquid mixing with the granitoid composition, rather than the original HAB, and it is uncertain what the liquidus equilibria of this mixture would be. The intermediate anorthosite rock category containing olivine and orthopyroxene provides further evidence for the mineral dichotomy in anorthosites being the result of variable amounts of crustal contamination, and shows how progressive contamination increases the orthopyroxene to olivine ratio in the rocks.

While the experiments crystallize plagioclase in the highest proportion of all phases, the maximum amount produced in any experiment is 60% plagioclase. To produce rocks with more than 90% plagioclase, other mechanisms of plagioclase enrichment must come into play. It has been suggested that continuous injections of new, primitive magma into the ponding magma chamber may partially melt the plagioclase crystals that have formed, and keep the magma saturated in plagioclase components (Wiebe, 1990). It is also possible that much of the mafic component crystallizing at depth is not carried up in the ascending crystal mush, since the mafic minerals have a higher density. However, cumulus olivine is seen in many rocks, as well as the 1 meter long opx megacrysts, and if these phases are carried from the Moho to the shallower crust in plagioclase crystal mushes, it does not seem likely that a very significant portion of the mafic minerals would not get entrained as well. The HLCA experiments performed at a range of pressures from 1 bar to 15 kbar indicate that the plagioclase stability field expands at low pressure (Fram and Longhi, 1992). Plagioclase may therefore crystallize in greater proportions during ascent of the crystal mush from the Moho towards the shallower crust, forming plagioclase-rich rocks. The simplest mechanism for emplacement of plagioclase-rich rocks is by plagioclase flotation. Morse (1968) stated that if anorthosites are cumulates that have a basaltic parent, plagioclase flotation must be the explanation for forming anorthosites. Evidence for plagioclase flotation in the rocks however, is rare (Ashwal, 1993; Morse, 1982; Scoates, 2000). Flotation of plagioclase depends on factors such as the depth at which crystallization and accumulation of plagioclase is taking place, and the composition of the plagioclase and the melt (Ashwal, 1993). Scoates (2000) performed density calculations for proposed high-alumina basaltic parental magmas and Fe-enriched residual liquids, and found that the density of the HAB liquids is greater than An_{40-60} plagioclase under all reasonable conditions. Basaltic melts have been shown in experiments to be more compressible than crystals, so that from ~6 kbar the melt would denser than plagioclase, and plagioclase as calcic as An_{90} would float (Kushiro and Fujii, 1977; Kushiro, 1980). Intermediate plagioclase could thus easily float in a basaltic melt at 1 - 2 kbar, and therefore, at lower crustal depths, substantial plagioclase should accumulate by flotation from a fractionating basaltic magma (Ashwal, 1993).

The experiments and data in this study address whether contamination by partial melts of the lower crust can change the composition of anorthosites from olivine-bearing to orthopyroxene-bearing. Some of the most convincing evidence for crustal contamination is the difference in isotopic signature of anorthosites that intruded into terranes of different ages. The anorthosites that intruded into older (commonly Archaean) terranes have isotopic signatures closer to crustal compositions, and are further displaced from the depleted mantle composition than those that intruded into younger (Proterozoic) terranes (Ashwal *et al.,* 1896; Bybee and Ashwal, 2015). It can be considered that, even though the major element composition of the lower crust may be poorly constrained, and may or may not be the same as the outcropping country rocks seen around the anorthosites, the isotopic nature of the whole terrane, from surface exposures of country rocks to the lower crust, is likely to be similar.

3.5.2 A mantle or crustal source for anorthosite parental magmas

The experiments in this study have shown that olivine-bearing anorthosites may form from a magma composition such as CMH_HAB, while opx-bearing anorthosites may form from a mixture of this magma with a granitoid contaminant. In addition to addressing the mineral dichotomy in Proterozoic anorthosites, the data shed light on whether anorthosites were derived from a mantle or a crustal source. The phase diagram constructed from experiments on CMH_HAB (Fig. 3.2) shows a liquid evolution path from the olivine stability field towards the ol-pl cotectic, and then upwards towards qtz as the liquid fractionates predominantly olivine and plagioclase, and lesser pyroxene. The liquids in the experiments evolve towards quartz-normative compositions with decreasing temperature. Extensive experimental work on the HLCA composition has made valuable contributions to the anorthosite debate. While the experiments of Fram and Longhi (1992) and Longhi *et al.*, (1999) have shown that HAB compositions such as HLCA are capable of producing anorthosites, the phase equilibria determined for HLCA at 11.5 kbar exhibit a fundamental difference from the data of this study, as discussed below.

Longhi *et al*. (1999) conducted experiments on HLCA between 1 bar and 13 kbar. The most complete data set for their study is at 11.5 kbar. The liquid compositions of these experiments and the resulting phase boundaries are shown in Figure 3.12A as dark grey circles and thick grey lines, along with the data for CMH_HAB (as in Fig. 3.2) for comparison. Many compositions proposed by various authors to be parental to anorthosites plot near HLCA. The most important feature of the HLCA liquids is that they evolve downwards, away from quartz, with decreasing temperature. The phase boundaries constructed from the data illustrate the presence of a thermal divide on the pl-opx cotectic, and the HLCA composition fortuitously plots on this thermal divide. Liquids positioned either above or below the thermal divide will therefore evolve to more quartz-rich compositions or towards nepheline-normative compositions, respectively. There is no way for a lower-SiO_2 magma to fractionate up the thermal divide to the region of HLCA. The presence of a thermal divide at 8 – 10 kbar is also indicated by other HAB experiments (Baker and Eggler, 1987; Bartels *et al.*, 1991). As a result of the thermal divide, a mantle-derived melt in the olivine stability field will evolve towards the ol-opx-sp (spinel) peritectic, react out olivine, crystallize opx + cpx + spinel for an interval, and then reach the opx-sp-pl peritectic, before evolving down along the pl-sp cotectic, away from qtz. A schematic of this liquid evolution path is shown in Figure 3.12B. This path results in nepheline-normative residual liquids. The implication of the thermal divide is that mantle-derived magmas in the olivine field cannot evolve to the composition of HLCA and the field of proposed anorthosite parental magmas, since they evolve away from qtz when they reach the plagioclase liquidus curve. The conclusion reached by Longhi *et al.* (1999) is that the anorthosite parental magmas cannot have been produced by fractionation of a more primitive, mantle-derived melt, due to the presence of the thermal divide. The parental magmas must have been formed by partial melting of a crustal composition already on the thermal divide, such as restite left over from an earlier stage of melting, or a foundered layered intrusion that had sunk out of weakened crust (Longhi *et al*., 1999). The phase boundaries for CMH_HAB however, clearly demonstrate the evolution of liquids upwards towards quartz with decreasing temperature (Fig. 3.12C). No thermal divide is present for the CMH_HAB composition at 10 kbar, and the data suggest that mantle-derived liquids *can* evolve towards the field of proposed parental magmas of the anorthosites.

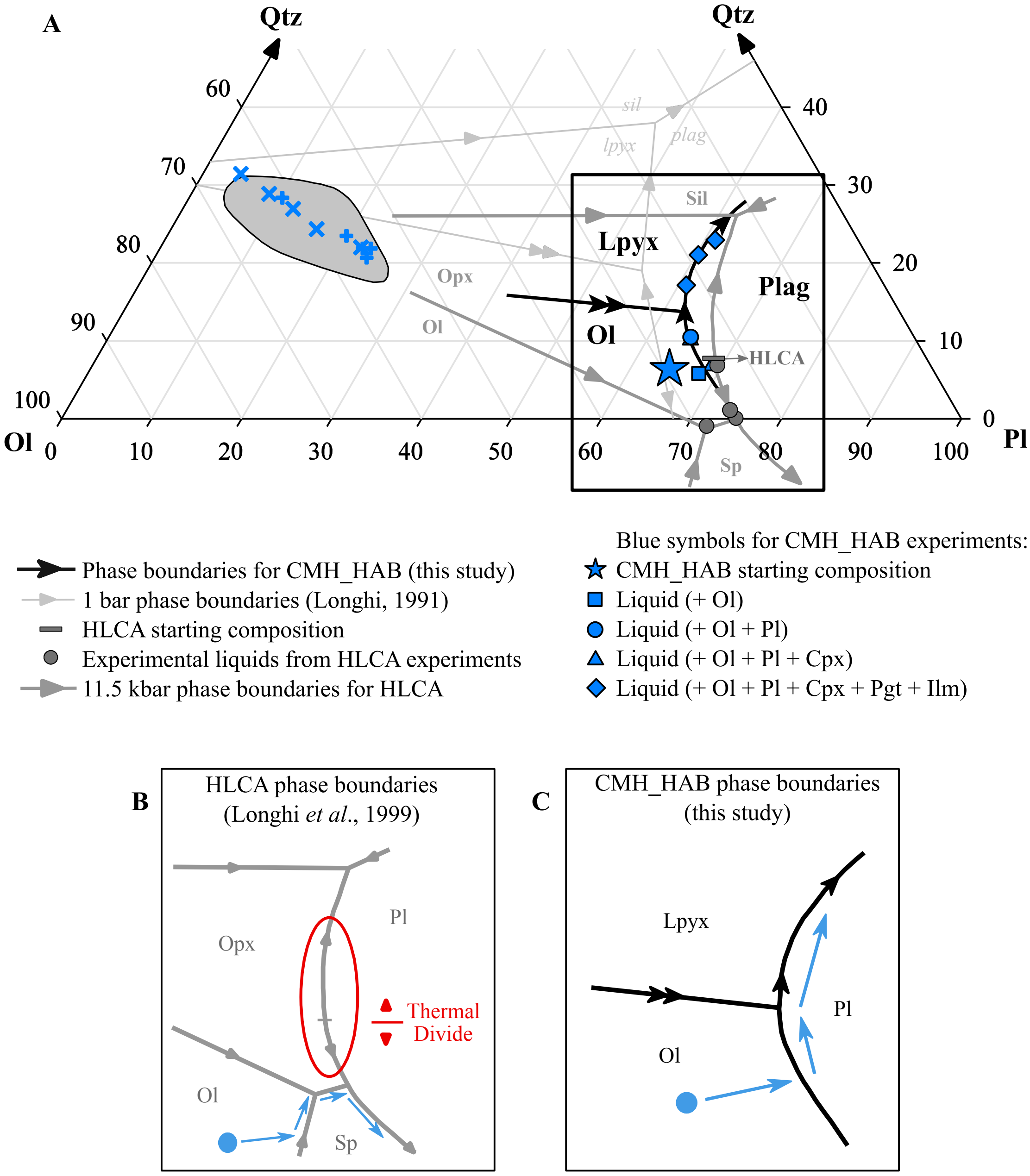

Figure 3.12 A) Liquidus equilibria for HLCA at 11.5 kbar (Longhi *et al.,* 1999) and CMH_HAB at 10 kbar (this study). 1 bar phase boundaries are shown as thin light grey lines for reference. B) Schematic representation of the path of a mantle-derived liquid (solid blue circle), beginning in the olivine stability field, according to the phase boundaries for HLCA (Longhi *et al.,* 1999). Blue arrows indicate the liquid evolution path. The liquid will eventually evolve away from quartz, towards nepheline-normative compositions, due to the presence of a thermal divide on the pl-opx cotectic. C) Schematic representation of the liquid evolution path (blue arrows) for a mantle-derived liquid (solid blue circle), according to the phase boundaries of CMH_HAB. No thermal divide is observed, and the liquid evolves towards more quartz-rich compositions.

The differences in phase equilibria for HLCA (Longhi *et al.,* 1999) and CMH_HAB (this study) are due the compositional-dependence of the topologies of the phase boundaries. The pseudoternary phase diagrams are an attempt to project a 10-component system onto a 3-component diagram, so the complex chemical systems are being extensively simplified. While HLCA and CMH_HAB are both high-alumina basaltic compositions and have both been shown to be capable of producing anorthositic products, small differences in the starting compositions have noticeable effects on the positions of the phase boundaries. The alumina content of both compositions is approximately 17.5 wt. %, but CMH_HAB is more primitive (Mg# = 60) than HLCA (Mg# = 52). The experiments on HLCA by Longhi *et al.* (1999) were done over a range of pressures, allowing for an assessment of the effects of pressure on the phase boundaries. The ol-opx boundary shifts further away from quartz at higher pressure. This helps to explain the position of the 10 kbar CMH_HAB ol-opx boundary, closer to quartz than the HLCA boundary is at 11.5 kbar. The range of pressures tested in the HLCA experiments showed the appearance of the pl-opx thermal divide at 5 kbar. The thermal divide is absent in experiments at pressures below 5 kbar. The experiments also showed that the thermal divide moves further away from quartz with increasing pressure. In addition, the stability fields of opx and spinel were shown to intersect at ~10 kbar, so at pressures of 10 kbar and higher, spinel was a stable phase in some HLCA experiments. No spinel was produced in any experiments on CMH_HAB reported in this work. It is noted by Longhi *et al.* (1999) that these transitions in phase boundaries occur at higher pressures for more magnesian compositions, and may not occur at all in extreme cases. Since CMH_HAB has a higher Mg# than HLCA, this may explain some of the differences in the phase diagrams. The intersection of the spinel and opx fields would occur at a pressure higher than 10 kbar for CMH_HAB, so it is likely that spinel would be a stable phase in higher pressure experiments. Since the thermal divide moves further away from quartz with increasing pressure, it is possible that there is a thermal divide for CMH_HAB, but only at pressures higher than 10 kbar. Experiments on CMH_HAB at higher pressures may reveal the presence of a thermal divide, if it exists, since the increased pressure would shift the thermal divide downwards (away from quartz) into the investigated region of the phase diagram. However, since the thermal divide for HLCA is stable from as little as 5 kbar, it seems unlikely that a thermal divide for CMH_HAB would not yet be stable by as much as 10 kbar.

To produce the range of anorthosite compositions from olivine-bearing to opx-bearing, it is suggested by Longhi *et al*. (1999) that assimilation of a granitic component into a primitive mantle-derived melt, coupled with fractionation, could change the liquid path to pass through HLCA, but only at pressures less than 4 kbar, where the thermal divide is not stable. At higher pressure, the thermal divide was suggested to represent a barrier “even to the most favorable conditions of AFC" (Assimilation - Fractional Crystallization; Longhi *et al*., 1999). More isotopically evolved opx-bearing anorthosites are suggested to have formed by the assimilation of granitic material at shallower depths in the crust, into an olivine-bearing plagioclase suspension. Mantle-derived magmas are suggested by Longhi *et al.* (1999) to require a much greater degree of assimilation. The experiments on CMH_HAB in this study show that contamination at high pressure can indeed produce opx-bearing anorthosites, and that the liquid evolution curve does pass through HLCA and the field of proposed parental magmas. Crustal contamination of the magma at shallower levels or during ascent may occur, but the fact that the anorthosites are likely to have intruded as crystal-rich mushes suggests that much of the contamination must have happened at depth, in order to crystallize opx-bearing mineral assemblages. The presence of high-alumina orthopyroxene megacrysts that formed at high pressure also suggests that the magmas must have been contaminated at high pressure to place orthopyroxene on the liquidus. In the KAC, some whole-rock anorthosites have been shown to have similar ε_{Nd} to their constituent plagioclase and pyroxene mineral separates, implying contamination prior to crystallization of these minerals. Other anorthosite samples show differences in ε_{Nd} between whole-rocks and mineral separates, suggesting that in some cases, subsequent contamination took place after the crystallization of earlier formed plagioclase and pyroxene (Gleiβner *et al.*, 2011). Similar features are seen in the oxygen isotopic signatures of anorthosites (Gleiβner *et al.*, 2010).

The experiments on HLCA show evolution of mantle-derived liquids away from quartz and anorthosite parental magmas, which was interpreted by Longhi *et al.* (1999) to indicate that the parental magmas cannot be mantle-derived. It is worth noting that the 11.5 kbar phase boundaries for HLCA (Longhi *et al.,* 1999) were constructed based on only four experimental liquid compositions (shown as the grey circles on Fig. 3.12A). In addition, these experiments were done over a fairly narrow temperature range (1175 ºC – 1270 ºC; 33 % – 76 % melt), as seen in their close proximity to each other on the diagram. The phase diagram produced in this work for CMH_HAB was constructed from the liquid compositions of eight experiments over a larger range of temperatures (1120 ºC – 1330 ºC) and degrees of fractionation (~9 % to 96 % melt). The results of the CMH_HAB experiments clearly show a liquid evolution trend towards more quartz-rich compositions, and show that mantle-derived magmas can indeed produce anorthosite parental magmas. In another study, calculations on the crystallization paths of primitive basaltic compositions (Longhi, 2005), suggested that the primitive compositions would not reach plagioclase saturation at high enough Mg# (50 - 60) to match the array of proposed parental magma compositions. CMH_HAB, however, would have already fractionated ~17% plagioclase by the time the liquid reached an Mg# of 51. In addition, minor quartz has been observed in the interstices of leuconorites in many anorthosite complexes (Ranson, 1981; Wiebe, 1978), as well as in myrmekitic intergrowths with calcic plagioclase (Dymek and Schiffries, 1987). Quartz has also been documented in intergrowths with K-feldspar, interpreted by Demaiffe and Hertogen (1981) to be trapped residual liquid, and in graphic intergrowths in late-stage pegmatitic pods in some complexes. High Fe, Ti and P, as well as extreme LREE enrichment in these pods suggest that they are the highly fractionated and crystallized from residual liquids in the anorthosite system (Bybee *et al.,* 2015). These features suggest that the residual liquids were quartz-, and not nepheline-saturated. The discrepancies between the two sets of experiments highlight the compositional sensitivity of phase equilibria. The experiments on HLCA and their interpretation by Longhi *et al*. (1999) cannot be disregarded in debates on the source of Proterozoic anorthosites, and it is likely that lower Mg# HAB compositions may fractionate towards Si-poor compositions. However, the conclusion that anorthosites *cannot* be mantle-derived, because of the thermal divide, has been shown by the experiments on CMH_HAB (this study) to be erroneous. It is clear that some compositions have a thermal divide while others do not, and that the presence or absence of the divide is crucial in understanding anorthosite petrogenesis. An investigation into the factors controlling whether or not a magma composition exhibits a thermal divide would be interesting and most likely fruitful in understanding the behavior of high-alumina basalts and anorthosite petrogenesis.

3.6 PETROGENESIS OF PROTEROZOIC ANORTHOSITES

The results of the experiments in this study, combined with field observations and geochemistry of olivine-bearing and orthopyroxene-bearing anorthosites in the KAC and other anorthosite occurrences from around the world, allow for further refinement of existing models of Proterozoic anorthosite petrogenesis. The close match between mineral assemblages and phase compositions between experiments on CMH_HAB and CMH+KAC, and natural leucotroctolites and leuconorites, supports the hypothesis that lower crustal contamination of a high-alumina basaltic parental magma can produce the range of mineral assemblages observed in anorthosite complexes. While the experiments do not directly assess the isotopic compositions, it may be inferred that crustal contamination is likely to explain the isotopic variability in anorthosites as well. A petrogenetic model consistent with the observations and measurements reported in this study, is presented below.

Partial melting of a depleted upper-mantle source generates basaltic melts that rise towards the base of the crust, possibly fractionating mafic phases (olivine ± orthopyroxene ± clinopyroxene) during ascent. Extraction of mafic phases would enrich the magma in Al_2O_3, and lower the Mg#, forming an evolved, high-alumina basaltic composition. The early-forming mafic phases may remain as mafic cumulates in the lower crust, or sink back into the mantle (Ashwal, 1993), but the occurrence of rare megacrysts of clinopyroxene suggest that even some of these very early phases may eventually be emplaced in the middle crust with the anorthosites (Owens and Dymek, 1995; Philpotts, 1966). Ponding of the high-alumina basaltic magma at the Moho would initiate partial melting of the surrounding lower crust, producing the coeval granitoid suite associated with the anorthosites. A portion of the granitoid magma would likely be assimilated into the ponding HAB, enriching the magma in SiO_2, and increasing the ratio of Na_2O to CaO. The process of assimilation of crustal melts would also decrease the Nd and Pb isotopic compositions of the magma, and increase the I_{Sr}, $\delta^{18}O$, and trace element concentrations. The silica-enriched basaltic magma would have orthopyroxene on its liquidus, and start to crystallize HAOMs. The absence of Eu anomalies in the most primitive HAOMs is evidence for the sole fractionation of opx before plagioclase saturation is reached. Plagioclase starts to crystallize, and rises to the top of the chamber, due to it being less dense than the liquid at lower crustal depths (Ashwal, 1993; Kushiro, 1980; Kushiro and Fujii, 1977; Morse, 1968; Scoates, 2000). Accumulations of plagioclase at Moho depths would be less dense than the surrounding country rocks, and would thus start to rise diapirically as crystal-liquid mixtures, entraining some of the HAOMs (Ashwal, 1993; Longhi and Ashwal, 1985). Plagioclase and interstitial opx ± cpx ± pgt would continue to crystallize during ascent of crystal mushes, and the high-alumina opx megacrysts that formed at high pressures would exsolve plagioclase upon cooling at lower pressures. The increased plagioclase stability field at lower pressures may maintain the crystallization of large proportions of plagioclase during ascent of the mushes. Upon reaching the emplacement level in the shallow crust, the mushes would solidify as leuconorites or orthopyroxene-bearing anorthosites, possibly crystallizing minor amounts of quartz in the interstices between plagioclase and pyroxenes.

Because earlier-formed magmas partially melted the surrounding lower crustal country rocks, preconditioning the country rocks and rendering them more refractory, subsequent pulses of primitive, mantle-derived magma ponding at the Moho would experience no or very little assimilation. The new HAB magma would crystallize olivine as the liquidus phase, and would reach plagioclase saturation after a small amount of cumulus olivine had formed. Olivine and plagioclase would crystallize simultaneously, before the positive buoyancy was achieved by sufficient plagioclase formation. The olivine-plagioclase mush could then rise through the crust, along the same pre-existing pathways formed from the previous leuconoritic mushes, or through new conduits. Interstitial mafic phases would form with decreasing temperature during ascent, and leucotroctolites would be emplaced in and around the slightly older leuconorites. These processes are likely to have produced Proterozoic massif-type anorthosite complexes, composed of several coalesced plutons with variable mineral assemblages and isotopic compositions. The rising mushes may have experienced additional minor contamination by mid-crustal country rocks during ascent. The granitoids formed by partial melting of the lower crust during ponding of the parental magmas would be emplaced during and after the intrusion of the anorthosites, and their emplacement may even facilitate the rise of the anorthositic diapirs (Ashwal, 1993; Longhi and Ashwal, 1985).

4 Modeling Anorthosite Petrogenesis in MELTS

4.1 INTRODUCTION

There are many contrasting hypotheses on anorthosite petrogenesis, and testing some of these is slowly helping to build a complete story of the generation of anorthosites in the Proterozoic Eon. Given the number of unanswered questions in anorthosite petrogenesis, finding innovative ways to constrain the processes that may lead to the formation of these intrusions is imperative to our understanding of the Proterozoic Earth. One of the crucial questions is the composition of the anorthosite parental magma, and whether this magma originated from partial melting of the mantle or the crust. While experiments provide a well-controlled method to test this and some other aspects of anorthosite petrogenesis, testing every possible combination of magma composition and conditions is unrealistic. One way of testing these variables is using thermodynamic and phase equilibria models. While such models have limitations, they can be a useful way to test how changing the magma composition and intensive variables (such as temperature, pressure, water content, and oxygen fugacity) affects the results.

The synthetic starting compositions (CMH_HAB and CMH+KAC) used in both the baseline and contamination experiments in this work (Chapter 3) were modeled using the MELTS algorithm (Asimow and Ghiorso, 1998; Ghiorso *et al.*, 2002; Smith and Asimow, 2005). Isobaric calculations over a range of temperatures from superliquidus (1300 ºC) to subsolidus (900 ºC) were performed in alphaMELTS (Smith and Asimow, 2005) in an attempt to determine the extent to which the experimental results could be corroborated. Phase proportions and compositions were calculated for every 25°C of temperature decrease. The aim was to assess how well the MELTS models could replicate the experimental results, and calibrate the model for these types of compositions, so that the MELTS models may be used to test the effects of varying certain parameters on the evolution of the system. If MELTS can accurately predict the liquid evolution and phase compositions for HAB liquids, the effects of small variations in the parental magma composition, with variable amounts of added contaminants, as well as the effects of pressure, water content, and oxygen fugacity, may be tested and applied to problem of anorthosite genesis.

4.2 MODELING AT 10 KBAR

The modeling performed in MELTS at 10 kbar for the experimental starting compositions closely reproduces the liquid evolution trends of the experiments discussed in Chapter 3. The order, proportions and compositions of crystallizing phases differ from the experiments, but the liquid trends plot close to the experimental liquids on ternary diagrams, and the temperature range for the crystallization of phases is very similar to the experimental temperatures calculated by the Fe-Mg thermometer.

4.2.1 Baseline experiments

The MELTS modeling for the baseline, uncontaminated high-alumina basalt starting composition was done using the average microprobe composition for the glass, CMH_HAB, produced in 100% melting experiments. The models do produce the correct mineral phases, but not in the same order or proportions as in the experiments, and some additional phases are also produced. The experiments have olivine on the liquidus, followed by plagioclase, clinopyroxene, pigeonite, and ilmenite with decreasing temperature. The melts models at 10 kbar and at an oxygen fugacity at the Quartz-Fayalite-Magnetite (QFM) buffer have clinopyroxene as the liquidus phase, followed at lower temperature by garnet, and only thereafter by olivine and plagioclase, as well as pigeonite. The main discrepancies are the occurrence of garnet in the MELTS results, and the order of appearance of the main phases. The liquid evolution path has a similar general trend to the observed experimental liquid compositions, but the trend does not match exactly, due to the order of phases differing from the experiments. Running the model at higher fO_2 (Hematite-Magnetite, HM) still yields clinopyroxene at the liquidus, but yields plagioclase as the second crystallizing phase, followed by olivine and also by a substantial amount of orthopyroxene (enstatite). The HM model does not produce any garnet, and the liquid evolution curve matches the more evolved experimental liquids slightly better than for the QFM model. A summary of the compositions of phases and liquids produced in the experiments and in the MELTS models at QFM and HM is shown in Figure 4.1.

The proportions of each phase in the lowest temperature experiment are displayed in Table 4.1 below, along with the phase proportions in the MELTS models at fO_2 of QFM and HM at the nearest temperature, for comparison. A low temperature experiment is used to compare phase proportions, since all the phases are present in significant amounts. The MELTS values have been normalized, since minor amounts of spinel and/or whitlockite appear and disappear at certain stages of crystallization. It is clear that the proportions of olivine and plagioclase are severely underestimated in the MELTS models, while pyroxene abundances are overestimated. It is also evident that the solidus temperature is higher in the QFM model than in the experiments, since a much smaller fraction of melt remains at a similar temperature, while the HM MELTS model has a solidus temperature lower than the experiments. Since the experiments were run at 10 kbar, they just fall into the pressure range where pMELTS (Ghiorso *et al.,* 2002) may be applicable. This algorithm is a high-pressure mode for MELTS calibrated mainly to yield more accurate results for peridotitic compositions from 10 to 30 kbar. Models were tested using both MELTS and pMELTS, but little to no difference in mineral proportions or compositions was observed.

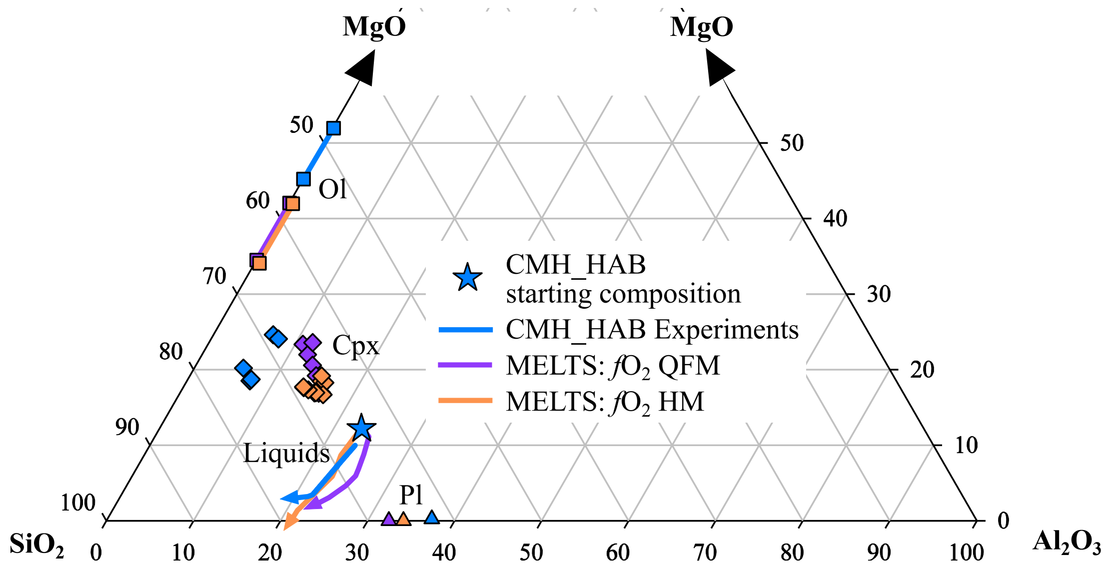

Figure 4.1 Liquid and phase compositions in CMH_HAB experiments and MELTS models at fO_2 QFM and HM. Average plagioclase compositions were used because the compositions in each group are similar and cluster very close together. The range of olivine compositions for each group is shown, with the two most extreme end members connected by a line. Note that the olivine compositions in the QFM and HM MELTS models plot in almost exactly the same position. Clinopyroxene compositions show more variation, and so all points are plotted. Liquid trends are shown as arrows pointing in the direction of decreasing temperature.

Table 4.1 Normalized phase proportions in the lowest temperature CMH_HAB experiment compared to MELTS models at fO_2 of QFM and HM at the closest corresponding temperature. Numbers in parentheses indicate the order of the phases in the crystallization sequence.

	T (°C)	Melt %	Ol %	Pl %	Grt %	Cpx %	Pgt %	Opx %
Experiments	1128	13.84	21.63 (1)	50.46 (2)	-	12.11 (3)	2.90 (4)	-
MELTS QFM	1125	1.89	0.38 (3)	33.98 (3)	17.93 (2)	18.56 (1)	27.26 (3)	-
MELTS HM	1125	24.15	0.17 (3)	27.66 (2)	-	30.29 (1)	-	17.73 (3)

In terms of mineral compositions, the plagioclase produced in the experiments is better matched by that predicted by the HM model, while the compositions of all the mafic phases in the experiments are more closely matched by those in the QFM model. The plagioclase in both MELTS models has a lower An content (QFM = An_{47-49}, HM = An_{58-68}) than the experimentally-produced plagioclase (An_{63-68}), but the major element compositions of the HM plagioclase are closer to the experimental plagioclase. This is due to plagioclase being the second phase to crystallize in the HM model (after cpx), the same as in the experiments (after olivine), while in the QFM model, plagioclase is one of the last phases to crystallize. Generally, the MELTS models produce mafic phases that are higher in Ca and Al than in the experiments. This is likely due to the underestimation of the proportion of plagioclase in the models. The clinopyroxene produced by the MELTS models has a higher Mg# than the experimental cpx, since the MELTS models have cpx as the first liquidus phase. The olivine in the models is extremely enriched in Mn relative to the experimental olivine, and has a lower Mg#, due to the later occurrence of olivine in the models, as opposed to it being the first liquidus phase in the experiments.

The liquid lines of descent (LLD) produced by the MELTS models generally match the experimental liquid evolution trends well. Due to the differences in the order of appearance of phases in the MELTS models and the CMH_HAB experiments, there are some minor differences in the LLDs on the pl-ol-qtz pseudoternary diagram (Fig. 4.2). Note that a simpler projection scheme has been used for the ternary diagrams in this Chapter, projecting from the wollastonite component in terms of oxygen units (Grove, 1993), as opposed to projecting from wollastonite and ilmenite as in the scheme of Longhi (1991). The MELTS models do not produce ilmenite or other oxides as a crystallizing phase, so the projection scheme of Grove (1993) is more appropriate, and generates simpler phase diagrams. The diagram shows that neither the QFM nor the HM liquids evolve close enough to the plagioclase apex of the diagram before starting to crystalize plagioclase. The experiments fractionate olivine alone before reaching Pl saturation, causing the LLD to evolve away from olivine and toward the Pl field before curving towards the qtz side of the diagram, whereas the MELTS models only fractionate some clinopyroxene before plagioclase saturation. Once plagioclase joins the assemblage, the HM LLD matches the experimental liquids slightly better than the QFM LLD does. In spite of these discrepancies between the experimental and MELTS liquids, the MELTS models do produce a close estimation of the liquid evolution, and this highlights the effectiveness of the MELTS calculations in predicting the liquid evolution trends for this type of composition.

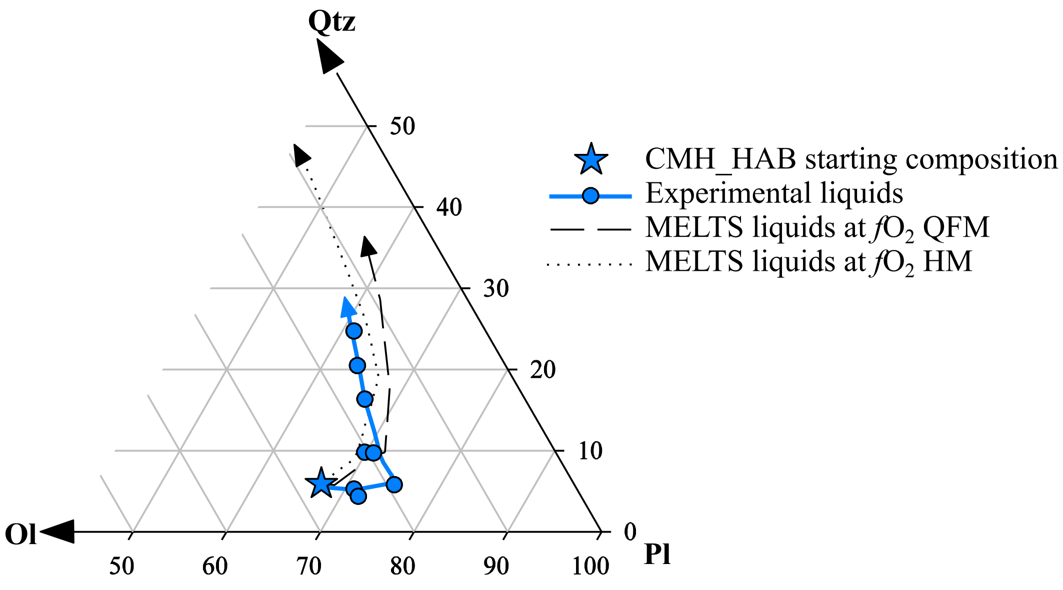

Figure 4.2 CMH_HAB experimental liquids, and liquids produced in MELTS at 10 kbar, projected from wollastonite onto the pl-qtz-ol pseudoternary as per the projection scheme of Grove (1993). Arrows point in the direction of decreasing temperature.

4.2.2 Contamination experiments

Modeling the contaminated composition CMH+KAC in MELTS yields similar results to the baseline runs, with a good match in liquid evolution, but some discrepancies in phase proportions and compositions. The liquid evolution trend matches the experimental liquids even closer than in the baseline models, but some important deviations are still apparent. The experiments produce orthopyroxene as the first liquidus phase, followed by plagioclase and pigeonite at lower temperatures. MELTS does give orthopyroxene as the first crystallizing phase in 10 kbar runs at fO_2 QFM, but it disappears again after one temperature interval (25°C) and is replaced by clinopyroxene. Pigeonite forms soon after, followed by plagioclase and then by a small amount of olivine. Pigeonite is exhausted at the time that orthopyroxene returns as a stable phase in the assemblage. The most obvious mismatch is the occurrence of a substantial amount of clinopyroxene in the MELTS models, while none is produced in the experiments. At higher fO_2 (HM), cpx is first on the liquidus, followed soon after by opx, which remains stable. Plagioclase joins the assemblage and is followed at lower temperature by a small fraction of olivine. While opx becomes stable earlier in the sequence in the HM models, the proportion of opx is not as great as at QFM. The proportions of phases in the lowest temperature contamination experiment and in the MELTS models at similar temperature are given in Table 4.2 below. The phase proportions were normalized to exclude minor amounts of spinel, garnet and whitlockite. As in the baseline models, the QFM solidus is at higher temperature and the HM solidus is at lower temperature than in the experiments.

While only ~14 % plagioclase has formed at the given temperature in the HM model, as much as 35% is present at lower temperatures in both models. Like in the baseline models, MELTS produces too much clinopyroxene relative to plagioclase. Over-stabilization of clinopyroxene in MELTS models compared to partial melting experiments was reported as one of the main problems in the improved high-pressure calibration of MELTS (Ghiorso *et al.*, 2002). The proportions of the other main phases, plagioclase and orthopyroxene, are fairly close to the proportions in the experiments.

Table 4.2 Normalized phase proportions in the lowest temperature CMH+KAC experiment, and MELTS models at fO_2 of QFM and HM at the closest corresponding temperature. Numbers in parentheses indicate the order of the phases in the crystallization sequence. Note that in the QFM model, opx crystallizes as the first liquidus phase, but it disappears after only one temperature interval, and only reappears at lower temperature. Pigeonite (pgt) crystallizes after pl in the QFM model, but is exhausted by the time opx becomes stable.

	T (°C)	Melt %	Opx %	Pl %	Pgt %	Cpx %	Ol %
Experiments	1078	43.10	18.67 (1)	29.72 (2)	8.04 (2)		
MELTS QFM	1075	30.04	21.20 (5)	30.90 (3)	(2)	17.72 (1)	<0.1 (4)
MELTS HM	1075	43.81	13.85 (2)	14.54 (3)		28.29 (1)	

The compositions of mineral phases in CMH+KAC experiments and MELTS models are plotted in Figure 4.3. The QFM and HM 10 kbar MELTS models produce plagioclase of very similar composition, and this composition is slightly different to that produced in the experiments. The MELTS plagioclase has a lower An content (QFM Plag = An_{31-45}; HM Plag = An_{33-48}) than experimental plag (An_{51-56}), as is the case in the baseline models on CMH_HAB. Neither model matches the experimental plagioclase composition better than the other. The orthopyroxene in the experiments is fairly well reproduced by the QFM MELTS model, but not by the HM model.

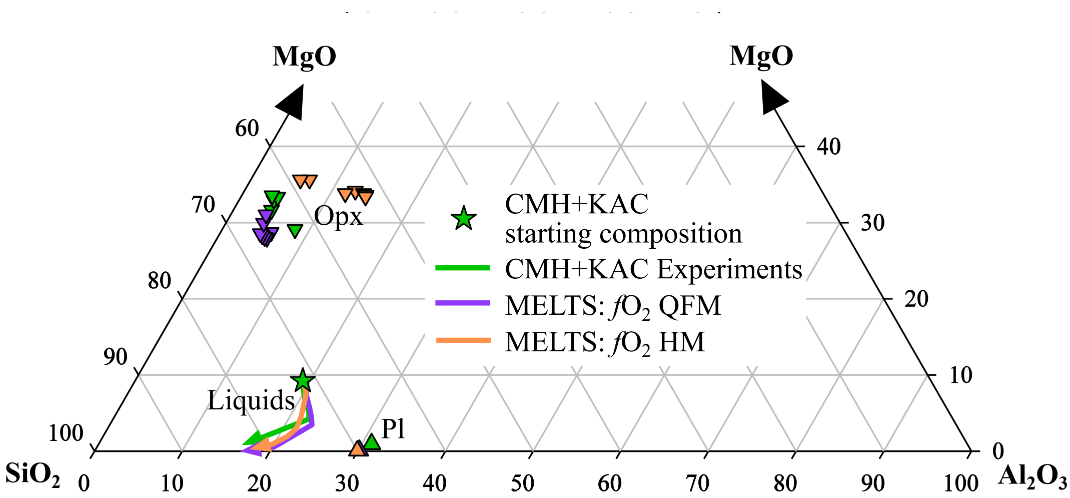

Figure 4.3 Liquid and phase compositions in contamination experiments on CMH+KAC, and MELTS models at fO_2 QFM and HM. Average plagioclase and orthopyroxene compositions have been used because the compositions in each group were similar and clustered very close together. Note that the plagioclase compositions for the QFM and HM models plot in the same place. Liquid trends are shown as arrows pointing in the direction of decreasing temperature.

Despite differences in crystallization order and phase proportions, the liquid line of descent for the QFM MELTS model at 10 kbar matches the experimental liquids very well (Fig. 4.4). The main discrepancy occurs at the apex of the liquid evolution trend line, where the liquid starts to evolve away from plagioclase and towards quartz. The experimental liquids fractionate further towards plagioclase before the liquid trend bends towards quartz. This difference is due to the higher proportion of opx fractionating in the experiments before plagioclase starts to crystallize, forcing the LLD further away from opx and towards plagioclase than the MELTS liquids. Despite these differences, the MELTS model at QFM and 10 kbar reproduces the LLD for the contaminated starting composition well.

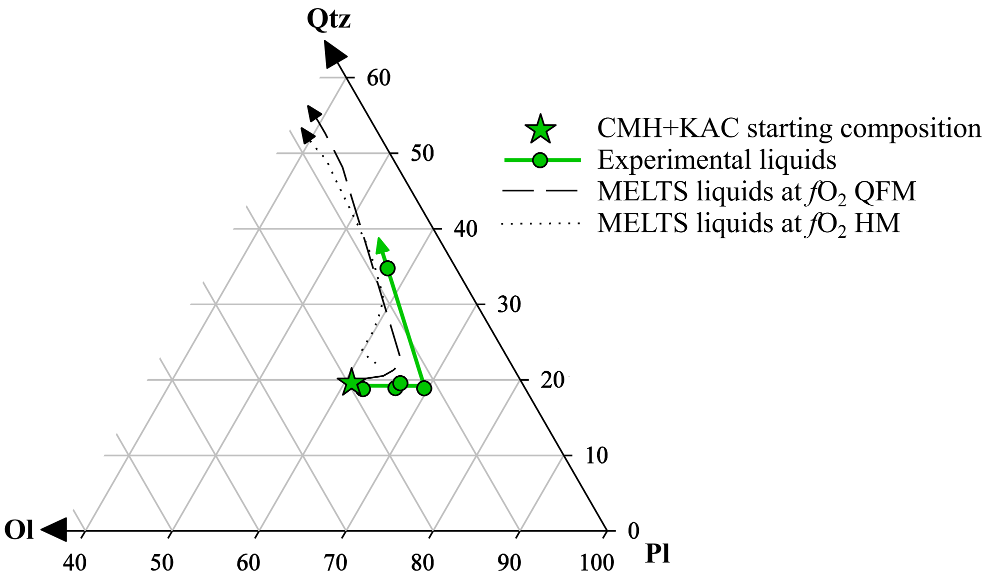

Figure 4.4 CMH+KAC experimental liquids, and liquids produced in MELTS at 10 kbar, projected from wollastonite onto the pl-qtz-ol pseudoternary, as per the projection scheme of Grove (1993). Arrows point in the direction of decreasing temperature.

4.3 USING MELTS TO TEST THE EFFECTS OF MELT COMPOSITION AND INTENSIVE VARIABLES

Despite not being able to accurately reproduce the relative proportions and compositions of experimental crystalline phases, MELTS models do predict the liquid evolution trends very well, and this is testament to the application of MELTS modeling to understanding the evolution of a range of magma compositions. While the modeling for the melt compositions in this study may not be used to accurately predict the order and proportions of crystallizing phases, the effects of certain variables on the evolution of the magma and the relative proportions of phases may be tested in the models.

4.3.1 Composition of the contaminant

Estimating the composition of partial melts of the lower crust is complicated by the poor constraints on the actual composition of the lower crust. This makes determination of a well-constrained contaminant composition for basaltic magmas ponding at the Moho, very difficult. Numerous experimental studies have focused on what the compositions of partial melts of the lower crust might be, in trying to address the formation of continental and arc crust. An extensive study involving partial melting experiments on natural amphibolites was conducted by Rapp and Watson (1995). The study assumed that the lower crust has a mafic composition, based on xenoliths and exposed cross-sections through the crust, and because underplating of basaltic magma is believed to be an important process in the growth of the crust. Since thickened mafic crust is thought to have the composition of amphibolite, garnet amphibolite, or eclogite, partial melting experiments on amphibolites and eclogites were performed at 8 – 32 kbar with 1 – 2 wt. % water. The results showed that all low degree partial melts of the amphibolites (1 – 40% melt) are in the compositional range of tonalite, trondjhemite, granodiorite, quartz-diorite and diorite (Rapp and Watson, 1995). None of the melts plot in the granite field, and none have K_2O as high as many of the typical granitoids in AMCG suites. Partial melting experiments on basaltic and andesitic greenstones and amphibolites were conducted over a range of pressures (up to ~ 7 kbar), and also produced low-K melts, plotting as granodiorites and trondjhemites (Beard and Lofgren, 1991). Higher-pressure melting experiments on basaltic amphibolites at 15 – 20 kbar did produce some high-K melts, but only for very low degrees of partial melting (<2%) and the Na:Ca ratio of the melts is higher than for typical anorthosite complex granitoids (Sen and Dunn, 1994).

Several of the partial melt compositions from experimental studies were tested in MELTS, and compared to the contamination experiments performed using the Red Granite KAC031/035, the composition CMH+KAC. Starting compositions were calculated by adding 30% of each contaminant to CMH_HAB, the same way the CMH+KAC composition was calculated for the experiments. The calculated compositions were run in MELTS. Despite the fact that most of the lower crustal partial melts in the amphibolite melting studies are K-poor tonalities and granodiorites, when added as contaminants to CMH_HAB, many produce liquid evolution paths very similar to that of CMH+KAC. Even with low K_2O, many of the melt compositions have high Na:Ca ratios, and most have high SiO_2 (>70 wt. %). The proportion of SiO_2 and the ratio of Na:Ca are the most important factors in contaminating a HAB magma to generate the anorthosite mineral assemblages, because the parental magma needs to become sufficiently Si-enriched to be shifted into the opx field from the olivine field. Higher Na_2O than CaO explains the production of more intermediate plagioclase in contaminated anorthosites. An important implication of these tests in MELTS is that, even if the lower crust is mafic rather than felsic, the partial melts are likely to be sufficiently SiO_2-rich to shift the mafic mineralogy from olivine to orthopyroxene in anorthosites, whether the melts are true potassic granites, or tonalities and granodiorites.

Based on isotope systematics and field relations in the Namibian portion of the Kunene Complex, it was suggested that the country rocks of the Epupa Complex, particularly the calc-silicates and metapelites, are a suitable contaminant for the parental magma of the anorthosites (Drüppel *et al.*, 2007; Gleiβner, 2011). It was suggested that between 10% and 30% assimilation of these rocks could account for the features of the orthopyroxene-bearing anorthosites in the Namibian KAC. Contamination calculations using several different rock compositions from the Epupa Complex were also performed and run in MELTS, again adding 30% of each contaminant to CMH_HAB. The results for contamination with a metavolcanic and a metagranite composition from the Epupa Complex gave similar liquid evolution trends to that of CMH+KAC, while a metagreywacke and calc-silicate did not. The metagreywacke and calc-silicate compositions did not have high enough SiO_2 to shift the contaminated magma into the opx field, and therefore these compositions do not appear to be suitable candidates for contamination of the parental HAB magma.

4.3.2 Amount of contamination

The amount of assimilation that is plausible for a basaltic magma ponding at the base of the crust is not easy to constrain, especially when the composition of the lower crust is unknown. In the Nain Complex, ≤20% assimilation of Archaean basement by the most primitive mafic composition documented for the complex has been shown to produce the full range of Nd isotopic compositions (Emslie *et al.*, 1994). In Laramie, bulk assimilation models indicate between 3% and 10% bulk assimilation of Archaean basement into the most primitive high-Al gabbro for producing the range of mineral assemblages in the anorthosites, and 10% mixing would account for the range of whole-rock Sr and Nd isotopic compositions (Frost *et al.*, 2010; Longhi *et al.*, 1999; Scoates and Frost, 1996). In the experiments on CMH_HAB and CMH+KAC, an amount of 30% of the granitoid contaminant was used, to ensure that the effects of contamination on the phase equilibria could be properly tested. A large volume of basaltic magma is likely to be able to partially melt and assimilate a substantial amount of surrounding country rock, especially if the lower crust is felsic. Nevertheless, 30% may seem like an unreasonably large amount of assimilation, so modeling with MELTS was used to assess the effects of variably contaminating the CMH_HAB starting composition with Si-rich material.

Figure 4.5 shows the liquid evolution (green line) of the experiments on CMH+KAC, the starting composition used in the contamination experiments. The same pseudoternary projection scheme is used as in Fig. 4.2 and Fig. 4.4 above. Also shown is the composition of CMH_HAB (uncontaminated), as well as the calculated hypothetical starting compositions of CMH_HAB mixed with 10% and 20% of the Red Granite composition. The liquid evolution trends produced by the MELTS models are shown as black dashed lines for each composition. It is clear that the liquid evolution predicted by the MELTS modeling for the CMH+KAC (30% contamination) composition very closely matches the observed experimental liquid trend. The close match between MELTS and the experimental liquids means the MELTS model can be used to predict the liquid evolution trends for the 10% and

20% contaminated starting compositions with some degree of confidence. The liquid evolution curves generated by MELTS for 10% and 20% contamination differ very little from those of the 30% contaminated composition. In addition, 10% and 20% contamination both produce orthopyroxene and no olivine in the MELTS models. The modeling suggests that even as little as 10% assimilation of a granitic composition will position the parental magma in the opx field rather than the olivine field, and thus produce opx-bearing anorthosites.

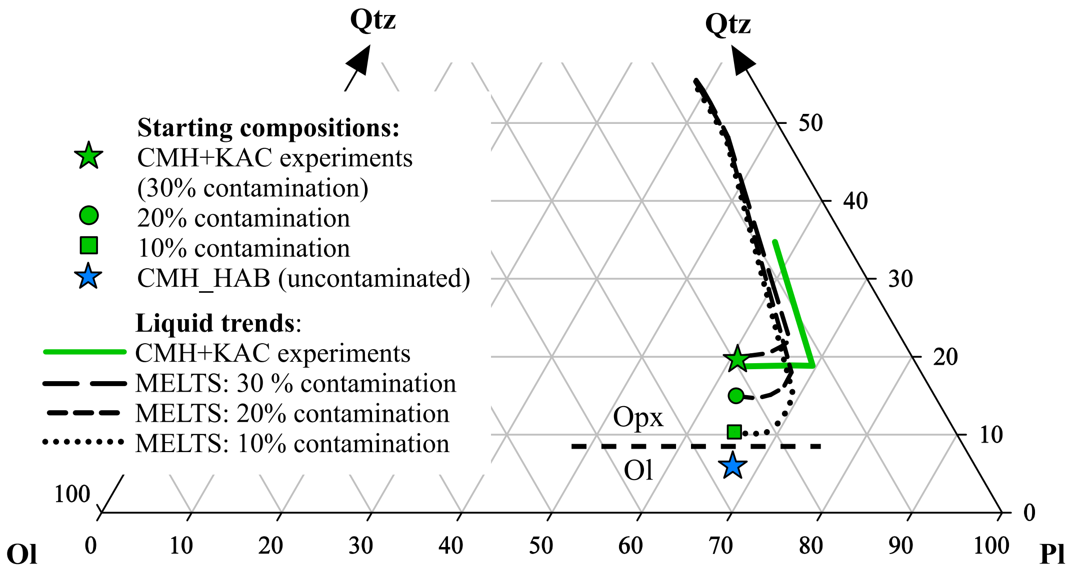

Figure 4.5 Calculated starting compositions of CMH_HAB combined with 10%, 20% and 30% of the Red Granite contaminant, along with the liquid evolution curves for each composition predicted by MELTS. Solid green line shows the actual liquid trend observed in experiments on CMH+KAC (30% contamination), and is more angular than in the phase diagrams of Chapter 3 due to a simpler projection scheme used here (projected from wollastonite by the projection scheme of Grove, 1993). The starting composition CMH_HAB (uncontaminated) is also shown for reference.

4.3.3 Effects of pressure

The MELTS models for CMH_HAB were run at lower pressures (5 kbar and 1 kbar) than the 10 kbar at which the experiments were conducted, to test the effects on the liquid evolution and phase assemblages. The main effect of decreased pressure is the increased stability of olivine and plagioclase. The liquidus temperature at 5 kbar is slightly lower than the 10 kbar models, at 1250°C as opposed to 1275°C. At 5 kbar, olivine is the first liquidus phase, and reaches a maximum proportion of about 7% at slightly lower temperatures. At the same temperature, only about 14% cpx is present, but this increases to more than 40% in the lower temperature calculations, again highlighting the overstability of cpx. When no melt remains, almost 50% plagioclase has crystallized. At 1 kbar, the liquidus is even lower, at 1225°C. Olivine is again the liquidus phase, and reaches about 17% in the more evolved stages of crystallization. The proportion of cpx is slightly lower than at 5 kbar, but is still overestimated at about 35%. About 57% plagioclase has crystallized by the time no liquid remains.

Another important pressure effect is the increased An content of plagioclase at lower pressures. At 10 kbar, the plagioclase ranges from An_{46} to An_{49}. In the 5 kbar models, the values increase slightly to An_{59-63}, and at 1 kbar it is even more calcic at An_{61-67}. In the 10 kbar MELTS models, the maximum proportion of plagioclase that forms at the lowest temperatures is between about 33% and 45%, depending on the oxygen fugacity (more plagioclase forms at higher fO_2). The 5 kbar and 1 kbar models crystallize ~50% and ~57% plagioclase, respectively. The increased proportion and An content of plagioclase at lower pressures is an important factor in anorthosite petrogenesis, and has been documented in experimental studies (Fram and Longhi, 1992; Green, 1969). Since Proterozoic massif-type anorthosites are thought to have begun crystallizing at depth, and are then thought to continue to crystallize polybarically during ascent into the shallow crust, it is likely that the range in plagioclase compositions observed in some complexes is a result of crystallization over a range of pressures. The increased proportions of plagioclase that form at lower pressure in the models is due to the increased plagioclase stability field at lower pressures, and is likely to play a role in the production of vast amounts of plagioclase relative to other minerals in the anorthosites. The MELTS models produce a maximum of 45% plagioclase at 10 kbar, and the 10 kbar experiments on CMH_HAB yield a maximum of ~50% plagioclase. Since Proterozoic anorthosites typically contain >75% plagioclase, and may even be composed almost entirely of plagioclase with <5% mafic minerals, this implies that another 25% to 50% plagioclase needs to form at lower pressures during ascent, to be emplaced as plagioclase-dominated rocks. Given the increased stability of plagioclase at progressively lower pressure, this is not an unrealistic condition. Alternatively, the plagioclase-enriched composition of the anorthosites may simply be the result of accumulation of plagioclase crystals. The increasingly calcic composition of the plagioclase at lower pressure is also important in Archaean anorthosites, since these contain much more calcic plagioclase than Proterozoic anorthosites.

It is interesting to note that the phase proportions produced in the 1 kbar MELTS model are very close to the experimental phase proportions of CMH_HAB. This is mainly due to the occurrence of olivine on the liquidus, as well as the significantly increased proportion of olivine, which is severely underestimated in the 10 kbar models. After olivine, the model produces plagioclase and then pigeonite at lower temperatures. In addition, the compositions of the phases at 1 kbar match the experimental compositions well. Plagioclase ranges from An_{61-67} in the MELTS plagioclase and from An_{63-68} in the CMH_HAB experiments, and most major elements show good agreement as well. Similar results are observed for olivine compositions, with the 1 kbar modeled olivine almost perfectly overlapping with experimental olivine in most major element compositions. Despite the very close match in phase proportions between the 1 kbar model and the experiments, the temperatures at which the similar phase proportions occur differ by more than 100°C, and the liquid evolution trends do not show a good match.

4.3.4 Effects of water

The effect of small amounts of water in the melts that produce anorthosites is a topic worth addressing, particularly in comparing Proterozoic massif-type anorthosites to Archaean megacrystic anorthosites. Proterozoic anorthosites are believed to have formed from anhydrous magmas, given the general lack of primary hydrous phases in the rocks (Ashwal, 1993; Longhi *et al*., 1999; Morse, 1982), and the typically anhydrous mineral assemblages in contact metamorphic aureoles (Berg, 1977). Archaean anorthosites are characterized by large equant plagioclase megacrysts in a mafic groundmass. The plagioclase has a high An content (usually >80%; Ashwal, 1993), which has been suggested to result from high water content in the mafic parental magmas, combined with lower pressure crystallization. This is supported by the presence of highly calcic plagioclase in hydrous experiments on high-Al basalts (Baker and Eggler, 1987; Sisson and Grove, 1993).

The effects of adding a small amount of water to the CMH_HAB composition are dependent on pressure. The MELTS models were run with the addition of 2 wt. % water to the starting composition at pressures of 10 kbar, 5 kbar, and 1 kbar. At 10 kbar, the addition of water completely destabilizes plagioclase. Olivine, garnet, cpx and opx make up the crystallizing assemblage, while no plagioclase is produced. At 5 kbar with 2 wt. % water, plagioclase does crystallize, but only at a late stage after olivine, garnet and cpx. The composition is more albitic (An_{34-49}) than the anhydrous plagioclase at 5 kbar (An_{59-63}). Hornblende and biotite start to form later in the sequence. At 1 kbar, the composition with 2 wt. % water produces slightly less plagioclase (~52% as opposed to 57% in the anhydrous model), but the composition is more calcic (An_{61-73}). A small amount of late-stage biotite is produced, but no amphibole. The modeling suggests that at higher pressure, the effect of water is to decrease the An content of plagioclase, until the pressure is high enough that plagioclase is unstable in the hydrous magma. At lower pressures, the presence of water increases the An content, but produces a smaller volume of plagioclase. The MELTS models testing the effects of water are in agreement with hydrous experiments on basaltic compositions (Sisson and Grove, 1993; Yoder, 1986). The MELTS results are summarized in Table 4.3. If these effects are an accurate representation of how natural systems of this composition behave, they have some important implications for the formation of both Archaean and Proterozoic anorthosites. The effects of water in the MELTS models suggest that Archaean anorthosites are likely to have formed at low pressures from magmas with a hydrous component. The destabilization of plagioclase at high pressures with the addition of such a small proportion of water suggests that, if Proterozoic anorthosites start to form at depth (indicated by HAOMs), there was no water present in the parental magma. An alternative worth considering is whether a liquid with a small fraction of water could fractionate the mafic phases indicated in the MELTS model at 10 kbar, with plagioclase crystallization suppressed. As the liquid begins to ascend to shallower levels in the crust and reach levels where plagioclase is stable in liquids containing water, the evolved liquid may have become extremely enriched in plagioclase components, and thereby crystallize a large amount of plagioclase. However, without the accumulation of buoyant plagioclase at depth, it is uncertain whether the magma would be able to rise to a level where plagioclase would be stable. Further modeling and experiments might be able to better constrain the likelihood of such processes.

Table 4.3 Summary of the effects of water and pressure on the An content of the crystallizing plagioclase in MELTS models on CMH_HAB. Numbers in the table are molar An contents of crystallizing plagioclase.

	10 kbar	5 kbar	1 kbar
Anhydrous	46 - 49	59 - 63	61 - 67
2% water	No plag	34 - 49	61 - 73

It is worth mentioning that the 1 kbar MELTS model with 2 wt. % water also matches the CMH_HAB experimental phase compositions very well. However, again the LLD for the model does not match the experimental liquids, and the temperatures at which the phase proportions match are very different.

It is interesting that only a very small proportion of hydrous minerals are produced in both the 10 kbar and 1 kbar models with 2% water. Biotite (< 2%) starts to form very late in the sequence, and only once all the melt has been consumed, suggesting that it is forming as a sub-solidus reaction product and not a primary magmatic phase. The model was also run with 5% water and the results show barely any difference from the 2% water model, with the same phase assemblage and less than 2% biotite produced after melt was exhausted. If the MELTS model is accurate, it suggests that small fractions of water in high-alumina basaltic melts may not necessarily result in substantial formation of primary hydrous minerals, and that the anhydrous mineral assemblages in the rocks may not exclusively rule out hydrous parental magmas. Morse (1982) points out that traces of water in the parental magma would be expected to manifest themselves in the late stage differentiates of the anorthosites if the water was not being incorporated into hydrous minerals, and that this is not observed in any differentiates. However, minor amounts of biotite and/or amphibole have been documented in some anorthosites, including Harp Lake (Emslie, 1980), Nain (Wiebe, 1979) and Kunene (Drüppel *et al.*, 2007; Gleißner, 2011; this study). They occur associated with pyroxenes or Fe-Ti oxides, and appear to have formed from late-stage, evolved liquids (Emslie, 1980). Based on these observations and the results of the MELTS models, small amounts of water in the parental magmas of Proterozoic anorthosites should not be excluded.

4.4 SUMMARY OF MELTS MODELING

The evolution of the CMH_HAB and CMH+KAC starting compositions at 10 kbar may be successfully modeled in MELTS to some extent. The experimental liquid evolution paths of both starting compositions are very closely reproduced by MELTS, as are the temperature ranges over which crystallization occurs. The phase assemblages produced by the models are mostly similar to the experimental results, but the proportions of phases are not accurate. The main discrepancies are the underestimation of olivine, and overestimation of clinopyroxene, a problem that has been documented for many compositions used to calibrate MELTS (Ghiorso *et al.,* 2002). Oxygen fugacity can have a noticeable effect on the evolution of the liquids. In the baseline experiments, a higher fO_2 value (HM) in the modeling produces a closer match to the late-stage experimental liquids, but the overall trend is better matched by the model at QFM. Modeling the contamination experiments at fO_2 QFM also produces a better match overall. The similarity between the MELTS models and the experimental liquids reiterates the lack of a thermal divide for this composition, since the liquids in the MELTS models evolve towards silica enrichment, just as the experiments do.

The main effect of decreased pressure is the increased stability of olivine and plagioclase, and the more calcic character of plagioclase. The effects of small amounts of water are pressure-dependent, destabilizing plagioclase at higher pressures, but producing more calcic plagioclase at lower pressures. The effects of water and pressure on the plagioclase produced from a HAB account for the characteristics of Archaean anorthosites.

The main problems in accurately reproducing the crystalline products of the experiments are related to different partitioning of elements into phases in melts of different composition.

With the incorporation into the MELTS algorithm of the properties of systems such as high-alumina basalts and other compositions investigated experimentally, thermodynamic models may be able to reproduce the liquid lines of descent of a broader range of compositions even more accurately, and possibly be applied to predicting phase proportions and compositions. Calibration with as wide a variety of compositions as possible will result in more constraints for the models and continuously improved outputs, so that these complex chemical systems may be modeled more accurately.

5 A Summary of the Effects and Implications of Crustal Contamination on Proterozoic Anorthosites

Proterozoic massif-type anorthosites occur as massive intrusions of plagioclase-dominated rocks. Despite decades of study, these enigmatic complexes remain a topic of much controversy. Aspects of their petrogenesis such as the parental magma composition, the source of this magma, the tectonic setting of the intrusions, how they were emplaced, as well as why they are restricted to a specific period of Earth's history, are all outstanding problems (Ashwal, 1993; Bybee *et al.,* 2014; Duchesne, 1984; Longhi, 2005; Morse, 1982). The basaltic mineralogy of the anorthosites, as well as experimental studies based on the anorthosite system, suggest that high-alumina basalt is the most likely parental magma composition (Ashwal, 1993; Fram and Longhi, 1992; Longhi *et al.,* 1999). The rocks have a crustal component in their isotopic signature (high I_{Sr} and $\delta^{18}O$, negative ε_{Nd}; Ashwal *et al.*, 1986; Demaiffe *et al.,* 1986; Gleiβner *et al.,* 2011; Peck *et al.,* 2010) and some workers have suggested that the parental magmas were formed by partial melting of lower crustal material (Bédard, 2001; Duchesne *et al*, 1999; Longhi, 2005; Schiellerup *et al.,* 2000; Taylor *et al.,* 1984). However, evidence for crustal contamination in the anorthosite complexes is abundant, and suggests that the rocks may instead have formed from mantle-derived melts that experienced contamination by country rocks, producing the crustal isotopic signatures (Ashwal *et al.*, 1986; Bybee and Ashwal, 2015; Frost *et al.,* 2010; Peck and Valley, 2000). Whether anorthosites were ultimately derived from the mantle or the crust has been one of the most highly debated topics in anorthosite petrogenesis for many years.

One of the characteristic features of Proterozoic anorthosite complexes is the occurrence of olivine-bearing and orthopyroxene-bearing anorthosites, commonly in the same complex. This feature is suggested to be caused by variable amounts of crustal contamination in the parental magmas. While there is impressive chemical and petrologic evidence for crustal contamination having played an important role in the producing the characteristics of anorthosites (trend of increasing I_{Sr} with decreasing ε_{Nd}, deviation from mantle isotopic signature in the direction of surrounding country rocks, quartz in late stage differentiates; Bybee *et al.,* 2014; Mitchell *et al.,* 1995; Wiebe, 1978) this theory has not been experimentally tested. This study aims to assess the effects of crustal contamination on mantle-derived magmas, to test whether contamination of a high-alumina basaltic magma can shift the mineralogy of the anorthosites from olivine-bearing to orthopyroxene-bearing. Experiments on a synthetic high-alumina basalt (HAB) composition were conducted at 10 kbar (the pressure indicated by high-alumina orthopyroxene megacrysts entrained in anorthosites; Emslie, 1975) and at a range of temperatures. Additional experiments on a mixture of the HAB with a likely contaminant composition were conducted under the same conditions, to test the effects of contamination on the crystallizing assemblage. The results of the experiments are compared to natural Proterozoic massif-type anorthosites around the world, and specifically applied to the Kunene Anorthosite Complex in Angola, which clearly exhibits the olivine-orthopyroxene dichotomy.

The Kunene Anorthosite Complex in southern Angola and northern Namibia is one of the largest massif-type anorthosite complexes in the world, with an aerial extent of ~18 000 km^2. Variability in mineral assemblages, textures, and chemistry is apparent across the complex, suggesting that it consists of several coalesced plutons with unique petrogenetic histories. Many rocks in the KAC have both olivine and orthopyroxene (and clinopyroxene), but the proportions of these minerals are highly variable. Olivine-bearing anorthosites, or leucotroctolites, are the dominant rock type in the northern section of the complex, while orthopyroxene-bearing rocks or leuconorites/leucogabbronorites are more abundant in the south. This distribution correlates with variations in mineral chemistry. Anorthosites in the northern portion of the complex have more calcic plagioclase ($An_{>70}$) while rocks in the southern portion have more intermediate plagioclase (mostly $An_{<61}$). Olivine- and orthopyroxene-bearing anorthosites are roughly separated by a belt of K-rich granitoids that are slightly younger than the anorthosites, known as the Red Granites. Coeval granitoids such as these occur associated with nearly all Proterozoic anorthosite complexes, and are believed to have formed by partial melting of the lower crust during ponding of the anorthosite parental magma (Emslie *et al.*, 1994; Hegner *et al.*, 2010; Maji *et al.*, 2010; Mayer *et al.*, 2004; McLelland *et al.*, 2010). The Red Granites also outcrop around the margins of the complex, particularly in the southern section, around the orthopyroxene-bearing anorthosites. Rocks north of the Red Granite belt are younger (by between ~8 m.y. and ~60 m.y.) than the orthopyroxene-bearing rocks to the south. The field relations and geochemistry of the rocks of the KAC are consistent with a model whereby orthopyroxene-bearing rocks formed from a HAB parental magma that was contaminated by partial melts of the lower crust during ponding of the magma. Granitic assimilants would enrich the HAB magma in SiO_2, and increase the Na:Ca ratio, causing orthopyroxene to crystallize instead of olivine, and producing less calcic plagioclase. Subsequent magma pulses were not able to assimilate any/as much of the lower crustal materials, and were emplaced as olivine-bearing anorthosites shortly afterwards. The Red Granites intruded in and around the anorthosites as lower crustal partial melts.

In order to test the effects of crustal contamination on HAB parental magmas, piston cylinder experiments on a synthetic high-alumina basaltic composition (CMH_HAB) were conducted at 10 kbar. The experiments produced olivine as the liquidus phase, followed by plagioclase, and at lower temperatures by clinopyroxene, pigeonite and ilmenite. The plagioclase produced in the experiments has An_{63-68}. To test the effects of contamination, 30% of a composition of a Red Granite sample was added to the original HAB, and the experiments were run on this composition (CMH+KAC) under the same conditions. Contaminated experiments produced orthopyroxene as the liquidus phase, followed by plagioclase and then by pigeonite at lower temperatures. The plagioclase in these experiments is more intermediate, with An_{51-56}. The experiments show that contamination of a HAB with a granitic component can shift the anorthosite phase assemblage from olivine-bearing to orthopyroxene-bearing. The experiments also show that the residual liquids evolve to more silica-rich compositions with decreasing temperature. This result is different to the experimental results of Longhi et al. (1999), who conducted experiments at 11.5 kbar on a slightly more evolved HAB composition (HLCA, with Mg# = 52 as opposed to CMH_HAB with Mg# = 60), and found that the residual liquids evolved away from quartz and towards nepheline with decreasing temperature. Longhi *et al*. (1999) concluded that a thermal divide was present on the plagioclase-pyroxene cotectic, and that mantle-derived melts saturated with olivine could therefore not evolve towards the compositional field of the proposed anorthosite parental magmas, since they are in the direction of higher silica. Therefore, they suggested that anorthosites must be derived from the crust and not the mantle. In contrast, the experimental results of the present study show a clear trend from the composition of mantle-derived magmas towards higher silica contents and the field of anorthosite parental magmas. According to this study, anorthosite parental magmas can indeed be derived from partial melting of the mantle.

Modeling the experiments using the MELTS algorithm (Ghiorso *et al.,* 2002) produces liquid evolution trends that match the experimental liquids very well, and thus, MELTS may be tentatively used to test the effects of varying certain environmental (temperature, pressure, oxygen fugacity, water content, etc.) and compositional variables on the liquid evolution of HAB magmas. The models show that while 30% contamination was used in the experiments, as little as 10% contamination shifts the starting composition from the olivine stability field into the orthopyroxene field. The orthopyroxene-bearing anorthosites could therefore have been produced by less than 10% assimilation of granitic material into the HAB magma. In terms of the environmental conditions, the models show that decreased pressure produces a higher volume of plagioclase, which is more calcic than at higher pressure. The effects of small quantities of water are pressure-dependent. At high pressure, water destabilizes plagioclase and prevents crystallization. At low pressure however, a small amount of water produces more calcic plagioclase, but in a smaller quantity. The effects of pressure and water modeled in MELTS may have implications for the formation of Archaean anorthosites, which contain megacrysts of highly calcic plagioclase. The MELTS models suggest that the Archaean anorthosites may have been formed at low pressure (~1 kbar) with a small amount of water in the parental magma.

The experimental work and field observations presented in this study have important implications for understanding Proterozoic massif-type anorthosite petrogenesis. The occurrence of olivine-bearing and orthopyroxene-bearing rocks in anorthosite complexes can be explained by variable amounts of crustal contamination of a high-alumina basalt parental magma. This result supports the hypothesis that the observed isotopic shift in opx-bearing anorthosites around the world, away from the depleted mantle and towards a more crustal signature, likely reflects contamination of a mantle-derived magma by crustal components. The phase equilibria for the HAB composition used in the experiments reported here shows that mantle-derived melts evolve towards more silica-rich compositions, and can thus pass through the field of proposed anorthosite parental magmas around other experimentally-studied HAB compositions (such as HLCA). A major finding of this study is that no thermal divide is present for the compositions investigated, allowing for formation of anorthosites directly from mantle-derived melts. Future experimental work should investigate the range of HAB compositions between that used in this study (CMH_HAB) and that used in Longhi *et al*. (1999; HLCA), to determine the factors affecting the presence or absence of the pl-opx thermal divide. A detailed investigation into the extent of variability in rock types and mineral chemistry across the Kunene Complex should also be performed, along with thorough petrographic and chemical work on the megacrysts of orthopyroxene and clinopyroxene, since these high-pressure phases are likely to provide valuable clues into the early stages of formation of the KAC and other complexes. An isotopic investigation into the country rocks of the KAC would be useful to assess whether the orthopyroxene-bearing anorthosites are displaced from the depleted mantle signature in the direction of the country rock composition. With every petrographic, geochemical, experimental and modeling investigation into anorthosite complexes around the world, more constraints are being placed on critical aspects of their petrogenesis, and fundamental pieces are slowly being added to the puzzle of Proterozoic anorthosites.

6 References

Anderson, J. L. (1980). Mineral equilibria and crystallization conditions in the late Precambrian Wolf River rapakivi massif, Wisconsin. *American Journal of Science* **280,** 289–332.

Ashwal, L. D. (1982). Mineralogy of mafic and Fe-Ti oxide-rich differentiates of the Marcy anorthosite massif, Adirondacks, New York. *The American Mineralogist* **67**, 14–27.

Ashwal, L.D. (1993). *Anorthosites*. Springer-Verlag, Berlin. 422pp.

Ashwal, L. D. (2010). The temporality of anorthosites. *The Canadian Mineralogist* **48**, 711–728.

Ashwal, L. D. & Bybee, G. M. (2017). Crustal evolution and the temporality of anorthosites (submitted). *Earth Science Reviews*

Ashwal, L. D. & Seifert, K. E. (1980). Rare earth element geochemistry of anorthosite and related rocks from the Adirondacks, N.Y. and other massif-type complexes. *Geological Society of America Bulletin*. **91**, 105–107; 659–684.

Ashwal, L. D. & Twist, D. (1994). The Kunene Complex, Angola/Namibia: a composite massif-type anorthosite complex. *Geological Magazine* **131**, 579–591.

Ashwal, L. D., Wooden, J. L. & Emslie, R. F. (1986). Sr, Nd and Pb isotopes in Proterozoic intrusives astride the Grenville Front in Labrador: Implications for crustal contamination and basement mapping. *Geochimica et Cosmochimica Acta.* **50**, 2571–2585.

Asimow, P.D., and M.S. Ghiorso, Algorithmic modifications extending MELTS to calculate subsolidus phase relations, *American Mineralogist*, **83**, 1127-1132.

Baker, D. R. & Eggler, D. H. (1987). Compositions of anhydrous and hydrous melts coexisting with plagioclase, augite, and olivine or low-Ca pyroxene from 1 atm to 8 kbar: Application to the Aleutian volcanic center of Atka. *The American Mineralogist* **72**, 12–28.

Bartels, K. S., Kinzler, R. J. & Grove, T. L. (1991). High pressure phase relations of primitive high-alumina basalts from Medicine Lake volcano, northern California. *Contributions to Mineralogy and Petrology* **108**, 253–270.

Beard, J. S. & Lofgren, G. E. (1991). Dehydration Melting and Water-Saturated Melting of Basaltic and Andesitic Greenstones and Amphibolites at 1, 3, and 6. 9 kb. *Journal of Petrology* **32**, 365–401.

Beattie, P. (1993). Olivine-melt and orthopyroxene-melt equilibria. *Contributions to Mineralogy and Petrology* **115**,103-111.

Bédard, J. H. (2001). Parental magmas of the Nain Plutonic Suite anorthosites and mafic cumulates: a trace element modelling approach. *Contributions to Mineralogy and Petrology* **141**, 747–771.

Beetz, P.F.W. (1933). Geology of south-west Angola, between Cunene and Luanda axis: *Transactions of the Geological Society of South Africa* **36**, 137–176.

Berg, J. H. (1977). Dry granulite mineral assemblages in the contact aureoles of the Nain complex, Labrador. *Contributions to Mineralogy and Petrology* **64,** 33–52.

Berg, J. H. (1980). Snowflake troctolite in the Hettasch intrusion, Labrador: Evidence for magma-mixing and supercooling in a plutonic environment. *Contributions to Mineralogy and Petrology* **72**, 339–351.

Bohlen, S. R. & Essene, E. J. (1978). Igneous Pyroxenes From Metamorphosed Anorthosite Massifs*. *Contributions to Mineralogy and Petrology* **65**, 433–442.

Boyd, F. R. & England, J. L. (1960). Apparatus for phase equilibrium studies at pressures up to 50 kilobars and temperatures up to 1750 °C, Journal of Geophysical Research **65**, 741–748.

Brower, A.M., Corfu, F., Bybee, G.M., Lehmann, J., Owen-Smith, T., (2016). Understanding magmatic timescales and magma dynamics in Proterozoic anorthosites: a geochronological investigation of the Kunene Complex (Angola). *AGU Fall Meeting*, **V53D-3146** (12-16 December, San Francisco).

Brown, R. L., Chappell, J. G., Moore, J. M. & Thompson, P. H. (1975). An ensimatic island arc and ocean closure in the Grenville Province of southeastern Ontario, Canada. *Geoscience Canada* **2,** 141–144.

Buddington, A. F. (1939). Adirondack igneous rocks and their metamorphism. *Geological Society of America Memoirs* **7**, 343pp

Bybee, G. M. (2013) High pressure megacrysts and lower crustal contamination: Probing a mantle source for Proterozoic massif-type anorthosites. *PhD Thesis*, University of the Witwatersrand.

Bybee, G. M. & Ashwal, L. D. (2015). Isotopic disequilibrium and lower crustal contamination in slowly ascending magmas: Insights from Proterozoic anorthosites. *Geochimica et Cosmochimica Acta* **167**, 286–300.

Bybee, G. M., Ashwal, L. D., Gower, C. F. & Hamilton, M. A. (2015). Pegmatitic Pods in the Mealy Mountains Intrusive Suite, Canada: Clues to the Origin of the Olivine–Orthopyroxene Dichotomy in Proterozoic Anorthosites. *Journal of Petrology* **56**, 845–868.

Bybee, G. M., Ashwal, L. D., Shirey, S. B., Horan, M., Mock, T. & Andersen, T. B. (2014a). Pyroxene megacrysts in Proterozoic anorthosites: Implications for tectonic setting, magma source and magmatic processes at the Moho. *Earth and Planetary Science Letters*. Elsevier B.V. **389**, 74–85.

Bybee, G. M., Ashwal, L. D., Shirey, S. B., Horan, M., Mock, T. & Andersen, T. B. (2014b). Debating the petrogenesis of Proterozoic anorthosites - Reply to comments by Vander Auwera et al. on "Pyroxene megacrysts in Proterozoic anorthosites: Implications for tectonic setting, magma source and magmatic processes at the Moho". *Earth and Planetary Science Letters*. Elsevier B.V. **401**, 381–383

Carvalho, H. (1982). Geologia de Angola (Geological map of Angola) 1:1,000,000. Instituto Investigacão Cientifica Tropical (Centro Geologia), Lisbon.

Carvalho, H. de, & Alves, P. (1990). Gabbro-anorthosite complex of SW Angola/NW Namibia: Instituto de Investigacao Cientifica Tropical, *Serie Ciencias da Terra Communicacoes* **2**, Departmento Ciencias da Terra, Lisboa, 66 p.

Carvalho, H. de, Crasto, J., Silva, Z. C. & Vialette, Y. (1987). The Kibaran cycle in Angola: A discussion: *Journal of Geology*, **22**, 85–102.

Carvalho, H., Tassinari, C. C. G., Alves, P. H., Guimaraes, F. & Simoes, M. C. (2000). Geochronological review of the Precambrian in western Angola: links with Brazil. *Journal of African Earth Sciences* **31**, 383–402.

Charlier, B., Duchesne, J.-C., Vander Auwera, J., Storme, J. Y., Maquil, R. & Longhi, J. (2010). Polybaric Fractional Crystallization of High-alumina Basalt Parental Magmas in the Egersund-Ogna Massif-type Anorthosite (Rogaland, SW Norway) Constrained by Plagioclase and High-alumina Orthopyroxene Megacrysts. *Journal of Petrology* **51**, 2515–2546.

Christensen, N. I. & Mooney, W. D. (1995). Seismic velocity structure and composition of the continental crust: a global view. *Journal of Geophysical Research* **100**, 9761–9788.

Demaiffe, D., Bingen, B., Wertz, P. & Hertogen, J. (1990). Geochemistry of the Lyngdal hyperites (S.W. Norway)" comparison with the monzonorites associated with the Rogaland anorthosite complex. *Lithos* **24**, 237–250.

Demaiffe, D. & Hertogen, J. (1981). Rare earth element geochemistry and strontium isotopic evolution of a massif-type anorthositic-charnockitic body: the Hidra Massif (Rogaland, SW Norway). *Geochimica et Cosmochimica Acta* **45**, 1545–1561.

Demaiffe, D., Weis, D., Michot, J. & Duchesne, J.-C. (1986). Isotopic constraints on the genesis of the Rogaland anorthositic suite (southwest Norway). *Chemical Geology* **57**, 167–179.

DePaolo, D. J. & Wasserburg, G. J. (1976). Inferences about magma sources and mantle structure from variations of $^{143}Nd/^{144}Nd$. *Geophysical Research Letters* **3**, 743–746.

Dewey, J. F. & Burke, K. C. A. (1973). Tibetan, Variscan and Precambrian basement reactivation: products of continental collision. *Journal of Geology* **81**, 683–692.

Draper, D. S. & Johnston, A. D. (1992). Anhydrous PT phase relations of an Aleutian high-MgO basalt: an investigation of the role of olivine-liquid reaction in the generation of arc high-alumina basalts. *Contributions to Mineralogy and Petrology* **112**, 501–519.

Drüppel, K., Littmann, S. & Okrusch, M. (2000). Geo- und isotopenchemische Untersuchungen der Anorthosite des Kunene-Intrusiv-Komplexes (KIK) in NW-Namibia. Berichte der Deutschen Mineralogischen Gesellschaft, Beihefte zum European *Journal of Mineralogy* **12**, 37.

Drüppel, K., Littmann, S., Romer, R. L. & Okrusch, M. (2007). Petrology and isotope geochemistry of the Mesoproterozoic anorthosite and related rocks of the Kunene Intrusive Complex, NW Namibia. *Precambrian Research* **156**, 1–31.

Ducea, M. (2001). The California Arc: Thick granitic batholiths, eclogitic residues, lithospheric-scale thrusting, and magmatic flare-ups. *GSA Today* **11**, 4–10.

Duchesne, J-C. (1990). Origin and evolution of monzonorites related to anorthosites. *Schweizerische Mineralogischeund Petrographische Mitteilungen* **7**,189-198.

Duchesne, J-C. (1984). Massif anorthosite: Another partisan review. *Feldspars and Feldspathoids*, 411–433.

Duchesne, J-C. (1978). Quantitative modeling of Sr, Ca, Rb and K in the Bjerkrem-Sogndal layered lopolith (S.W. Norway). *Contributions to Mineralogy and Petrology* **66,** 175-184.

Duchesne, J-C. & Demaiffe, D. (1978). Trace elements and anorthosite genesis. *Earth and Planetary Science Letters* **38**, 249–272.

Duchesne, J-C., Liegeois, J. P., Vander Auwera, J. & Longhi, J. (1999). The crustal tongue melting model and the origin of massive anorthosites. *Terra Nova* **11**, 100–105.

Duchesne, J-C., Roelandts, I., Demaiffe, D., Hertogen, J., Gijbels, R. & De Winter, J. (1974). Rare-Earth data on monzonoritic rocks related to anorthosites and their bearing on the nature of the parental magma of the anorthositic series. *Earth and Planetary Science Letters* **24**, 325–335.

Duchesne, J-C., Roelandts, I., Demaiffe, D. & Weis, D. (1985). Petrogenesis of monzonoritic dykes in the Egersund-Ogna anorthosite (Rogaland, S.W. Norway): trace elements and isotopic (Sr, Pb) constraints. *Contributions to Mineralogy and Petrology* **90**, 214–225.

Duchesne, J-C., Wilmart, E., Demaiffe, D. & Hertogen, J. (1989). Monozonorites from Rogaland (southwest Norway): a series of rocks coeval but not comagmatic with massif-type anorthosites. *Precambrian Research* **45**, 111–128.

Dymek, R. F. & Gromet, L. P. (1984). Nature and origin of orthopyroxene megacrysts from the St-Urbain anorthosite massif, Quebec. *The Canadian Mineralogist* **22**, 297–326.

Dymek, R. F. & Schiffries, C. M. (1987). Calcic myrmekite: possible evidence for the involvement of water during the evolution of andesine anorthosite from St-Urbain, Quebec.

Emslie, R. F. (1985). Proterozoic anorthosite massifs. In: Tobi, A., Touret, J. L. R. (eds) The Deep Proterozoic Crust in the North Atlantic provinces. NATO ASI Ser C, 158. Reidel, Dordrecht, 39–60 pp.

Emslie, R. F. (1980). Geology and petrology of the Harp Lake Complex, central Labrador: An example of Elsonian magmatism. *Geological Survey of Canada Bulletin* **293**, 1–145.

Emslie, R. F. (1978). Anorthosite massifs, Rapakivi granites, and late Proterozoic rifting of North America. *Precambrian Research* **7**, 61–98.

Emslie, R. F. (1975). Pyroxene megacrysts from anorthositic rocks: new clues to the sources and evolution of the parent magmas. *The Canadian Mineralogist* **13**, 138–145.

Emslie, R. F. (1971). Liquidus relations and subsolidus reactions in some plagioclase-bearing systems. *Carnegie Institute Washington Yearbook* **69**, 148–152.

Emslie, R. F. (1970). The geology of the Michikamau intrusion, Labrador. *Geological Survey of Canada, Papers*. 68-57, 85 pp.

Emslie, R. F. (1965). The Michikamau anorthositic intrusion, Labrador. *Canadian Journal of Earth Sciences* **2**, 385–399.

Emslie, R. F., Hamilton, M. A. & Theriault, R. J. (1994). Petrogenesis of a Mid-Proterozoic Anorthosite-Mangerite-Charnockite-Granite (AMCG) Complex: Isotopic and Chemical Evidence from the Nain Plutonic Suite. *The Journal of Geology* **102**, 539–558.

Emslie, R. F. & Hunt, P. A. (1990). Ages and petrogenetic significance of igneous mangerite-charnockite suites associated with massif anorthosites, Grenville Province. *The Journal of Geology* **98**, 213–231.

Fram, M. S. & Longhi, J. (1992). Phase equilibria of dikes associated with Proterozoic anorthosite complexes. *The American Mineralogist* **77**, 605–616.

Frost, B. R., Frost, C. D., Lindsley, D. H., Chamberlain, K. R., Swapp, S. M. & Scoates, J. S. (2010). Geochemical and isotopic evolution of the anorthositic plutons of the Laramie Anorthosite Complex: Explanations for variations in silica activity and oxygen fugacity of massif anorthosites. *The Canadian Mineralogist* **48**, 925–946.

Ghiorso, M. S., Hirschmann, M. M., Reiners, P. W. & Kress, V. C., III (2002). The pMELTS: A revision of MELTS for improved calculation of phase relations and major element partitioning related to partial melting of the mantle to 3 GPa. *Geochemistry, Geophysics, Geosystems* **3**, 1–35.

Gleiβner, P. (2011). Petrogenesis of anorthosites of the Mesoproterozoic Kunene Intrusive Complex, NW Namibia: evidence from stable and radiogenic isotope and lithophile and highly siderophile trace element composition. *PhD Thesis,* Planen Bauen Umwelt der Technischen Universität Berlin.

Gleiβner, P., Drüppel, K. & Becker, H. (2012). Osmium isotopes and highly siderophile element fractionation in the massif-type anorthosites of the Mesoproterozoic Kunene Intrusive Complex, NW Namibia. *Chemical Geology*. Elsevier B.V. **302-303**, 33–47.

Gleiβner, P., Drüppel, K. & Romer, R. L. (2011). The role of crustal contamination in massif-type anorthosites, new evidence from Sr-Nd-Pb isotopic composition of the Kunene Intrusive Complex, NW Namibia. *Precambrian Research*. Elsevier B.V. **185**, 18–36.

Gleiβner, P., Drüppel, K. & Taubald, H. (2010). Magmatic Evolution of Anorthosites of the Kunene Intrusive Complex, NW Namibia: Evidence from Oxygen Isotope Data and Trace Element Zoning. *Journal of Petrology* **51**, 897–919.

Gower, C. F., Kamo, S. L., Kwok, K., Krogh, T. E. (2008). Proterozoic southward accretion and Grenvillian orogenesis in the interior Grenville Province in eastern Labrador: Evidence from U-Pb geochronological investigations. *Precambrian Research* **165**, 61-95.

Gray, C. M. (1987). Strontium isotopic constraints on the origin of Proterozoic anorthosites. *Precambrian Research* **37**, 173–189.

Green, T. H. (1969). High-pressure experimental studies on the origin of anorthosite. *Canadian Journal of Earth Sciences* **6**, 427–440.

Grove, T. L. (1993). Corrections to expressions for calculating mineral components in "Origin of Calc-Alkaline Series Lavas at Medicine Lake Volcano by Fractionation, Assimilation and Mixing" and "Experimental Petrology of normal MORB near the Kane Fracture Zone: 22~176 mid-Atlantic ridge." *Contributions to Mineralogy and Petrology* **114**, 422–424.

Hacker, B. R., Kelemen, P. B. & Behn, M. D. (2015). Continental Lower Crust. *Annual Review of Earth and Planetary Sciences* **43**, 167–205.

Hacker, B. R., Kelemen, P. B. & Behn, M. D. (2011). Differentiation of the continental crust by relamination. *Earth and Planetary Science Letters*. Elsevier B.V. **307**, 501–516.

Hargraves, R. B. (1962). Petrology of the Allard Lake Anorthosite Suite, Quebec. In: Petrologic studies: a volume to honor A.F. Buddington, *Geological Society of America*, Denver, 163–189.

Hegner, E., Emslie, R. F., Iaccheri, L. M. & Hamilton, M. A. (2010). Sources of the Mealy Mountains and Atikonak River anorthosite-granitoid complexes, Grenvile Province, Canada. *The Canadian Mineralogist* **48**, 787–808.

Hervé, F., Pankhurst, R. J., Fanning, C. M., Calderón, M. & Yaxley, G. M. (2007). The South Patagonian batholith: 150 my of granite magmatism on a plate margin. *Lithos* **97**, 373–394.

Higgins, M. D. & van Breemen, O. (1989). Age of the Lac-St-Jean anorthosite intrusion and associated mafic rocks. *Geological Association of Canada - Mineral Association of Canada Prog. Abstr*, **14**, A84.

Hoffman, P. F. (1989). Speculations on Laurentia's first gigayear (2.0 to 1.0 Ga). *Geology* **17**, 135–138.

Huang, Y., Chubakov, V., Mantovani, F., Rudnick, R. L. & McDonough, W. F. (2013). A reference Earth model for the heat-producing elements and associated geoneutrino flux. *Geochemistry, Geophysics, Geosystems* **14**, 2003–2029

Johnston, A. D. (1986). Anhydrous P-T phase relations of near-primary high-alumina basalt from the South Sandwich Islands. *Contributions to Mineralogy and Petrology* **92**, 368–382.

Köstlin, E. C. (1974). The Kunene basic complex, northern South West Africa. In: Kröner, A. (ed), Contributions to the Precambrian Geology of Southern Africa **15**, *University of Cape Town Bulletin,* Cape Town, 123–135.

Köstlin, E. C. (1967). The geology of part of the Kunene basic complex, Kaokovel; South West Africa. *M.Sc. Dissertation*, University of Cape Town.

Kushiro, I. (1980). Viscosity, density, and structure of silicate melts at high pressures, and their petrological applications. In: Hargraves, R. B. (ed). Physics of magmatic processes. Princeton University Press, Princeton, NJ, pp 93–120.

Kushiro, I. & Fujii, T. (1977). Floatation of plagioclase in magma at high pressures and its bearing on the origin of anorthosite. *Proceedings of the Japan Academy, Series B* **53**, 262–266.

Lindsley, D. H., Frost, B. R., Frost, C. D. & Scoates, J. S. (2010). Petrology, geochemistry, and structure of the Chugwater Anorthosite, Laramie Anorthosite Complex, Southeastern Wyoming. *The Canadian Mineralogist* **48**, 887–923.

Longhi, J. (2005). A mantle or mafic crustal source for Proterozoic anorthosites? *Lithos* **83**, 183–198.

Longhi, J. (1991). Comparative liquidus equilibria of hypersthene- normative basalts at low pressure. The *American Mineralogist* **76,** 785–800.

Longhi, J. & Ashwal, L. D. (1985). Two-stage models for lunar and terrestrial anorthosites: Petrogenesis without a magma ocean. *Journal of Geophysical Research* **90**, 571–584.

Longhi, J., Fram, M. S., Vander Auwera, J. & Montieth, J. N. (1993). Pressure effects, kinetics, and rheology of anorthositic and related magmas. *The American Mineralogist* **78**, 1016–1030.

Longhi, J., Vander Auwera, J., Fram, M. S. & Duchesne, J.-C. (1999). Some Phase Equilibrium Constraints on the Origin of Proterozoic (Massif) Anorthosites and Related Rocks. *Journal of Petrology* **40**, 339–362.

Maier, W. D., Rasmussen, B., Fletcher, I. R., Li, C., Barnes, S.-J. & Huhma, H. (2013). The Kunene Anorthosite Complex, Namibia, and Its Satellite Intrusions: Geochemistry, Geochronology, and Economic Potential*. *Economic Geology* **108**, 953–986.

Maji, A. K., Patra, A. & Ghosh, P. (2010). An overview on geochemistry of Proterozoic massif-type anorthosites and associated rocks. *Journal of Earth System Science*, 861–878.

Mayer, A., Hofmann, A. W., Sinigoi, S. & Morais, E. (2004). Mesoproterozoic Sm–Nd and U–Pb ages for the Kunene Anorthosite Complex of SW Angola. *Precambrian Research* **133**, 187–206.

Mayer, A., Sinigoi, S., Miguel, L. G., Morais, E. & Petrini, R. (2000). Kibaran ages in the Kunene anorthositic complex [abs.]: *GeoLuanda 2000, Luanda, Angola*, May 21–24, Abstract Volume, p. 106.

McCourt, S., Armstrong, R. A., Jelsma, H. & Mapeo, R. B. M. (2013). New U-Pb SHRIMP ages from the Lubango region, SW Angola: insights into the Palaeoproterozoic evolution of the Angolan Shield, southern Congo Craton, Africa. *Journal of the Geological Society* **170**, 353–363.

McLelland, J. M. (1986). Pre-Grenvillian history of the Adirondacks as an anorogenic, bimodal caldera complex of mid-Proterozoic age. *Geology* **14**, 229–233.

McLelland, J. M., Chiarenzelli, J., Whitney, P., & Isachsen, Y. (1988). U-Pb zircon geochronology of the Adirondack Mountains and implications for their geologic evolution. *Geology* **16**, 920–924

McLelland, J. M., Selleck, B. W., Hamilton, M. A. & Bickford, M. E. (2010). Late- to post-tectonic setting of some major Proterozoic anorthosite-mangerite-charnockite-granite (AMCG) suites. *The Canadian Mineralogist* **48**, 1–22.

Menge, G.F.W. (1998). The antiformal structure and general aspects of the Kunene Complex, Namibia: *Zeitschrift der Deutschen Geologischen Gesellschaft* **149**, 431–448.

Menuge, J. F. (1988). The petrogenesis of massif anorthosites: a Nd and Sr isotopic investigation of the Proterozoic of Rogaland[Vest-Agder, SW Norway. *Contributions to Mineralogy and Petrology* **98**, 363–373.

Mitchell, J. N., Scoates, J. S. & Frost, C. D. (1995). High-Al gabbros in the Laramie Anorthosite Complex, Wyoming: implications for the composition of melts parental to Proterozoic anorthosite. *Contributions to Mineralogy and Petrology* **119**, 166–180.

Morais, E., Sinigoi, S., Mayer, A., Mucana, A., Miguel, L. G. & Neto, J. (1998). The Kunene gabbro-anorthosite complex: preliminary results based on new field and chemical data: *Africa Geoscience Review* **5**, 485–498.

Morisset, C. E., Scoates J. S., Weis D., & Friedman, R. M. (2009). U-Pb and $^{40}Ar/^{39}Ar$ geochronology of the Saint-Urbain and Lac Allard (Havre-Saint- Pierre) anorthosites and their associated Fe-Ti oxide ores, Québec: Evi- dence for emplacement and slow cooling during the collisional Ottawan orogeny in the Grenville Province. *Precambrian Research* **174**, 95–116.

Morse, S. A. (2006). Labrador massif anorthosites: Chasing the liquids and their sources. *Lithos* **89**, 202–221.

Morse, S. A. (1991). Basaltic magma from the crust is not a free option. *Eos Transactions of the American Geophysical Union* **72**, 161.

Morse, S. A. (1982). A partisan review of Proterozoic anorthosites. *American Mineralogist* **67,** 1087–1100.

Morse, S. A. (1975). Plagioclase lamellae in hypersthene, Tikkoatokhakh Bay, Labrador. *Earth and Planetary Science Letters* **26**, 331–336.

Morse, S. A. (1968). Layered intrusions and anorthosite genesis. In: Isachsen, Y. D. (ed) Origin of anorthosite and related rocks. *New York State Museum and Science Service Memoirs* **18**, 175–187.

Müntener, O. & Ulmer, P. (2006). Experimentally derived high-pressure cumulates from hydrous arc magmas and consequences for the seismic velocity structure of lower arc crust. *Geophysical Research Letters* **33**, L21308.

Nolan, K. M. & Morse, S. A. (1986). Marginal rocks resembling the estimated bulk composition of the Kiglapait Intrusion. *Geochimica et Cosmochimica Acta.* **50**, 2381–2386.

Owens, B. & Dymek, R. (1995). Significance of pyroxene megacrysts for massif anorthosite petrogenesis - constraints from the Labrieville, Quebec, pluton. *American Mineralogist* **80**,144-161.

Peck, W. H., Clechenko, C. C., Hamilton, M. A. & Valley, J. W. (2010). Oxygen isotopes in the Grenville and Nain AMCG suites: Regional aspects of the crustal component in massif anorthosites. *The Canadian Mineralogist* **48**, 763–786.

Peck, W. H. & Valley, J. W. (2000). Large crustal input to high D18O anorthosite massifs of the southern Grenville Province: new evidence from the Morin Complex, Quebec. *Contributions to Mineralogy and Petrology* **139**, 402–417.

Philpotts, A. R. (1966). Origin of the Anorthosite-Mangerite Rocks in Southern Quebec. *Journal of Petrology* **7**, 1–64.

Putirka, K. D. (2008). Thermometers and Barometers for Volcanic Systems. *Reviews in Mineralogy and Geochemistry* **69**, 61–120.

Ranson, W. A. (1981). Anorthosites of diverse magma types in the Puttuaaluk Lake area, Nain complex, Labrador. *Canadian Journal of Earth Science* **18**, 26–41.

Rapp, R. P. & Watson, E. B. (1995). Dehydration Melting of Metabasalt a t 8—32 kbar: Implications for Continental Growth and Crust-Mantle Recycling. *Journal of Petrology* **36**, 891–931.

Rivers, T., Martignole, J., Gower, C. F. & Davidson, A. (1989). New tectonic divisions of the Grenville Province, southeast Canadian Shield. *Tectonics* **8**, 63–84.

Robins, B., Tumyr, O., Tysseland, M. & Garman, L. D. (1997). The Bjerkreim–Sokndal layered intrusion, Rogaland, SW Norway: evidence from marginal rocks for a jotunite parent magma. *Lithos* **39**, 121–133.

Rudnick, R. L. & Fountain, D. M. (1995). Nature and composition of the continental crust: A lower crustal perspective. *Reviews of Geophysics* **33**, 267–309.

Rudnick, R. L. & Gao, S. (2003). Composition of the continental crust. *Treatise on Geochemistry* **3**, Elsevier- Pergamon, Oxford, 659 pp.

Schiellerup, H., Lambert, D. D., Prestvik, T., Robins, B., McBride, J. S. & Larsen, R. B. (2000). Re-Os isotopic evidence for a lower crustal origin of massif-type anorthosites. *Nature* **405**, 781–784.

Schmidt, M. E. & Grunder, A. L. (2010). Deep Mafic Roots to Arc Volcanoes: Mafic Recharge and Differentiation of Basaltic Andesite at North Sister Volcano, Oregon Cascades. *Journal of Petrology* **52**, 603–641.

Scoates, J. S. (2000). The plagioclase-magma density paradox re-examined and the crystallization of Proterozoic anorthosites. *Journal of Petrology* **41**, 627–649.

Scoates, J. S. & Chamberlain, K. R. (1997). Orogenic to Post-Orogenic Origin for the 1.76 Ga Horse Creek Anorthosite Complex, Wyoming, USA. *The Journal of Geology* **105**, 331-344.

Scoates, J. S. & Frost, C. D. (1996). A strontium and neodymium isotopic investigation of the Laramie anorthosites, Wyoming, USA: Implications for magma chamber processes and the evolution of magma conduits in Proteroxoic anorthosites. *Geochimica et Cosmochimica Acta.* **60**, 95–107.

Sen, C. & Dunn, T. (1994). Dehydration melting of a basaltic composition amphibolite at 1.5 and 2.0 GPa: implications for the origin of adakites. *Contributions to Mineralogy and Petrology* **117**, 394–409.

Seth, B., Armstrong, R. A., Brandt, S., Villa, I. M. & Kramers, J. D. (2003). Mesoproterozoic U–Pb and Pb–Pb ages of granulites in NW Namibia: reconstructing a complete orogenic cycle. *Precambrian Research* **126**, 147–168.

Silva, Z. C. G. (1992). Mineralogy and cryptic layering of the Kunene anorthosite complex of SW Angola and Namibia. *Mineralogical Magazine* **56**, 319–327.

Silva, Z. C. G. (1990). Geochemistry of the Gabbro-Anorthosite Complex of Southwest Angola. *Journal of African Earth Sciences* **10**, 683–692.

Simmons, E. C. & Hanson, G. N. (1978). Geochemistry and origin of anorthosites. *Contributions to Mineralogy and Petrology* **66**, 119–135.

Simpson, E. S. W. & Otto, J. D. T. (1960). On the Pre-cambrian anorthosite mass of southern Angola. *21st International Geological Congress, Copenhagen* 13, 216–227.

Sisson, T. W. & Grove, T. L. (1993). Temperatures and H20 contents of low-MgO high-alumina basalts. *Contributions to Mineralogy and Petrology* **113**, 167–184.

Slejko, F. F., Demarchi, G. & Morais, E. (2002). Mineral chemistry and Nd isotopic composition of two anorthositic rocks from the Kunene complex (South Western Angola). *Journal of African Earth Sciences* **35**, 77–88.

Smith, P. M. & Asimow, P. D. (2005). Adiabat_1ph: A new public front-end to the MELTS, pMELTS, and pHMELTS models. *Geochemistry, Geophysics, Geosystems* **6**, art. no. Q02004, doi:10.1029/2004GC000816.

Stone, P. & Brown, G. M. (1958). The Quihita-Cunene Layered Gabbroic Intrusion of South-west Angola. *Geological Magazine* 195–207.

Streckeisen, A. (1976). To each plutonic rock its proper name. *Earth Science Reviews* **12**, 1–33.

Taylor, S. R., Campbell, M. T., McCulloch, M. T. & McLennan, S. M. (1984). A lower crustal origin for massif-type anorthosites. *Nature* **311**, 372–374.

Tegtmeyer, A. & Kröner, A. (1985). U–Pb zircon ages for granitoid gneisses in northern Namibia and their significance for Proterozoic crustal evolution of Southwestern Africa. *Precambrian Research* **28**, 311–326.

Torquato, J. R., Silva, A. T. S. F., da Cordani, U. G. & Kawashita, K. (1979). A evolução geológica do Cinturão Móvel do Quipungo no Oci- dente de Angola. *Anais Academia Brasileira Ciências* **51**, 133– 143.

Vander Auwera, J. & Longhi, J. (1994). Experimental study of a jotunite (hypersthene monzodiorite): constraints on the parent magma composition and crystallization conditions (P, T, fO_2) of the Bjerkreim-Sokndal layered intrusion (Norway). *Contributions to Mineralogy and Petrology* **118**, 60–78.

Vander Auwera, J., Longhi, J. & Duchesne, J-C. (2000). The effect of pressure on D_{Sr} (plag/melt) and D_{Cr} (opx/melt): implications for anorthosite petrogenesis. *Earth and Planetary Science Letters* **178,** 303–314.

Vander Auwera, J., Longhi, J. & Duchesne, J-C. (1998). A Liquid Line of Descent of the Jotunite (Hypersthene Monzodiorite) Suite. *Journal of Petrology* **39**, 439–468.

Vlaar, N. J. (1985). Precambrian geodynamical constraints. *The Deep Proterozoic Crust in the North Atlantic Provinces*. Springer Netherlands, 3–20.

Wiebe, R. A. (1990). Evidence for unusually feldspathic liquids in the Nain complex, Labrador. *The American Mineralogist* **75**, 1–12.

Wiebe, R. A. (1979). Anorthositic dikes, southern Nain Complex, Labrador. *The American Journal of Science* **279**, 394–410.

Wiebe, R. A. (1978). Anorthosite and related plutons, southern Nain complex, Labrador. *Canadian Journal of Earth Science* **15**, 1326–1340.

Wiebe, R. A. (1986). Lower Crustal Cumulate Nodules in Proterozoic Dikes of the Nain Complex: Evidence for the Origin of Proterozoic Anorthosites. *Journal of Petrology* **27**, 1253–1275.

Wiebe, R. A. & Snyder, D. (1993). Slow, dense replenishments of a basic magma chamber: the layered series of the Newark Island layered intrusion, Nain, Labrador. *Contributions to Mineralogy and Petrology* **113,** 59–72.

Wilson, J. R., Robins, B., Nielsen, F. M., Duchesne, J-C. & Vander Auwera, J. (1996). The Bjerkreim-Sokndal Layered Intrusion, Southwest Norway. *Layered Intrusions*, 231–255.

Xue, S. & Morse, S. A. (1994). Chemical characteristics of plagioclase and pyroxene megacrysts and their significance to the petrogenesis of the Nain anorthosites. *Geochimica et Cosmochimica Acta.* **58**, 4317–4331.

Yoder, H. S. (1968). Experimental studies bearing on the origin of anorthosite. *Origin of anorthosite and related rocks.* University of the State of New York, Albany, 13–23.

Appendix A

KAC Sample descriptions

LEUCOTROCTOLITES

KAC012/014	Leucotroctolite
Hand specimen:	Medium-coarse grained. Cumulus Pl (~1 cm), with smaller mafics (Ol and Opx; <5 mm). Mafics appear both intercumulus and cumulus. Olivine appears as rusty red-brown color. Abundant clots of magnetite (± Ilm), 1-2 cm across and commonly porphyritic. Clots have positive relief and are segregated into bands in some areas. Large (up to 10 cm) autoliths of more Pl-rich, coarser grained material are abundant.
Thin section:	Euhedral Pl. Abundant cumulus olivine, generally surrounded/rimmed by Cpx and/or Opx. Cpx/Opx rims commonly large and may surround more than one Ol as well as smaller Pl grains, forming an ophitic texture. Oxide minerals occur as rounded, ophitic grains with inclusions of Ol, and also as irregular blobs intergrown with Opx. Biotite grains are commonly associated with the oxide minerals.

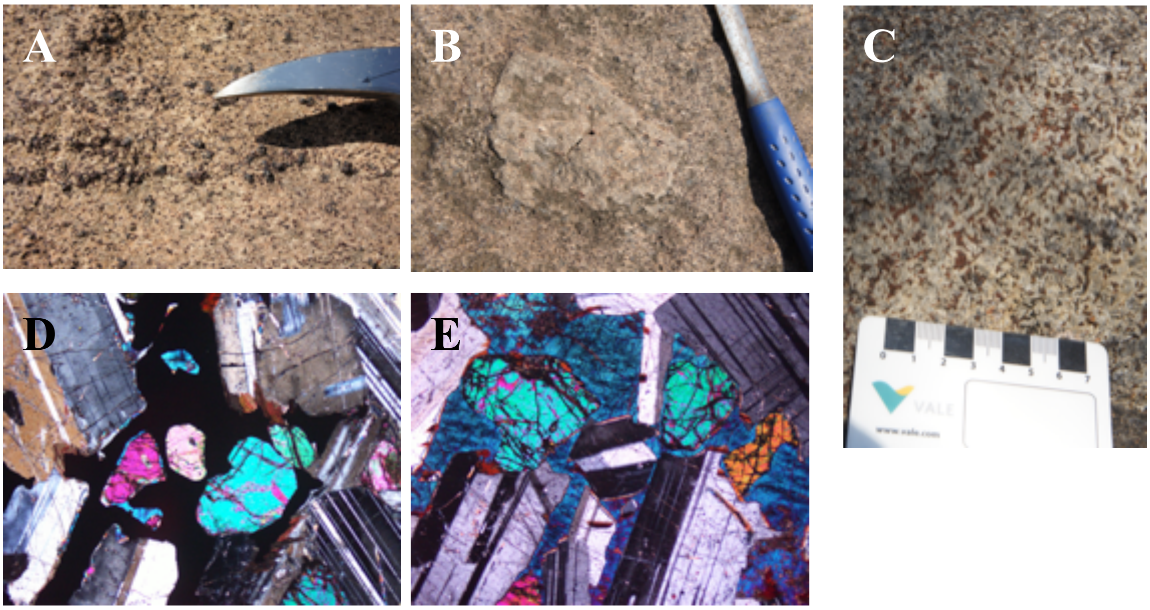

Figure A1 A) Weathered surface with magnetite/ilmenite clots showing some magmatic foliation. B) Autolith of feldspathic composition in leucotroctolite host. C) Cumulus plagioclase with mainly interstitial olivine and pyroxene. D) Interstitial oikocrystic oxide with inclusions of olivine and Cpx. E) Cumulus olivine and plagioclase surrounded by interstitial oikocrystic Cpx.

KAC017/022 — Olivine leucogabbronorite

Hand specimen: Very coarse-grained, Pl grains up to 3-4 cm. Interstitial mafics (Ol + Px). Ol is rusty brown color on weathered surface.

Thin section: Euhedral Pl. Olivine is both interstitial and cumulus and also occurs as small inclusions within large Pl grains. Small Pl grains are also observed as inclusions in Ol, suggesting simultaneous growth of Pl and Ol. Ol commonly has thick rims of Cpx and/or Opx. Opx and Cpx also occur as interstitial minerals. Some Ol is altered to iddingsite , and some sericitization of Pl is seen.

KAC081/075 — Anorthosite

Hand specimen: Dark gray color, >95% Pl (1-2 cm) with only small grains of interstitial Bt observed. Weakly magnetic. Fresh surface is vitreous and dark grey.

Thin section: Mainly fresh, euhedral Pl. Interstitial pockets of subhedral Ol, Bt, Ox, and some Ap. Olivine also occurs as small independent cumulus grains. Bt commonly totally rims Ol.

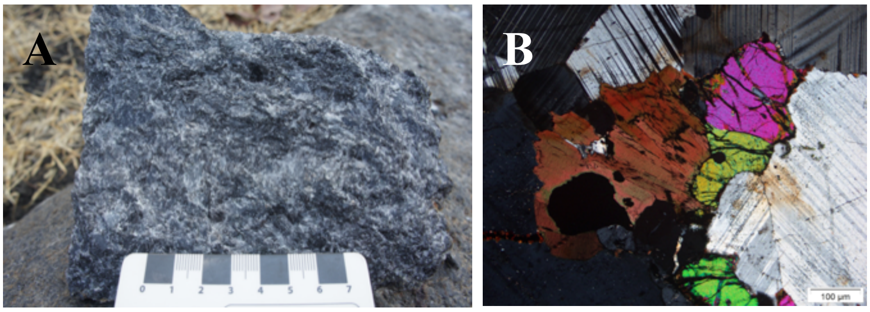

Figure A2 A) Dark-colored, massive appearance on fresh surface. B) Olivine, biotite and oxide in an pocket interstitial to cumulus plagioclase.

KAC099/093 — Leucotroctolite

Hand specimen: Coarse-grained. Cumulus euhedral-subhedral Pl (1-2 cm) with smaller mafic minerals (Ol + Px), some mafics form interconnected interstitial networks and other appears more cumulus. Ol appears yellow-green and fresh and also as rusty and weathered. Small amount of oxides present. Weathered surface is pockmarked.

Thin section: Fresh, euhedral Pl. Intercumulus and cumulus Ol, commonly with a thin rim of Opx and/or Cpx. Oxide minerals are irregular-shaped and commonly associated with pyroxenes, often intergrown and forming symplectites.

KAC114/104 | Pyroxene-bearing leucotroctolite

Hand specimen: Patchy texture. Feldspathic patches (Pl ~2 cm) surrounded by more mafic material, with Pl surrounded by interstitial porphyritic networks of mafics. Mafic material is rusty brown, mostly Ol. No obvious size difference between feldspathic and more mafic regions, but Pl in mafic material appears slightly more rounded.

Thin section: Pl mostly euhedral and cumulus, but also some smaller, sub-anhedral grains, often associated with Ol. Some Pl seems recrystallized along grain boundaries, and there are some pockets of small anhedral Pl and mafic minerals. Olivine is cumulus and intercumulus and commonly has Px reaction rims. Some Ol inclusions in Pl and vice versa. A few small oxides generally intergrown with Px, and commonly associated with Bt.

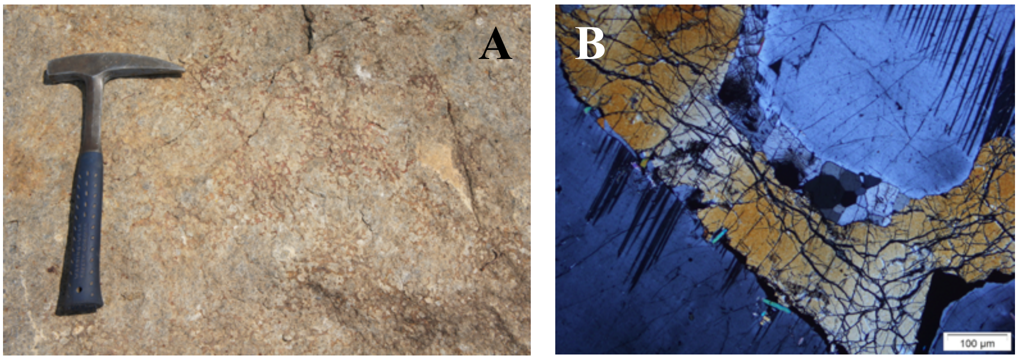

Figure A3 A) Patchy texture observed, showing feldspathic patches in more mafic leucotroctolitic material. B) Cumulus plagioclase with interstitial olivine and rim of Opx.

KAC122/111 | Leucotroctolite

Hand specimen: Medium-grained (<1 cm) Pl with smaller intercumulus Ol and Px. Some rusty brown Ol.

Thin section: Cumulus Pl. Cumulus and interstitial Ol with reaction rims of Opx and Cpx. Inclusions of Ol in large Pl grains and vice versa. Some recrystallization of large Pl grains along boundaries, and some Px slightly chloritized.

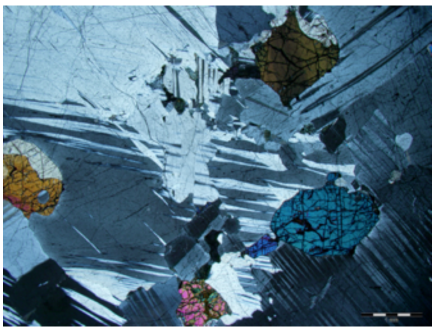

Figure A4 Recrystallized plagioclase and cumulus olivine showing orthopyroxene rims

<u>KAC135/124</u>	<u>Pyroxene-bearing leucotroctolite</u>
Hand specimen:	Medium-coarse grained, some Pl ~5 mm, others up to 3-4 cm. Carlsbad twins very apparent in large grains. Interstitial (+ some cumulus) rusty brown Ol. Some Pl grains are quite rounded/blocky, and some smaller Pl is included in interstitial mafics.
Thin section:	Cumulus Pl, cumulus and interstitial Ol. Feldspathic patches surrounded by more mafic material. In Pl-rich patches, grain boundaries commonly recrystallized and grains exhibit bent twins and/or undulatory extinction. Ol commonly has Opx/Cpx rims. A few small oxides intergrown with Opx.

<u>KAC151/145B</u>	<u>Leucotroctolite</u>
Hand specimen:	Sample is from quarry block showing block structure. Large (m-scale) angular or rounded blocks of feldspathic material within/mingling with more mafic-rich, material, which is pegmatitic in some areas. Sample is from more mafic material. Pl is subhedral to anhedral with highly variable grain size, from ~1 cm and up to 10-15 cm. Interconnected Ol networks are interstitial to Pl. Some Ol show dark rims (Px/Mgt?).
Thin section:	Large cumulus Pl. Cumulus olivine grains form iterconnected networks interstitial to Pl. Oxides in interstitial pockets are commonly rimmed by Opx/Cpx and/or Ol. Thin Opx rims commonly occur on Ol grains between Ol and Pl. Small amount of Bt and interstitial Cpx.

<u>KAC139/127</u>	<u>Anorthosite</u>
Hand specimen:	Pl dominated (>90%). Pl crystals ~1 cm, quite blocky and square-shaped with some rounded corners. Few interstitial Ol. Some Pl is labradorescent and some Pl megacrysts (~10 cm) observed.
Thin section:	Large subhedral Pl, commonly with rounded edges. Olivine is both cumulus and intercumulus between/around Pl grains. Small proportion of Opx, commonly in symplectic intergrowths with oxides. Some pockets of smaller Pl grains in porphyritic Ol/Px

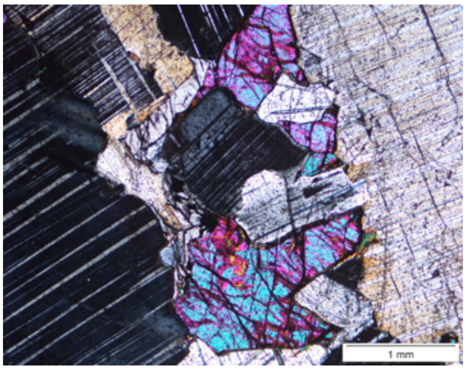

Figure A5 Subhedral, rounded plagioclase grains with intercumulus olivine oikocryst. Note rim of orthopyroxene on olivine.

OLIVINE LEUCOGABBRONORITES

KAC047/047	Olivine leuconorite
Hand specimen:	Light grey-brown weathered surface. Coarse-grained (1-2 cm Pl) with smaller intercumulus mafic minerals. Mafics are dark brown (Px) and some rusty red-brown (Ol). Some mafic minerals also seem cumulus. Quite recrystallized and cumulate textures not clear in many places. There are veins and metasomatized areas nearby. Also nearby are megacrysts of Opx, although they are interstitial.
Thin section:	Subhedral Pl grains with recrystallized grain boundaries, undulatory extinction and bent twins. Mafics are mainly intercumulus Opx and some small cumulus Ol with prominent Opx rims. Very small fraction of Cpx. Few oxides seen, generally as very small grains along Ol grain boundaries.

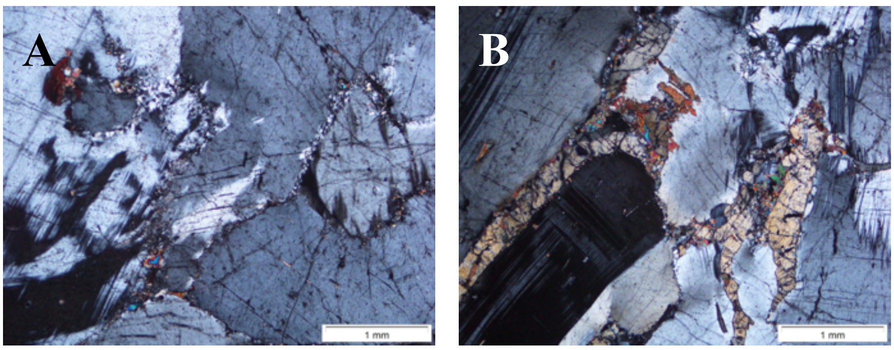

Figure A6 A) Deformed plagioclase grains showing recrystallized grain boundaries. B) Sub-anhedral plagioclase grains in a network of intercumulus orthopyroxene.

KAC054/053 — Olivine Leuconorite

Hand specimen: Coarse-grained (1-3 cm Pl) with smaller intercumulus Opx. Some patches of finer-grained Pl-rich material. Some thin white veins and white rim of recrystallization along irregular-shaped Pl grains. Nearby Opx megacrysts up to 30cm, most are intercumulus but some are euhedral.

Thin section: Some Pl euhedral and fresh, other grains more rounded and recrystallized, with bent twins. Olivine and Opx are interstitial to Pl, with prominent Opx rims on Ol. Some rounded oxide minerals associated with Bt and Opx. No Cpx observed in thin section.

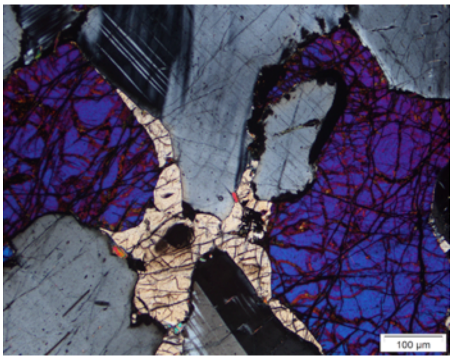

Figure A7 Cumulus plagioclase and olivine with interstitial orthopyroxene

KAC144/139 — Olivine leucogabbronorite

Hand specimen: Medium-grained (1-2 cm), pale grey Pl with some intercumulus Opx, but also some small cumulus Opx grains. Some pockmarks from weathering of Opx. Small amount of oxide minerals. There is some magmatic foliation running parallel to the surrounding valleys and ridges. Some shear bands also cross-cut the foliation.

Thin section: Cumulus fresh Pl, many triple point junctions. Cumulus and intercumulus Ol with prominent Px rims, as well as interstitial Opx and Cpx. Some olivine altered to iddingsite. Opaques associated with mafic minerals and Bt.

KAC147/142 — Olivine leucogabbronorite

Hand specimen: Very similar to KAC144/139 (from nearby). Medium-grained with interstitial Px and Ol as well as foliation and shear bands.

Thin section: Cumulus Pl with some cumulus and intercumulus Ol. Prominent rims of Opx/Cpx on Ol, and also some interstititial Opx and Cpx. Some olivine altered to iddingsite. Few interstitial opaques associated with Bt.

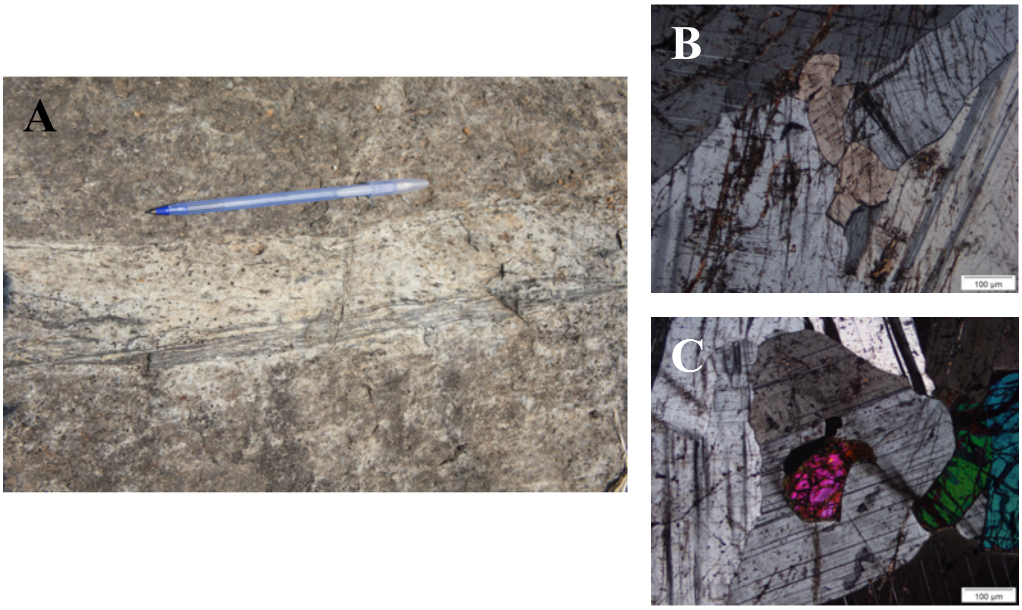

Figure A8 A) Narrow shear band cross-cutting foliated anorthosite. B) Cumulus plagioclase and orthopyroxene. C) Plagioclase with an inclusion on olivine that has started to alter to iddingsite.

LEUCOGABBRONORITES

<u>KAC041/042A</u> <u>Leucogabbronorite</u>

Hand specimen: Medium-grained (3-4 mm). Euhedral Pl and interstitial brown Opx. Some patches (~20 cm) of more mafic-rich material. Also some autoliths of felsic material.

Thin section: Eu-subhedral Pl with variable grain size. Cumulus and interstitial Opx. Small Cpx generally only adjacent to or on rims of Opx. No Olivine present. Many very small oxide grains.

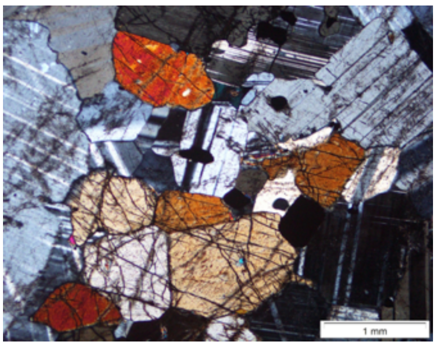

Figure A9 Cumulus plagioclase and orthopyroxene

KAC065/062 Anorthosite

Hand specimen: Coarse-grained (2-3 cm Pl). Mainly Pl (>90%). Small dark brown mafics, (Px or Ox), but cumulate texture not very clear. Clots of oxide minerals associated with pyroxenes, and sometimes in stringers or large patches (~10 cm). Outcrop has some large intercumulus Opx megacrysts (~20 cm). Some patches (~5 cm) of pegmatitic material with higher mafic proportion.

Thin section: Very Pl-rich. Cumulus Pl with irregular oxide minerals that are commonly oikocrysts and include small Pl grains. Oxides nearly always associated with Bt. No Px or Ol observed in thin section.

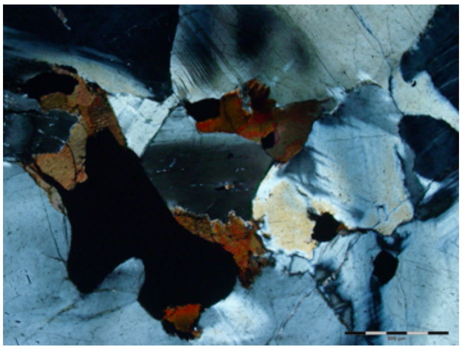

Figure A10 Plagioclase and irregular oxide mineral, surrounded by biotite

KAC067/65B Leuconorite

Hand specimen: Outcrop has a finer-grained (1-2 cm) section adjacent to a pegmatitic (~4-7 cm) section of the same composition. Sample is from finer-grained section and has cumulus Pl with an interconnected intercumulus Opx network. Some Pl megacrysts from the pegmatitic section continue into the finer section. No oxides visible in hand specimen.

Thin section: Eu-subhedral Pl with large intercumulus Opx oikocrysts. Pl commonly displays undulatory extinction and deformed/kinked twins. Few small oxide minerals observed. No Cpx or Olivine.

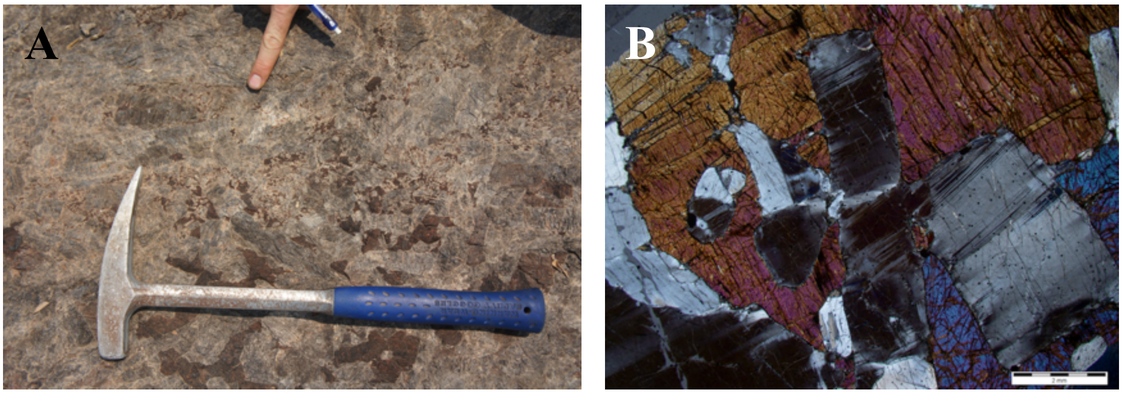

Figure A11 A) Pegmatitic leuconorite adjacent to finer-grained leuconorite with cumulus plagioclase and interstitial networks of Opx. B) Deformed plagioclase laths with large Opx oikocrysts.

<u>KAC083/076</u> <u>Anorthosite</u>

Hand specimen: Coarse-grained (1-2 cm), predominantly Pl with small proportion of intercumulus Opx. Some Pl recrystallized along grain boundaries. Some thin white metasomatic veins running through outcrop. Nearby outcrops have Px megacrysts.

Thin section: Large cumulus Pl with few interstitial Opx and Cpx. No Ol and very few oxides. Pl grains are deformed in some places and not fresh. Pyroxenes slightly altered.

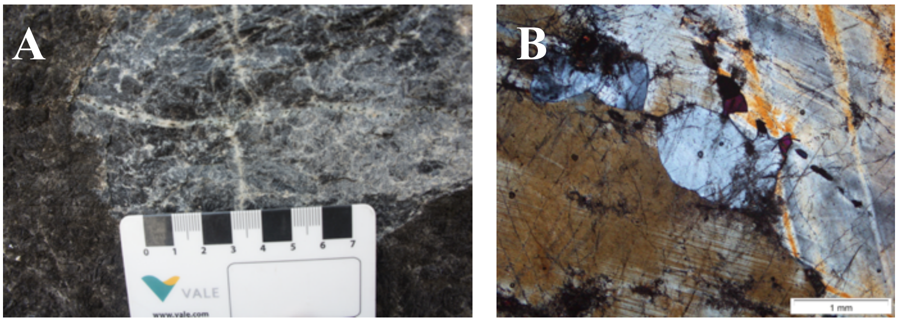

Figure A11 A) Dark colored anorthosite with white metasomatic veins. B) Deformed plagioclase with few very small and irregular pyroxene grains.

<u>KAC172/160</u> <u>Anorthosite</u>

Hand specimen: Coarse-grained, 2-3 cm Pl, some up to ~5 cm. Small interstitial Cpx and Opx, but low mafic proportion (<5%). Some pegmatitic patches with more Opx and some Ox. Outcrop shows strong foliation in some sections.

Thin section: Large, fresh cumulus Pl. Few small Opx and/or Cpx and Ox between large Pl laths as well as included in laths. No foliation apparent in thin section for this sample.

Appendix B

Major element data for all KAC samples (Major oxides in wt. %)

Table B1 Plagioclase

		Comment	SiO_2	TiO_2	Al_2O_3	FeO*	MnO	MgO	CaO	Na_2O	K_2O	Cr_2O_3	BaO	Total	Name	An
Leucotroctolites		Incl in Cpx	54.97	0.04	27.89	0.43	0.00	0.03	10.73	5.13	0.60	0.00	0.05	99.88	Lab	54
		Interm	54.42	0.07	28.17	0.31	0.00	0.03	11.24	5.03	0.34	0.01	0.02	99.63	Lab	55
		Margin	55.01	0.12	27.89	0.27	0.00	0.03	10.92	5.37	0.27	0.00	0.01	99.89	Lab	53
		Core	54.38	0.13	27.64	0.67	0.00	0.03	10.88	5.06	0.37	0.00	0.07	99.23	Lab	54
		Margin	55.59	0.05	27.05	0.29	0.00	0.04	10.37	5.76	0.43	0.00	0.04	99.63	And	50
		Core	54.45	0.10	28.03	0.31	0.01	0.04	11.25	4.94	0.39	0.01	0.04	99.58	Lab	56
		Margin	55.21	0.06	26.92	0.62	0.02	0.48	10.12	5.41	0.53	0.00	0.03	99.41	Lab	51
		Margin	55.40	0.07	27.38	0.25	0.00	0.04	10.32	5.48	0.49	0.01	0.05	99.48	Lab	51
		Interm	53.09	0.08	28.58	0.26	0.00	0.03	12.19	4.48	0.36	0.01	0.03	99.11	Lab	60
		Core	54.11	0.05	27.93	0.29	0.01	0.03	11.37	5.00	0.45	0.00	0.06	99.30	Lab	56
		Interm	52.78	0.06	28.35	0.63	0.02	0.46	11.32	4.50	0.39	0.01	0.09	98.59	Lab	58
		Margin	54.81	0.00	27.84	0.30	0.01	0.02	11.06	5.24	0.20	0.01	0.00	99.49	Lab	54
		Core	53.14	0.09	29.09	0.26	0.00	0.03	12.41	4.52	0.27	0.00	0.01	99.81	Lab	60
		Interm	55.23	0.14	27.90	0.26	0.02	0.03	10.67	5.20	0.39	0.00	0.04	99.87	Lab	53
		Btw Ol & Ox	55.32	0.04	27.84	0.43	0.02	0.04	10.84	5.41	0.27	0.01	0.00	100.21	Lab	53
		Btw Ol & Ox	54.48	0.05	27.64	0.47	0.00	0.04	10.84	5.19	0.40	0.01	0.01	99.12	Lab	54
		Margin	54.78	0.05	27.76	0.28	0.02	0.02	11.04	5.20	0.41	0.00	0.00	99.56	Lab	54
	KAC	Interm	54.58	0.08	27.42	0.68	0.02	0.18	10.51	5.24	0.47	0.00	0.05	99.23	Lab	53
	012/014	Core	54.19	0.07	27.73	0.28	0.01	0.03	11.12	5.07	0.43	0.00	0.07	99.00	Lab	55
		With Ox incl	52.93	0.00	29.37	0.16	0.00	0.02	12.56	4.48	0.27	0.00	0.00	99.79	Lab	61
		With Ox incl	52.52	0.02	29.15	0.18	0.01	0.02	12.76	4.37	0.29	0.00	0.00	99.33	Lab	62
		Margin	54.36	0.01	27.88	0.32	0.00	0.03	11.15	5.12	0.40	0.01	0.03	99.31	Lab	55
		Core	54.66	0.06	27.91	0.29	0.02	0.03	10.96	5.28	0.39	0.01	0.07	99.67	Lab	53
		Margin	55.54	0.01	27.01	0.34	0.00	0.03	10.24	5.54	0.57	0.00	0.03	99.32	Lab	51
		Interm	55.26	0.10	27.17	0.27	0.00	0.02	10.51	5.52	0.52	0.00	0.06	99.43	Lab	51
		Margin	55.30	0.09	27.01	0.33	0.00	0.04	10.16	5.67	0.36	0.00	0.00	98.96	And	50
		Interm	54.59	0.09	27.88	0.25	0.00	0.04	11.16	5.08	0.38	0.00	0.02	99.49	Lab	55
		Interm	52.93	0.10	28.73	0.27	0.01	0.03	12.29	4.48	0.35	0.00	0.03	99.22	Lab	60
		Core	52.34	0.08	29.02	0.27	0.00	0.02	12.60	4.22	0.31	0.01	0.02	98.89	Lab	62
		Core	52.67	0.07	29.11	0.26	0.03	0.05	12.64	4.32	0.32	0.00	0.05	99.52	Lab	62
		Interm	53.11	0.09	29.01	0.27	0.00	0.04	12.36	4.40	0.34	0.01	0.00	99.62	Lab	61
		Margin	54.83	0.13	28.24	0.31	0.00	0.03	11.16	5.04	0.51	0.00	0.03	100.28	Lab	55
		Margin	52.92	0.07	26.46	3.78	0.01	0.71	9.56	4.99	0.40	0.00	0.06	98.96	Lab	51
		Core	53.92	0.11	27.96	0.31	0.00	0.03	11.40	4.96	0.34	0.00	0.01	99.04	Lab	56
		Margin	55.72	0.11	27.22	0.28	0.00	0.03	10.21	5.68	0.45	0.00	0.04	99.73	And	50
		Core	54.21	0.11	27.93	0.31	0.02	0.02	11.28	5.04	0.40	0.01	0.00	99.33	Lab	55
		Margin	49.62	0.02	31.53	0.27	0.00	0.03	15.43	2.82	0.12	0.00	0.00	99.84	Byt	75
		Interm	50.31	0.01	30.80	0.42	0.01	0.27	14.72	3.16	0.16	0.00	0.03	99.89	Byt	72
		Interm	50.38	0.05	31.19	0.27	0.00	0.02	14.93	3.10	0.13	0.00	0.02	100.09	Byt	73
		Margin	49.36	0.00	31.46	0.27	0.00	0.03	15.50	2.71	0.10	0.01	0.02	99.46	Byt	76
		Core	50.14	0.02	31.28	0.27	0.00	0.03	15.20	3.07	0.13	0.00	0.01	100.15	Byt	73
		Margin	48.47	0.02	31.08	0.27	0.00	0.01	15.74	2.73	0.08	0.00	0.00	98.40	Byt	76
		Core	50.16	0.05	30.77	0.22	0.01	0.02	14.55	3.31	0.15	0.01	0.06	99.31	Byt	71
		Core	50.24	0.05	30.83	0.26	0.00	0.02	14.80	3.17	0.12	0.01	0.01	99.51	Byt	72
		Margin	48.20	0.00	32.21	0.31	0.01	0.05	16.40	2.36	0.05	0.03	0.01	99.63	Byt	79
		Margin	47.01	0.01	32.39	0.55	0.05	0.09	17.08	1.97	0.05	0.01	0.05	99.26	Byt	83
		Core	50.52	0.04	30.58	0.30	0.00	0.04	14.53	3.25	0.15	0.00	0.02	99.43	Byt	71
		Inclusion in Ol	48.21	0.02	31.38	0.97	0.13	0.17	15.58	2.60	0.09	0.00	0.02	99.17	Byt	77
		Margin	44.90	0.02	27.32	4.54	0.06	7.03	11.15	1.81	0.09	0.00	0.06	96.98	Byt	77
	KAC	Interm	51.76	0.05	29.78	0.32	0.01	0.23	13.45	3.87	0.23	0.01	0.00	99.71	Lab	66
	017/022	Interm	51.49	0.04	30.14	0.26	0.01	0.00	13.93	3.71	0.20	0.00	0.05	99.83	Lab	67
		Interm	51.20	0.07	30.09	0.21	0.01	0.01	13.92	3.72	0.21	0.00	0.04	99.48	Lab	67
		Core	51.36	0.04	30.28	0.22	0.00	0.02	13.90	3.68	0.19	0.00	0.01	99.70	Lab	68
		Margin	47.76	0.03	31.11	1.39	0.00	1.12	15.32	2.49	0.07	0.00	0.03	99.32	Byt	77
		Margin	49.71	0.03	31.26	0.26	0.00	0.05	15.06	3.09	0.11	0.00	0.04	99.61	Byt	73
		Core	51.30	0.01	30.37	0.25	0.02	0.02	13.84	3.55	0.15	0.00	0.02	99.53	Lab	68
		Interm	49.18	0.15	27.62	2.24	0.01	3.59	11.81	3.28	0.20	0.02	0.02	98.12	Lab	67
		Margin	50.50	0.06	30.85	0.26	0.00	0.10	14.42	3.33	0.16	0.01	0.04	99.73	Byt	71
		Interm	50.57	0.03	30.69	0.33	0.01	0.03	14.49	3.32	0.17	0.01	0.00	99.65	Byt	71
		Interm	50.89	0.04	30.71	0.20	0.00	0.02	14.45	3.42	0.17	0.00	0.07	99.97	Byt	70
		Core	48.87	0.00	29.60	0.74	0.01	1.16	15.00	3.06	0.18	0.00	0.01	98.63	Byt	73
		Margin	49.62	0.05	29.79	1.04	0.03	1.49	13.43	3.27	0.15	0.03	0.04	98.94	Lab	69
		Core	52.03	0.04	29.85	0.25	0.00	0.02	13.45	3.98	0.23	0.00	0.00	99.85	Lab	65
		Interm	51.47	0.03	29.89	0.53	0.01	0.30	13.32	3.84	0.19	0.00	0.02	99.60	Lab	66
		Margin	54.85	0.01	27.63	0.21	0.03	0.01	10.72	5.45	0.39	0.00	0.04	99.34	Lab	52
		Interm	55.72	0.01	26.99	0.14	0.01	0.00	10.04	5.76	0.51	0.00	0.06	99.24	And	49
	KAC	Interm	55.73	0.04	26.91	0.14	0.00	0.01	10.28	5.75	0.54	0.00	0.08	99.48	And	50
	081/075	Margin	55.22	0.01	27.36	0.19	0.00	0.02	10.42	5.49	0.53	0.01	0.02	99.27	Lab	51
		Core	55.09	0.22	24.38	1.29	0.01	1.48	11.47	5.04	0.48	0.00	0.00	99.46	Lab	56
		Interm	55.68	0.02	26.87	0.14	0.01	0.00	10.09	5.56	0.59	0.02	0.04	99.02	Lab	50

		Comment	SiO_2	TiO_2	Al_2O_3	FeO*	MnO	MgO	CaO	Na_2O	K_2O	Cr_2O_3	BaO	Total	Name	An
Leucotroctolites	KAC 099/093	Margin	50.11	0.06	30.55	0.39	0.01	0.06	14.47	3.19	0.25	0.00	0.01	99.09	Byt	71
		Interm	50.38	0.07	30.54	0.40	0.00	0.05	14.33	3.22	0.23	0.00	0.02	99.25	Byt	71
		Margin	49.78	0.07	30.62	0.44	0.00	0.05	14.57	3.11	0.24	0.03	0.02	98.93	Byt	72
		Margin	50.83	0.07	30.34	0.35	0.01	0.04	14.09	3.44	0.26	0.01	0.00	99.44	Lab	69
		Interm	50.98	0.05	30.17	0.37	0.01	0.05	14.05	3.46	0.28	0.00	0.02	99.44	Lab	69
		Interm	51.55	0.13	29.55	0.44	0.01	0.06	13.28	3.77	0.31	0.01	0.01	99.12	Lab	66
		Interm	48.54	0.10	31.58	0.43	0.00	0.05	15.83	2.47	0.15	0.00	0.00	99.15	Byt	78
		Core	50.29	0.09	30.48	0.43	0.00	0.07	14.31	3.09	0.24	0.02	0.01	99.02	Byt	72
		Margin	49.40	0.05	30.82	0.77	0.02	0.26	14.50	2.88	0.19	0.00	0.03	98.92	Byt	74
		Interm	49.28	0.02	31.12	0.40	0.01	0.03	15.04	2.81	0.20	0.00	0.00	98.90	Byt	75
		Interm	51.68	0.44	29.31	0.66	0.00	0.08	13.06	3.90	0.37	0.00	0.03	99.54	Lab	65
		Interm	50.45	0.10	30.36	0.40	0.00	0.04	14.32	3.30	0.23	0.00	0.02	99.23	Byt	71
		Margin	50.93	0.10	30.24	0.42	0.00	0.05	14.03	3.46	0.26	0.01	0.03	99.53	Lab	69
		Core	49.16	0.06	30.44	0.73	0.00	0.46	14.58	3.08	0.21	0.00	0.00	98.72	Byt	72
		Margin	49.41	0.07	29.92	0.44	0.00	0.07	14.22	3.03	0.29	0.01	0.00	97.46	Byt	72
		Interm	49.20	0.03	31.24	0.44	0.01	0.04	15.19	2.80	0.21	0.01	0.03	99.20	Byt	75
		Core	50.31	0.09	30.52	0.46	0.00	0.05	14.34	3.27	0.25	0.00	0.00	99.31	Byt	71
		Core	50.61	0.08	30.35	0.39	0.02	0.06	14.07	3.44	0.25	0.00	0.00	99.27	Lab	69
		Core	50.42	0.04	30.65	0.33	0.02	0.07	14.33	3.32	0.23	0.00	0.00	99.43	Byt	70
		Core	50.07	0.09	30.61	0.39	0.00	0.04	14.61	3.13	0.24	0.02	0.00	99.22	Byt	72
		Margin	51.06	0.11	29.40	0.42	0.02	0.05	13.40	3.52	0.26	0.00	0.01	98.26	Lab	68
		Core	51.09	0.03	29.99	0.41	0.00	0.05	13.87	3.51	0.25	0.00	0.04	99.24	Lab	69
		Interm	51.34	0.16	29.74	0.45	0.01	0.07	13.69	3.57	0.26	0.00	0.03	99.33	Lab	68
		Core	50.26	0.12	29.86	0.42	0.00	0.06	14.05	3.30	0.25	0.01	0.00	98.33	Byt	70
		Margin	49.73	0.08	30.70	0.48	0.01	0.06	14.82	3.08	0.22	0.00	0.01	99.18	Byt	73
		Interm	51.36	0.06	29.97	0.39	0.00	0.04	13.61	3.69	0.26	0.00	0.00	99.39	Lab	67
		Margin	50.76	0.05	30.37	0.29	0.01	0.03	14.24	3.32	0.26	0.00	0.01	99.36	Byt	70
		Interm	51.63	0.11	29.38	0.38	0.00	0.05	13.42	3.83	0.29	0.02	0.03	99.14	Lab	66
	KAC 114/104	Incl in Px	49.18	0.04	31.40	0.33	0.00	0.02	15.75	2.78	0.11	0.01	0.00	99.62	Byt	76
		Incl in Px	48.60	0.00	31.93	0.25	0.00	0.02	16.20	2.41	0.09	0.00	0.04	99.54	Byt	79
		Incl in Px	46.75	0.02	33.42	0.19	0.00	0.02	17.78	1.62	0.02	0.00	0.00	99.82	Byt	86
		Incl in Px	48.16	0.00	32.28	0.40	0.00	0.04	16.59	2.25	0.11	0.01	0.04	99.88	Byt	80
		Incl in Px	47.83	0.03	32.14	0.43	0.00	0.02	16.65	2.26	0.11	0.01	0.05	99.53	Byt	80
			50.22	0.05	30.72	0.32	0.00	0.02	14.64	3.32	0.18	0.00	0.03	99.50	Byt	71
			50.70	0.02	30.53	0.35	0.00	0.03	14.51	3.43	0.15	0.00	0.03	99.75	Byt	70
			50.26	0.04	30.60	0.29	0.00	0.02	14.74	3.28	0.14	0.00	0.03	99.40	Byt	71
			48.57	0.03	31.90	0.33	0.00	0.04	16.18	2.44	0.13	0.00	0.03	99.65	Byt	79
			50.66	0.04	30.57	0.33	0.00	0.03	14.58	3.33	0.19	0.01	0.03	99.77	Byt	71
			50.36	0.02	30.79	0.36	0.00	0.18	14.62	3.24	0.12	0.01	0.04	99.74	Byt	71
	KAC 122/111		48.97	0.05	31.57	0.32	0.00	0.04	15.68	2.65	0.12	0.00	0.00	99.40	Byt	77
			50.08	0.02	30.94	0.29	0.00	0.06	15.10	3.09	0.14	0.02	0.04	99.78	Byt	73
			49.46	0.02	31.40	0.31	0.02	0.04	15.55	2.82	0.14	0.00	0.00	99.76	Byt	75
			49.53	0.03	31.29	0.33	0.00	0.04	15.49	2.83	0.14	0.01	0.02	99.71	Byt	75
			49.68	0.02	31.28	0.28	0.01	0.03	15.36	2.96	0.13	0.00	0.03	99.78	Byt	74
			49.25	0.05	31.48	0.38	0.03	0.12	15.76	2.77	0.14	0.00	0.03	100.01	Byt	76
		Incl in Ol	49.02	0.00	31.63	0.24	0.02	0.02	15.79	2.69	0.09	0.00	0.00	99.50	Byt	76
			48.84	0.09	31.33	0.31	0.00	0.03	15.75	2.52	0.13	0.01	0.00	99.01	Byt	78
			50.09	0.01	31.29	0.28	0.00	0.03	15.41	2.99	0.17	0.00	0.01	100.28	Byt	74
		Core	49.56	0.04	31.98	0.32	0.01	0.03	15.77	2.76	0.13	0.00	0.02	100.62	Byt	76
		Interm	49.46	0.06	31.52	0.36	0.00	0.02	15.65	2.72	0.12	0.00	0.00	99.91	Byt	76
		Margin	48.46	0.01	32.05	0.34	0.01	0.03	16.43	2.34	0.10	0.01	0.00	99.78	Byt	80
			48.28	0.00	32.45	0.26	0.00	0.03	16.54	2.29	0.08	0.01	0.00	99.94	Byt	80
		Interm	48.96	0.05	31.57	0.31	0.00	0.02	15.91	2.67	0.12	0.00	0.01	99.62	Byt	77
		Margin	48.51	0.33	31.24	0.62	0.02	0.53	15.62	2.53	0.12	0.00	0.02	99.54	Byt	77
		Interm	48.87	0.03	31.92	0.31	0.00	0.02	16.06	2.54	0.11	0.00	0.01	99.87	Byt	78
	KAC 135/124		48.89	0.01	31.39	0.27	0.01	0.03	15.94	2.72	0.11	0.00	0.00	99.37	Byt	76
			48.76	0.06	31.69	0.30	0.01	0.02	15.96	2.56	0.10	0.00	0.02	99.48	Byt	78
			48.41	0.02	31.69	0.28	0.00	0.02	16.27	2.61	0.08	0.01	0.00	99.39	Byt	78
		Btw opx	48.28	0.04	31.72	0.32	0.00	0.03	16.58	2.41	0.08	0.00	0.01	99.47	Byt	79
			50.02	0.05	30.77	0.71	0.00	0.06	14.93	3.20	0.18	0.00	0.00	99.92	Byt	72
			48.95	0.06	31.55	0.28	0.01	0.02	16.00	2.65	0.13	0.00	0.00	99.65	Byt	77
			49.52	0.06	31.28	0.33	0.00	0.02	15.41	2.89	0.12	0.00	0.03	99.66	Byt	75
			48.59	0.07	31.68	0.35	0.01	0.02	16.23	2.62	0.11	0.00	0.03	99.71	Byt	77
		Incl in Opx	46.89	0.00	32.45	0.87	0.01	0.22	17.05	1.95	0.03	0.00	0.01	99.48	Byt	83
		Incl in Ol	47.97	0.01	31.71	0.41	0.00	0.04	16.64	2.36	0.09	0.00	0.02	99.25	Byt	80
		Btw Ol	47.89	0.01	31.98	0.61	0.00	0.35	16.19	2.29	0.06	0.01	0.01	99.40	Byt	80
			48.72	0.05	31.37	0.29	0.00	0.02	16.12	2.66	0.10	0.00	0.00	99.33	Byt	77
			49.13	0.04	31.29	0.35	0.01	0.02	15.78	2.77	0.11	0.01	0.00	99.51	Byt	76
			50.29	0.05	30.63	0.31	0.00	0.03	14.78	3.33	0.14	0.00	0.00	99.56	Byt	71
			50.52	0.02	30.33	0.28	0.00	0.05	14.69	3.37	0.17	0.01	0.03	99.47	Byt	71
		Incl in Opx	47.10	0.03	32.64	0.41	0.00	0.03	17.33	1.92	0.05	0.00	0.02	99.53	Byt	83
			48.14	0.16	31.97	0.37	0.00	0.02	16.23	2.48	0.09	0.01	0.02	99.49	Byt	78
	KAC 139/127	Incl in Opx	50.65	0.05	31.06	0.40	0.00	0.03	14.87	3.23	0.23	0.00	0.01	100.53	Byt	72
		Margin	51.02	0.03	30.81	0.40	0.01	0.03	14.73	3.38	0.20	0.01	0.03	100.65	Byt	71
		Interm	51.71	0.24	30.17	0.45	0.00	0.04	13.91	3.65	0.25	0.00	0.05	100.47	Lab	68
		Core	50.10	0.03	31.21	0.38	0.00	0.04	15.21	2.99	0.18	0.01	0.01	100.16	Byt	74
		Margin	50.15	0.11	31.35	0.48	0.01	0.05	15.16	2.99	0.14	0.00	0.04	100.48	Byt	74
		Core	50.80	0.05	30.92	0.40	0.00	0.05	14.74	3.19	0.13	0.01	0.00	100.29	Byt	72
		Margin	50.01	0.01	31.39	0.45	0.00	0.05	15.38	2.90	0.18	0.00	0.01	100.38	Byt	75
		Core	50.50	0.02	31.41	0.41	0.01	0.05	15.08	2.93	0.17	0.00	0.00	100.58	Byt	74
		Margin	51.49	0.08	29.47	0.47	0.01	0.12	13.34	3.85	0.44	0.00	0.00	99.27	Lab	66
		Interm	51.78	0.06	30.32	0.41	0.00	0.05	14.08	3.62	0.27	0.00	0.04	100.63	Lab	68
		Core	50.76	0.06	30.49	0.40	0.00	0.04	14.75	3.22	0.20	0.02	0.01	99.95	Byt	72
		Core	49.90	0.06	31.49	0.44	0.00	0.05	15.41	2.81	0.21	0.00	0.00	100.37	Byt	75
		Incl in Opx	47.07	0.01	33.78	0.55	0.01	0.04	17.79	1.67	0.09	0.01	0.00	101.02	Byt	85

		Comment	SiO_2	TiO_2	Al_2O_3	FeO*	MnO	MgO	CaO	Na_2O	K_2O	Cr_2O_3	BaO	Total	Name	An
Leucotroctolites	KAC 151/145 B	Margin	48.53	0.03	32.74	0.34	0.00	0.02	16.58	2.26	0.08	0.00	0.03	100.61	Byt	80
		Interm	50.09	0.02	31.58	0.36	0.01	0.02	15.17	3.00	0.17	0.00	0.05	100.47	Byt	74
		Interm	49.80	0.02	31.66	0.34	0.00	0.02	15.32	2.93	0.14	0.02	0.00	100.25	Byt	74
		Core	49.99	0.04	31.84	0.34	0.00	0.04	15.26	2.92	0.17	0.00	0.04	100.64	Byt	74
		Core	50.67	0.02	31.11	0.29	0.00	0.04	14.72	3.36	0.12	0.01	0.00	100.34	Byt	71
		Margin	46.91	0.00	33.79	0.33	0.01	0.04	17.84	1.67	0.02	0.00	0.02	100.63	Byt	86
		Margin	50.01	0.02	31.81	0.32	0.00	0.03	15.33	2.96	0.14	0.00	0.02	100.64	Byt	74
		Interm	50.12	0.08	31.56	0.28	0.00	0.02	15.30	3.02	0.14	0.01	0.05	100.58	Byt	74
		Core	50.80	0.03	30.98	0.30	0.00	0.02	14.64	3.30	0.18	0.02	0.01	100.28	Byt	71
		Margin	48.90	0.00	32.17	0.32	0.00	0.02	16.12	2.56	0.08	0.00	0.00	100.17	Byt	78
		Interm	49.40	0.05	32.04	0.24	0.00	0.02	15.71	2.69	0.12	0.00	0.04	100.31	Byt	76
		Margin	49.78	0.03	32.25	0.33	0.01	0.02	15.54	2.72	0.10	0.01	0.00	100.79	Byt	76
		Interm	49.95	0.05	31.78	0.28	0.00	0.04	15.33	2.91	0.14	0.00	0.04	100.52	Byt	74
Olivine leucogabbronorites	KAC 047/047		52.75	0.04	29.18	0.11	0.00	0.02	12.59	4.43	0.27	0.00	0.01	99.40	Lab	61
		Margin	50.89	0.02	30.52	0.15	0.01	0.01	14.03	3.68	0.16	0.00	0.00	99.47	Lab	68
			52.69	0.02	29.10	0.29	0.00	0.08	12.45	4.40	0.23	0.01	0.05	99.31	Lab	61
			52.61	0.03	29.35	0.20	0.00	0.02	12.82	4.19	0.31	0.00	0.05	99.57	Lab	63
			52.75	0.00	29.24	0.16	0.02	0.01	12.58	4.42	0.32	0.00	0.04	99.55	Lab	61
			52.62	0.01	29.09	0.15	0.00	0.02	12.61	4.34	0.33	0.00	0.09	99.26	Lab	62
			52.51	0.02	29.33	0.18	0.00	0.02	12.68	4.31	0.32	0.02	0.04	99.43	Lab	62
			52.42	0.01	29.24	0.17	0.01	0.01	12.85	4.35	0.29	0.00	0.03	99.39	Lab	62
			52.63	0.05	29.18	0.21	0.00	0.02	12.71	4.37	0.27	0.01	0.00	99.44	Lab	62
			52.46	0.00	29.37	0.16	0.01	0.01	12.55	4.36	0.30	0.01	0.03	99.25	Lab	61
		Margin	51.08	0.04	30.23	0.12	0.01	0.02	13.91	3.79	0.14	0.00	0.02	99.37	Lab	67
			52.77	0.05	29.24	0.16	0.02	0.02	12.68	4.41	0.28	0.00	0.02	99.66	Lab	61
			52.47	0.06	29.22	0.14	0.02	0.01	12.56	4.43	0.26	0.00	0.00	99.18	Lab	61
		Margin	52.87	0.02	29.08	0.12	0.02	0.01	12.59	4.40	0.31	0.00	0.02	99.43	Lab	61
			52.87	0.00	28.97	0.18	0.00	0.01	12.37	4.46	0.32	0.00	0.00	99.19	Lab	61
			53.03	0.02	29.17	0.17	0.00	0.01	12.38	4.49	0.31	0.01	0.03	99.61	Lab	60
			51.52	0.11	28.32	0.81	0.02	0.05	12.88	4.33	0.31	0.00	0.02	98.37	Lab	62
		Margin	51.06	0.01	30.31	0.27	0.01	0.02	13.77	3.63	0.23	0.00	0.06	99.36	Lab	68
		Interm	52.63	0.03	29.20	0.17	0.00	0.02	12.60	4.37	0.28	0.00	0.03	99.33	Lab	61
		Interm	52.51	0.06	29.14	0.14	0.00	0.01	12.44	4.39	0.29	0.00	0.05	99.04	Lab	61
		Core	51.85	0.20	28.72	0.32	0.00	0.03	12.55	4.30	0.24	0.02	0.01	98.23	Lab	62
		Core	52.66	0.03	29.03	0.15	0.00	0.00	12.40	4.34	0.29	0.01	0.00	98.92	Lab	61
		Core	52.74	0.02	29.02	0.13	0.00	0.02	12.30	4.54	0.29	0.00	0.04	99.08	Lab	60
		Margin	51.85	0.00	29.50	0.17	0.00	0.02	12.91	4.16	0.25	0.00	0.03	98.89	Lab	63
			50.94	0.04	30.38	0.20	0.00	0.01	13.99	3.59	0.24	0.00	0.02	99.40	Lab	68
		Margin	51.70	0.02	29.91	0.16	0.00	0.02	13.33	3.99	0.24	0.01	0.00	99.39	Lab	65
		Margin	50.91	0.03	30.12	0.22	0.00	0.00	13.75	3.62	0.30	0.00	0.03	98.98	Lab	68
		Interm	52.67	0.03	29.17	0.21	0.02	0.03	12.57	4.32	0.31	0.00	0.02	99.34	Lab	62
		Core	52.87	0.02	29.12	0.19	0.00	0.02	12.51	4.46	0.32	0.00	0.04	99.56	Lab	61
	KAC 048/048	Btw Opx Mgxsts	47.86	0.02	31.73	0.28	0.01	0.03	16.10	2.44	0.05	0.00	0.02	98.54	Byt	78
		Btw Opx Mgxsts	47.57	0.01	32.19	0.26	0.00	0.00	16.80	2.11	0.03	0.01	0.03	99.01	Byt	81
		Btw Opx Mgxsts	47.27	0.02	32.46	0.23	0.01	0.02	16.80	2.08	0.04	0.00	0.05	98.98	Byt	82
		Btw Opx Mgxsts	48.26	0.00	31.83	0.22	0.00	0.00	16.06	2.42	0.03	0.02	0.01	98.85	Byt	79
		Lamellae	47.97	0.68	8.99	10.54	0.13	15.72	11.70	1.32	0.37	0.07	0.03	97.52	Byt	83
		Margin	46.22	0.00	33.09	0.41	0.01	0.01	17.86	1.68	0.03	0.01	0.03	99.35	Byt	85
		Margin	47.35	0.01	32.58	0.49	0.00	0.02	17.06	2.04	0.04	0.02	0.06	99.67	Byt	82
		Lamellae	46.33	0.08	15.88	14.39	0.22	13.74	6.36	0.60	0.11	0.00	0.00	97.71	Byt	85
	KAC 054/053	Interm	51.71	0.02	29.45	0.25	0.00	0.03	13.41	3.99	0.28	0.00	0.03	99.17	Lab	65
		Margin	50.48	0.02	30.30	0.22	0.02	0.01	14.39	3.47	0.19	0.00	0.01	99.11	Lab	70
		Core	52.84	0.02	28.75	0.25	0.02	0.05	12.44	4.52	0.35	0.00	0.00	99.24	Lab	60
		Interm	52.36	0.03	29.12	0.21	0.01	0.03	12.86	4.33	0.26	0.00	0.00	99.21	Lab	62
		Interm	51.84	0.02	29.69	0.16	0.00	0.02	13.28	4.06	0.23	0.01	0.04	99.35	Lab	64
		Core	52.78	0.04	28.65	0.17	0.00	0.03	12.29	4.47	0.33	0.00	0.05	98.81	Lab	60
		Margin	49.77	0.00	30.86	0.26	0.03	0.01	14.69	3.23	0.16	0.00	0.00	99.01	Byt	72
		Margin	50.53	0.00	30.25	0.26	0.00	0.12	14.04	3.44	0.18	0.00	0.02	98.84	Lab	69
		Core	53.32	0.01	28.44	0.16	0.00	0.01	12.12	4.66	0.34	0.00	0.03	99.09	Lab	59
		Interm	51.86	0.02	29.63	0.15	0.00	0.02	13.25	4.03	0.18	0.01	0.03	99.18	Lab	64
		Margin	48.56	0.04	31.29	0.26	0.00	0.03	15.25	2.85	0.20	0.00	0.02	98.50	Byt	75
		Interm	52.88	0.00	28.78	0.22	0.00	0.03	12.41	4.47	0.34	0.00	0.07	99.20	Lab	61
		Interm	53.01	0.30	28.31	0.37	0.01	0.04	12.00	4.56	0.38	0.01	0.03	99.02	Lab	59
		Core	53.34	0.01	28.43	0.25	0.00	0.02	12.15	4.67	0.36	0.00	0.01	99.24	Lab	59
		Margin	50.79	0.00	30.02	0.23	0.01	0.03	14.08	3.61	0.21	0.00	0.05	99.03	Lab	68
		Core	52.27	1.24	26.61	1.29	0.05	1.18	11.26	4.65	0.39	0.01	0.03	98.98	Lab	57
		Margin	52.16	0.03	29.28	0.23	0.00	0.02	13.19	4.20	0.26	0.00	0.00	99.37	Lab	63
		Interm	53.46	0.00	28.64	0.17	0.00	0.01	12.02	4.63	0.36	0.00	0.04	99.33	Lab	59
		Core	53.54	0.03	28.65	0.17	0.02	0.03	12.01	4.63	0.40	0.00	0.02	99.50	Lab	59
	KAC 144/139	Margin	52.70	0.05	29.04	0.25	0.01	0.01	12.68	4.40	0.23	0.00	0.00	99.37	Lab	61
		Interm	53.49	0.06	28.38	0.22	0.01	0.02	11.88	4.76	0.31	0.01	0.03	99.17	Lab	58
		Interm	53.59	0.08	28.29	0.21	0.01	0.03	12.01	4.81	0.34	0.00	0.02	99.39	Lab	58
		Margin	52.51	0.04	28.77	0.22	0.00	0.02	12.67	4.43	0.29	0.01	0.03	98.99	Lab	61
		Interm	53.62	0.06	28.15	0.23	0.01	0.04	11.79	4.88	0.35	0.02	0.05	99.20	Lab	57
		Interm	53.68	0.07	28.09	0.21	0.01	0.04	11.72	4.94	0.36	0.01	0.00	99.13	Lab	57
		Interm	53.59	0.05	28.14	0.26	0.01	0.01	11.68	4.86	0.36	0.00	0.07	99.03	Lab	57
		Core	53.70	0.03	28.22	0.21	0.01	0.03	11.70	4.94	0.35	0.01	0.03	99.23	Lab	57
		Core	53.91	0.02	28.11	0.18	0.02	0.02	11.79	4.92	0.38	0.00	0.03	99.38	Lab	57
Leucogabbronorites	KAC 041/042 A		56.49	0.04	26.50	0.26	0.01	0.01	9.63	5.73	0.47	0.01	0.12	99.27	And	48
			56.81	0.03	26.77	0.20	0.00	0.01	9.85	5.93	0.38	0.00	0.09	100.07	And	48
			56.81	0.04	26.61	0.22	0.02	0.02	9.66	5.98	0.40	0.01	0.16	99.93	And	47
		Incl in Opx	56.55	0.03	26.84	0.23	0.00	0.01	10.03	5.80	0.37	0.00	0.08	99.94	And	49
		Incl in Opx	56.11	0.00	26.92	0.28	0.13	0.01	10.12	5.79	0.27	0.00	0.08	99.71	And	49
		Incl in Opx	56.43	0.05	26.75	0.35	0.00	0.02	9.86	5.84	0.29	0.00	0.03	99.62	And	48
			56.78	0.03	26.56	0.24	0.03	0.02	9.67	5.94	0.41	0.00	0.12	99.80	And	47

		Comment	SiO_2	TiO_2	Al_2O_3	FeO*	MnO	MgO	CaO	Na_2O	K_2O	Cr_2O_3	BaO	Total	Name	An
Leucogabbronorites			56.95	0.07	26.51	0.25	0.00	0.02	9.80	5.84	0.48	0.00	0.14	100.06	And	48
			56.68	0.06	27.08	0.26	0.00	0.03	10.26	5.72	0.28	0.03	0.11	100.51	And	50
			57.07	0.06	26.53	0.27	0.00	0.01	9.74	5.96	0.40	0.00	0.05	100.09	And	47
			56.83	0.05	26.60	0.23	0.00	0.02	9.68	6.09	0.32	0.02	0.07	99.91	And	47
	KAC 041/042 A		56.83	0.06	26.70	0.23	0.02	0.01	9.77	5.84	0.36	0.00	0.07	99.89	And	48
		Incl in Opx	57.19	0.00	26.47	0.50	0.00	0.01	9.32	6.12	0.31	0.00	0.00	99.92	And	46
			55.95	0.01	26.50	0.24	0.00	0.03	9.59	5.51	1.03	0.00	0.18	99.04	And	49
		Incl in Ol	56.51	0.01	26.82	0.36	0.00	0.02	10.01	6.00	0.20	0.01	0.08	100.02	And	48
		Incl in Ol	55.45	0.00	27.41	0.26	0.02	0.02	10.59	5.36	0.50	0.01	0.21	99.83	Lab	52
			57.45	0.06	26.28	0.27	0.00	0.04	9.07	6.11	0.45	0.02	0.06	99.81	And	45
			57.01	0.07	27.00	0.24	0.01	0.03	8.63	5.96	0.81	0.00	0.07	99.83	And	44
		Rim	54.82	0.02	28.53	0.09	0.01	0.00	11.18	5.08	0.36	0.01	0.01	100.11	Lab	55
		Interm	54.20	0.03	28.58	0.19	0.01	0.02	11.50	4.79	0.53	0.00	0.05	99.90	Lab	57
		Interm	54.56	0.09	28.52	0.07	0.00	0.01	11.34	5.05	0.39	0.00	0.00	100.03	Lab	55
		Core	54.63	0.04	28.56	0.16	0.00	0.03	11.22	4.87	0.56	0.00	0.07	100.14	Lab	56
		Margin	53.82	0.02	29.19	0.28	0.01	0.02	12.08	4.71	0.39	0.00	0.00	100.51	Lab	59
		Interm	54.34	0.04	28.79	0.16	0.01	0.01	11.51	4.86	0.40	0.00	0.00	100.12	Lab	57
		Core	54.61	0.07	28.52	0.15	0.01	0.02	11.23	5.09	0.47	0.01	0.02	100.18	Lab	55
		Interm	54.55	0.07	28.64	0.13	0.01	0.02	11.30	4.99	0.44	0.00	0.00	100.14	Lab	56
		Margin	55.15	0.06	29.06	0.15	0.00	0.02	11.49	4.93	0.24	0.02	0.01	101.11	Lab	56
		Interm	55.44	0.04	28.09	0.13	0.00	0.01	10.73	5.24	0.47	0.02	0.04	100.22	Lab	53
	KAC 065/062	Core	55.64	0.06	27.66	0.21	0.01	0.13	10.15	5.39	0.61	0.02	0.03	99.91	Lab	51
		Interm	55.96	0.05	27.91	0.12	0.00	0.02	10.44	5.50	0.42	0.00	0.00	100.41	Lab	51
		Interm	55.89	0.06	27.76	0.13	0.00	0.01	10.41	5.57	0.49	0.01	0.03	100.35	Lab	51
		Core	55.78	0.08	27.79	0.09	0.00	0.00	10.29	5.34	0.60	0.00	0.02	100.00	Lab	52
		Core	55.80	0.01	27.60	0.11	0.00	0.00	10.30	5.56	0.56	0.02	0.02	99.99	Lab	51
		Margin	55.36	0.00	28.37	0.13	0.00	0.01	10.72	5.18	0.49	0.00	0.00	100.26	Lab	53
		Interm	55.69	0.05	27.83	0.12	0.00	0.01	10.26	5.43	0.58	0.00	0.04	100.02	Lab	51
		Interm	55.98	0.06	27.88	0.12	0.01	0.03	10.12	5.52	0.50	0.00	0.05	100.26	Lab	50
		Core	55.88	0.07	27.72	0.12	0.01	0.00	10.36	5.57	0.49	0.01	0.02	100.23	Lab	51
		Margin	54.23	0.06	28.96	0.13	0.01	0.01	11.39	4.90	0.47	0.01	0.04	100.19	Lab	56
		Interm	55.16	0.04	28.34	0.11	0.00	0.01	10.83	5.36	0.49	0.02	0.03	100.38	Lab	53
		Core	55.45	0.08	28.15	0.11	0.00	0.01	10.48	5.29	0.54	0.00	0.02	100.14	Lab	52
		Margin	54.86	0.09	28.32	0.10	0.00	0.01	11.11	5.11	0.44	0.00	0.03	100.07	Lab	55
		Interm	53.20	0.13	27.76	0.18	0.00	0.03	11.52	4.86	0.38	0.00	0.05	98.11	Lab	57
		Interm	53.40	0.02	28.26	0.17	0.00	0.02	11.93	4.61	0.32	0.00	0.02	98.75	Lab	59
		Margin	53.12	0.10	28.13	0.21	0.01	0.14	11.66	4.63	0.34	0.00	0.01	98.34	Lab	58
		Interm	54.48	0.04	28.05	0.15	0.01	0.03	11.05	4.97	0.41	0.00	0.01	99.20	Lab	55
		Interm	53.46	0.04	28.36	0.16	0.02	0.01	11.68	4.74	0.30	0.00	0.00	98.77	Lab	58
		Interm	54.60	0.00	28.30	0.17	0.00	0.01	11.23	4.92	0.36	0.00	0.02	99.61	Lab	56
		Interm	55.02	0.05	28.10	0.25	0.01	0.01	10.70	5.11	0.40	0.00	0.06	99.70	Lab	54
		Core	54.81	0.02	27.73	0.16	0.02	0.00	10.72	5.16	0.35	0.00	0.01	98.96	Lab	53
		Core	55.00	0.00	27.95	0.13	0.01	0.01	10.81	5.25	0.35	0.00	0.01	99.54	Lab	53
		Core	54.73	0.01	27.94	0.14	0.00	0.03	11.06	5.02	0.41	0.00	0.00	99.34	Lab	55
		Margin	53.53	0.01	28.41	0.17	0.00	0.00	11.62	4.69	0.35	0.00	0.00	98.78	Lab	58
		Core	54.42	0.00	27.77	0.18	0.00	0.00	11.07	4.98	0.41	0.00	0.00	98.84	Lab	55
		Core	54.44	0.00	27.61	0.17	0.01	0.02	11.08	5.15	0.46	0.02	0.00	98.96	Lab	54
		Core	54.40	0.07	27.77	0.17	0.00	0.02	10.83	5.03	0.41	0.00	0.03	98.72	Lab	54
		Core	53.87	0.07	27.82	0.23	0.02	0.01	11.13	4.98	0.40	0.01	0.07	98.60	Lab	55
		Margin	53.47	0.01	28.42	0.15	0.02	0.01	11.84	4.75	0.28	0.00	0.03	98.98	Lab	58
		Margin	53.55	0.04	28.98	0.14	0.00	0.02	11.89	4.64	0.24	0.00	0.04	99.53	Lab	59
		Interm	53.89	0.01	28.33	0.17	0.00	0.01	11.66	4.77	0.36	0.01	0.00	99.20	Lab	57
		Core	53.82	0.06	28.06	0.18	0.00	0.01	11.32	4.83	0.44	0.00	0.04	98.75	Lab	56
		Core	54.39	0.03	28.01	0.18	0.00	0.01	11.15	4.96	0.37	0.00	0.03	99.12	Lab	55
		Core	54.37	0.09	28.32	0.16	0.00	0.01	11.38	4.89	0.38	0.00	0.06	99.67	Lab	56
	KAC 067/065 B	Interm	53.69	0.04	28.37	0.15	0.00	0.02	11.65	4.76	0.35	0.02	0.00	99.05	Lab	57
		Margin	52.31	0.01	28.97	0.20	0.01	0.00	12.38	4.19	0.50	0.00	0.04	98.61	Lab	62
		Core	53.74	0.06	27.95	0.15	0.00	0.03	11.18	5.02	0.38	0.00	0.02	98.53	Lab	55
		Core	54.56	0.07	27.93	0.13	0.00	0.02	11.15	5.16	0.40	0.01	0.00	99.43	Lab	54
		Core	54.31	0.13	27.95	0.25	0.00	0.01	11.16	5.04	0.43	0.01	0.07	99.36	Lab	55
		Interm	54.52	0.03	27.79	0.22	0.01	0.00	11.05	5.05	0.43	0.00	0.03	99.12	Lab	55
		Margin	52.93	0.00	28.65	0.38	0.00	0.20	12.04	4.31	0.31	0.00	0.00	98.82	Lab	61
		Margin	52.44	0.03	28.30	0.66	0.01	0.52	11.73	4.43	0.33	0.02	0.02	98.50	Lab	59
		Margin	53.62	0.06	28.52	0.17	0.01	0.01	11.75	4.66	0.34	0.00	0.02	99.16	Lab	58
		Interm	54.24	0.02	28.66	0.16	0.01	0.02	11.35	4.05	1.65	0.00	0.26	100.40	Lab	61
		Core	54.95	0.09	27.83	0.16	0.00	0.01	10.94	5.04	0.40	0.00	0.05	99.47	Lab	55
		Rim	53.92	0.03	28.92	0.16	0.00	0.01	11.65	4.69	0.38	0.00	0.01	99.77	Lab	58
		Interm	53.98	0.04	28.21	0.13	0.01	0.02	11.66	4.90	0.31	0.00	0.06	99.32	Lab	57
		Intern	53.92	0.04	28.08	0.22	0.02	0.07	11.56	4.84	0.47	0.00	0.01	99.23	Lab	57
		Core	54.33	0.05	27.65	0.21	0.01	0.00	10.85	5.03	0.35	0.00	0.03	98.52	Lab	54
		Core	53.97	0.00	27.77	0.16	0.00	0.01	11.07	5.02	0.43	0.00	0.03	98.47	Lab	55
		Core	53.97	0.05	27.89	0.23	0.01	0.03	11.02	5.05	0.39	0.01	0.06	98.70	Lab	55
		Core	54.45	0.03	27.98	0.24	0.02	0.11	11.15	5.02	0.44	0.00	0.00	99.44	Lab	55
		Intermed	54.11	0.05	27.93	0.13	0.00	0.02	11.22	4.90	0.40	0.00	0.04	98.80	Lab	56
		Margin	53.41	0.03	28.63	0.20	0.00	0.01	11.76	4.61	0.33	0.00	0.00	98.98	Lab	59
		Interm	53.94	0.04	28.46	0.16	0.00	0.02	11.61	4.81	0.36	0.00	0.02	99.42	Lab	57
		Core	54.81	0.02	28.28	0.20	0.00	0.02	11.17	5.06	0.44	0.00	0.00	100.00	Lab	55
		Interm	54.32	0.04	28.63	0.19	0.00	0.02	11.25	4.82	0.38	0.00	0.00	99.65	Lab	56
		Interm	53.90	0.00	28.41	0.16	0.00	0.00	11.69	4.74	0.36	0.01	0.03	99.30	Lab	58

		Comment	SiO_2	TiO_2	Al_2O_3	FeO*	MnO	MgO	CaO	Na_2O	K_2O	Cr_2O_3	BaO	Total	Name	An
Leucogabbronorites	KAC 069/067 A	Incl in mgxst	55.98	0.02	26.72	0.17	0.01	0.00	9.73	5.78	0.48	0.00	0.05	98.94	And	48
		Incl in mgxst	55.42	0.04	26.94	0.55	0.02	0.01	10.35	5.63	0.44	0.00	0.02	99.42	Lab	50
		Incl in mgxst	54.93	0.02	27.23	0.39	0.00	0.00	10.69	5.42	0.32	0.01	0.02	99.03	Lab	52
		Incl/Lam	54.64	0.01	27.82	0.30	0.00	0.00	11.09	5.18	0.36	0.00	0.01	99.41	Lab	54
		Incl/Lam	54.78	0.02	27.78	0.31	0.00	0.01	11.26	5.12	0.36	0.01	0.00	99.65	Lab	55
		Incl/Lam	54.53	0.04	27.79	0.28	0.00	0.02	11.39	5.20	0.33	0.00	0.00	99.58	Lab	55
	KAC 083/076	margin	54.79	0.02	27.78	0.17	0.00	0.02	11.03	5.31	0.43	0.00	0.03	99.58	Lab	53
		Interm	54.42	0.05	27.23	0.23	0.01	0.08	10.82	5.25	0.43	0.00	0.01	98.53	Lab	53
		Core	54.72	0.05	27.46	0.21	0.00	0.00	10.75	5.24	0.45	0.00	0.06	98.94	Lab	53
		margin	53.27	0.00	27.92	0.15	0.01	0.00	11.45	5.08	0.29	0.00	0.01	98.18	Lab	55
		Interm	54.42	0.03	27.54	0.17	0.00	0.01	10.98	5.15	0.46	0.00	0.03	98.79	Lab	54
		Core	54.50	0.11	27.66	0.18	0.00	0.02	10.88	5.36	0.39	0.00	0.01	99.11	Lab	53
		Core	54.50	0.02	27.68	0.19	0.00	0.02	11.07	5.24	0.35	0.00	0.02	99.09	Lab	54
		Margin	53.99	0.01	27.98	0.16	0.00	0.02	11.42	5.02	0.35	0.01	0.04	99.00	Lab	56
		Core	54.44	0.03	27.80	0.18	0.00	0.00	11.01	5.19	0.47	0.00	0.05	99.17	Lab	54
		Core	54.52	0.03	27.40	0.22	0.00	0.01	10.85	5.17	0.52	0.00	0.00	98.72	Lab	54
		Core	54.52	0.02	27.58	0.19	0.00	0.00	10.86	5.26	0.45	0.00	0.00	98.88	Lab	53
		Margin	54.06	0.06	27.55	0.21	0.00	0.00	11.11	5.12	0.38	0.00	0.06	98.55	Lab	55
		Core	54.61	0.03	27.75	0.18	0.00	0.02	10.98	5.28	0.41	0.00	0.03	99.29	Lab	53
		Interm	54.24	0.03	27.20	0.26	0.01	0.01	10.60	5.47	0.45	0.01	0.05	98.33	Lab	52
		Margin	55.35	0.02	27.34	0.19	0.00	0.01	10.73	5.50	0.42	0.01	0.01	99.58	Lab	52
		Interm	55.00	0.03	27.45	0.18	0.00	0.01	10.73	5.40	0.45	0.00	0.05	99.30	Lab	52
		Interm	54.96	0.06	27.20	0.23	0.00	0.01	10.58	5.50	0.52	0.00	0.00	99.06	Lab	52
		Interm	54.97	0.00	27.39	0.20	0.00	0.01	10.59	5.52	0.49	0.00	0.04	99.21	Lab	51
		Margin	55.17	0.05	27.34	0.18	0.00	0.00	10.65	5.41	0.45	0.00	0.00	99.25	Lab	52
	KAC 147/142	Margin	53.89	0.05	28.10	0.34	0.02	0.03	11.44	4.93	0.52	0.01	0.01	99.34	Lab	56
		Margin	53.78	0.04	28.06	0.25	0.02	0.04	11.62	4.88	0.42	0.02	0.04	99.17	Lab	57
		Core	55.10	0.04	27.38	0.14	0.00	0.01	10.64	5.33	0.50	0.00	0.03	99.17	Lab	52
		Interm	54.94	0.06	27.60	0.13	0.00	0.00	10.86	5.44	0.24	0.02	0.07	99.36	Lab	52
		Margin	54.11	0.03	28.00	0.15	0.01	0.02	11.28	5.07	0.40	0.00	0.01	99.08	Lab	55
		Margin	52.02	0.03	26.86	2.50	0.08	1.34	10.41	4.54	0.40	0.00	0.03	98.21	Lab	56
		Margin	54.30	0.03	28.20	0.09	0.00	0.00	11.45	5.14	0.17	0.00	0.02	99.40	Lab	55
		Core	55.13	0.06	27.43	0.13	0.01	0.01	10.68	5.49	0.37	0.00	0.01	99.32	Lab	52
		Margin	53.84	0.02	28.21	0.17	0.02	0.02	11.72	4.83	0.37	0.00	0.00	99.20	Lab	57
		Margin	54.14	0.06	28.16	0.16	0.00	0.01	11.59	5.09	0.27	0.00	0.05	99.53	Lab	56
		Core	55.40	0.05	27.42	0.17	0.00	0.01	10.63	5.41	0.47	0.00	0.05	99.61	Lab	52
		Core	55.16	0.04	27.57	0.10	0.00	0.02	10.66	5.58	0.33	0.00	0.05	99.51	Lab	51
		Core	54.42	0.02	27.82	0.18	0.01	0.02	11.28	5.18	0.48	0.00	0.07	99.48	Lab	55
		Margin	54.70	0.03	27.74	0.15	0.00	0.01	11.15	5.10	0.54	0.00	0.01	99.43	Lab	55
		Core	55.16	0.06	27.65	0.20	0.00	0.03	11.10	5.25	0.47	0.00	0.00	99.92	Lab	54
		Core	55.01	0.03	27.75	0.22	0.01	0.03	10.91	5.31	0.39	0.00	0.06	99.72	Lab	53
		Core	55.43	0.07	27.31	0.16	0.01	0.03	10.68	5.28	0.58	0.01	0.02	99.58	Lab	53
		Core	55.62	0.07	27.32	0.13	0.01	0.02	10.55	5.42	0.57	0.00	0.03	99.74	Lab	52
		Core	55.03	0.06	27.42	0.17	0.01	0.01	10.66	5.31	0.52	0.00	0.00	99.19	Lab	53
		Interm	53.97	0.03	28.15	0.15	0.00	0.00	11.56	4.93	0.45	0.00	0.00	99.24	Lab	56
		Core	55.19	0.03	27.37	0.16	0.00	0.00	10.59	5.29	0.54	0.00	0.03	99.20	Lab	53
		Interm	54.97	0.02	27.96	0.20	0.00	0.03	11.34	4.99	0.52	0.00	0.05	100.08	Lab	56
		Core	55.17	0.06	27.61	0.14	0.00	0.02	10.77	5.44	0.50	0.00	0.02	99.73	Lab	52
		Margin	54.04	0.02	27.06	1.30	0.03	0.58	10.76	5.07	0.49	0.00	0.07	99.42	Lab	54
		Margin	54.82	0.07	27.85	0.14	0.00	0.02	10.98	5.18	0.53	0.00	0.03	99.62	Lab	54
		Margin	55.08	0.03	27.77	0.19	0.01	0.03	10.88	5.22	0.60	0.02	0.01	99.84	Lab	54
	KAC 172/160	Margin	53.67	0.00	28.82	0.12	0.02	0.03	12.32	4.69	0.32	0.00	0.07	100.06	Lab	59
		Interm	54.53	0.03	27.69	0.27	0.00	0.12	11.46	5.06	0.40	0.00	0.01	99.57	Lab	56
		Interm	54.99	0.01	28.00	0.13	0.00	0.02	11.11	4.91	0.86	0.00	0.13	100.16	Lab	56
		Interm	54.95	0.03	28.04	0.18	0.02	0.00	11.28	4.87	0.41	0.00	0.01	99.79	Lab	56
		Core	53.68	0.31	28.06	0.46	0.02	0.01	11.54	4.82	0.47	0.00	0.05	99.42	Lab	57
		Core	55.11	0.05	27.70	0.18	0.00	0.00	11.09	5.10	0.43	0.00	0.00	99.66	Lab	55
		Core	54.07	0.00	28.42	0.19	0.00	0.01	11.72	4.84	0.40	0.02	0.00	99.67	Lab	57
		Core	54.15	0.04	28.49	0.19	0.01	0.01	11.86	4.82	0.43	0.00	0.04	100.04	Lab	58
		Core	54.27	0.01	28.18	0.23	0.02	0.00	11.63	4.90	0.43	0.00	0.02	99.69	Lab	57
		Core	54.09	0.00	28.65	0.17	0.00	0.02	12.03	4.90	0.35	0.01	0.06	100.28	Lab	58
		Core	53.37	0.00	28.64	0.16	0.02	0.01	12.21	4.57	0.35	0.01	0.03	99.37	Lab	60
		Core	54.30	0.04	28.15	0.15	0.00	0.01	11.44	4.93	0.42	0.00	0.01	99.45	Lab	56
		Margin	55.16	0.00	28.07	0.17	0.00	0.01	11.10	5.16	0.46	0.00	0.00	100.13	Lab	54
		Interm	55.23	0.02	27.91	0.21	0.01	0.01	11.08	5.29	0.44	0.00	0.00	100.20	Lab	54
		Interm	55.15	0.02	27.71	0.16	0.00	0.01	11.10	5.26	0.42	0.01	0.01	99.85	Lab	54
		Interm	54.57	0.04	27.73	0.14	0.02	0.01	11.01	5.30	0.41	0.00	0.01	99.24	Lab	53
		Interm	55.04	0.03	27.68	0.26	0.00	0.07	11.03	5.11	0.47	0.00	0.02	99.71	Lab	54
		Core	55.01	0.04	27.69	0.18	0.01	0.01	10.86	5.26	0.46	0.00	0.02	99.54	Lab	53
		Margin	54.95	0.06	27.99	0.22	0.01	0.01	10.94	5.10	0.49	0.00	0.01	99.78	Lab	54

Table B2 Olivine

		Comment	SiO_2	TiO_2	Al_2O_3	FeO*	MnO	MgO	CaO	Na_2O	K_2O	Cr_2O_3	NiO	ZnO	Total	Name	Fo
Leucotroctolites			36.84	0.01	0.02	33.38	0.49	30.60	0.05	0.00	0.01	0.01	0.08	0.03	101.53	Hyal	62
			36.65	0.02	0.01	32.50	0.46	30.59	0.05	0.01	0.00	0.01	0.09	0.03	100.41	Hyal	63
			36.53	0.02	0.01	33.09	0.45	30.42	0.07	0.00	0.00	0.01	0.08	0.04	100.72	Hyal	62
			37.05	0.03	0.00	32.40	0.47	31.13	0.08	0.00	0.00	0.02	0.07	0.02	101.27	Hyal	63
			36.40	0.01	0.02	33.74	0.49	29.36	0.05	0.01	0.00	0.00	0.08	0.04	100.21	Hyal	61
		Interm	36.30	0.01	0.02	34.45	0.47	29.07	0.07	0.02	0.00	0.00	0.08	0.04	100.54	Hyal	60
		Core	36.40	0.02	0.01	34.76	0.47	29.13	0.04	0.00	0.00	0.00	0.07	0.03	100.94	Hyal	60
		Margin	36.21	0.01	0.00	34.44	0.46	29.03	0.06	0.00	0.00	0.00	0.07	0.04	100.32	Hyal	60
			36.14	0.03	0.01	35.06	0.49	28.30	0.04	0.01	0.00	0.02	0.09	0.03	100.21	Hyal	59
			35.91	0.00	0.01	35.39	0.48	28.59	0.06	0.01	0.00	0.02	0.08	0.04	100.58	Hyal	59
		Margin	36.64	0.01	0.00	33.22	0.49	30.23	0.04	0.01	0.01	0.01	0.09	0.03	100.77	Hyal	62
	KAC	Core	36.63	0.01	0.01	33.16	0.43	29.98	0.06	0.00	0.00	0.01	0.08	0.03	100.40	Hyal	62
	012/014	Interm	36.59	0.01	0.01	33.40	0.45	30.19	0.05	0.00	0.00	0.00	0.08	0.02	100.80	Hyal	62
		Core	36.53	0.03	0.02	34.60	0.50	29.26	0.06	0.01	0.00	0.01	0.08	0.03	101.12	Hyal	60
		Margin	36.36	0.00	0.02	34.41	0.49	28.86	0.04	0.00	0.00	0.01	0.08	0.04	100.31	Hyal	60
		Interm	36.34	0.01	0.00	35.34	0.52	28.42	0.06	0.00	0.00	0.00	0.08	0.05	100.82	Hyal	59
		Interm	36.29	0.00	0.00	35.46	0.49	28.40	0.04	0.01	0.00	0.00	0.07	0.05	100.82	Hyal	59
		Margin	37.86	0.00	0.01	26.78	0.36	34.99	0.02	0.01	0.01	0.00	0.16	0.02	100.21	Hyal	70
		Interm	36.30	0.04	0.01	35.12	0.48	28.59	0.05	0.00	0.00	0.00	0.06	0.04	100.70	Hyal	59
		Interm	36.34	0.07	0.00	35.10	0.52	28.54	0.05	0.02	0.00	0.00	0.08	0.04	100.77	Hyal	59
		Core	36.65	0.01	0.00	33.95	0.46	29.73	0.05	0.00	0.01	0.01	0.08	0.03	100.97	Hyal	61
		Margin	36.80	0.01	0.02	33.72	0.44	29.79	0.04	0.00	0.00	0.00	0.07	0.04	100.93	Hyal	61
			36.63	0.00	0.01	33.34	0.47	30.25	0.04	0.01	0.00	0.01	0.08	0.03	100.88	Hyal	62
			36.71	0.01	0.00	33.00	0.48	30.22	0.06	0.01	0.01	0.01	0.08	0.03	100.61	Hyal	62
			38.43	0.02	0.01	24.17	0.34	37.82	0.02	0.00	0.00	0.00	0.17	0.01	100.99	Chrys	74
			38.30	0.02	0.00	24.17	0.36	37.72	0.02	0.01	0.00	0.00	0.17	0.02	100.79	Chrys	74
			38.69	0.00	0.02	24.02	0.32	37.64	0.02	0.00	0.00	0.00	0.17	0.02	100.90	Chrys	74
		Margin	38.15	0.00	0.01	24.15	0.32	38.00	0.01	0.00	0.00	0.01	0.16	0.02	100.83	Chrys	74
	KAC	Core	38.15	0.00	0.02	24.35	0.32	37.75	0.01	0.02	0.00	0.01	0.16	0.03	100.82	Chrys	73
	017/022	Margin	38.35	0.01	0.00	23.70	0.31	38.12	0.01	0.01	0.00	0.00	0.17	0.01	100.69	Chrys	74
			38.31	0.01	0.00	24.54	0.34	37.58	0.02	0.00	0.01	0.00	0.18	0.02	101.01	Chrys	73
			38.65	0.00	0.00	24.32	0.32	37.85	0.03	0.00	0.00	0.00	0.17	0.02	101.36	Chrys	74
			38.32	0.01	0.01	24.34	0.36	37.78	0.03	0.00	0.00	0.01	0.17	0.02	101.05	Chrys	73
		Margin	38.40	0.00	0.00	24.24	0.33	37.74	0.02	0.00	0.00	0.00	0.17	0.02	100.92	Chrys	74
		Core	38.21	0.00	0.01	24.36	0.34	37.26	0.03	0.01	0.00	0.00	0.17	0.02	100.41	Chrys	73
	KAC		35.64	0.00	0.02	38.21	0.46	26.39	0.03	0.00	0.00	0.00	0.01	0.03	100.79	Hyal	55
	081/075		35.42	0.00	0.02	38.31	0.44	25.88	0.02	0.01	0.00	0.00	0.01	0.01	100.12	Hyal	55
		Margin	38.57	0.00	0.00	23.77	0.32	37.49	0.03	0.02	0.01	0.00	0.16	0.02	100.39	Chrys	74
		Near symp	38.19	0.01	0.00	24.58	0.36	36.92	0.02	0.00	0.01	0.00	0.15	0.01	100.26	Chrys	73
		Rimmed by Cpx	38.28	0.01	0.00	25.00	0.37	36.81	0.04	0.00	0.01	0.00	0.16	0.03	100.71	Chrys	72
		Core	37.89	0.03	0.00	25.18	0.34	36.20	0.02	0.00	0.00	0.00	0.15	0.01	99.82	Chrys	72
		Interm	38.21	0.00	0.00	25.21	0.41	36.42	0.02	0.01	0.01	0.01	0.15	0.03	100.49	Chrys	72
		Interm	38.20	0.01	0.00	24.49	0.35	36.51	0.02	0.00	0.00	0.00	0.16	0.02	99.77	Chrys	73
	KAC	Core	38.19	0.01	0.00	24.75	0.35	36.30	0.04	0.00	0.00	0.01	0.15	0.01	99.81	Chrys	72
	099/093	Margin	38.25	0.02	0.00	25.05	0.39	36.61	0.04	0.02	0.00	0.00	0.16	0.02	100.55	Chrys	72
		Margin	38.30	0.00	0.01	25.10	0.39	36.57	0.05	0.00	0.01	0.01	0.15	0.02	100.62	Chrys	72
		Core	38.34	0.01	0.01	24.68	0.39	36.54	0.05	0.01	0.00	0.00	0.16	0.01	100.21	Chrys	73
		Margin	38.09	0.01	0.01	24.88	0.38	36.58	0.02	0.01	0.01	0.01	0.15	0.03	100.17	Chrys	72
		Core	38.17	0.00	0.00	25.17	0.36	36.39	0.04	0.01	0.04	0.00	0.15	0.02	100.35	Chrys	72
		Margin	38.65	0.02	0.01	24.48	0.36	37.35	0.02	0.00	0.01	0.00	0.17	0.03	101.09	Chrys	73
		Interm	38.09	0.00	0.00	25.12	0.39	36.56	0.04	0.00	0.00	0.00	0.16	0.02	100.38	Chrys	72
		Core	38.23	0.01	0.00	24.88	0.35	36.49	0.02	0.00	0.00	0.00	0.16	0.02	100.20	Chrys	72
	KAC		37.50	0.01	0.01	26.51	0.40	35.76	0.02	0.00	0.00	0.00	0.10	0.03	100.34	Chrys	71
	114/104		37.87	0.00	0.00	25.87	0.35	36.02	0.03	0.00	0.01	0.00	0.10	0.03	100.28	Chrys	71
			38.72	0.02	0.00	25.25	0.36	36.86	0.03	0.01	0.00	0.00	0.14	0.01	101.40	Chrys	72
		Core	38.27	0.00	0.01	25.41	0.37	36.55	0.03	0.00	0.00	0.01	0.15	0.02	100.82	Chrys	72
		Margin	38.12	0.00	0.01	25.44	0.35	36.44	0.02	0.01	0.00	0.01	0.14	0.02	100.56	Chrys	72
		Core	38.23	0.01	0.00	25.69	0.36	36.79	0.02	0.02	0.01	0.00	0.14	0.02	101.29	Chrys	72
	KAC	Margin	38.27	0.01	0.00	25.44	0.34	36.67	0.02	0.00	0.00	0.00	0.14	0.04	100.93	Chrys	72
	122/111	Core	37.83	0.01	0.01	25.48	0.36	36.75	0.02	0.01	0.01	0.00	0.13	0.02	100.63	Chrys	72
		Margin	38.21	0.00	0.01	25.38	0.34	36.69	0.02	0.00	0.00	0.00	0.13	0.03	100.81	Chrys	72
			38.28	0.01	0.01	25.71	0.34	36.80	0.02	0.01	0.00	0.00	0.14	0.02	101.34	Chrys	72
			38.12	0.00	0.01	25.56	0.34	36.60	0.01	0.00	0.00	0.00	0.16	0.04	100.84	Chrys	72
			38.03	0.00	0.01	25.41	0.38	36.62	0.01	0.00	0.01	0.00	0.14	0.03	100.64	Chrys	72
		Rimmed by Opx	37.86	0.02	0.01	26.90	0.36	35.61	0.02	0.00	0.00	0.00	0.16	0.03	100.97	Chrys	70
	KAC	Rimmed by Opx	38.59	0.01	0.01	26.89	0.38	36.46	0.01	0.02	0.00	0.00	0.14	0.03	102.54	Chrys	71
	135/124	Rimmed by Opx	37.72	0.02	0.00	26.60	0.38	36.10	0.02	0.00	0.00	0.01	0.14	0.03	101.02	Chrys	71
		Rimmed by Opx	37.62	0.01	0.00	27.06	0.37	35.37	0.02	0.00	0.00	0.02	0.13	0.03	100.63	Hyal	70
		Rimmed by Opx	37.72	0.00	0.00	27.29	0.39	35.45	0.01	0.01	0.00	0.01	0.13	0.01	101.02	Hyal	70
	KAC	Core	36.19	0.01	0.01	35.35	0.45	28.58	0.03	0.00	0.00	0.03	0.06	0.01	100.72	Hyal	59
	139/127	Margin	36.27	0.01	0.02	35.26	0.46	28.82	0.03	0.00	0.00	0.00	0.05	0.03	100.95	Hyal	59

		Comment	SiO_2	TiO_2	Al_2O_3	FeO*	MnO	MgO	CaO	Na_2O	K_2O	Cr_2O_3	NiO	ZnO	Total	Name	Fo
Leucotroctolite	KAC 151/145 B	Interstitial	37.39	0.00	0.00	30.32	0.41	33.11	0.02	0.01	0.01	0.01	0.09	0.03	101.40	Hyal	66
		Interstitial	37.39	0.00	0.00	29.94	0.43	33.01	0.03	0.00	0.00	0.00	0.09	0.03	100.92	Hyal	66
			37.21	0.01	0.00	30.08	0.45	32.81	0.02	0.01	0.00	0.02	0.08	0.03	100.72	Hyal	66
		Rimmed by Opx	37.50	0.01	0.01	29.97	0.42	33.09	0.02	0.02	0.00	0.00	0.10	0.02	101.16	Hyal	66
		Rimmed by Opx	37.56	0.00	0.01	29.85	0.47	32.95	0.02	0.01	0.00	0.00	0.09	0.02	100.98	Hyal	66
Olivine leucogabbronorites	KAC 047/047		37.67	0.00	0.02	27.45	0.32	34.35	0.02	0.01	0.00	0.00	0.16	0.02	100.02	Hyal	69
			37.75	0.00	0.00	27.73	0.33	34.57	0.02	0.00	0.00	0.01	0.16	0.02	100.58	Hyal	69
			37.79	0.01	0.00	27.53	0.34	34.71	0.01	0.00	0.00	0.00	0.16	0.02	100.58	Hyal	69
			37.91	0.00	0.00	26.52	0.32	35.41	0.02	0.02	0.01	0.00	0.15	0.03	100.39	Chrys	70
			38.08	0.00	0.01	26.42	0.33	35.59	0.03	0.02	0.00	0.00	0.16	0.02	100.66	Chrys	71
			38.24	0.01	0.08	24.92	0.27	34.96	0.03	0.02	0.01	0.00	0.15	0.01	98.70	Chrys	71
			38.11	0.00	0.00	26.31	0.33	35.90	0.02	0.01	0.02	0.00	0.16	0.02	100.89	Chrys	71
		Margin	37.94	0.00	0.00	25.96	0.37	35.74	0.03	0.00	0.01	0.00	0.16	0.01	100.23	Chrys	71
		Interm	37.98	0.00	0.00	26.28	0.35	35.81	0.01	0.00	0.00	0.00	0.16	0.01	100.61	Chrys	71
		Core	37.94	0.00	0.01	26.00	0.36	35.73	0.03	0.00	0.00	0.00	0.18	0.03	100.28	Chrys	71
			38.02	0.00	0.02	26.54	0.37	35.54	0.01	0.01	0.00	0.01	0.17	0.02	100.70	Chrys	70
	KAC 054/053	Margin	37.41	0.00	0.00	26.54	0.33	35.35	0.02	0.01	0.00	0.01	0.15	0.03	99.85	Chrys	70
		Margin	37.77	0.02	0.00	26.41	0.34	35.68	0.01	0.00	0.00	0.00	0.15	0.02	100.40	Chrys	71
		Core	37.55	0.00	0.01	26.55	0.34	35.30	0.02	0.01	0.00	0.00	0.15	0.02	99.95	Chrys	70
		Interstitial	37.44	0.00	0.01	26.40	0.36	35.20	0.04	0.03	0.00	0.00	0.15	0.03	99.66	Chrys	70
		Interstitial	37.26	0.01	0.00	26.45	0.36	35.14	0.03	0.00	0.00	0.01	0.14	0.01	99.41	Chrys	70
		Interstitial	37.49	0.00	0.00	25.94	0.36	35.92	0.02	0.01	0.00	0.01	0.14	0.03	99.92	Chrys	71
	KAC 144/139	Rimmed by Cpx	36.91	0.00	0.00	29.73	0.38	33.31	0.02	0.00	0.01	0.00	0.11	0.04	100.51	Hyal	67
		Rimmed by Cpx	36.57	0.01	0.01	29.14	0.37	33.07	0.01	0.00	0.00	0.00	0.11	0.02	99.31	Hyal	67
		Rimmed by Cpx	37.19	0.01	0.00	29.54	0.37	33.49	0.02	0.00	0.00	0.00	0.10	0.02	100.74	Hyal	67
		Rimmed by Cpx	36.67	0.00	0.00	29.37	0.33	33.33	0.01	0.01	0.00	0.00	0.10	0.03	99.85	Hyal	67
	KAC 147/142	Rimmed by Px	37.74	0.00	0.00	30.89	0.37	32.46	0.02	0.02	0.01	0.01	0.12	0.02	101.66	Hyal	65
		Rimmed by Px	36.49	0.00	0.02	31.78	0.40	31.51	0.02	0.00	0.00	0.00	0.10	0.01	100.33	Hyal	64
		Rimmed by Px	36.97	0.01	0.01	31.37	0.37	31.79	0.02	0.01	0.00	0.00	0.12	0.03	100.70	Hyal	64
		Rimmed by Px	36.75	0.00	0.00	30.89	0.41	32.07	0.02	0.01	0.00	0.01	0.10	0.01	100.27	Hyal	65
		Rimmed by Px	36.90	0.01	0.00	31.18	0.38	31.82	0.02	0.00	0.00	0.01	0.11	0.03	100.46	Hyal	65
		Rimmed by Px	36.68	0.00	0.00	30.91	0.38	32.08	0.01	0.00	0.00	0.01	0.11	0.03	100.21	Hyal	65
		Rimmed by Px	36.51	0.02	0.00	31.39	0.36	31.47	0.01	0.00	0.00	0.00	0.10	0.02	99.88	Hyal	64
		Rimmed by Px	36.71	0.00	0.00	31.10	0.38	31.73	0.00	0.00	0.01	0.00	0.12	0.02	100.07	Hyal	65
		Adj to Ox	37.00	0.02	0.02	31.74	0.40	31.64	0.02	0.00	0.00	0.01	0.11	0.02	100.98	Hyal	64
		Adj to Ox	36.71	0.01	0.02	31.13	0.37	31.36	0.02	0.00	0.00	0.01	0.12	0.02	99.77	Hyal	64
			36.64	0.00	0.01	31.38	0.42	31.42	0.01	0.01	0.00	0.00	0.10	0.01	100.00	Hyal	64
			36.90	0.01	0.01	30.87	0.41	31.79	0.02	0.00	0.00	0.00	0.13	0.02	100.16	Hyal	65
			36.80	0.02	0.01	31.40	0.41	31.75	0.03	0.00	0.00	0.01	0.12	0.03	100.58	Hyal	64
			36.62	0.01	0.00	31.81	0.42	31.34	0.02	0.00	0.00	0.00	0.12	0.03	100.37	Hyal	64
			36.72	0.01	0.00	31.51	0.40	31.70	0.03	0.01	0.01	0.00	0.11	0.03	100.53	Hyal	64
			36.84	0.01	0.00	31.44	0.41	31.66	0.02	0.01	0.00	0.00	0.11	0.02	100.52	Hyal	64

Table B3 Orthopyroxene

		Comment	SiO_2	TiO_2	Al_2O_3	FeO*	MnO	MgO	CaO	Na_2O	K_2O	Cr_2O_3	NiO	ZnO	Total	Name	Mg#
Leucotroctolites	KAC 012/014	Rim on Ol	53.48	0.35	0.95	19.93	0.47	23.45	1.62	0.02	0.00	0.00	0.03	0.04	100.34	En	68
		Rim on Ol	53.10	0.38	0.91	20.43	0.41	23.20	1.40	0.02	0.00	0.00	0.03	0.03	99.90	En	67
		Rim on Ol	53.34	0.22	0.90	20.27	0.42	23.64	1.05	0.02	0.00	0.00	0.01	0.02	99.91	En	68
			53.52	0.25	0.80	20.62	0.45	23.30	1.18	0.01	0.00	0.02	0.01	0.03	100.22	En	67
		Symp with Ox	53.31	0.24	0.87	20.53	0.48	23.45	1.12	0.01	0.00	0.00	0.02	0.02	100.07	En	67
		Symp with Ox	53.79	0.23	0.85	20.63	0.47	23.45	1.07	0.01	0.00	0.00	0.02	0.04	100.56	En	67
			53.49	0.22	0.77	20.25	0.49	23.25	1.30	0.02	0.00	0.00	0.02	0.03	99.86	En	67
		Symp with Ox	53.49	0.28	0.83	20.80	0.47	23.58	0.99	0.02	0.00	0.00	0.02	0.02	100.50	En	67
		Symp with Ox	53.49	0.27	0.82	20.97	0.47	23.53	0.97	0.00	0.00	0.00	0.03	0.03	100.59	En	67
		Rimming Ol	53.84	0.21	2.36	16.12	0.32	26.49	0.90	0.03	0.00	0.01	0.04	0.02	100.32	En	75
		Interm	53.01	0.32	0.91	20.16	0.46	23.02	1.86	0.03	0.00	0.02	0.02	0.03	99.84	En	67
		Interm	53.10	0.37	0.91	20.60	0.45	23.05	1.28	0.02	0.00	0.00	0.02	0.02	99.82	En	67
			53.54	0.33	0.86	20.38	0.46	23.45	1.19	0.02	0.01	0.00	0.02	0.03	100.27	En	67
			53.83	0.22	0.84	19.74	0.48	24.28	0.92	0.01	0.00	0.00	0.01	0.02	100.36	En	69
	KAC 017/022		54.08	0.15	1.78	14.98	0.29	28.05	0.53	0.00	0.00	0.01	0.03	0.01	99.91	En	77
			54.20	0.22	1.99	15.00	0.35	27.71	0.62	0.00	0.00	0.01	0.03	0.00	100.13	En	77
			54.21	0.22	1.73	15.13	0.35	27.82	0.62	0.02	0.01	0.00	0.03	0.03	100.17	En	77
			54.71	0.26	2.04	15.19	0.34	27.96	0.85	0.00	0.00	0.00	0.03	0.02	101.40	En	77
		Rim on Ol	54.35	0.29	1.95	15.09	0.36	27.51	0.76	0.01	0.00	0.00	0.03	0.03	100.38	En	76
		Rim on Ol	54.33	0.27	1.99	15.31	0.36	27.70	0.71	0.01	0.01	0.02	0.03	0.03	100.77	En	76
		Rim on Ol	54.12	0.30	2.07	15.22	0.31	27.72	0.74	0.00	0.00	0.02	0.03	0.02	100.55	En	76
		Rim on Ol	54.17	0.17	1.97	14.89	0.34	27.59	0.90	0.01	0.00	0.03	0.03	0.03	100.13	En	77
		Rim on Ol	53.60	0.14	1.98	14.90	0.29	27.33	0.64	0.01	0.00	0.01	0.02	0.02	98.94	En	77
		Rim on Cpx	54.16	0.19	1.87	16.17	0.37	27.27	0.52	0.01	0.00	0.01	0.03	0.01	100.61	En	75
		Rim on Ol	54.69	0.22	2.13	15.17	0.36	27.98	0.51	0.00	0.00	0.01	0.02	0.01	101.10	En	77
		Rim on Ol	53.92	0.15	1.98	15.47	0.36	27.30	0.45	0.01	0.01	0.00	0.03	0.02	99.70	En	76
		Rim on Ol	53.95	0.14	1.98	15.19	0.36	27.49	0.46	0.00	0.00	0.00	0.03	0.02	99.62	En	76
	KAC 099/093	Rim on Ox	54.23	0.34	1.87	15.01	0.34	27.10	1.00	0.01	0.01	0.01	0.03	0.02	99.97	En	76
		Rim on Ox	53.98	0.37	1.71	15.24	0.37	27.21	1.09	0.03	0.00	0.03	0.03	0.02	100.09	En	76
		Symp with Ox	54.85	0.17	1.62	14.97	0.36	27.77	0.55	0.01	0.01	0.03	0.03	0.02	100.38	En	77
		Rim on Ox	54.52	0.26	1.72	15.28	0.37	27.50	0.83	0.01	0.01	0.02	0.02	0.02	100.54	En	76
		Rim on Ox	54.34	0.36	1.84	14.94	0.34	27.15	0.72	0.01	0.01	0.01	0.03	0.01	99.76	En	76
		Rim on Cpx	53.94	0.25	1.64	16.85	0.41	26.10	0.71	0.01	0.00	0.02	0.03	0.02	99.98	En	73
		Rim on Cpx	53.89	0.32	1.68	16.92	0.42	25.74	0.87	0.00	0.00	0.00	0.04	0.03	99.89	En	73
			54.21	0.24	1.83	15.66	0.36	27.17	0.67	0.01	0.01	0.02	0.03	0.00	100.21	En	76
		Margin	54.13	0.35	1.80	15.56	0.37	26.80	1.06	0.02	0.00	0.02	0.04	0.00	100.15	En	75
	KAC 114/104		54.07	0.28	1.50	16.72	0.37	26.69	0.91	0.01	0.00	0.01	0.01	0.01	100.58	En	74
			54.10	0.19	1.13	17.43	0.35	26.22	0.70	0.01	0.00	0.01	0.02	0.03	100.19	En	73
			53.82	0.20	1.15	17.92	0.37	25.98	0.70	0.01	0.01	0.00	0.02	0.02	100.20	En	72
		Rim on Ol	53.81	0.12	1.52	16.16	0.33	26.60	0.84	0.02	0.00	0.00	0.02	0.02	99.44	En	75
		Rim on Ol	53.79	0.25	1.68	16.29	0.37	26.71	1.05	0.02	0.00	0.00	0.01	0.01	100.18	En	75
			54.12	0.21	0.79	18.59	0.41	25.31	0.71	0.00	0.00	0.01	0.02	0.03	100.20	En	71
			53.98	0.15	0.84	19.35	0.45	24.98	0.54	0.02	0.00	0.00	0.03	0.03	100.37	En	70
		Incl in Plag	53.46	0.23	0.81	19.46	0.40	24.26	0.85	0.03	0.00	0.01	0.03	0.03	99.57	En	69
	KAC 122/111		54.32	0.23	1.43	16.23	0.35	27.05	0.70	0.03	0.01	0.05	0.03	0.02	100.45	En	75
			54.79	0.21	1.50	15.79	0.34	27.40	0.73	0.02	0.00	0.04	0.03	0.02	100.87	En	76
			54.47	0.30	1.64	15.58	0.36	27.47	0.99	0.02	0.00	0.01	0.04	0.02	100.90	En	76
		Rim on Ol	53.92	0.33	1.70	15.85	0.36	26.77	1.06	0.02	0.00	0.02	0.03	0.02	100.08	En	75
		Rim on Ol	54.22	0.27	1.68	15.75	0.33	26.93	0.96	0.02	0.01	0.02	0.03	0.03	100.25	En	75
		Incl in Plag	54.20	0.22	1.61	15.81	0.37	27.20	0.79	0.01	0.00	0.01	0.04	0.00	100.26	En	75
		Incl in Plag	54.02	0.22	1.57	16.87	0.39	26.50	0.75	0.01	0.01	0.01	0.03	0.01	100.39	En	74
		Rim on Ol	54.32	0.24	1.51	15.62	0.36	27.26	0.70	0.00	0.00	0.03	0.03	0.02	100.09	En	76
		Rim on Ol	54.16	0.32	1.76	15.91	0.33	27.07	0.87	0.00	0.00	0.02	0.04	0.03	100.51	En	75
		Rim on Ol	54.23	0.27	1.56	15.76	0.37	27.01	1.03	0.02	0.00	0.02	0.04	0.03	100.34	En	75
		Rim on Ol	54.72	0.19	1.24	15.66	0.33	27.46	0.67	0.01	0.00	0.02	0.03	0.02	100.35	En	76
	KAC 135/124	Rim on Ol	53.84	0.34	1.47	16.46	0.36	26.21	1.02	0.01	0.00	0.01	0.05	0.02	99.79	En	74
		Rim on Ol	54.27	0.23	1.38	16.35	0.34	26.82	0.83	0.01	0.00	0.01	0.04	0.02	100.30	En	75
		Interstitial	54.55	0.19	0.89	17.14	0.40	26.28	0.78	0.01	0.00	0.01	0.03	0.02	100.30	En	73
		Interstitial	54.06	0.27	1.03	17.78	0.38	26.00	0.81	0.01	0.01	0.00	0.03	0.02	100.40	En	72
		Rim on Ol	54.61	0.21	1.07	16.37	0.36	27.01	0.52	0.01	0.00	0.00	0.03	0.02	100.21	En	75
		Rim on Ol	54.27	0.24	0.98	16.83	0.39	26.70	0.66	0.01	0.00	0.02	0.04	0.03	100.17	En	74
		Rim on Ol	50.98	0.03	3.39	16.78	0.45	25.07	0.59	0.00	0.02	0.00	0.02	0.02	97.35	En	73
		Rim on Ol	54.65	0.04	1.14	16.46	0.36	27.33	0.38	0.01	0.00	0.00	0.03	0.03	100.43	En	75
		Interstitial	53.85	0.33	1.24	16.99	0.38	26.17	1.14	0.01	0.00	0.02	0.03	0.03	100.19	En	73
		Interstitial	54.18	0.22	1.17	17.20	0.35	26.22	0.73	0.00	0.00	0.03	0.03	0.03	100.16	En	73
		Interstitial	53.92	0.30	1.34	17.06	0.40	26.04	0.83	0.02	0.00	0.03	0.02	0.01	99.97	En	73
	KAC 139/127	Rim on Ox	52.89	0.24	0.83	22.67	0.47	21.98	0.89	0.02	0.00	0.01	0.02	0.04	100.06	En	63
		Rim on Ox	52.90	0.22	0.83	22.91	0.48	22.09	0.79	0.03	0.00	0.01	0.02	0.03	100.31	En	63
		Rim on Ol	53.57	0.09	1.03	20.36	0.41	23.91	0.65	0.02	0.01	0.00	0.02	0.02	100.09	En	68
			53.26	0.13	1.04	21.08	0.46	23.59	0.67	0.03	0.00	0.00	0.01	0.03	100.30	En	67
			53.02	0.28	0.96	22.39	0.48	22.38	0.91	0.02	0.01	0.01	0.02	0.03	100.51	En	64
			52.97	0.24	0.90	22.17	0.50	22.21	0.81	0.02	0.00	0.00	0.02	0.02	99.86	En	64
		Symp with Ox	53.18	0.22	1.06	21.96	0.50	22.96	0.78	0.02	0.01	0.00	0.01	0.03	100.73	En	65
	KAC 151/145	Rim on Ol	54.30	0.18	1.20	17.84	0.44	25.48	0.78	0.01	0.00	0.01	0.02	0.03	100.29	En	72
		Rim on Ol	54.29	0.15	1.27	18.01	0.39	25.61	0.68	0.01	0.00	0.00	0.03	0.02	100.46	En	72

		Comment	SiO_2	TiO_2	Al_2O_3	FeO*	MnO	MgO	CaO	Na_2O	K_2O	Cr_2O_3	NiO	ZnO	Total	Name	Mg#
Olivine Leucogabbronorites	KAC 047/047	Rim on Ol	53.72	0.16	2.53	16.65	0.35	26.45	0.62	0.01	0.00	0.03	0.04	0.02	100.58	En	74
		Rim on Ol	54.02	0.18	2.11	16.57	0.31	26.57	0.51	0.00	0.00	0.01	0.02	0.00	100.31	En	74
			53.83	0.22	1.97	16.58	0.31	26.30	0.61	0.02	0.00	0.02	0.03	0.02	99.91	En	74
		Core	54.24	0.16	1.87	16.60	0.29	26.54	0.48	0.01	0.00	0.02	0.05	0.00	100.25	En	74
			54.31	0.04	1.84	16.61	0.35	26.35	0.50	0.01	0.00	0.01	0.03	0.01	100.07	En	74
			54.24	0.12	2.09	16.63	0.33	26.44	0.47	0.01	0.00	0.00	0.04	0.01	100.38	En	74
			53.96	0.12	2.29	16.93	0.34	26.11	0.52	0.01	0.01	0.02	0.03	0.02	100.36	En	73
			54.44	0.03	1.98	16.22	0.35	27.06	0.50	0.00	0.01	0.00	0.04	0.03	100.67	En	75
			54.16	0.04	1.76	16.18	0.34	27.02	0.51	0.01	0.00	0.00	0.04	0.03	100.09	En	75
		Rim on Ol	54.58	0.02	1.66	16.26	0.32	26.94	0.38	0.01	0.00	0.00	0.03	0.02	100.22	En	75
		Rim on Ol	53.76	0.22	2.40	16.07	0.33	26.59	0.59	0.01	0.00	0.03	0.04	0.02	100.07	En	75
	KAC 048/048	Megacryst	52.38	0.08	1.29	22.19	0.42	22.34	0.59	0.01	0.00	0.02	0.02	0.05	99.39	En	64
		Megacryst	52.84	0.10	1.13	22.30	0.42	22.37	0.57	0.01	0.00	0.03	0.02	0.03	99.82	En	64
		Megacryst	52.73	0.10	1.36	22.27	0.46	22.41	0.51	0.01	0.00	0.06	0.01	0.02	99.94	En	64
		Megacryst	52.76	0.09	1.04	22.00	0.44	22.42	0.63	0.01	0.01	0.03	0.02	0.04	99.49	En	64
		Megacryst	52.82	0.10	1.40	22.02	0.43	22.16	1.31	0.01	0.00	0.03	0.02	0.03	100.33	En	64
		Megacryst	55.57	0.06	1.09	18.18	0.52	20.75	1.71	0.12	0.02	0.04	0.02	0.04	98.12	En	67
		Megacryst	52.35	0.11	1.84	21.30	0.43	22.58	0.63	0.00	0.00	0.06	0.02	0.04	99.36	En	65
		Megacryst	52.33	0.11	1.72	21.08	0.41	22.34	1.33	0.00	0.00	0.03	0.01	0.03	99.39	En	65
		Megacryst	53.52	0.15	1.69	21.26	0.42	22.16	1.76	0.02	0.01	0.04	0.02	0.03	101.08	En	65
		Megacryst	51.76	0.19	1.99	19.10	0.38	21.44	5.13	0.03	0.00	0.05	0.02	0.02	100.11	En	67
		Megacryst	53.17	0.07	1.21	21.68	0.41	22.76	0.57	0.00	0.00	0.04	0.01	0.02	99.94	En	65
		Megacryst	52.62	0.15	1.88	19.93	0.38	21.15	4.21	0.05	0.00	0.06	0.01	0.01	100.45	En	65
		Megacryst	52.53	0.11	1.76	21.65	0.46	22.24	0.98	0.00	0.00	0.05	0.02	0.04	99.84	En	65
		Megacryst	52.09	0.12	1.84	21.65	0.41	22.36	1.16	0.02	0.00	0.04	0.01	0.03	99.73	En	65
	KAC 054/053	Rim on Ol	53.78	0.02	2.10	16.16	0.31	26.87	0.35	0.01	0.00	0.00	0.03	0.01	99.64	En	75
		Rim on Ol	52.53	0.18	3.13	17.24	0.30	25.86	0.59	0.01	0.00	0.03	0.04	0.02	99.93	En	73
			52.84	0.12	3.01	16.93	0.32	26.08	0.44	0.00	0.00	0.00	0.03	0.00	99.77	En	73
			52.28	0.15	3.59	16.80	0.29	25.38	0.60	0.03	0.01	0.00	0.04	0.01	99.18	En	73
			52.16	0.20	3.06	17.11	0.29	24.91	1.02	0.01	0.00	0.00	0.03	0.02	98.81	En	72
			52.70	0.10	3.07	17.12	0.32	25.93	0.50	0.01	0.00	0.02	0.03	0.02	99.82	En	73
			53.66	0.00	1.65	16.44	0.30	27.02	0.36	0.01	0.00	0.01	0.03	0.03	99.51	En	75
		Rim on Ol	54.60	0.02	1.36	15.57	0.33	27.55	0.26	0.01	0.00	0.02	0.02	0.03	99.77	En	76
		Rim on Ol	54.28	0.01	1.82	16.01	0.31	27.25	0.36	0.01	0.00	0.00	0.04	0.02	100.11	En	75
		Rim on Ox	52.69	0.11	2.59	17.96	0.37	24.96	0.55	0.01	0.00	0.00	0.03	0.01	99.28	En	71
		Rim on Ox	52.81	0.13	2.36	18.16	0.36	25.15	0.52	0.00	0.00	0.02	0.03	0.01	99.55	En	71
		Rim on Ox	52.91	0.11	2.21	18.12	0.35	24.94	0.54	0.01	0.00	0.01	0.03	0.04	99.27	En	71
	KAC 147/142	Rim on Ol	52.31	0.20	2.19	18.50	0.36	24.71	0.78	0.03	0.00	0.05	0.03	0.02	99.18	En	70
		Rim on Ol	52.74	0.18	2.14	18.56	0.38	24.61	0.74	0.02	0.00	0.03	0.02	0.01	99.43	En	70
		Rim on Ol	52.82	0.22	2.05	18.33	0.36	24.57	0.89	0.01	0.01	0.06	0.02	0.01	99.35	En	70
		Rim on Ol	52.08	0.26	2.04	19.11	0.36	24.28	0.88	0.03	0.00	0.04	0.03	0.01	99.12	En	69
Leucogabbronorites	KAC 041/042 A		52.70	0.17	0.66	22.94	0.73	22.01	0.79	0.01	0.00	0.00	0.02	0.04	100.07	En	63
			52.60	0.20	0.94	22.15	0.70	21.57	1.40	0.03	0.00	0.01	0.01	0.04	99.65	En	63
			52.68	0.22	0.89	22.62	0.72	22.02	0.79	0.00	0.01	0.01	0.01	0.04	100.01	En	63
			52.66	0.22	0.78	22.83	0.74	22.25	0.86	0.02	0.00	0.00	0.02	0.05	100.43	En	63
			52.86	0.20	0.72	22.37	0.69	22.30	0.87	0.01	0.00	0.01	0.02	0.04	100.09	En	64
			52.85	0.21	0.92	22.63	0.70	22.34	0.80	0.01	0.00	0.00	0.01	0.03	100.50	En	64
			52.76	0.18	0.92	22.69	0.70	22.20	0.80	0.00	0.00	0.00	0.01	0.05	100.31	En	64
			51.05	3.12	0.66	23.92	0.70	21.78	0.79	0.02	0.00	0.00	0.02	0.06	102.12	En	62
			52.64	0.18	0.86	22.55	0.77	22.30	1.16	0.01	0.00	0.01	0.03	0.03	100.54	En	64
			52.89	0.19	0.83	22.63	0.69	22.04	0.96	0.00	0.00	0.00	0.02	0.05	100.30	En	63
			52.90	0.18	0.84	22.65	0.66	22.35	0.75	0.00	0.00	0.01	0.02	0.04	100.40	En	64
			52.69	0.23	0.92	22.92	0.74	22.08	0.80	0.01	0.00	0.01	0.01	0.04	100.45	En	63
	KAC 067/065 B		52.83	0.13	2.02	19.32	0.39	24.62	0.69	0.01	0.00	0.07	0.04	0.03	100.16	En	69
			52.82	0.14	2.18	18.95	0.35	24.12	0.82	0.02	0.00	0.05	0.05	0.03	99.54	En	69
		Margin	53.01	0.14	1.79	19.05	0.39	24.61	0.52	0.01	0.00	0.05	0.03	0.02	99.61	En	70
			52.83	0.14	2.31	19.91	0.39	23.82	0.51	0.03	0.01	0.04	0.03	0.03	100.05	En	68
			53.45	0.17	1.94	18.99	0.38	24.46	0.63	0.02	0.00	0.05	0.04	0.01	100.14	En	70
		Margin	53.30	0.16	1.69	18.75	0.38	24.84	0.57	0.01	0.01	0.04	0.02	0.02	99.78	En	70
		Margin	53.16	0.20	1.77	19.38	0.38	24.51	0.57	0.00	0.00	0.07	0.04	0.03	100.12	En	69
			53.57	0.09	1.70	18.89	0.34	24.88	0.45	0.01	0.01	0.06	0.04	0.02	100.06	En	70
			53.41	0.16	1.87	17.87	0.38	24.79	1.18	0.01	0.00	0.07	0.04	0.02	99.81	En	71
		Core	53.38	0.11	1.67	19.01	0.34	24.80	0.43	0.03	0.00	0.06	0.04	0.01	99.87	En	70
		Margin	53.51	0.10	1.45	18.31	0.39	24.59	1.35	0.02	0.00	0.06	0.03	0.03	99.83	En	71
			52.98	0.12	1.93	19.19	0.38	24.56	0.65	0.01	0.00	0.03	0.04	0.02	99.91	En	70
			53.69	0.17	1.08	18.34	0.48	25.32	0.57	0.01	0.00	0.04	0.03	0.02	99.75	En	71
		Interm	53.02	0.15	1.87	19.50	0.37	24.08	0.58	0.02	0.00	0.04	0.03	0.02	99.69	En	69
		Margin	53.47	0.15	1.92	18.43	0.37	24.97	0.68	0.01	0.00	0.03	0.04	0.01	100.10	En	71
	KAC 069/067 A	Incl in mgxst	51.72	0.13	2.34	22.15	0.50	22.00	0.56	0.01	0.00	0.05	0.03	0.04	99.53	En	64
		Incl in mgxst	51.57	0.12	2.48	22.27	0.50	21.67	0.91	0.01	0.01	0.06	0.03	0.01	99.64	En	63
		Incl in mgxst	51.48	0.10	2.60	22.59	0.45	21.94	0.52	0.01	0.00	0.05	0.02	0.03	99.79	En	63
		Incl/Lamellae	52.36	0.11	1.23	22.51	0.55	22.17	0.59	0.02	0.00	0.06	0.03	0.02	99.65	En	64
		Incl/Lamellae	51.50	0.26	1.66	22.81	0.49	21.58	0.60	0.02	0.00	0.07	0.04	0.02	99.05	En	63
		Incl/Lamellae	50.99	0.13	2.65	23.55	0.52	21.25	0.60	0.00	0.01	0.07	0.04	0.03	99.84	En	62
		Incl/Lamellae	51.70	0.14	2.74	22.61	0.51	21.54	0.60	0.03	0.00	0.06	0.04	0.03	100.00	En	63
		Incl/Lamellae	51.20	0.15	2.81	23.30	0.47	21.17	0.59	0.01	0.00	0.06	0.04	0.01	99.81	En	62
		Incl/Lamellae	51.11	0.14	2.72	22.98	0.52	21.22	0.55	0.01	0.00	0.07	0.03	0.04	99.39	En	62
		Incl/Lamellae	51.22	0.12	2.68	23.07	0.48	21.45	0.61	0.01	0.00	0.05	0.04	0.04	99.77	En	62

Table B4 Clinopyroxene

		Comment	SiO_2	TiO_2	Al_2O_3	FeO*	MnO	MgO	CaO	Na_2O	K_2O	Cr_2O_3	NiO	ZnO	Total	Name	Mg#
Leucotroctolites	KAC 012/014	In Ox oik	51.69	0.74	2.22	8.42	0.23	14.57	21.85	0.33	0.01	0.03			100.12	Aug	76
		Rim on Ox	51.73	0.56	2.11	8.93	0.21	14.36	21.79	0.31	0.01	0.03			100.05	Aug	74
		In Ox oik	50.83	1.05	2.32	8.73	0.22	14.04	21.71	0.38	0.00	0.04	0.02	0.00	99.35	Di	74
		In Ox oik	51.67	0.60	1.97	8.76	0.24	14.50	21.69	0.30	0.00	0.04	0.02	0.02	99.83	Aug	75
			50.86	0.89	2.68	9.12	0.27	14.01	21.23	0.34	0.00	0.03	0.02	0.00	99.45	Aug	73
		Rim on Ol	51.79	0.71	2.13	8.69	0.25	14.48	21.78	0.34	0.00	0.05	0.01	0.02	100.25	Aug	75
		Rim on Ol	51.54	0.65	2.04	8.84	0.25	14.63	21.12	0.33	0.00	0.03	0.02	0.01	99.46	Aug	75
		Interm	51.11	0.89	2.42	9.11	0.26	14.06	21.26	0.37	0.00	0.01	0.01	0.01	99.53	Aug	73
			51.24	0.77	2.53	8.78	0.25	14.16	21.49	0.35	0.00	0.03	0.01	0.01	99.62	Aug	74
		Interm	50.95	0.94	2.65	8.98	0.26	13.97	21.46	0.38	0.00	0.02	0.03	0.00	99.62	Aug	73
		Rim on Ol	50.50	0.91	3.97	6.45	0.14	14.27	22.89	0.41	0.01	0.08	0.02	0.00	99.65	Di	80
			51.66	0.78	2.12	8.90	0.22	14.46	21.36	0.35	0.00	0.03	0.00	0.01	99.89	Aug	74
			51.05	0.82	2.13	9.21	0.24	14.27	21.10	0.35	0.00	0.01	0.02	0.01	99.21	Aug	73
		Rim on Ol	51.86	0.57	1.92	8.61	0.25	14.63	21.96	0.32	0.00	0.04	0.01	0.02	100.18	Aug	75
		In Ox oik	51.81	0.56	2.09	8.39	0.23	14.62	22.00	0.31	0.00	0.06	0.01	0.03	100.12	Aug	76
	KAC 017/022	Incl in Plag	50.71	0.95	3.61	7.36	0.20	14.23	22.28	0.45	0.00	0.04	0.02	0.01	99.86	Di	78
		Incl in Plag	51.69	0.57	2.48	7.10	0.18	14.44	22.80	0.40	0.01	0.00	0.03	0.00	99.70	Di	78
		Incl in Plag	51.95	0.48	2.37	7.41	0.21	15.03	22.08	0.42	0.01	0.00	0.02	0.00	99.98	Di	78
		Incl in Plag	52.55	0.27	1.62	7.82	0.17	14.06	23.43	0.36	0.01	0.00	0.03	0.00	100.32	Di	76
		Incl in Plag	50.99	0.97	3.62	6.62	0.22	14.38	22.84	0.44	0.01	0.04	0.02	0.01	100.16	Di	79
		Incl in Plag	49.64	1.04	4.80	6.91	0.15	14.38	21.32	0.38	0.02	0.05	0.05	0.01	98.75	Di	79
		Surr by Opx	51.32	0.95	3.65	7.59	0.18	16.13	19.92	0.42	0.00	0.08	0.03	0.00	100.27	Aug	79
			52.02	0.62	3.36	9.44	0.22	16.07	19.41	0.29	0.01	0.10	0.03	0.01	101.58	Aug	75
			50.86	0.83	3.54	7.83	0.21	14.97	20.74	0.43	0.00	0.16	0.02	0.01	99.60	Aug	77
			50.95	0.90	3.82	8.36	0.21	15.41	20.18	0.45	0.00	0.15	0.03	0.00	100.46	Aug	77
	KAC 099/093	Margin	50.61	0.93	3.38	6.73	0.16	14.95	22.58	0.29	0.00	0.01	0.02	0.01	99.66	Di	80
		Interm	51.00	0.91	2.96	7.33	0.21	15.06	21.96	0.28	0.01	0.02	0.02	0.01	99.77	Di	79
		Symp with Ox	51.25	0.73	2.78	6.49	0.16	15.09	22.71	0.23	0.00	0.00	0.02	0.01	99.46	Di	81
		Rim on Ol	50.93	0.80	2.97	6.94	0.20	14.95	22.44	0.29	0.01	0.04	0.02	0.00	99.58	Di	79
		Rim on Ol	50.90	0.89	3.22	6.87	0.22	14.74	22.82	0.28	0.00	0.03	0.02	0.00	100.00	Di	79
		Core	50.69	0.96	3.48	7.27	0.22	14.39	22.34	0.38	0.01	0.05	0.02	0.00	99.81	Di	78
		Margin	51.06	0.89	3.23	7.12	0.20	14.57	22.44	0.36	0.03	0.05	0.03	0.00	99.97	Di	78
		Core	51.03	0.87	3.39	7.39	0.21	15.76	20.79	0.29	0.01	0.04	0.02	0.01	99.80	Aug	79
		Margin	49.09	0.88	3.27	6.78	0.21	14.83	22.88	0.30	0.01	0.02	0.02	0.00	98.30	Di	80
		Rim on Ol	50.45	1.00	3.41	6.67	0.19	14.90	22.30	0.30	0.02	0.04	0.02	0.01	99.30	Di	80
		Tiny relict	52.38	0.38	2.49	5.93	0.18	14.90	23.58	0.22	0.01	0.00	0.03	0.00	100.12	Di	82
		Rim on Ol	51.69	0.48	2.49	5.89	0.15	15.32	23.39	0.26	0.02	0.02	0.02	0.02	99.75	Di	82
		Rim on Ol	48.39	0.19	17.82	3.67	0.10	8.42	21.75	0.45	0.02	0.03	0.01	0.00	100.85	Di	80
	KAC 114/104	With Ox	51.06	0.74	2.61	8.59	0.20	14.51	21.34	0.33	0.01	0.02	0.01	0.00	99.42	Aug	75
		With Ox	50.79	0.79	2.64	10.11	0.21	15.25	19.47	0.29	0.02	0.00	0.03	0.01	99.61	Aug	73
		With Ox	50.16	0.94	2.95	8.10	0.25	14.13	22.14	0.40	0.01	0.01	0.01	0.01	99.11	Di	76
	KAC 122/111	Margin	51.31	0.80	3.16	6.97	0.19	14.77	22.22	0.39	0.00	0.15	0.02	0.00	99.98	Di	79
		Margin	51.15	0.84	3.22	7.66	0.21	15.62	20.75	0.35	0.01	0.14	0.02	0.02	99.99	Aug	78
	KAC 151/145B	Rim on Ol	52.72	0.36	1.95	6.60	0.22	15.09	22.59	0.23	0.00	0.05	0.01	0.01	99.83	Di	80
Olivine Leucogabbronorites	KAC 047/047	Relict grain	52.01	0.34	2.76	6.75	0.12	14.42	23.55	0.36	0.00	0.00	0.01	0.00	100.35	Di	79
		Relict grain	50.81	0.60	3.63	7.00	0.17	13.84	23.50	0.38	0.00	0.00	0.03	0.00	99.95	Di	78
		Relict grain	51.65	0.39	2.59	6.93	0.16	14.04	23.65	0.34	0.00	0.00	0.02	0.01	99.78	Di	78
		Relict grain	50.35	0.85	3.71	7.11	0.15	13.80	22.77	0.48	0.00	0.02	0.03	0.01	99.27	Di	78
	KAC 048/048	Incl in mgxst	51.84	0.32	1.92	7.88	0.16	13.97	23.08	0.26	0.00	0.11	0.01	0.00	99.55	Di	76
		Incl in mgxst	52.42	0.29	1.77	8.06	0.20	14.18	23.09	0.30	0.00	0.08	0.01	0.01	100.41	Di	76
	KAC 144/139	Rim on Ol	49.76	0.89	3.72	7.52	0.17	14.12	22.17	0.50	0.01	0.04	0.02	0.00	98.92	Di	77
		Rim on Ol	50.07	0.95	3.73	7.30	0.20	14.13	22.34	0.47	0.00	0.01	0.02	0.00	99.22	Di	78
		Rim on Ol	49.84	0.66	3.28	8.43	0.18	15.06	20.69	0.41	0.01	0.00	0.01	0.01	98.58	Aug	76
		Rim on Ol	50.18	0.73	3.46	7.31	0.18	14.05	22.44	0.42	0.00	0.00	0.01	0.00	98.79	Di	77
		Rim on Ol	50.38	0.86	3.70	7.35	0.15	14.14	22.30	0.47	0.01	0.03	0.02	0.01	99.42	Di	77
	KAC 147/142	Rim on Ol	50.82	0.77	3.56	7.84	0.19	13.94	22.57	0.47	0.00	0.09	0.01	0.00	100.26	Di	76
		Interstitial	50.28	0.85	3.74	8.30	0.20	13.46	22.07	0.46	0.01	0.11	0.02	0.00	99.50	Di	74
		Interstitial	49.83	0.96	3.95	8.03	0.18	13.33	22.28	0.58	0.00	0.14	0.02	0.00	99.30	Di	75
		Interstitial	50.59	0.69	3.31	8.40	0.19	13.92	21.84	0.44	0.00	0.07	0.01	0.01	99.47	Di	75
		Interstitial	50.26	0.96	3.86	8.33	0.18	13.50	21.62	0.56	0.00	0.11	0.02	0.01	99.41	Di	74
		Incl in Pl	49.95	1.01	3.96	8.21	0.19	13.33	22.14	0.55	0.00	0.12	0.02	0.01	99.49	Di	74
		Incl in Pl	50.18	0.88	3.64	8.24	0.22	13.43	22.45	0.46	0.00	0.11	0.02	0.00	99.63	Di	74
		Incl in Pl	50.30	0.97	3.88	8.21	0.20	13.45	22.29	0.55	0.00	0.08	0.02	0.01	99.96	Di	74
Leucogabbronorites	KAC 041/042A		51.95	0.35	1.56	8.97	0.37	14.17	22.41	0.31	0.01	0.01	0.01	0.01	100.13	Di	74
			52.04	0.35	1.56	8.92	0.34	13.98	22.31	0.33	0.00	0.02	0.02	0.03	99.90	Di	74
			51.81	0.33	1.70	10.00	0.33	13.63	21.79	0.42	0.00	0.02	0.01	0.00	100.04	Aug	71
			51.58	0.33	1.79	9.66	0.35	13.57	22.04	0.39	0.00	0.01	0.02	0.02	99.76	Di	71
			51.85	0.34	1.50	9.05	0.35	13.91	22.10	0.37	0.04	0.02	0.01	0.03	99.57	Di	73
	KAC 067/065B		50.66	0.84	3.52	7.14	0.16	13.84	22.90	0.44	0.00	0.09	0.02	0.03	99.65	Di	78

		Comment	SiO_2	TiO_2	Al_2O_3	FeO*	MnO	MgO	CaO	Na_2O	K_2O	Cr_2O_3	NiO	ZnO	Total	Name	Mg#
Leucogabbronorites	KAC 069/067A	Megacryst	48.67	0.98	4.91	9.39	0.23	11.91	22.19	0.70	0.00	0.13	0.01	0.03	99.15	Di	69
		Megacryst	49.27	0.90	4.68	9.44	0.24	12.14	21.73	0.73	0.00	0.13	0.02	0.00	99.28	Di	70
		Megacryst	49.05	0.93	4.88	9.19	0.22	12.20	21.97	0.73	0.00	0.09	0.02	0.00	99.28	Di	70
		Megacryst	49.83	0.81	3.95	9.11	0.21	12.36	22.26	0.67	0.01	0.13	0.02	0.01	99.37	Di	71
		Megacryst	49.16	0.86	4.70	9.53	0.21	12.02	22.12	0.77	0.00	0.16	0.02	0.00	99.55	Di	69
		Megacryst	49.08	0.94	4.98	9.51	0.21	11.93	22.18	0.74	0.00	0.14	0.02	0.00	99.73	Di	69
		Megacryst	48.85	0.81	4.81	9.81	0.24	12.53	20.58	0.77	0.00	0.12	0.01	0.01	98.54	Di	69
		Megacryst	49.00	0.85	4.92	9.55	0.21	11.94	21.92	0.76	0.01	0.15	0.03	0.00	99.34	Di	69
		Megacryst	49.17	0.84	4.62	9.55	0.25	12.01	21.89	0.81	0.00	0.14	0.02	0.02	99.32	Di	69
		Megacryst	49.43	0.80	4.24	9.35	0.23	12.51	22.10	0.67	0.00	0.13	0.02	0.00	99.48	Di	70
		Megacryst	49.31	0.89	4.72	10.26	0.26	12.56	20.47	0.73	0.00	0.13	0.02	0.03	99.38	Aug	69
		Megacryst	49.21	0.91	4.60	10.66	0.20	12.47	20.74	0.72	0.01	0.14	0.03	0.00	99.69	Aug	68
	KAC 083/076	Core	49.57	0.77	3.72	10.54	0.24	11.59	22.61	0.54	0.00	0.01	0.01	0.00	99.60	Di	66
		Margin	49.59	0.84	3.62	10.57	0.26	11.46	22.69	0.58	0.00	0.00	0.01	0.00	99.62	Di	66
		Interstitial	49.89	0.58	3.38	10.07	0.25	11.85	22.82	0.53	0.00	0.00	0.02	0.01	99.40	Di	68
		Interstitial	49.38	0.75	3.53	10.44	0.25	11.60	22.79	0.53	0.00	0.01	0.03	0.01	99.32	Di	66
		Incl in Plag	49.16	0.85	3.67	10.84	0.21	11.33	22.60	0.59	0.00	0.00	0.02	0.02	99.29	Di	65
		Incl in Plag	49.37	0.80	3.54	10.64	0.21	11.37	22.49	0.57	0.00	0.00	0.02	0.01	99.02	Di	66
	KAC 172/160	Rim on Ox	50.25	0.76	3.68	8.41	0.25	13.28	22.61	0.45	0.00	0.01	0.02	0.01	99.73	Di	74
		Rim on Ox	49.98	0.68	3.49	8.29	0.18	13.14	23.34	0.39	0.00	0.00	0.01	0.01	99.51	Di	74
		Rim on Ox	50.69	0.69	3.38	8.29	0.22	13.20	22.98	0.44	0.01	0.00	0.01	0.01	99.92	Di	74
		Rim on Ox	50.44	0.65	3.35	8.40	0.22	13.02	23.19	0.40	0.00	0.01	0.03	0.01	99.72	Di	73

Table B5 Detection limits and standard deviations for electron microprobe analyses

		Si	Ti	Al	Fe	Mn	Mg	Ca	Na	K	Cr	Ba	Ni	Zn
Plagioclase	Detection limits (ppm)	157	405	134	365	325	170	300	216	251	297	676	-	-
	Standard deviation (1σ; wt. %)	0.24	0.04	0.15	0.05	0.03	0.02	0.15	0.10	0.06	0.02	0.06	-	-
Mafic silicates	Detection limits (ppm)	170	212	147	348	192	311	171	179	137	277	-	159	232
	Standard deviation (1σ; wt. %)	0.26	0.02	0.04	0.26	0.04	0.17	0.09	0.02	0.01	0.02	-	0.01	0.02

Appendix C

Thermometry calculations

To calculate the temperatures for the experiments, several different thermometers were investigated. The thermometers given in a review paper on barometry and thermometry of volcanic systems were tested (Putrika, 2008). Liquid thermometers, based solely on the MgO contents of the glass (Helz and Thornber, 1987; Yang *et al.* 1996), produced reasonable results, all within ~30°C of each other for each experiment. However, thermometers that use both liquid and mineral compositions can better constrain the temperature. Olivine-liquid thermometers calculate temperature using the partitioning of Mg between olivine and liquid. The olivine-liquid thermometers of Beattie (1993) and Putrika *et al.* (2007) are considered the most precise, for anhydrous and hydrous systems respectively. The Beattie (1993) thermometer is also capable of calculating temperatures for olivine-free systems, using only the liquid composition, and calculating the temperature at which the liquid would be saturated with olivine at a given pressure. For this reason, and the high precision, the Beattie (1993) thermometer was used for the experiments in this study, since the contaminated experiments did not contain olivine. Figure C1 below summarizes the precision of the Beattie (1993) thermometer. Note the high precision for anhydrous systems.

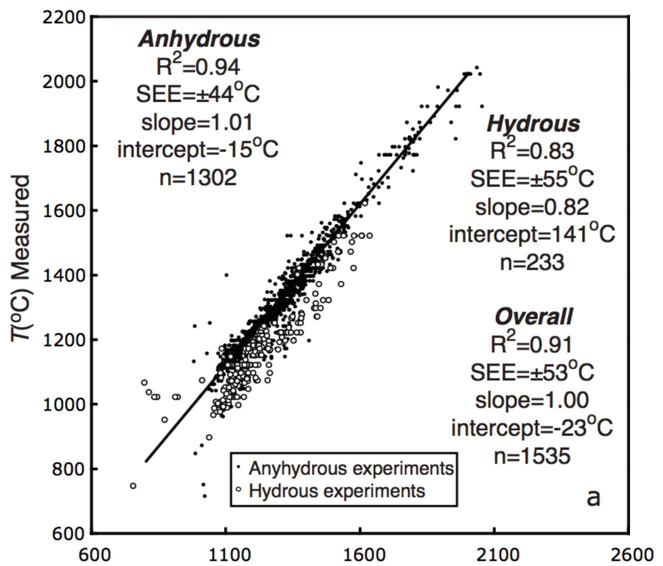

Figure C1 Precision of the Beattie (1993) olivine-liquid thermometer, based on Mg partitioning between olivine and liquid.

The thermometer uses the following equations:

1. $$T°C = \frac{13603+4.943\times10^{-7}(P\times10^{9}-10^{-5})}{6.26+2lnD_{Mg}^{ol-liq}+2\ln\left[1.5\left(C_{NM}^{liq}\right)\right]+2\ln\left[3\left(C_{SiO_2}^{liq}\right)\right]-NF} - 273.15$$

Where

$$C_{NM}^{liq} = X_{FeO}^{liq} + X_{MnO}^{liq} + X_{MgO}^{liq} + X_{CaO}^{liq} + X_{CoO}^{liq} + X_{NiO}^{liq}$$

$$C_{SiO_2}^{liq} = X_{SiO_2}^{liq} + X_{NaO_{0.5}}^{liq} + X_{KO_{0.5}}^{liq} + X_{TiO_2}^{liq}$$

$$NF = \frac{7}{2}\ln\left(1 - X_{AlO_{1.5}}^{liq}\right) + 7\ln\,(1 - X_{TiO_2}^{liq})$$

X_b^a = the cation fraction of b in phase a

For the olivine-absent systems, the following equation must be substituted into equation 1:

$$D_{Mg}^{ol-liq} = \frac{0.666 - (-0.049\times X_{MnO}^{liq} + 0.027\times X_{FeO}^{liq})}{X_{MgO}^{liq} + 0.259\times X_{MnO}^{liq} + 0.2999\times X_{FeO}^{liq}}$$

The temperatures calculated using the olivine-liquid thermometer are believed to be accurate. The range of temperatures is similar to those in other experimental studies on high-alumina basalts (Johnston, 1986; Bartels *et al.* 1991; Fram and Longhi, 1992). The temperatures also fit the trends in the composition of liquids in the experiments, with temperature decreasing with Mg# and melt fraction. Figure C2 shows the calculated temperatures of the baseline and contaminated experiments against the Mg# of the glass in each experiment. Note the slight upturn in temperatures at the lowest Mg#. These low temperature experiments have very low Mg#, and may have run at temperatures too low for all phases to equilibrate in the run times of the experiments. At lower temperatures, the diffusion rates of elements into phases are lower, so more time is required for equilibrium to be reached. Equilibrium is essential for calculating temperatures using geothermometers, so the temperatures of the three most evolved experiments may be less precise.

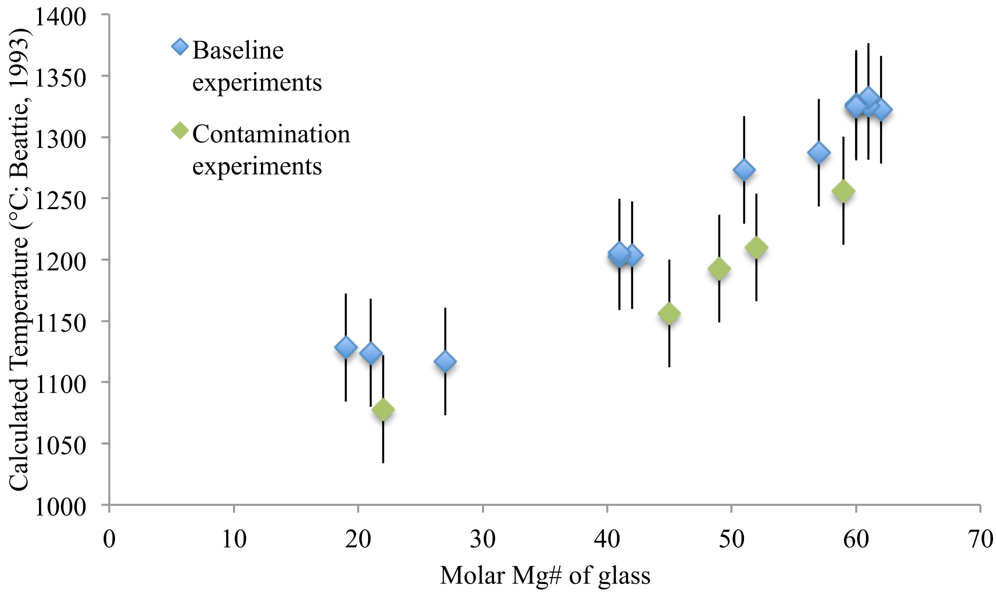

Figure C2 Calculated temperatures for baseline and contaminated experiments with ±44°C error bars, plotted against Mg# of the glass in each experiment.

Appendix D

Major element data for glass and phases in experiments (Major oxides in wt. %).

Table D1 Glasses

	SiO_2	TiO_2	Al_2O_3	FeO*	MnO	MgO	CaO	Na_2O	K_2O	P_2O_5	Total
CMH16-4	47.92	0.81	17.84	10.52	0.11	9.78	9.77	3.09	0.32	0.21	100.37
	47.85	0.88	17.60	10.46	0.08	9.79	9.74	3.04	0.32	0.20	99.95
	47.78	0.79	17.64	10.54	0.07	9.77	9.76	2.73	0.31	0.22	99.59
	47.78	0.92	17.47	10.42	0.09	9.75	9.80	3.09	0.30	0.20	99.83
	47.99	0.75	17.91	10.44	0.13	9.79	9.71	3.02	0.33	0.22	100.29
	47.76	0.87	17.53	10.50	0.09	9.81	9.80	2.99	0.31	0.20	99.86
	47.90	0.92	17.86	10.71	0.13	9.83	9.78	2.94	0.30	0.18	100.54
	48.00	0.88	17.79	10.37	0.08	9.84	9.81	3.13	0.30	0.20	100.41
	47.59	0.79	17.71	10.47	0.11	9.78	9.80	2.85	0.32	0.14	99.55
	47.81	0.87	17.73	10.65	0.12	9.78	9.52	2.95	0.30	0.16	99.89
T1290-1	46.96	0.83	16.87	10.36	0.06	9.04	8.74	2.55	0.29	0.16	95.86
	47.20	0.78	16.68	10.37	0.07	8.98	8.67	2.23	0.29	0.17	95.45
	46.95	0.85	17.09	10.45	0.07	8.99	8.84	2.05	0.30	0.15	95.74
CMH16-11	48.35	0.81	17.68	10.51	0.07	9.29	9.33	3.10	0.31	0.18	99.62
	48.08	0.85	17.70	10.66	0.07	9.34	9.30	3.17	0.30	0.19	99.66
	48.13	0.87	17.84	10.67	0.09	9.36	9.05	3.08	0.28	0.19	99.56
	48.03	0.80	17.72	10.55	0.09	9.37	9.31	3.07	0.30	0.15	99.38
	48.00	0.88	17.96	10.79	0.09	9.37	9.20	3.16	0.30	0.19	99.93
	47.86	0.80	17.85	10.66	0.07	9.26	9.22	3.18	0.29	0.18	99.38
T1350-1	48.99	0.91	17.66	10.94	0.06	9.35	9.17	2.35	0.36	0.17	99.96
	48.93	0.84	17.48	11.04	0.13	9.40	9.03	2.23	0.29	0.12	99.48
	47.44	0.84	16.71	11.03	0.07	9.10	8.79	2.21	0.29	0.13	96.60
	48.85	0.83	17.52	10.88	0.11	9.33	9.12	2.26	0.28	0.18	99.36
	48.71	0.84	17.73	11.04	0.13	9.34	9.18	2.37	0.29	0.18	99.81
	48.82	0.79	17.73	10.97	0.11	9.39	9.01	2.30	0.29	0.11	99.52
	48.84	0.82	17.54	10.91	0.07	9.54	9.10	2.64	0.30	0.24	99.98
	48.84	0.83	17.84	10.94	0.09	9.45	9.02	2.23	0.33	0.22	99.79
	48.76	0.84	17.64	11.14	0.08	9.63	9.27	2.32	0.33	0.15	100.16
	48.64	0.82	17.31	10.88	0.09	9.43	9.11	2.15	0.27	0.17	98.88
T1315-1	48.44	0.87	17.28	10.75	0.08	9.02	8.97	2.66	0.30	0.19	98.55
	48.37	0.82	17.45	10.75	0.11	9.18	9.13	2.27	0.36	0.16	98.59
	48.56	0.87	17.29	10.78	0.08	9.38	9.13	2.56	0.32	0.16	99.15
T1225-1	48.69	0.86	18.51	10.72	0.09	8.01	9.48	2.42	0.34	0.19	99.32
	48.43	0.89	18.47	10.67	0.09	8.05	9.64	2.52	0.33	0.15	99.23
	48.69	1.00	18.42	10.70	0.08	7.93	9.60	2.31	0.31	0.20	99.25
	48.69	0.88	18.61	10.45	0.05	7.73	9.54	2.57	0.30	0.18	99.00
	48.44	0.83	18.38	10.67	0.10	7.84	9.71	2.37	0.32	0.12	98.78
	48.62	0.81	18.39	10.74	0.09	8.05	9.61	2.34	0.34	0.12	99.11
	48.75	0.80	18.47	10.80	0.10	7.93	9.56	2.73	0.33	0.24	99.71
	48.27	0.90	18.74	10.77	0.09	8.03	9.67	2.34	0.31	0.26	99.40
	48.76	0.88	18.34	10.73	0.12	7.97	9.47	2.34	0.35	0.09	99.05
	48.74	0.88	18.35	10.55	0.10	7.98	9.66	2.51	0.32	0.16	99.24
CMH16-6	48.42	1.01	17.49	12.54	0.11	7.50	9.75	2.42	0.39	0.28	99.91
	48.33	0.87	18.38	11.79	0.05	7.27	9.79	2.73	0.38	0.19	99.78
	48.26	0.91	18.25	12.05	0.10	7.31	9.83	2.60	0.41	0.24	99.96
	48.61	1.12	17.55	12.35	0.13	7.32	9.86	2.65	0.42	0.20	100.22
	48.60	1.28	16.58	12.25	0.09	7.50	10.01	2.51	0.38	0.28	99.48
	48.37	1.18	16.91	12.96	0.08	7.27	9.74	2.51	0.40	0.24	99.66
	48.39	1.08	17.84	12.20	0.15	7.25	9.83	2.61	0.37	0.21	99.93
	48.76	1.26	16.86	12.65	0.11	7.10	9.87	2.49	0.41	0.27	99.77
	48.82	1.38	16.60	12.46	0.14	7.28	9.93	2.54	0.38	0.34	99.87
	49.42	1.54	16.11	12.73	0.09	7.17	9.91	2.38	0.40	0.39	100.14
1250-5	49.82	1.63	15.54	13.12	0.14	5.30	9.36	2.44	0.52	0.21	98.09
	49.87	1.66	15.57	12.89	0.12	5.19	9.18	2.82	0.55	0.19	98.04
	49.61	1.70	15.60	13.28	0.11	5.19	9.15	2.67	0.52	0.29	98.12
	49.55	1.63	15.67	13.15	0.15	5.14	9.15	2.47	0.53	0.28	97.72
	49.74	1.54	15.52	12.95	0.13	5.20	9.41	2.82	0.57	0.25	98.12
	49.86	1.63	15.65	12.97	0.09	5.42	9.30	2.46	0.51	0.33	98.23
	49.62	1.65	15.83	13.08	0.12	5.02	9.25	2.85	0.53	0.20	98.15
	49.83	1.80	15.66	12.93	0.11	5.11	8.98	2.65	0.58	0.22	97.86
	49.86	1.71	15.44	12.94	0.12	5.24	9.38	2.75	0.53	0.42	98.41
	49.95	1.57	15.54	13.01	0.16	5.33	9.22	2.53	0.54	0.27	98.10
1200-4	49.00	1.69	16.01	12.98	0.07	4.76	8.91	3.10	0.65	0.41	97.57
	49.36	1.66	16.10	12.92	0.12	4.80	8.60	3.07	0.69	0.28	97.61
	49.42	1.65	16.21	12.78	0.09	4.80	8.73	3.24	0.67	0.29	97.89
	48.49	1.62	16.58	13.05	0.10	4.81	8.53	3.26	0.72	0.25	97.42
	48.72	1.66	16.44	12.53	0.13	5.03	8.86	3.11	0.66	0.27	97.40
	49.08	1.66	16.01	12.92	0.14	5.13	9.07	2.99	0.63	0.25	97.88
	49.14	1.54	15.95	12.88	0.11	5.19	9.13	2.78	0.59	0.31	97.61
	49.36	1.58	16.03	12.67	0.15	5.16	9.03	3.08	0.62	0.24	97.92
	49.26	1.62	16.00	12.95	0.13	5.25	9.17	3.09	0.63	0.26	98.36
	49.67	1.55	16.06	12.65	0.10	5.13	8.99	2.73	0.62	0.17	97.67
CMH16-3	48.80	1.86	16.51	13.40	0.06	5.37	9.06	2.63	0.70	0.43	98.81
	49.04	1.88	16.56	13.52	0.09	5.54	9.25	2.69	0.64	0.44	99.66
	49.29	1.85	16.25	13.32	0.18	5.28	9.04	2.46	0.60	0.38	98.66
	48.90	1.87	14.95	13.53	0.13	4.95	8.57	2.14	0.74	0.36	96.13
	49.41	1.79	15.81	13.32	0.09	5.07	8.74	2.56	0.64	0.34	97.77
	48.99	1.75	16.52	13.49	0.12	5.31	9.11	2.33	0.64	0.37	98.62
	49.67	1.82	16.54	13.34	0.10	5.34	9.00	2.41	0.62	0.41	99.26
1325-1	50.96	1.97	14.88	11.94	0.07	2.50	5.90	2.99	1.58	0.80	93.59
	50.10	2.04	15.08	12.22	0.09	2.52	6.04	3.00	1.63	0.86	93.58
	51.84	2.07	15.06	11.18	0.08	2.47	5.97	2.09	1.33	0.60	92.69
	51.45	2.05	15.14	11.30	0.14	2.44	6.07	2.41	1.34	0.67	92.99
	52.26	2.27	15.16	10.52	0.12	2.12	5.65	1.75	1.42	0.84	92.11
	51.91	1.92	15.34	10.19	0.09	2.14	5.70	2.00	1.40	0.96	91.65
	51.80	2.16	15.62	10.98	0.13	2.44	6.17	1.86	1.36	0.83	93.35
	50.71	2.19	14.71	12.45	0.09	2.24	5.96	2.14	1.36	0.88	92.72
1300-2	51.65	2.00	14.76	14.10	0.15	2.43	7.21	2.14	1.46	1.35	97.24
	50.92	2.33	14.57	15.98	0.11	1.82	7.08	2.43	1.28	1.12	97.64
	51.59	2.06	14.64	14.91	0.13	2.04	6.73	2.49	1.47	1.06	97.12
	51.97	1.98	15.15	14.32	0.19	2.13	6.84	2.42	1.45	0.91	97.37
	51.86	2.10	14.63	14.28	0.12	2.24	6.93	2.35	1.51	1.22	97.23
	52.03	2.04	14.92	14.04	0.13	2.31	7.07	2.48	1.34	1.04	97.40
	51.13	2.04	14.72	15.05	0.12	2.36	7.08	2.07	1.39	1.14	97.11

	SiO_2	TiO_2	Al_2O_3	FeO*	MnO	MgO	CaO	Na_2O	K_2O	P_2O_5	Total
1275-2	50.74	2.22	13.73	16.39	0.18	2.12	6.99	2.75	1.39	0.71	97.24
	50.63	2.20	13.71	15.96	0.14	2.06	7.03	2.61	1.47	0.79	96.61
	50.71	2.13	13.85	16.19	0.11	2.14	6.89	2.74	1.40	0.85	97.01
	50.26	2.67	13.50	16.52	0.10	2.14	7.15	2.71	1.35	0.73	97.13
	50.75	2.09	13.93	15.85	0.17	2.21	6.72	2.77	1.59	0.96	97.03
	51.33	2.18	13.56	16.54	0.14	1.96	6.95	2.81	1.36	0.57	97.40
	53.79	1.95	13.96	14.25	0.16	2.03	6.41	2.99	1.78	0.81	98.14
	52.65	2.15	13.77	15.41	0.09	1.81	6.48	2.87	1.71	0.72	97.66
	51.52	2.23	13.55	15.98	0.13	1.87	6.89	2.91	1.54	0.56	97.20
CMH+ KAC10	56.95	0.79	15.41	7.98	0.14	6.39	7.00	3.03	1.34	0.13	99.16
	56.86	0.71	15.25	8.05	0.08	6.54	6.98	2.75	1.33	0.12	98.67
	56.78	0.68	15.51	7.91	0.13	6.50	7.12	2.79	1.31	0.15	98.88
	56.76	0.76	15.47	7.98	0.08	6.45	7.16	2.76	1.30	0.10	98.81
	56.54	0.79	15.44	8.03	0.07	6.48	7.13	2.71	1.29	0.16	98.64
	56.53	0.72	15.51	8.08	0.08	6.56	7.19	2.98	1.28	0.13	99.06
	56.38	0.81	15.50	8.06	0.08	6.55	7.22	3.00	1.26	0.13	99.00
	56.14	0.75	15.42	8.01	0.05	6.55	7.20	2.83	1.25	0.18	98.38
	56.32	0.73	15.43	8.16	0.11	6.51	7.30	2.63	1.27	0.13	98.58
	56.40	0.74	15.45	8.20	0.06	6.59	7.33	2.71	1.25	0.16	98.88
	56.37	0.76	15.37	8.11	0.07	6.49	7.21	2.75	1.27	0.16	98.55
	56.44	0.72	15.41	8.24	0.09	6.63	7.25	2.82	1.25	0.15	99.00
	56.07	0.73	15.37	8.16	0.13	6.57	7.26	2.90	1.24	0.13	98.56
	56.34	0.77	15.37	8.11	0.09	6.62	7.26	2.86	1.25	0.14	98.81
	56.33	0.73	15.31	8.10	0.08	6.68	7.39	2.93	1.24	0.12	98.92
	56.42	0.71	15.30	8.04	0.11	6.67	7.23	2.73	1.26	0.14	98.61
	56.83	0.75	15.25	8.08	0.06	6.66	7.21	2.95	1.25	0.14	99.17
	56.73	0.76	15.27	8.01	0.08	6.58	7.19	2.81	1.27	0.14	98.83
	57.11	0.68	15.43	7.93	0.11	6.46	7.10	3.04	1.31	0.14	99.32
	57.34	0.70	15.31	7.70	0.09	6.39	7.08	2.86	1.33	0.13	98.92
CMH+ KAC8	57.21	0.80	16.99	7.64	0.07	4.55	6.99	3.23	1.44	0.22	99.13
	57.08	0.83	16.84	7.71	0.04	4.55	6.99	2.93	1.45	0.29	98.71
	56.93	0.87	16.84	7.88	0.07	4.59	7.12	3.06	1.41	0.20	98.96
	56.87	0.81	16.89	7.85	0.09	4.51	7.09	2.79	1.44	0.23	98.58
	56.48	0.86	17.05	7.97	0.11	4.58	7.23	3.02	1.42	0.23	98.95
	56.68	0.81	16.95	8.13	0.06	4.69	7.31	3.02	1.42	0.26	99.31
	57.09	0.82	16.76	7.93	0.06	4.67	7.04	2.92	1.38	0.19	98.85
	56.50	0.84	17.25	8.03	0.11	4.53	7.18	3.00	1.44	0.20	99.08
	57.21	0.77	16.75	7.80	0.08	4.55	7.03	2.92	1.44	0.23	98.78
	57.20	0.86	16.68	7.91	0.06	4.67	7.04	2.85	1.43	0.16	98.86
	57.86	0.79	16.42	7.65	0.09	4.61	7.09	2.98	1.44	0.28	99.20
	57.51	0.77	16.41	7.65	0.11	4.65	7.08	2.99	1.37	0.26	98.79
	57.53	0.78	16.29	7.79	0.10	4.65	7.10	2.64	1.40	0.27	98.55
	57.41	0.82	16.39	7.74	0.06	4.70	7.17	3.03	1.40	0.22	98.94
	57.08	0.78	16.69	7.84	0.08	4.71	7.24	2.93	1.39	0.23	98.95
	57.12	0.80	16.56	7.83	0.08	4.70	7.25	2.98	1.35	0.20	98.85
	57.32	0.82	16.80	7.85	0.09	4.68	7.35	3.04	1.38	0.21	99.55
	57.55	0.77	16.44	7.69	0.11	4.67	7.14	2.91	1.40	0.22	98.89
	57.62	0.73	16.42	7.73	0.10	4.72	7.26	2.89	1.37	0.22	99.05
	57.58	0.73	16.32	7.75	0.06	4.75	7.18	3.00	1.37	0.22	98.96
	57.51	0.84	16.33	7.74	0.09	4.71	7.11	2.96	1.39	0.18	98.87
	57.63	0.81	16.31	7.87	0.08	4.75	7.07	2.85	1.38	0.15	98.91
	57.58	0.78	16.55	7.72	0.09	4.71	7.04	2.95	1.39	0.22	99.02
	57.51	0.78	16.42	7.81	0.08	4.64	7.16	2.83	1.39	0.24	98.84
	57.48	0.87	16.68	7.64	0.06	4.62	7.08	2.90	1.41	0.15	98.90
	57.80	0.81	16.46	7.70	0.10	4.62	6.97	3.23	1.41	0.19	99.30
CMH+ KAC6	57.02	0.80	17.07	7.91	0.12	4.11	6.92	3.02	1.42	0.14	98.53
	57.47	0.77	17.20	7.80	0.09	4.05	7.11	3.17	1.45	0.15	99.27
	57.17	0.84	17.39	7.79	0.07	4.05	7.02	3.11	1.47	0.13	99.04
	57.55	0.86	17.24	7.59	0.06	4.09	7.09	2.95	1.45	0.16	99.03
	57.41	0.79	16.85	7.77	0.11	4.20	6.87	2.98	1.42	0.16	98.56
	57.00	0.88	17.16	7.81	0.01	4.22	7.14	2.94	1.40	0.17	98.73
	57.77	0.82	16.93	7.64	0.09	4.16	7.00	2.78	1.46	0.11	98.76
	57.62	0.83	17.22	7.88	0.07	4.31	6.80	2.98	1.46	0.14	99.30
	57.18	0.78	17.21	7.82	0.12	4.18	7.13	3.07	1.42	0.15	99.05
	57.81	0.78	17.17	7.64	0.07	4.13	6.78	3.26	1.45	0.14	99.24
CMH+ KAC4	58.26	0.89	17.71	7.43	0.05	3.20	7.08	3.46	1.66	0.11	99.84
	57.82	0.78	17.34	7.49	0.10	3.48	7.11	3.24	1.51	0.14	99.01
	58.01	0.82	17.81	7.04	0.07	3.25	7.07	3.04	1.58	0.18	98.88
	57.25	0.88	17.78	7.52	0.05	3.36	7.35	3.32	1.46	0.16	99.14
	57.36	0.80	17.53	7.57	0.06	3.48	7.48	3.28	1.48	0.20	99.22
	57.53	0.85	17.78	7.50	0.09	3.36	7.33	3.14	1.49	0.22	99.28
	58.13	0.86	17.34	7.32	0.06	3.33	6.96	3.16	1.49	0.21	98.85
	58.51	0.78	17.44	6.83	0.06	3.17	7.14	3.24	1.59	0.15	98.90
	57.85	0.85	18.06	7.02	0.04	3.13	7.13	3.22	1.59	0.19	99.07
	58.13	0.84	17.26	7.36	0.11	3.49	7.09	3.32	1.53	0.20	99.34
CMH+ KAC9	61.81	1.56	13.96	8.45	0.11	1.29	5.04	2.84	2.71	0.29	98.06
	61.88	1.59	14.01	8.28	0.06	1.32	5.08	2.71	2.72	0.29	97.93
	61.92	1.53	14.04	8.30	0.08	1.31	5.05	2.69	2.73	0.29	97.95
	61.15	1.55	14.03	8.85	0.07	1.37	5.17	2.53	2.64	0.26	97.62
	61.55	1.49	13.93	8.66	0.05	1.31	5.07	2.74	2.70	0.34	97.84
	61.77	1.64	13.70	8.03	0.08	1.26	4.99	2.69	2.77	0.34	97.28
	62.37	1.61	13.81	8.02	0.06	1.34	4.93	2.63	2.79	0.28	97.84
	62.36	1.43	13.73	8.14	0.11	1.37	4.98	2.81	2.75	0.29	97.97
	62.26	1.51	13.98	8.17	0.03	1.28	4.96	2.96	2.80	0.26	98.21
	61.60	1.77	14.08	8.17	0.07	1.31	5.08	2.78	2.75	0.30	97.90
	61.73	1.68	13.96	8.28	0.07	1.32	5.13	2.71	2.76	0.30	97.94
	61.55	1.46	14.17	8.59	0.07	1.37	5.11	2.73	2.65	0.29	97.98
	61.38	1.45	13.87	8.56	0.08	1.38	5.14	2.66	2.68	0.26	97.44
	61.75	1.63	14.02	8.55	0.09	1.28	5.12	2.67	2.73	0.28	98.12
	62.03	1.45	13.95	8.37	0.07	1.38	5.05	2.77	2.73	0.32	98.12
	61.90	1.50	14.03	8.46	0.07	1.36	5.18	2.85	2.69	0.30	98.34
	62.02	1.70	14.05	8.23	0.09	1.34	5.08	2.79	2.76	0.30	98.34
	62.66	1.53	13.97	8.08	0.09	1.34	4.92	2.84	2.75	0.29	98.47

Table D2 Plagioclase

	SiO_2	TiO_2	Al_2O_3	FeO*	MgO	CaO	Na_2O	K_2O	Total
CMH16-6	51.00	0.04	30.62	0.48	0.21	13.36	3.56	0.10	99.36
	51.32	0.02	30.79	0.49	0.19	13.60	4.07	0.11	100.59
	52.26	0.03	30.61	0.40	0.20	13.08	3.94	0.12	100.64
	51.33	0.04	30.67	0.37	0.20	13.31	3.64	0.13	99.69
	51.29	0.03	30.65	0.35	0.21	13.32	3.95	0.11	99.91
	51.81	0.04	30.58	0.31	0.20	12.90	4.10	0.11	100.05
	51.38	0.04	30.54	0.50	0.19	13.23	4.01	0.11	100.00
	51.64	0.06	30.13	0.50	0.21	13.10	4.01	0.13	99.78
	51.23	0.06	30.82	0.54	0.20	13.40	3.76	0.12	100.13
T1250-5	51.12	0.05	31.34	0.44	0.16	13.91	3.76	0.10	100.88
	51.14	0.05	31.12	0.39	0.19	13.74	3.62	0.09	100.33
	50.53	0.02	30.68	0.58	0.17	13.56	3.99	0.10	99.64
	51.09	0.03	31.16	0.46	0.15	13.71	3.55	0.10	100.26
	51.20	0.05	31.13	0.43	0.16	13.73	3.60	0.09	100.38
	50.97	0.03	31.33	0.41	0.19	13.89	3.64	0.09	100.56
	51.50	0.06	31.26	0.46	0.18	13.62	3.64	0.10	100.83
	50.98	0.02	31.09	0.37	0.21	13.82	3.85	0.10	100.43
	51.62	0.05	30.88	0.43	0.17	13.42	3.88	0.10	100.54
	51.17	0.04	31.09	0.37	0.21	13.77	3.72	0.10	100.47
	51.31	0.04	31.12	0.39	0.17	13.64	3.91	0.10	100.68
	51.17	0.10	30.63	0.90	0.33	13.69	3.64	0.10	100.57
	50.59	0.06	30.66	0.45	0.18	13.56	3.74	0.09	99.32
	51.05	0.04	31.12	0.43	0.17	13.76	3.66	0.11	100.35
	51.28	0.03	31.33	0.37	0.16	13.74	3.88	0.10	100.90
	51.31	0.05	31.11	0.33	0.18	13.61	3.82	0.11	100.51
	51.45	0.03	30.85	0.34	0.16	13.59	3.73	0.09	100.25
	51.45	0.05	31.16	0.44	0.18	13.48	4.46	0.10	101.33
T1200-4	51.84	0.04	30.69	0.50	0.12	12.99	4.32	0.12	100.62
	51.26	0.06	31.21	0.53	0.17	13.57	3.81	0.10	100.72
	51.61	0.06	30.76	0.41	0.14	13.13	4.27	0.11	100.50
	51.13	0.03	30.40	0.62	0.13	13.05	3.96	0.13	99.45
	51.94	0.04	30.98	0.45	0.14	13.27	3.98	0.11	100.91
	51.55	0.03	31.39	0.61	0.15	13.66	3.90	0.11	101.40
	51.24	0.04	31.62	0.37	0.16	13.83	3.68	0.09	101.02
	51.56	0.04	31.36	0.36	0.15	13.58	3.79	0.11	100.95
CMH16-3	50.77	0.09	30.82	0.71	0.31	13.45	3.26	0.13	99.53
	50.81	0.06	30.58	0.54	0.15	13.34	4.02	0.13	99.62
T1325-1	51.32	0.05	30.95	0.45	0.21	13.50	3.58	0.13	100.17
	51.65	0.05	30.84	0.56	0.13	13.32	3.90	0.14	100.59
	51.61	0.07	30.52	0.62	0.17	13.15	3.95	0.14	100.23
	52.59	0.04	30.18	0.52	0.23	12.75	4.30	0.14	100.74
	51.53	0.03	30.62	0.56	0.14	13.22	3.79	0.14	100.03
	51.68	0.06	30.68	0.51	0.16	13.18	4.20	0.16	100.63
	51.66	0.06	30.81	0.48	0.20	13.28	3.65	0.15	100.29
	51.48	0.02	30.24	0.42	0.17	12.82	3.91	0.16	99.21
	51.90	0.05	30.53	0.58	0.15	12.96	3.94	0.17	100.27
	51.94	0.10	30.50	0.65	0.17	13.09	4.15	0.17	100.78
	51.71	0.03	30.29	0.66	0.21	13.04	4.13	0.14	100.22
T1300-2	52.40	0.06	30.40	0.59	0.14	12.84	4.10	0.15	100.68
	51.83	0.05	30.64	0.50	0.16	13.10	3.99	0.14	100.41
	51.65	0.05	30.67	0.49	0.14	13.30	4.12	0.17	100.59
	51.77	0.06	30.84	0.48	0.18	13.16	3.85	0.13	100.48
	52.54	0.07	30.10	0.45	0.13	12.59	4.27	0.20	100.35
	52.05	0.06	30.57	0.53	0.13	12.94	3.93	0.16	100.37
	51.93	0.03	30.72	0.40	0.18	13.37	4.09	0.13	100.85
	52.85	0.08	30.28	0.56	0.11	12.62	4.42	0.18	101.09
	52.38	0.05	30.20	0.61	0.19	12.82	4.20	0.17	100.62
	51.87	0.03	30.57	0.55	0.13	13.05	3.89	0.17	100.26
T1275-2	51.75	0.05	30.46	0.52	0.19	13.14	3.93	0.13	100.16
	51.05	0.06	31.06	0.45	0.20	13.69	3.86	0.11	100.47
	52.09	0.05	30.82	0.54	0.16	13.21	3.93	0.13	100.94
	51.57	0.04	30.37	0.54	0.15	13.00	4.02	0.16	99.86
	51.67	0.06	30.16	0.58	0.21	12.85	4.07	0.14	99.75
	52.07	0.07	29.94	0.49	0.16	12.73	4.30	0.16	99.92
	53.52	0.05	30.59	0.51	0.16	12.31	4.50	0.18	101.83
	52.06	0.02	30.40	0.36	0.22	12.88	4.19	0.15	100.27
CMH+ KAC4	57.02	0.34	23.22	3.05	1.92	8.97	4.90	0.85	100.28
	56.92	0.30	24.23	2.01	0.74	9.32	4.93	0.78	99.23
	57.69	0.34	24.22	2.34	0.79	9.01	5.18	0.85	100.42
	58.19	0.46	22.73	3.47	1.45	8.63	5.05	0.95	100.92
CMH+ KAC9	54.74	0.07	28.47	0.53	0.11	11.30	4.71	0.47	100.39
	54.63	0.06	28.28	0.54	0.11	11.37	4.70	0.48	100.16
	56.48	0.06	27.44	0.61	0.16	10.45	5.10	0.54	100.83
	56.59	0.07	27.13	0.56	0.16	10.05	5.13	0.54	100.23
	55.74	0.08	27.80	0.52	0.18	10.77	5.10	0.46	100.65
	55.99	0.07	27.60	0.37	0.14	10.54	5.05	0.56	100.31
	55.62	0.06	27.89	0.32	0.15	10.90	4.80	0.52	100.26
	55.49	0.03	28.46	0.43	0.16	11.35	4.64	0.45	101.02
	55.51	0.07	28.27	0.58	0.14	11.00	4.89	0.54	100.99
	56.14	0.04	27.97	0.48	0.15	10.73	4.84	0.48	100.83
	54.34	0.06	29.14	0.57	0.10	11.74	4.53	0.44	100.91
	55.68	0.04	28.15	0.61	0.17	11.02	4.68	0.46	100.80
	56.28	0.06	27.59	0.51	0.17	10.44	5.11	0.48	100.64
	55.43	0.07	28.14	0.57	0.12	11.01	4.90	0.50	100.75
	55.39	0.05	27.96	0.49	0.15	10.72	4.99	0.50	100.24

Table D3 Orthopyroxene

	SiO_2	TiO_2	Al_2O_3	FeO*	MnO	MgO	CaO	Na_2O	Total
CMH16-3	52.14	0.28	4.20	13.38	0.13	26.39	2.46	0.04	99.03
	50.38	0.30	6.20	12.45	0.15	25.86	2.32	0.09	97.75
	51.13	0.35	6.42	13.20	0.11	25.96	2.25	0.16	99.58
	51.43	0.33	5.27	13.20	0.12	26.19	2.40	0.08	99.02
	51.75	0.27	5.80	13.05	0.15	26.30	2.36	0.08	99.77
	52.19	0.31	5.40	12.71	0.14	26.45	2.86	0.06	100.13
	51.75	0.29	5.88	12.65	0.16	26.59	2.24	0.05	99.59
	52.15	0.28	5.61	13.03	0.12	26.69	2.15	0.08	100.11
	51.75	0.30	5.85	12.82	0.12	26.40	2.29	0.06	99.58
CMH+ KAC10	54.49	0.18	2.69	11.89	0.16	28.98	1.39	0.02	99.80
	54.13	0.17	3.16	11.90	0.17	28.74	1.52	0.03	99.82
	54.07	0.20	3.60	11.97	0.14	28.72	1.39	0.04	100.13
	53.98	0.17	3.17	11.94	0.15	28.77	1.61	0.04	99.83
	54.35	0.18	3.04	11.90	0.13	28.95	1.44	0.04	100.03
	54.39	0.21	3.10	11.39	0.13	28.66	1.69	0.08	99.65
	54.39	0.16	2.39	12.00	0.14	28.87	1.43	0.02	99.40
	54.13	0.18	3.24	11.92	0.15	28.90	1.35	0.07	99.94
	54.10	0.17	3.27	11.93	0.14	28.81	1.43	0.03	99.88
	54.16	0.18	3.07	11.86	0.12	28.82	1.50	0.03	99.74
CMH+ KAC8	53.66	0.21	3.74	12.43	0.15	28.26	1.53	0.04	100.00
	53.76	0.21	4.13	12.79	0.13	28.22	1.60	0.03	100.87
	53.29	0.22	4.65	12.58	0.14	28.08	1.55	0.05	100.57
	54.96	0.18	3.46	11.46	0.13	29.88	1.42	0.05	101.54
	53.71	0.22	4.19	12.75	0.14	27.92	1.63	0.06	100.62
	53.07	0.20	4.00	12.57	0.13	27.54	1.71	0.03	99.24
	53.61	0.23	4.56	12.16	0.15	28.43	1.56	0.05	100.76
	54.00	0.19	3.81	11.10	0.11	29.29	1.27	0.03	99.79
	53.93	0.20	4.16	12.45	0.13	28.26	1.51	0.02	100.65
	54.23	0.18	3.19	11.77	0.11	29.27	1.32	0.04	100.12
	54.59	0.13	2.14	11.35	0.11	29.67	1.33	0.03	99.35
	54.78	0.13	2.22	12.12	0.15	29.42	1.45	0.05	100.32
	54.20	0.16	3.45	11.35	0.16	29.42	1.34	0.09	100.17
	54.13	0.18	3.63	11.65	0.15	29.14	1.41	0.02	100.31
	54.59	0.17	3.25	11.59	0.16	29.44	1.43	0.02	100.65
	53.72	0.19	3.42	11.87	0.18	28.71	1.50	0.01	99.60
	54.28	0.17	3.47	11.67	0.16	29.25	1.35	0.03	100.38
	53.78	0.19	3.69	11.72	0.10	28.93	1.34	0.05	99.80
	53.18	0.22	3.88	12.15	0.17	28.09	1.71	0.05	99.45
	53.75	0.20	4.15	12.34	0.14	28.47	1.53	0.05	100.63
	54.00	0.21	4.19	12.22	0.15	28.52	1.52	0.06	100.87
	54.19	0.19	3.55	11.06	0.15	29.69	1.27	0.05	100.15
	54.63	0.17	3.27	11.55	0.13	29.68	1.27	0.01	100.71
	53.95	0.17	3.24	11.39	0.12	29.30	1.26	0.01	99.44
CMH+ KAC6	54.41	0.19	3.42	12.27	0.14	28.84	1.32	0.03	100.62
	54.01	0.19	3.49	12.48	0.12	28.78	1.35	0.05	100.48
	53.56	0.22	4.20	12.66	0.16	28.11	1.33	0.03	100.29
	54.95	0.14	2.20	12.76	0.14	28.54	1.85	0.08	100.65
	53.94	0.20	3.76	12.84	0.16	28.10	1.43	0.05	100.48
	54.40	0.18	3.82	12.06	0.13	28.99	1.29	0.05	100.93
	54.27	0.19	2.19	13.83	0.18	27.00	2.49	0.09	100.25
	53.65	0.21	4.00	12.77	0.15	27.99	1.34	0.01	100.12
CMH+ KAC4	52.08	0.25	4.29	13.74	0.17	25.45	2.87	0.11	98.95
	53.00	0.25	3.94	13.49	0.19	26.01	2.82	0.10	99.79
	53.43	0.24	3.40	13.16	0.17	26.65	2.59	0.06	99.70
	54.56	0.18	2.81	13.37	0.17	27.18	2.58	0.11	100.96
CMH+ KAC9	49.67	0.35	8.03	16.33	0.19	22.88	2.14	0.09	99.68
	50.67	0.43	4.60	19.15	0.20	21.96	2.06	0.08	99.15
	51.06	0.37	5.57	18.07	0.19	22.96	1.95	0.03	100.20

Table D4 Augite

	SiO_2	TiO_2	Al_2O_3	FeO*	MnO	MgO	CaO	Na_2O	Total
T1200-4	51.13	0.73	5.92	11.48	0.15	17.63	0.29	13.28	100.61
	51.89	0.62	4.38	13.26	0.20	19.34	0.26	10.61	100.55
CMH16-3	48.84	1.11	4.47	16.83	0.24	14.93	12.65	0.29	99.37
	49.03	0.83	3.30	20.68	0.28	16.77	7.41	0.10	98.41
	49.35	0.92	3.49	19.46	0.19	16.67	8.04	0.17	98.29
	49.09	0.66	3.20	19.21	0.25	17.22	7.98	0.15	97.75
	47.77	1.11	3.47	20.38	0.22	13.55	10.89	0.25	97.65
	47.96	1.17	3.74	19.89	0.25	14.65	9.95	0.23	97.84
	48.59	1.31	5.40	14.13	0.20	14.22	14.96	0.36	99.17
	48.42	1.63	5.01	13.67	0.18	14.11	15.29	0.30	98.61
	48.20	1.15	3.80	19.55	0.28	13.84	11.41	0.23	98.46
T1325-1	47.77	2.31	5.24	13.67	0.18	11.02	0.31	18.62	99.11
	48.87	1.94	4.30	13.85	0.18	12.47	0.27	17.41	99.28
	48.30	2.15	4.59	15.16	0.20	12.18	0.28	16.60	99.45
	47.62	2.34	5.22	14.59	0.21	11.62	0.27	17.26	99.13
	48.84	2.03	4.10	13.93	0.21	12.87	0.27	16.98	99.23
T1300-2	49.96	0.95	2.83	21.45	0.25	13.79	0.18	9.48	98.89
	50.02	0.84	3.08	20.98	0.27	14.77	0.22	9.98	100.14
	51.01	0.70	1.46	21.71	0.28	13.94	0.14	11.00	100.25
T1275-2	48.95	1.62	4.09	17.61	0.25	11.96	0.26	15.26	100.01
	49.43	1.19	3.96	17.31	0.26	13.56	0.27	14.28	100.27
	48.25	2.04	4.99	17.77	0.23	11.30	0.40	15.59	100.56
	49.00	1.74	5.01	15.67	0.20	12.47	0.35	15.90	100.32
	48.31	2.10	5.93	14.26	0.20	12.30	0.36	16.59	100.05

Table D5 Pigeonite

	SiO_2	TiO_2	Al_2O_3	FeO*	MnO	MgO	CaO	Na_2O	Total
CMH16-6	51.03	0.56	7.99	12.44	0.15	22.02	7.04	0.23	101.47
	52.36	0.37	6.08	13.18	0.14	24.43	4.49	0.14	101.18
	51.00	0.64	7.48	12.32	0.16	21.73	7.48	0.18	100.98
T1325-1	50.08	0.63	1.92	23.36	0.31	16.02	0.14	6.27	98.72
	50.32	0.77	2.68	22.37	0.28	16.63	0.13	6.20	99.38
T1300-2	51.80	0.40	1.18	23.44	0.31	17.56	0.05	5.30	100.05
1275-2	49.93	0.76	2.49	23.75	0.29	13.51	0.15	9.21	100.09
	50.17	1.16	3.00	21.71	0.23	16.04	0.17	7.82	100.31
	48.60	1.55	3.72	22.69	0.26	12.46	0.18	10.90	100.36
CMH+ KAC4	52.57	0.30	4.29	15.08	0.20	23.64	4.41	0.14	100.62
	52.62	0.31	4.19	14.10	0.19	25.03	3.65	0.12	100.21
	52.14	0.28	4.76	13.75	0.18	24.97	3.19	0.09	99.36
	52.49	0.26	4.04	14.38	0.18	24.64	3.87	0.16	100.02
	51.49	0.28	5.02	14.92	0.20	23.32	3.88	0.16	99.27
	52.18	0.30	4.92	14.64	0.19	23.87	4.25	0.12	100.47
	52.84	0.31	4.85	13.74	0.20	25.20	3.62	0.09	100.84
	52.55	0.35	4.60	14.02	0.20	24.76	3.96	0.10	100.54
	51.66	0.35	5.50	14.73	0.18	22.77	5.20	0.14	100.53
	52.23	0.32	4.70	14.29	0.19	24.15	4.12	0.07	100.07
	51.16	0.36	4.98	14.68	0.21	22.55	5.10	0.15	99.20
	52.55	0.29	4.11	14.06	0.18	24.71	3.85	0.13	99.88
CMH+ KAC9	50.74	0.47	2.14	22.63	0.28	16.87	5.82	0.14	99.09
	50.83	0.49	3.36	20.77	0.25	18.62	5.38	0.08	99.78
	50.84	0.51	3.64	19.83	0.30	18.68	5.78	0.12	99.70
	50.42	0.57	3.31	20.86	0.28	16.98	7.07	0.11	99.60
	50.56	0.72	4.80	18.06	0.23	18.80	6.36	0.20	99.73
	50.99	0.46	3.46	19.73	0.23	19.30	5.22	0.15	99.54
	50.66	0.48	2.26	22.65	0.24	16.85	5.85	0.12	99.11

Table D6 Olivine

	SiO_2	TiO_2	Al_2O_3	FeO*	MnO	MgO	CaO	Na_2O	Total
T1225-1	38.90	0.02	0.13	17.99	0.15	41.92	0.01	0.24	99.34
	39.18	0.02	0.05	17.62	0.14	42.62	0.01	0.23	99.86
	39.10	0.01	0.08	17.95	0.10	42.46	0.00	0.25	99.95
CMH16-6	38.96	0.04	0.04	22.49	0.14	39.80	0.35	0.04	101.86
	38.86	0.04	0.07	23.39	0.18	39.02	0.40	0.02	101.99
	38.25	0.03	0.07	22.18	0.16	39.50	0.36	0.02	100.57
T1250-5	37.30	0.05	0.04	27.21	0.19	35.34	0.00	0.26	100.39
	37.83	0.04	0.01	27.77	0.20	35.18	0.00	0.27	101.30
	38.13	0.02	0.05	25.84	0.20	36.95	0.02	0.25	101.47
	37.69	0.03	0.04	26.76	0.18	35.93	0.00	0.27	100.90
	38.46	0.02	0.02	24.45	0.19	37.57	0.00	0.32	101.04
	38.20	0.02	0.04	25.65	0.19	36.75	0.00	0.27	101.12
	38.24	0.02	0.05	24.40	0.17	37.87	0.00	0.27	101.04
T1200-4	38.58	0.04	0.03	23.46	0.17	38.64	0.00	0.27	101.18
	37.59	0.01	0.06	24.97	0.17	36.84	0.05	0.28	99.96
	38.24	0.02	0.07	25.00	0.18	37.07	0.00	0.33	100.91
	38.26	0.02	0.05	26.30	0.17	36.54	0.04	0.32	101.70
	37.82	0.03	0.03	24.45	0.19	37.48	0.03	0.29	100.33
CMH16-3	37.42	0.01	0.07	24.04	0.14	37.67	0.31	0.00	99.67
	37.47	0.03	0.04	24.08	0.19	37.41	0.33	0.00	99.57
	37.37	0.03	0.06	24.82	0.15	36.98	0.36	0.00	99.76
	37.38	0.03	0.03	25.69	0.18	36.50	0.33	0.03	100.17
	37.41	0.04	0.06	25.55	0.20	36.37	0.37	0.02	100.01
	37.48	0.04	0.06	24.28	0.14	37.54	0.31	0.02	99.86
	37.12	0.02	0.02	25.91	0.16	36.10	0.35	0.01	99.69
T1325-1	36.91	0.03	0.00	31.51	0.21	31.15	0.00	0.35	100.15
	36.55	0.04	0.02	32.51	0.22	29.89	0.01	0.35	99.60
	36.53	0.04	0.01	33.46	0.23	29.42	0.00	0.35	100.03
	36.75	0.03	0.03	32.09	0.25	30.68	0.00	0.34	100.17
T1300-2	36.53	0.06	0.03	31.86	0.22	30.97	0.00	0.28	99.95
	36.91	0.03	0.04	32.30	0.23	31.00	0.00	0.31	100.83
	37.17	0.04	0.01	29.59	0.22	32.95	0.00	0.25	100.24
T1275-2	37.15	0.03	0.06	29.80	0.20	33.38	0.06	0.34	101.03
	37.22	0.04	0.02	31.07	0.23	32.26	0.01	0.35	101.20
	36.79	0.06	0.01	31.73	0.25	31.64	0.02	0.41	100.90

Table D7 Ilmenite

	TiO_2	Al_2O_3	FeO*	MnO	MgO	Total
T1325-1	52.27	0.36	42.24	0.26	3.97	99.10
	52.47	0.36	42.04	0.26	4.05	99.18
	52.56	0.37	41.38	0.22	4.52	99.04
	52.32	0.36	41.08	0.20	4.53	98.50
	52.65	0.35	42.21	0.23	3.95	99.38
	52.11	0.39	41.78	0.27	4.28	98.83
	52.12	0.38	41.56	0.26	4.28	98.61
	52.50	0.39	41.73	0.26	4.21	99.10
	52.34	0.34	41.68	0.24	4.15	98.76
T1275-2	51.34	0.32	45.40	0.28	2.19	99.54
	52.14	0.31	44.18	0.29	2.62	99.54
	50.96	0.42	44.11	0.26	2.39	98.13
	52.07	0.32	44.68	0.26	2.61	99.92
	51.83	0.34	44.59	0.20	2.78	99.74
	52.29	0.29	44.67	0.22	2.49	99.96
	52.14	0.28	44.33	0.23	2.66	99.65
T1300-2	51.75	0.33	43.13	0.23	3.14	98.58
	52.19	0.31	43.74	0.26	3.06	99.55
	52.09	0.32	43.49	0.26	3.02	99.17
	52.20	0.41	43.54	0.25	2.86	99.27
	52.56	0.31	43.60	0.28	2.88	99.65
	52.19	0.32	43.89	0.21	3.06	99.67
	52.23	0.30	43.56	0.25	3.01	99.35
	52.04	0.38	43.30	0.25	3.19	99.15